LBNE-INDIA

Proposal of Indian Institutions and Fermilab Collaboration for Participation in the Long-Baseline Neutrino Experiment at Fermilab

(*A Proposal to Design and Build a High-Resolution Near Detector and to Contribute to the Liquid Argon Far Detector*)

to

Department of Atomic Energy and

Department of Science and Technology

Government of India

Edited by

Brajesh Choudhary, Raj Gandhi, Sanjib R. Mishra, Shekhar Mishra and James Strait

Indian Institutions and Fermilab Collaboration

12 December 2012

Contents

Contents i

List of Figures v

List of Tables ix

1 LBNE-India: Executive Summary 1

2 LBNE-India: Science Case 6
2.1 Why is Neutrino Physics Important? . . . 8
2.2 The Long-Baseline Neutrino Experiment: An Opportunity for India . . . 11
2.2.1 Overview of LBNE . . . 11
2.2.2 Proposal to Build an LBNE Near Detector . . . 12
2.2.3 Proposal to Contribute to the LBNE Far Detector . . . 13
2.3 LBNE Physics Goals and Capabilities . . . 13
2.3.1 Overall Science Goals . . . 13
2.3.2 Sensitivities Required to Achieve LBNE's Primary Physics Objectives . 15
2.3.3 Near Detector Measurements Required to Achieve LBNE's Primary Objectives . . . 17
2.4 The Role and Importance of a Near Detector for LBNE . . . 17
2.5 Principal Goals of the Proposed Near Detector . . . 18
2.6 The LBNE Near Detector as an Indigenous Indian Effort: Rich in Benefits and Spin-offs . . . 18
2.6.1 Manpower Training and Development . . . 19
2.6.2 Technical Knowledge Transfer Resulting from Close Collaboration . . . 19
2.6.3 Synergy with the Indian Neutrino Observatory (INO) Program . . . 20
2.6.4 Significant International Partnership and DAE/DST Ownership . . . 21
2.7 Potential Benefits from Significant Participation in the LBNE Far Detector Project 22
2.8 Technical and Logistical Challenges . . . 22

3 An Overview of the High Resolution Near Detector for LBNE 24
3.1 Goals of the Near Detector . . . 24
3.2 Detector Components and Geometry . . . 26
3.3 Salient Features of the Detector . . . 30
3.4 Neutrino Event Pictures as Expected in the Proposed Detector . . . 32

3.5 Measurable Quantities . . . 33
3.6 Expected Detector Resolutions . . . 34
3.7 The LBNE Beam . . . 36
3.8 Expected Statistics . . . 36
3.9 Challenges of Precision Oscillation Studies at LBNE . . . 36
3.10 Trigger and Rates . . . 42

4 The Detector Design **44**
4.1 Straw Tube Tracker . . . 44
4.2 Electromagnetic Calorimeter . . . 48
4.3 Dipole Magnet . . . 49
4.4 Muon-ID Detector . . . 52
4.5 Detector Assembly . . . 58

5 Physics Sensitivity Studies **65**
5.1 Momentum-Measurement of Particles and Particle-ID . . . 65
5.2 Charged Particle Measurement . . . 65
5.3 Electron-ID: Transition Radiation . . . 66
5.4 Electromagnetic Shower Measurement in ECAL . . . 67
5.5 Proton ID and Charged-Kaon ID . . . 67
5.6 Neutrino and Antineutrino Flux Measurement . . . 68
5.7 Low-Energy Absolute Flux: Neutrino-Electron Neutral Current Scattering . . . 70
5.8 High-Energy Absolute Flux: Neutrino-Electron Charged Current Scattering . . . 72
5.9 Low-Energy Absolute Flux: QE in Water and Heavy-Water Targets . . . 74
5.10 Relative Neutrino and Antineutrino Flux Measurement and the FD/ND Ratio . . . 76
5.10.1 Flavor Content of the Beam: $\boldsymbol{\nu_\mu, \bar{\nu}_\mu, \nu_e, \bar{\nu}_e}$ . . . 82
5.10.2 Effects of High Δm^2 Oscillations on the Flux Extraction . . . 83
5.10.3 External Constraints from Hadro-production Measurements . . . 84
5.11 Quasi-Elastic Interaction . . . 84
5.12 Sensitivity Studies of ν_e-CC and $\bar{\nu}_e$-CC . . . 88
5.13 Measurement of Neutral Pions, Photons, and $\pi^\pm$ in Neutral and Charged Current Events . . . 93
5.14 Measurement of Strange Mesons and Hyperons in ν-Interactions . . . 98
5.15 Constraining the Neutrino-Induced Background to Proton Decay . . . 98
5.16 Measurement of Neutral Current Events . . . 100
5.17 Electroweak Precision Measurment: Weak Mixing Angle . . . 104
5.18 Strangeness Content of the Nucleon . . . 108
5.19 Isospin Physics and Sum-Rules . . . 112
5.20 Nucleon Structure, Parton Distribution Functions, and QCD Studies . . . 113
5.21 Neutrino-Nuclear Interactions and Nuclear Effects . . . 115
5.22 Search for Heavy Neutrinos . . . 117
5.23 Search for Non-Standard Interactions: High Δm^2 Neutrino Oscillations . . . 119

6 The R&D Plans for Near Detector **122**

6.1 Simulation Studies . . . 122
6.2 R&D for the Straw Tube Tracker . . . 123
6.3 R&D for the Electromagnetic Calorimeter . . . 124
6.4 R&D for the Muon-ID Detector . . . 124
6.5 Prototyping . . . 124

7 Near Detector Fabrication and Manufacturing Infrastructure 125
7.1 Fabrication of the Straw Tube Tracker . . . 125
7.1.1 Fabrication Steps . . . 125
7.1.2 Nuclear Targets . . . 134
7.1.3 STT Fabrication Laboratories/Factories . . . 138
7.2 Fabrication of the Electromagnetic Calorimeter . . . 142
7.2.1 Fabrication Steps . . . 142
7.2.2 ECAL Fabrication Laboratories/Factories . . . 144
7.3 Fabrication of the Dipole Magnet . . . 144
7.4 Fabrication of the the Muon-ID Detector . . . 145
7.5 Role of Industries . . . 145
7.6 Schedule for the Fabrication . . . 145
7.7 Preliminary Engineering Drawings (STT, ECAL, Assembled Detector) . . . 145

8 Proposed Contribution to the Liquid Argon Far Detector 148
8.1 Overview of the Liquid Argon Far Detector . . . 148
8.1.1 Cryostat Construction . . . 149
8.1.2 Cryogenic and LAr Purification Systems . . . 149
8.1.3 Time Projection Chamber . . . 153
8.1.4 Electronics, Readout and Data Acquisition . . . 153
8.1.5 Photon-Detection System . . . 157
8.2 Potential Areas of Indian Contribution to the LBNE Far Detector . . . 157

9 LBNE-India: Project Management and Execution 160
9.1 Management . . . 160
9.2 Timeline . . . 160
9.3 Near Detector Technology Selection and Review . . . 161

A Expected Physics Papers from HIRESMNU 163

References 173

List of Figures

2–1 Phased timeline for LBNE 7
2–2 A comparison of masses of particles in the Standard Model, from [1]. 9
2–3 Schematic view of the LBNE underground detector option 13
2–4 3σ sensitivities for Θ_{13}, mass hierarchy and CP violation 15
2–5 (Anti)neutrino event rates for unoscillated and oscillated ν_μ spectra 16
2–6 Accelerator and atmospheric neutrino parameter sensitivities for LBNE 16

3–1 Sketch of the proposed HIRESMNU detector 27
3–2 Layout of the HIRESMNU with external, downstream muon-ID detector 28
3–3 Candidate NC Event in a Calorimeter vs Active-Tracker 29
3–4 A ν_μ CC Event Candidate in NOMAD 32
3–5 A $\bar{\nu}_e$ CC Event Candidate in NOMAD 33
3–6 Reconstruction of event kinematics in ECAL 34
3–7 A neutrino radiograph of the NOMAD drift chambers 35
3–8 **p** resolution of a $\nu_\mu(\bar{\nu}_\mu)$-CC induced μ^- (μ^+) and $\nu_e(\overline{\nu}_e)$-CC induced e^- (e^+) . 35
3–9 Schematic of the LBNE neutrino beamline 37
3–10 Composition of ν_μ-CC, $\mu^- X$ at a Near Location 38
3–11 Compilation of the inclusive ν_μ-nucleon cross section measurements 40
3–12 Compilation of the inclusive $\bar{\nu}_\mu$-nucleon cross section measurements 41
3–13 Neutrino quasi-elastic cross section by NOMAD and MiniBOONE experiments 42

4–1 Layout of the straw layers and cross section of an STT Module. 46
4–2 Sketch of a basic STT module for the measurement of nuclear effects 46
4–3 Schematic of the ATLAS STT Endplug 47
4–4 Schematic of the STT Readout. 48
4–5 Preliminary Schematic of the DownStream or Forward ECAL. 50
4–6 DownStream (DS) or Forward ECAL 50
4–7 Specifications of the Barrel ECAL 51
4–8 UpStream (UP) ECAL 51
4–9 Magnet yoke assembly of the UA1/NOMAD dipole magnet. 53
4–10 Yoke and coil of the UA1/NOMAD dipole magnet. 53
4–11 Coil and coil-assembly of the UA1/NOMAD dipole magnet. 54
4–12 Specs of the UA1/NOMAD dipole magnet. 54
4–13 Sketch of one of the C-sections constituting the magnet return yoke 55
4–14 Cross section of a Resistive Plate Chamber 57

4–15 Preliminary engineering drawing of STT with the DS and US ECAL 59
4–16 STT with the DS and US ECAL: YZ View 60
4–17 STT with the DS and US ECAL on the rack 61
4–18 STT with the DS and US ECAL with muon-ID detector 62
4–19 Isometric and YZ views of a half-size detector; the neutrino is incident from the right in the YZ view. 63
4–20 Top and XY views of the fully assembled half-size detector. 64

5–1 p resolution of a $\nu_\mu(\bar{\nu}_\mu)$-CC induced μ^- (μ^+) and $\nu_e(\overline{\nu_e})$-CC induced e^- (e^+) . 66
5–2 Comparison of the TR of a 5 GeV muon and a 2 GeV electron. 67
5–3 Electron TR-ID Efficiency as a function of the electron momentum 68
5–4 The dE/dx plot for ν_μ-induced QE and background proceses 69
5–5 Comparison of Θ and ζ distributions of NuElas signal and background 72
5–6 Comparison of derived and incident E_ν 73
5–7 The ζ distribution of the μ^- from IMD and the background 75
5–8 Relative ν_μ flux using Low-ν_0 method 78
5–9 Relative $\bar{\nu}_\mu$ flux using Low-ν_0 method 78
5–10 Effect of QE and Res variations on the relative ν_μ flux using Low-ν_0 method . 79
5–11 Model errors estimated in the relative ν_μ and $\bar{\nu}_\mu$ flux using Low-ν_0 method . . 80
5–12 Effect of E_μ- and E_{Had} energy scale variation on the ν_μ flux using Low-ν_0 method 81
5–13 The ν_μ-QE events where μ^- and p are reconstructed, the 2-Track QE topology 86
5–14 Multivariate (NN) separation of the QE-signal from the Res/DIS-background . 87
5–15 The efficiency and purity of ν_μ-QE induced $\mu^- p$ topology in HIRESMNU. . . . 88
5–16 Histogram of $E_{Vis} - E_\nu$ for the 2-Track QE-candidates in NOMAD 89
5–17 Cross-section of QE vs E_ν for 1-Track and 2-Track topologies in NOMAD. . . 90
5–18 Comparison of kinematic quantities between the e^- and μ^- events 91
5–19 Efficiency and purity of the ν_e-CC sample as a function of the ν_e-energy 92
5–20 An exclusive two-photon event in NOMAD. 94
5–21 Another exclusive two-photon event in NOMAD. 94
5–22 π^0 reconstruction efficiency as a function of π^0 energy in NC events, HIRESMNU. 95
5–23 Reconstruction of π^0 in inclusive ν_μ-CC events in NOMAD (preliminary). . . . 96
5–24 Reconstruction of π^0 in inclusive NC events in NOMAD (preliminary). 97
5–25 NOMAD events with a single visible photon 99
5–26 Reconstructed V^0's in ν_μ CC event candidate in NOMAD 100
5–27 Reconstructed K^0_S in NOMAD. 101
5–28 The measured Armenteros plot of detached vertices in NOMAD. 102
5–29 No-Muon Sample: Kinematic correlations in CC and NC events 103
5–30 Feynman diagrams for the three main Neutral Current processes 104
5–31 Expected sensitivity to $\sin^2\theta_W$ from the LBNE ND for a 700 kW beam 108
5–32 Sensitivity of NC/CC to strange contribution to spin of nucleon 111
5–33 Feynman diagrams pertaining to sterile neutrinos 118

7–1 Straw Tube Tracker Module Assembly: Steps 1 and 2 131
7–2 Straw Tube Tracker Module Assembly: Step 3 132

7–3 Straw Tube Tracker Module Assembly: Step 4. 133
7–4 Straw Tube Tracker Module Assembly: Step 5. 134
7–5 Straw Tube Tracker Module Assembly: Layout and sealing the module. 135
7–6 Straw Tube Tracker Module Assembly: Step 6. 136
7–7 Straw Tube Tracker front-end board 136
7–8 Straw Tube Tracker high-voltage and ground board 137
7–9 Straw Tube Tracker Circuit Board 137
7–10 Straw Tube Tracker module 138
7–11 Straw Tube Tracker Basket 139
7–12 Straw Tube Tracker Basket Assembly 140
7–13 Module of argon gas in pressurized tube, positioned upstream of the STT . . . 141
7–14 Assembly of STT and Barrel-ECAL embedded in the dipole 146
7–15 (Preliminary engineering drawing) Assembly of the complete HIRESMNU. . . 147

8–1 FD Configuration 150
8–2 Plan view of the two-cryostat detector showing trusswork on top of detector . . 151
8–3 Vertical slice of detector (cross section C-C in Figure 8–4) 152
8–4 TPC modular construction concept 154
8–5 Conceptual front-end electronics architecture 155
8–6 Block diagram of the DAQ conceptual architecture 156
8–7 Photon detection system 158

List of Tables

3–1 Improved subdetectors in HIRESMNU compared to NOMAD 31
3–2 Expected Events in a 5-Year ν-Run 39

4–1 Parameters of the UA1/NOMAD dipole magnet 52

5–1 Precisions achievable from in situ ν_μ and ν_e flux measurements 70
5–2 NuElas Selection Cuts 71
5–3 IMD selection and backgrounds 74
5–4 Uncertainties on the $\mathcal{R}^\nu$ measurement, NuTeV vs LBNE 106
5–5 Coefficients entering Equation 5.10 for NC elastic scattering 109
5–6 Expected proton range for the low-density ($\rho \sim 0.1\ g/cm^3$) tracker 111

1 LBNE-India: Executive Summary

A striking development in neutrino physics is the discovery that the three kinds of neutrinos have very small masses and can oscillate from one kind to another, a fact which starkly differs from the tenets of the Standard Model. Neutrinos have shown us details of the solar core, provided clues to the mechanism of supernova explosions, and most likely play an important role in the early Universe. They may even be responsible for the observed preponderance of matter over antimatter. These properties imply that neutrinos play critical roles across many fields of physics and make them uniquely suitable as probes.

Physicists have learned much over the past decade about building and operating large neutrino detectors and intense neutrino beams. The unique capabilities and accelerator infrastructure at Fermilab together with a far detector site 1,300 km away — a distance optimal for oscillation studies and not currently available at any existing facility — at the Sanford Underground Research Facility (SURF) at the former Homestake mine in Lead, South Dakota, present an extraordinary opportunity to develop a world-leading program of long-baseline neutrino science.

The proposed Long-Baseline Neutrino Experiment (LBNE) aims to measure the parameters that characterize three-flavor neutrino oscillations, study a phenomenon known as CP-violation, which may help explain the matter-antimatter imbalance, and determine the relative ordering of neutrino masses.

The LBNE Project is currently organized into four second-level projects: Beamline, Near Detector Systems, Liquid Argon Far Detector and Conventional Facilities to house the technical systems.

The LBNE experiment plans to take physics data starting in 2023, initially with a 708 kW beam extracted from the existing Main Injector but using a new neutrino beamline. Later, a beam power of roughly 2.3 MW would be possible with Project X. India is already an integral part of Project X at Fermilab. *Collaboration between Indian institutions and Fermilab on both accelerator and neutrino physics would enable Indian physicists and engineers to participate in the world's leading neutrino physics and detector development program, while building infrastructure and similar accelerator and detector facilities in India.*

In January 2010, the US Department of Energy (DOE) approved LBNE's Mission Need, a milestone known as Critical Decision-0 (CD-0), thus formally creating the LBNE Project. In December 2012, CD-1 was approved by the DOE, which approves the full conceptual design, and authorizes the project to complete the design and begin to prepare for construction. The LBNE Project is charged with developing the experimental and conventional facilities that will enable the LBNE Science Collaboration to achieve the scientific mission established at CD-0. LBNE Project team members also belong to the Science Collaboration; this overlap promotes strong teamwork for development of the best possible technical designs.

In 2008, a group of scientists and engineers came together to form the LBNE Science Collaboration, and Indian physicists from the Indian Institutions and Fermilab Collaboration (IIFC) joined LBNE the following year. By now, the LBNE collaboration has grown to comprise more than 350 collaborators from more than 60 institutions from universities and national laboratories in the United States, India, Italy, Japan, and the UK. The LBNE collaboration seeks and anticipates further international participation.

The primary goal of the LBNE Science Collaboration is to perform a world-leading, long-baseline neutrino oscillation experiment with unprecedented sensitivity and precision and thereby determine the neutrino mass hierarchy (i.e., the ordering of neutrino masses), CP violation in neutrino mixing, and the value of the mixing parameters. The experiment's capability to perform simultaneous determinations of these quantities is a unique feature among not just the long-baseline experiments, but among all neutrino experiments worldwide. This will be accomplished by using a new high-intensity, broadband neutrino beam and a high-resolution, multi-kilotonne liquid argon far detector. Searches for proton decay and the neutrino spectrum from a supernova collapse are among the long-term goals of LBNE.

The core scientific capability of LBNE will be significantly enhanced by a high-resolution near neutrino detector. We propose to design and build a near detector in India that will not only add to the capabilities of the overall LBNE oscillation program, but will also independently conduct precision measurements of quantities such as neutrino-nucleon and neutrino-nuclear cross sections, electroweak parameters, sum-rules and sensitive searches for new physics, with previously unachievable precision, potentially leading to additional discoveries in neutrino physics.

Goals of LBNE-India:

In May 2010, Dr. Srikumar Banerjee, then Secretary of the DAE, gave the Indian Institutions and Fermilab Collaboration (IIFC) a mandate to develop a physics program to complement the accelerator collaboration. He specifically asked that we develop a program that:

• Provides rich physics and is capable of producing 50–100 PhDs from the Indian institutions

• Strengthens India's scientific infrastructure

• Constitutes a significant contribution to the Fermilab project with a DAE/DST ownership

• Shares synergy with the ongoing research programs in India, including the INO program

This proposal to collaborate on the LBNE detector and physics programs meets the mandate given to the IIFC. The IIFC held meetings in January 2011 and June 2011, and submitted an initial draft proposal to the DAE in August 2011 through Prof. M. Barma, Director of the Tata Institute of Fundamental Research (TIFR). After receiving further encouragements from DAE, the collaboration has continued to meet and has developed this proposal.

Physics and Technology:

The physics of the LBNE near detector program is very rich and would enable more than a hundred unique physics and engineering PhD topics and generate over 200 papers. It would also provide training and experience in building several detectors and associated technology development projects. It is envisioned that students would receive a complete training in state-of-the-art technology and physics.

The high-level physics goals of this proposal are:

(1): Measure the absolute and relative flux of all four neutrino species, ν_μ, $\bar{\nu}_\mu$, ν_e and $\bar{\nu}_e$, including the energy scales of neutrinos and antineutrinos, as required to normalize the oscillation signals at the Far Detector

(2): Measure the cross section of neutrino- and antineutrino-induced inclusive and exclusive processes across a large energy range (0.5–50 GeV) to 3% precision, to aid in the interpretation of the oscillation signals in the Far Detector

(3): Measure the yield of particles produced in neutrino interactions such as neutral and charged pions/kaons, which are the dominant backgrounds to oscillation signals

(4): Precisely measure the fundamental electroweak and strong interaction parameters that are accessible to neutrino physics

(5): Contribute to the design and construction of the liquid argon detector at the far site and conduct analyses

(6): Participate in any aspect of the LBNE science program

The High-level Detector Technology Development:

The LBNE detector is made up of near and far detector complexes. This proposal would enable India scientists and engineers (DAE/DST) to have a significant ownership of the near detector, while making significant ($\sim$10%) contribution to the full LBNE Project. The scope of the proposal encompasses:

(A) LBNE Near Detector: Design, fabricate, install and operate a high-resolution near detector at Fermilab. The detector, which will require significant R&D, will comprise a straw tube tracker (STT) with transition radiation capability, an electromagnetic calorimeter (ECAL) surrounding the STT, a dipole magnet surrounding the ECAL and the STT, and muon-ID detectors instrumenting both the magnet and a station downstream of the magnet.

The sensitivity studies show that the proposed detector will achieve the stated goals, will set a new standard in precision neutrino measurements and will generate over a hundred PhDs in particle, nuclear and engineering physics.

This detector R&D and infrastructure development at Indian institutions will build on and strengthen the existing expertise in India. This would also create a synergy with and strengthen the physics results of the INO detector.

The design of the Near Detector proposed in this document will meet the scientific goals of LBNE and satisfy the mandate given to the neutrino task of IIFC by DAE. This design is the subject of study within the LBNE Science Collaboration, with full and equal Indian participation. As these studies progress over the next $\simeq$12 months, the design of the Near Detector may evolve from what is described here. The final design will be subject to a review called jointly by the LBNE-India and LBNE-USA Project Managers, to evaluate the detector conceptual design in light of the DAE mandates, LBNE's scientific goals and the design's technical feasibility, cost and schedule.

(B) LBNE Far Detector: Participation in and contribution to the development of the new liquid argon technology and construction of the Far Detector would bring new technical expertise to India. Here our investigations are preliminary, but possible lead areas of work include the time projection chamber, either the cold electronics or the data acquisition system, or the advanced cryogenics and liquid argon purification systems.

LBNE is seeking to expand the work on the Far Detector into a fully global collaboration in which India would be an important partner. The specific areas of Indian research and participation will be determined in the context of this developing global collaboration over the next year or two.

Plan:

The research program will include physics studies, detailed Monte Carlo simulations to determine the design parameters for the subdetectors, construction of prototype subdetectors that will be calibrated in a test beam at Fermilab, construction of infrastructure at the DAE/DST institutions and at Indian industries for the fabrication of the detector components, construction of the full-scale detector, and finally, installation and testing of the detector at Fermilab. The task is expected to take about ten to eleven years.

We are requesting timely approval of this proposal, which would enable us to prepare a Project Execution Plan by May 31st 2013 for approval by DAE-DST.

2 LBNE-India: Science Case

Central to our quest to understand the Universe and its evolution is the knowledge of how fundamental particles interact and the laws governing the forces that exist between them. We have made very significant strides towards the realization of this goal over the last five decades, aided by vigorous experimental exploration at higher and higher energies, conducting measurements with increasingly higher precision, and supplemented by imaginative and bold theoretical exploration.

Our efforts have led to a self-consistent and well tested theory of fundamental forces and particles, referred to as the Standard Model. However, from accumulated evidence and present-day theoretical constructs, it is clear that the Standard Model must be incomplete. It fails to answer crucially important questions, such as why matter dominates over antimatter in the Universe, the nature of dark matter and dark energy, why the masses of elementary particles are what they are, and how quantum mechanics is to be reconciled with gravity in a fundamental way.

The weight and import of these fundamental questions requires a multi-pronged approach to understanding Nature at the deepest level. Among these efforts, Neutrino Physics provides an important probe for discovering physics beyond the Standard Model, because answers to crucial questions about neutrinos are directly linked to a fundamental understanding of our Universe.

Compared to existing neutrino experiments around the world, the Long-Baseline Neutrino Experiment (LBNE), Fermilab's flagship project, is the most ambitious effort yet to conduct neutrino research with unprecedented sensitivity. It will herald a world-class neutrino program with the long-term vision of a large detector in a high-intensity, broad-band neutrino beam from Fermilab. When fully built and functional, it will serve as a high-precision detector for both beam and extraterrestrial neutrinos over a broad energy range.

The LBNE Project scope includes construction of experimental systems and facilities at two separate geographical locations, including the following major elements, as proposed in LBNE's Mission Need statement [2]:

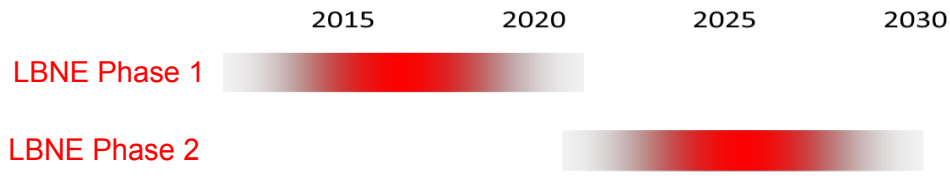

Figure 2–1: Phased timeline for LBNE

- an intense neutrino beam aimed at a far site
- detectors located at the near site just downstream of the neutrino source
- a massive neutrino detector located at the far site

According to present plans and US Department of Energy (DOE) budget constraints, LBNE will be implemented in a phased program with increasing scientific capabilities at each phase, as pictured in Figure 2–1. As noted by Dr. W.F Brinkman, Director of the DOE Office of Science, in his letter of March 19, 2012 to Pier Oddone, Director of Fermilab, the peak cost of LBNE, despite the excellence of the science, could not be accommodated in the current US budgetary climate. The letter required that the project be proposed in distinct phases, and encouraged international collaboration on a major scale.

In the LBNE Conceptual Design, a proton beam extracted from the Fermilab Main Injector is used to produce a neutrino beam that travels through the Earth's mantle to a detector located 1,300 km away at the Sanford Underground Research Facility, SURF, the site of the former Homestake Mine in Lead, South Dakota. A 10-kilotonne liquid argon Far Detector will be installed near the surface with an embankment constructed above it.

LBNE received the CD-0 approval by DOE in early 2010 and has just received CD-1 approval as of December 10, 2012.

Subsequent phases of the LBNE project will include construction of a near neutrino detector at the Fermilab site and construction of a larger far detector placed deep underground at SURF. It is, however, clear that concurrent construction (to the extent possible) of a near detector and a larger, upgraded underground far detector would be highly desirable from the scientific point of view. This amounts to accelerating the currently proposed (phased) LBNE time-line. We view this as an excellent opportunity for India to step in, become a chief partner and contribute materially in facilitating and accelerating the fundamental science achievable by LBNE.

We propose that India build the LBNE near neutrino detector (ND), which is not included in the first phase of LBNE. The ND will be designed, prototyped and fabricated in Indian research and industrial laboratories with funding from the Indian DAE/DST. Such an endeavor will be rich in scientific dividends, and is expected to generate over 100 PhDs in particle,

nuclear, and engineering physics, and over 250 publications in peer-reviewed journals. It will constitute critical and substantial participation in LBNE, contribute to interpreting the Indian Neutrino Observatory (INO) measurements and those of other long-baseline experiments, and establish substantial technical expertise in India. Our proposal provides a clear and significant way to put an Indian stamp on a highly important science and technology project.

Subject to further study and discussion, we would also like to contribute to and participate in the LBNE Far Detector development and physics, which will employ cutting-edge liquid argon purification technology, cold electronics and cryogenics technology which could be of immense potential use in future DAE/DST scientific endeavors.

In this chapter, after briefly listing the important unanswered fundamental questions in neutrino physics (Section 2.1). We discuss the present status of the LBNE Project, which we believe offers a major collaborative opportunity for India (Section 2.2). We then list and describe the major physics goals and capabilities of LBNE as currently envisaged (Section 2.3). Subsequent sections summarize the benefits and the physics-rich role of an ND, for which details are given in subsequent sections (2.4 and 2.5). We then describe the multi-faceted advantages that would accrue if India were to participate in an important and substantive way in LBNE by building the ND indigenously (Section 2.6). Finally, we describe the challenges in, and the opportunities offered by, the proposed research (Section 2.8).

2.1 Why is Neutrino Physics Important?

Neutrinos are the most abundant of matter particles in the Universe. Decades after its discovery, the neutrino, however, remains one of Nature's most enigmatic particles. It exists in three "flavors", each associated with one of the three generations of charged fermions (e, μ and τ), but carries no charge of its own. The flavors are known to mix (or *oscillate*), but other properties of the neutrino such as mass, the hierarchy of generations and its mixing parameters, though fundamental to our understanding of how the Universe evolved from its creation during the Big Bang to its present state, remain elusive. It is important to note that neutrino mass and its generational mixing provide perhaps the firmest evidence we have of physics beyond the Standard Model (SM), the theory that encompasses the current knowledge about the fundamental forces and interactions in the Universe.

An intriguing fact of the SM is that the neutrino mass is orders of magnitude smaller than the lightest charged-fermion mass, see Figure 2–2. Thus, neutrinos may offer a new, different and complementary view into the origin of mass. They could also provide indirect information on the energy scale of a grand unified theory not reachable by direct means such as collider experiments. Since mixing in the lepton sector is different from that in the quark sector, neutrinos may provide a different insight into flavor physics, answering questions such as why are there three generations, why do they mix, and why do we have a matter versus antimatter

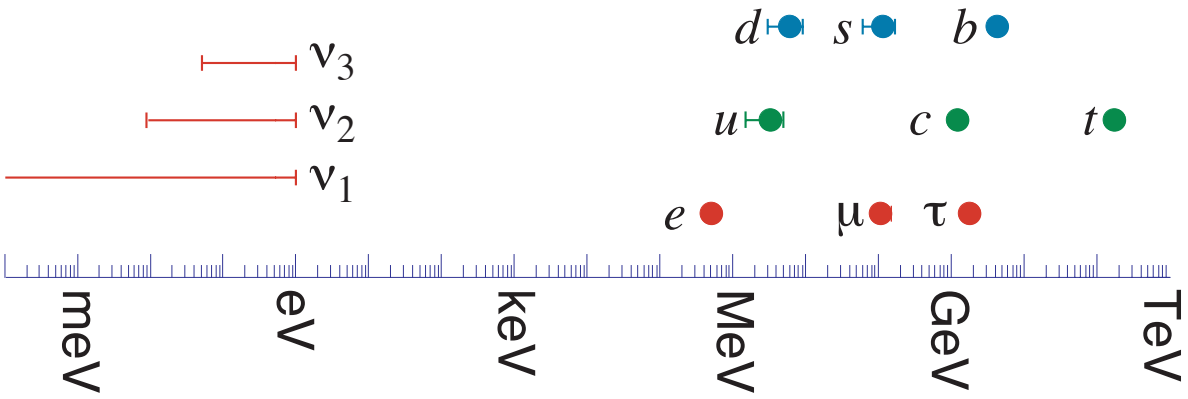

Figure 2–2: A comparison of masses of particles in the Standard Model, from [1].

asymmetry in the Universe? The CP (charge and parity) violation in the neutrino sector could be related to the baryon asymmetry of the Universe. Neutrinos may also form a component of dark matter. Neutrino experiments can be sensitive to small effects in particle physics, for example, a violation of unitarity, non-standard interactions, and CP and CPT (charge, parity and time) violations. Discovery of such non-standard interactions could unveil important new physics and lead to fundamental modifications to our picture of the microscopic world. Such effects have so far been inaccessible to other conventional accelerator-based experiments in particle physics.

We list below important open questions in Neutrino Physics whose answers could fundamentally alter our current understanding of the way Nature operates at its most fundamental level:

- *What is the absolute mass of the neutrino?* Whereas at least two of the three neutrino flavors are known to have mass, their absolute masses are not known. The tritium beta decay and neutrinoless double-beta decay experiments are pursuing this question.
- *Is the neutrino its own anti-particle?* Neutrinoless double-beta decay experiments such as CUORECINO/CUORE, NEMO3/SUPERNEMO, GERDA, EXO, SNO++, COBRA and MAJORANA are conducting increasingly sensitive searches to answer this question.
- *The mixing angle between the first and the third generations of neutrinos*, Θ_{13}, has been recently measured by the reactor experiments [4], [5], [6]. A precise measurement of Θ_{13} in both neutrino and antineutrino oscillations is critically important not only because it is a fundamental parameter but also because its value will determine the strategy best suited to address many other fundamental questions in neutrino physics, such as CP violation.
- *Do neutrino oscillations violate CP? What is the value of the CP-violating phase, δ_{CP}, which so far is completely unknown? Is the CP violation among neutrinos related to*

the CP violation in the quark sector? Can the leptonic CP violation explain the matter-antimatter asymmetry in the Universe (Leptogenesis)?

- *What is the neutrino mass hierarchy (MH)? Is it 'normal', ($m_3 > m_2 > m_1$), analogous to the charged leptons and quarks, or is it 'inverted' ($m_2 > m_1 > m_3$)?* Not only does the neutrino MH influence the sensitivity of neutrinoless double-beta decay experiments, it is also a critical input for understanding the origin and pattern of masses and for building theories beyond the SM. Among the neutrino experiments, not only will the LBNE experiment have the highest sensitivity to the MH, it will also simultaneously conduct an incisive search for CP violation. The ICAL detector at the INO facility may be able to answer this question with approximately 500 megatonne-years or more of data (at least 10 years of operation after completion).

  It must be noted that no other existing or proposed experiment can simultaneously probe δ_{CP} and the MH as precisely as LBNE will.

- *Is the mixing between the second- and third-generation neutrinos maximal ($\Theta_{23} = 45$ degrees)? If so, why? Will it indicate new symmetries or new selection rules?* Several operational and planned experiments such as T2K and NOvA may address this question, but the most precise measurement of Θ_{23} will come from the LBNE experiment.

- *Will the pattern of neutrino mixing provide insights towards unification of the fundamental forces?*

- *What can we learn by measuring the intense flux of neutrinos from a supernova within our galaxy? Can we observe the neutrino remnants of supernovae that have occurred since the beginning of time?* Provided that the LBNE Far Detector has neutron-detection capability, the proposed experiment will offer the best sensitivity for discovering relic supernova neutrinos.

- *What can neutrinos tell us about new physics beyond the Standard Model?* Possibilities include deviation of the weak mixing angle (WMA) from those determined at the hadron and lepton colliders, violation of sum-rules and isospin symmetry. Open questions include: Are there large Δm^2 oscillations as hinted at by the LSND and MiniBooNE experiments? Are there nonstandard interactions?

- *Is there a fourth neutrino?* If the coupling of such hypothetical neutrinos to the Z^0 were suppressed, then the Z^0-width measurement at LEP would not rule them out, and LBNE might be sensitive to it.

2.2 The Long-Baseline Neutrino Experiment: An Opportunity for India

2.2.1 Overview of LBNE

The proposed LBNE experiment is the most ambitious neutrino project yet. The Far Detector will be located at the Sanford Underground Research Facility (SURF) in South Dakota, ∼1,300 km from the neutrino source (Fermilab), see Figure 2–3. The far location is chosen to provide the maximal sensitivity to the mass hierarchy and the CP violation.

After extensive design studies and detailed scientific debate between two far detector options, a single-module large water Cerenkov detector and a liquid argon time projection chamber (LArTPC), the latter was chosen. Both surface and underground locations for the FD have been studied. The latter is clearly preferable, because of superior background suppression and physics reach, but is significantly more expensive.

The experiment, with its large detector tonnage at the far location, and with the addition of a fine-grained near detector (not budgeted for in phase 1) to better constrain the systematic errors, will be able to conduct the most precise measurements on parameters such as Θ_{13}, Δm^2_{23}, Θ_{23} and its maximality, CP-violation and the mass hierarchy. (These capabilities are described in detail in subsequent chapters of this report.)

The main phase 1 scope elements on the Fermilab site, also referred to as the Near Site, include:

- a primary beamline (consisting of magnets and support equipment) to extract protons from the Fermilab Main Injector and transport the resulting proton beam to a target (where approximately 85% of the protons interact, producing pions and kaons)
- a target and target hall complex
- magnetic focusing horns to direct pions and kaons into a decay pipe
- the decay pipe in which these particles decay into neutrinos
- a beam absorber at the end of the decay pipe to absorb both the residual secondary particles and the primary protons that did not interact in the target
- an array of muon-ID detectors downstream of the absorber to provide information about the neutrino-beam production
- conventional facilities to support the technical components of the primary proton beam, the neutrino beam and the muon-ID detectors

The main scope elements at SURF, the Far Site, include:

- a 10-kilotonne fiducial-mass liquid argon TPC Far Detector (on the surface)
- conventional facilities to house and support the technical components of the Far Detector

The baseline (distance from neutrino source to the Far Detector) of 1,300 km is chosen to provide the maximal sensitivity to the mass-hierarchy and the CP-violation. The experiment will use a 708 kW proton beam at 120 GeV impinging upon a graphite target. The secondary mesons will be focused via horns and other beamline elements that make up the target hall which is 49 m long. The focused charged particles, e.g., $\pi^{\pm}$, $K^{\pm}$ and protons, along with neutral particles, enter into a 4-m diameter, 204-m-long decay pipe (these dimensions are somewhat preliminary). At the end of the decay pipe the hadrons are stopped by an absorber and the large number of muons are ranged out by a 210-m-thick rock shield. The ND hall is at the end of the muon rock-shield, with the ND itself 459 m from the primary target. Figure 3–9 illustrates the beam layout. The neutrino fluxes are simulated using these beam parameters.

The experiment's large detector tonnage at the far location will enable precise measurements on parameters such as Θ_{13}, Δm^2_{23}, Θ_{23} and its maximality, CP-violation and the mass hierarchy, however, a high-resolution ND would greatly add to the physics capabilities both in range and reach. (These capabilities are described in detail in subsequent chapters of this proposal.) We point out that the lack of an ND to provide these systematic constraints would limit the core science goals of LBNE after two to three years of operation.

The current situation presents favorable circumstances and increases motivations for international collaboration, in which participation and financial contributions by foreign stakeholders would lead to a truly superior and world-class program that delivers physics results of unprecedented quality.

2.2.2 Proposal to Build an LBNE Near Detector

We propose that India contribute by building a near detector for LBNE. The entire effort, from design to prototype to fabrication of the ND subdetectors, will be done by the Indian institutions over the coming decade. The subdetectors will be shipped to and assembled at Fermilab, and installed in the LBNE beamline. The IIFC-νP will be deeply involved in data-taking and analysis tasks. Such a composite endeavor will generate $\simeq$100 PhDs in particle, nuclear and engineering physics, and the hardware R&D and fabrication will greatly enhance India's infrastructure capability in particle and nuclear physics. The entire effort will be a critical and substantial contribution to LBNE where DAE/DST can claim 'ownership'. The precision neutrino data accumulated by the proposed ND will help elucidate and interpret

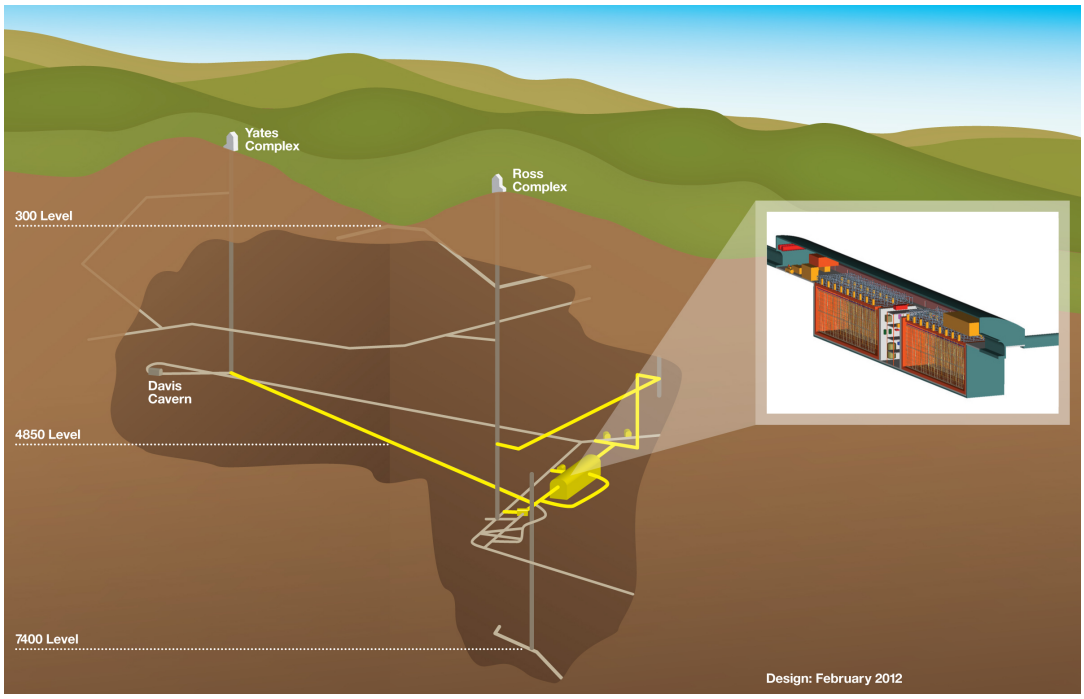

Figure 2–3: Schematic view of the LBNE underground detector option

INO measurements and those of other oscillation experiments, and engender a large technical know-how in India.

2.2.3 Proposal to Contribute to the LBNE Far Detector

We also propose that India contribute to the FD development which uses cutting-edge liquid argon technology. Involvement in the FD construction will enhance the cryogenic expertise in India which could be of immense potential use in future DAE-DST scientific research. The details of the LBNE project as currently envisaged can be found at the experiment's website: *lbne.fnal.gov*.

2.3 LBNE Physics Goals and Capabilities

2.3.1 Overall Science Goals

The full science program planned for LBNE is broad and rich (a full report is available in [3]). It includes the following physics goals:

A. Primary Objectives:

- Precision measurements of parameters governing $\nu_\mu \rightarrow \nu_e$ and $\bar{\nu}_\mu \rightarrow \bar{\nu}_e$ oscillations, which implies the measurement of the third mixing angle Θ_{13}, the CP violating phase δ_{CP}, and determination of the mass hierarchy (sign of $|\Delta m^2_{23}|$)
- Precision measurements of parameters governing ν_μ and $\bar{\nu}_\mu$ disappearance, Θ_{23} and Δm^2_{23}
- Search for proton decay in one or more decay modes such as $p \rightarrow K^+\nu$ and $p \rightarrow e^+\pi^0$, $p \rightarrow e^+K^0$
- Detection of the neutrino flux and energy spectrum from a core collapse supernova within our galaxy, should one occur during the lifetime of the experiment

B. Purpose of the Proposed Near Detector:

- **The primary objective of the Near Detector** is to make precision measurements necessary to achieve the primary physics objectives listed above.
- **Additional objectives of the Near Detector** are studies of neutrino interactions with unparalleled precision leading to:
  - Structure of weak current
  - Electroweak physics
  - Nucleon and nuclear structure including tests/measurements of QCD
  - New physics

C. Secondary objectives of LBNE:

- Other accelerator-based neutrino oscillation measurements
- Atmospheric neutrinos
- Astrophysical phenomena using cosmic neutrinos
- Search for new, unexpected phenomena

D. Additional secondary objectives of LBNE:

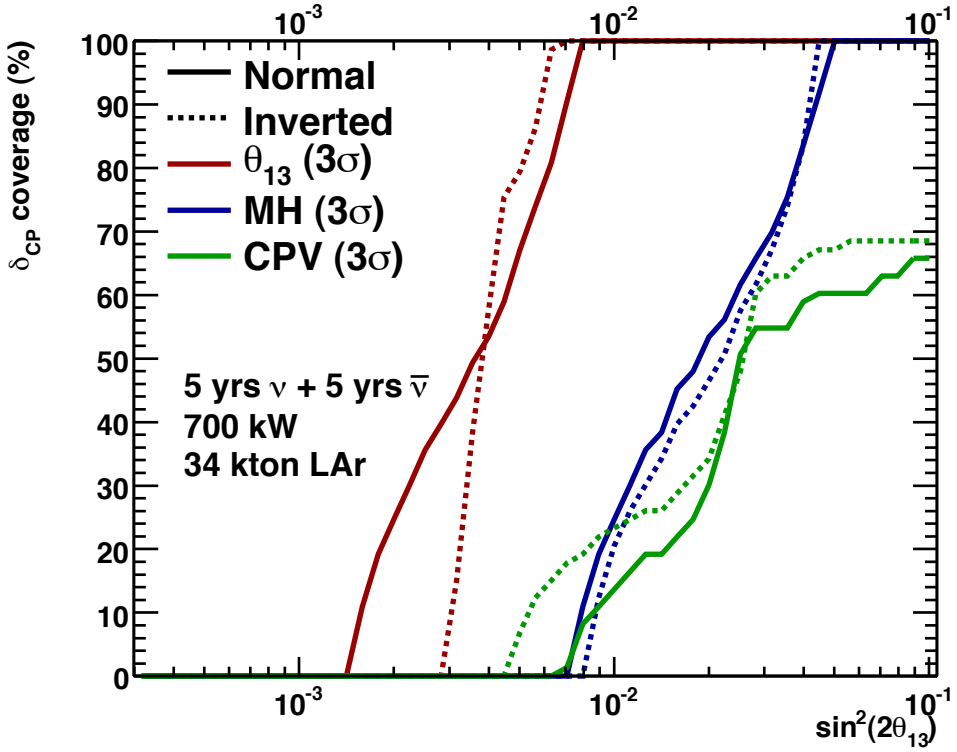

Figure 2–4: 3σ sensitivities for Θ_{13}, mass hierarchy and CP violation for assumed normal (solid curves) and inverted (dotted curves) hierarchies for the full-fledged version (Phase 2) of the LBNE LAr-FD.

- Detection of the diffuse supernova neutrinos
- Solar neutrinos
- Geophysical neutrinos

2.3.2 Sensitivities Required to Achieve LBNE's Primary Physics Objectives

Figure 2–4 shows the sensitivity to δ_{CP} versus $\sin^2(2\Theta_{13})$ for the full 34-kilotonne LArTPC detector envisaged for phase 2 of LBNE. Important recent results from reactor experiments have shown that Θ_{13} is large ($\sin^2 2\Theta_{13} = 0.09 \pm 0.02$), and hence the capabilities are more accurately reflected by the values in the far-right of this figure. Note that sensitivities are constrained by the range of the accessible δ_{CP}, shown along the vertical axis.

LBNE will buttress and strengthen accuracies of neutrino mass and mixing parameters via a study of long-baseline oscillations. In Figure 2–5 we show the ν_μ and $\bar{\nu}_\mu$ event rates with and without oscillations. The figures show the spectacular sensitivity for precision oscillation studies available to LBNE, if only we could constrain the systematic precision — which this

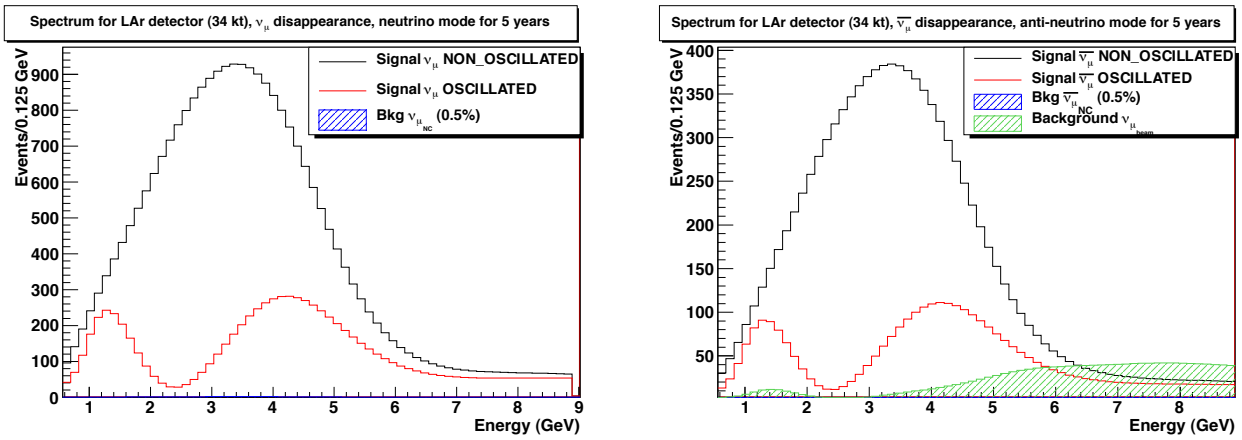

Figure 2–5: Neutrino (left panel) and anti-neutrino (right-panel) event rates for both the un-oscillated (black) and oscillated (red) muon neutrino spectra, with assumed 5 year runs for each case, from [2], for the full version of LBNE (Phase 2).

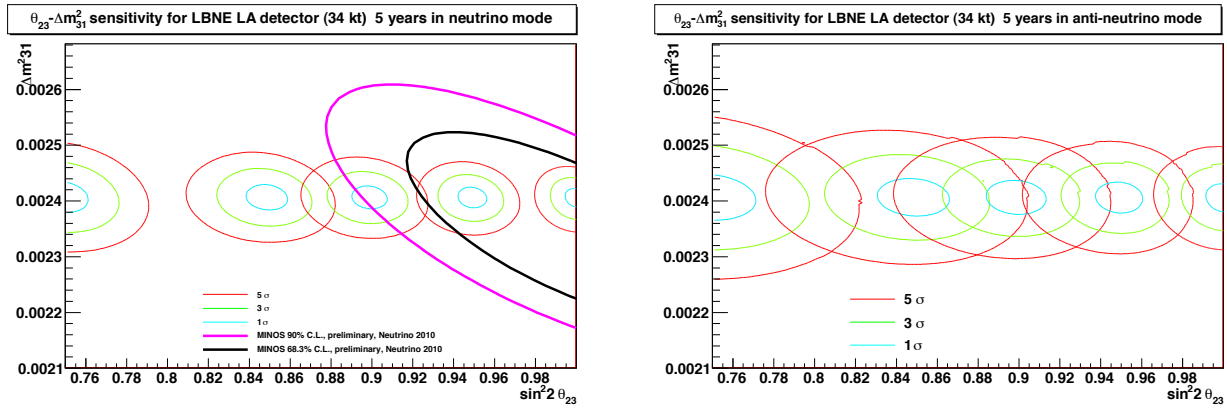

Figure 2–6: Accelerator and atmospheric neutrino parameter sensitivities for LBNE; other specifications are the same as in Figure 2–5.

proposal addresses. Also shown are the low backgrounds that the experiment has to contend with. The exposures are shown for five years each of operating in neutrino and antineutrino modes. Figure 2–6 presents corresponding sensitivity to the accelerator and atmospheric neutrino parameters achievable by the experiment.

The present time, while the LBNE phase 1 and phase 2 schedule and capabilities are still being fixed, offers an excellent opportunity for new stakeholders to propose contributions that would enhance the project and accelerate its schedule. In subsequent sections, we describe our vision for how India may very fruitfully participate in this fundamental and exciting effort in a manner that not only leads to discovery but also to crucial scientific and technological spin-offs in the near future.

2.3.3 Near Detector Measurements Required to Achieve LBNE's Primary Objectives

In particular a high-resolution Near Detector could make measurements that would significantly enhance LBNE's overall sensitivity. Measurements required to achieve LBNE's primary objectives include the relative abundance and energy spectra of all four neutrino species, ν_μ, $\bar{\nu}_\mu$, ν_e, and $\bar{\nu}_e$; neutrino and antineutrino cross-sections; and the yields of neutral and charged mesons produced by the neutrino interactions that constitute the dominant backgrounds to the oscillation signals in the Far Detector.

2.4 The Role and Importance of a Near Detector for LBNE

As neutrino oscillation physics enters the era of precision measurements, it is important to recognize the paradigm shift that is taking place vis-a-vis the role played by a near detector. Earlier efforts focused on building identical detectors (to the extent possible) at the near and far sites with the goal of minimizing oscillation-related systematic errors. It has gradually become clear that this traditional ND concept is insufficient and we need to reinvent the ND for the future oscillation measurements.

In a neutrino oscillation experiment one looks for alterations in the composition of a neutrino beam as it propagates from its source to a FD hundreds of kilometers distant. In this context, a measurement folds together at least three distinguishable but overlapping tasks. First, one must characterize the instrumental response of the FD to a neutrino interaction with any given parameters; for example, what ionization in a liquid argon detector should one expect in response to a quasi-elastic (QE) interaction of a neutrino with a particular energy. Second, to detect alterations in the beam between source and FD, one must thoroughly characterize the beam at the source. Third, because the very large mass of the FD forces compromise in its ability to distinguish signal events from other types of events, one must determine the prevalence of those other types of events. The second and third tasks are both duties of the ND.

Additionally, because of the very low rate at which neutrinos interact, the statistical error of neutrino experiments has (historically) dominated the systematic error. In the upcoming generation of neutrino oscillation experiments (such as LBNE) the increased intensity of the beam and the increased scale of the FD will greatly enhance the number of events detected. On the other hand, the effects that we seek to illuminate are considerably more subtle than those of the first generation oscillation experiments, e.g. Super Kamiokande, MINOS. In these circumstances the systematic error will overtake the statistical errors if they are not attended to punctiliously. The ability to constrain systematic error rests squarely on the competence of the ND. Finally, a near detector capable of meeting the aforementioned challenges of neutrino oscillation will be physics-rich in its own right (as described below), and provide an important arena for detector development and research into new technologies.

2.5 Principal Goals of the Proposed Near Detector

The LBNE ND will fulfill the following four principal goals. First, it will determine the absolute and relative abundances of the four neutrino species, ν_μ, $\bar{\nu}_\mu$, ν_e, and $\bar{\nu}_e$ in the LBNE beam as a function of neutrino energy (E_ν). Second, it will determine the absolute energy scale for neutrinos and antineutrinos, a factor which determines value of the mass (Δm^2) parameter. Third, it will determine the rate of charged and neutral pion production both in charged current (CC) and neutral current (NC) interactions. (The pions are the predominant source of background both for ν_e appearance and $\nu_\mu(\bar{\nu}_\mu)$ disappearance measurements.) Fourth, assuming the neutrino flux is well measured, the ND will determine neutrino cross sections on argon. Knowledge of the cross sections at the values of E_ν typical of the LBNE beam is essential for predicting both the signal and the background at the FD.

A tacit assumption underlies all neutrino oscillation experiments. The ND measures an unoscillated ν_μ ($\bar{\nu}_\mu$) spectrum. However, if oscillations occur at large Δm^2, as suggested by the LSND/MiniBooNE anomaly, a topic which has lately generated considerable excitement, then the ND neutrino spectra are considerably more complex and interesting. A future neutrino oscillation program must have an ND that is capable of either measuring this effect $\nu_\mu \rightarrow \nu_e$ *and* $\bar{\nu}_\mu \rightarrow \bar{\nu}_e$, or of constraining the background process that gave rise to the LSND/MiniBooNE anomaly. (This is addressed in Sections 5.10 and 5.22.)

An extremely important physics payoff is an accurate measurement of quasi-elastic, resonance and deep inelastic processes to the total cross-section in 0.5–20 GeV. (Currently NOMAD and MiniBooNE QE measurements disagree at 35% in this energy region; this can only be resolved by a precision near detector such as the one proposed in this document.) Finally, there may be physics beyond the SM, as suggested by existing anomalies in short-baseline experiments. Thus, it is possible that new interactions exist which, at present, are unknown to us. These non-standard interactions must (at low energies) be much weaker in strength than the known SM interactions. A high-resolution near detector at LBNE would provide a potent tool to probe such new physics.

2.6 The LBNE Near Detector as an Indigenous Indian Effort: Rich in Benefits and Spin-offs

We propose to design, conduct R&D on and fabricate the LBNE Near Detector in India, install it in the LBNE beamline at Fermilab, and use it to conduct numerous analyses relevant to the oscillation and non-oscillation physics. The ND, dubbed HIRESMNU [7], will be a high-resolution tracker with transition radiation capability, surrounded by calorimetry and embedded in a magnetic field with muon-ID capability. It will be capable of fulfilling the physics goals listed in Section 2.5. In this section we describe the significant advantages of

this proposed project, separate from the physics capabilities.

2.6.1 Manpower Training and Development

Given the above description of physics and detector development, it is obvious that numerous PhDs will result from this program, energizing the entire particle physics program in India for future generations. We expect at least 100 PhDs will result from the full program of collaboration described here, trained by experts both from India and the US in cutting-edge technology and science in the fields of particle physics, detector design and development, nuclear physics and engineering. About 250 high-quality, peer-reviewed journal publications are expected to be an output of this endeavor.

We propose to operate three factories at suitable locations in India in order to execute full-scale fabrication of subdetector modules. These fabrication sites will provide a fertile training ground for Bachelor's and Master's degree students from science and engineering colleges across the country who will be engaged in both long- and short-term projects related to this effort. This will be described in more detail Chapter 7.

2.6.2 Technical Knowledge Transfer Resulting from Close Collaboration

We propose to design and fabricate the subdetectors for the ND in close collaboration with the US institutions. In the efforts leading to the present proposal, we have been working closely with colleagues from University of South Carolina (Carolina), Fermi National Accelerator Laboratory (Fermilab), and Los Alamos National Laboratory (LANL). The work towards this effort can be broken up into discrete tasks, on which US colleagues will be working with us closely. It is expected that many technical experts and physicists from the US will spend extended periods working with the Indian physicists, engineers, students and technicians at the fabrication facilities in India.

The first task is a detailed simulation of the detector leading to the choice of optimal parameters of the ND subdetectors.

The second and third (concurrent) tasks are construction of the critical prototype detectors and the layout of laboratories and infrastructure in India where the full ND will be fabricated. The prototype detectors as planned will comprise smaller versions of the actual detectors plus and one module each of the full subdetectors. The small prototype detectors will be subjected to measurements in test beams of electrons, muons, photons, pions and protons of well-defined momenta. The test beam measurements, conducted either at Fermilab or CERN, will provide the critical inputs for the full detector design.

The fourth task will be the fabrication of the full-scale detectors at the India-based fabrication facilities.

The fifth and final task will be installing the subdetectors and operating the ND at Fermilab, which will lead us into a decade-long adventure of data acquisition, measurements and discovery.

The entire process is expected to be rich in scientific and technical knowledge exchange, in the best traditions of previous international efforts towards a worthwhile scientific goal.

2.6.3 Synergy with the Indian Neutrino Observatory (INO) Program

The future of HEP will advance along three principal areas of inquiry — the energy frontier (LHC and future lepton colliders), the intensity frontier (neutrino and other fixed-target experiments such as muon and kaon physics), and the cosmic frontier. At present the Indian HEP community is involved in the energy frontier at LHC, the intensity frontier through neutrino experiments at Fermilab, and the cosmic frontier in India.

Indian physicists are currently working on the construction of an atmospheric neutrino experiment called India-based Neutrino Observatory (INO). This national effort aims to revive the culture of experimental particle physics in India.

The INO collaboration currently consists of 20 Indian institutions and one from the US (University of Hawaii). INO is a 50-kilotonne magnetized iron and resistive plate chamber (RPC) detector that will detect atmospheric neutrino and anti-neutrino interactions with iron nuclei via the charge of the corresponding emergent muons. The magnetic field allows the separation of negative from positive muons and, thereby, the separation of neutrinos from anti-neutrinos. The experiment is expected to be situated approximately 1000 meters below a mountain in a cavern in Tamil Nadu state of India. The details of the project can be found at the experiment's website: *www.imsc.res.in/ ino*.

The primary aims of the INO experiment are:

1. Measurement of neutrino oscillation parameters Δm^2_{23} and $\sin^2\Theta_{23}$ and observation of distinct L/E signature. The INO experiment has the widest reach in L/E measurement of any of the present or proposed neutrino experiments

2. Discrimination between the normal and inverted mass hierarchy of the neutrino mass eigenstates via the observation of matter-enhanced oscillation probabilities

3. Search for CPT violation

4. Resolution of the mixing degeneracy between ν_2 and ν_3

The physics goals of INO and those of LBNE, as described above, have a considerable amount of overlap and synergy. Manpower trained on LBNE can contribute to INO and vice-versa. The expertise and training gained by Indian students, postdocs and researchers as they participate in the flagship neutrino program of the US can be put to important use in the national project over the coming years.

The primary goal of both INO and the LBNE ND and FD programs is a quantitative understanding of the intrinsic properties of neutrinos and neutrino-interactions. The first challenge is arriving at a complete determination of the elements of the neutrino mixing matrix. This will include precise measurement of parameters such as mass-squared-difference and mixing angles such as Θ_{23} and Θ_{13}, mass hierarchy of the neutrinos and the CP-violating phase delta (δ_{CP}). The efforts include increasingly precise measurements of the known parameters, mixing angles and mass differences.

The second challenge, sharing a deep synergy with the first, is a set of precision neutrino-interaction measurements. Low-energy neutrino interactions are poorly understood. To make a subtle discovery in a next-generation neutrino experiment, one needs to measure neutrino-interaction cross sections, topologies, energy-scales, intrinsic properties, and so on, with a very high-resolution detector. We aim to participate in neutrino measurements whose precision is on a par with the lepton and hadron collider (e^+e^- and $p\bar{p}$) measurements. The high-intensity frontier at Fermilab, with the advent of the LBNE experiment, offers a rare opportunity to achieve this and it is important for Indian institutions to play a critical role in these future endeavors. Such efforts will not only boost our experimental capability, they will help us establish INO as a complementary, indigenous neutrino experiment with compelling physics.

Participation in LBNE that encompasses design, fabrication, installation of new apparatus and an reevaluation of existing data offers a unique opportunity to train a cadre of students and post-docs. Equally importantly, Fermilab possesses state-of-art expertise in detector design, large-scale fabrication, gas systems, data-acquisition, and other areas that they have generously offered to share with us. Learning these advanced techniques from experts will prepare us for the INO project as well as launch a next generation experiment in India.

2.6.4 Significant International Partnership and DAE/DST Ownership

Execution of the ND proposal to design, develop and contribute a principal detector system to a major high energy physics project will send a clear 'can-do' message from India to the scientific world. It will highlight the dedication and expertise of Indian scientists and

engineers, and demonstrate both India's capability to successfully engage in cutting-edge, high-precision science and technology and its commitment to deliver a highly sophisticated state-of-the-art detector to an international project. This would be a significant detector on which to put a DAE/DST stamp.

2.7 Potential Benefits from Significant Participation in the LBNE Far Detector Project

It is widely believed that liquid argon detectors, specifically liquid argon time projection chambers (LArTPCs) will play a major role in the future of particle detection. Such detectors combine the advantages of electronic detectors and bubble chambers. Argon, a gas at room temperature, condenses to a liquid when cooled to cryogenic temperatures. LArTPC technology uses liquid argon as a target material. The detection method is based on the collection of ionization electrons, resulting from particle interactions in the liquid argon, onto wire planes immersed in the fluid. Under the influence of an electric field, the electrons drift to the wire planes, thereby creating a signal.

The DOE is currently supporting the R&D effort for this technology of the future by funding a small liquid-argon detector prototype called ArgoNeuT [8]. In the next few years, Fermilab will analyze neutrino data using the new MicroBooNE detector, a 70-tonne liquid-argon detector.

While Indian participation in the LBNE LAr-FD effort is still under discussion, it is clear that this would be highly advantageous both from the physics point of view as well as technologically. It would allow Indian participants to get hands-on experience with techniques that dovetail with the DAE/DST broader goals, for example, advanced cryogenics and creation of high-purity conditions for cold electronics technologies.

2.8 Technical and Logistical Challenges

In addition to the unique opportunities available through broad participation in and commitment to the LBNE Project, challenges will present themselves. A known challenge is the current lack of workers with the appropriate skills to do the very precise work involved in creating cutting-edge detector components.

Although the technology required for the detector development is largely available in India, it will still require mastering new technologies and developing the workforce and infrastructure at the participating institutions. Except for a few universities in India, where some hardware infrastructure exists, the major facilities are limited to DAE institutions. Furthermore,

universities are not staffed with trained engineers and technicians to build detectors. The culture is such that that even well trained hardware experts at universities do not get the opportunity to participate in detector development in a significant way. We intend to change this trend by developing two to three centers among the collaborating institutions where detector development can proceed with the support of established DAE institutions.

As described in Chapters 4 and 5, the ND consists of three detector systems: the straw tube tracker (STT), electromagnetic calorimeter (ECAL) and muon-ID detectors, and a dipole magnet.

The large dipole magnet will need to produce a uniform magnetic field and construction of such a magnet is quite challenging. However, the Fermilab magnet design group has world leadership in designing and building precision magnets, and our engineers in industry will have the opportunity to work closely with these experts in our facilities.

Muon-ID detectors are typically constructed using either glass- or Bakelite-based RPC modules and the technology for both types exists in India. Indian groups are in fact already in the process of building about 100 Bakelite-based RPC modules for the CMS experiment and about 30,000 glass-based RPC modules for the INO-ICAL experiment. Our proposed LBNE ND, HIRESMNU, calls for about 500 Bakelite-based RPC modules. In our opinion, building of the muon-ID detector does not pose a challenge.

The proposed ECAL will be constructed of lead-scintillator bars extruded with wavelength-shifting fibers fitted inside the bars. Indian groups regularly build scintillator-based calorimeters and have also started extruding scintillators domestically, but India has not extruded scintillator with wavelength-shifting fiber. This challenge offers an opportunity to gain these skills and reduce the cost of detector development.

Indian institutions have not built an STT in the recent past. We will need to gain the skills to both set up the facilities for building it and to actually build it.

Meeting these challenges will strengthen India's scientific capabilities for decades to come. The HIRESMNU program will give India an opportunity to contribute significantly to a highly sophisticated, international, state-of-the-art experiment. Developing the knowledge base and facilities in India for cutting-edge science and technology, and successfully delivering a high-quality near detector will enhance the standing of India's science community in the world's eyes, and carry a clear and meaningful DAE/DST imprint.

3 An Overview of the High Resolution Near Detector for LBNE

We propose a high-resolution neutrino experiment within a dipole magnetic field, HIRESMNU [7] as the near detector (ND) for LBNE.

3.1 Goals of the Near Detector

Taking advantage of the unprecedented neutrino and antineutrino fluxes available at Fermilab for LBNE, HIRESMNU combines large statistics with high resolution in the reconstruction of neutrino events. High resolution in the ND is imperative to achieve the highest precision in the measurements of the elements of the neutrino mass matrix, and to have redundant measurements to establish a discovery should something entirely unexpected be observed in the FD. The proposed $3.5\times3.5\times7.5$ m^3 active near detector surrounded by an electromagnetic calorimeter (ECAL), all of which is placed inside a dipole magnetic field of $\boldsymbol{B \approx 0.4}$ T will have the density of liquid hydrogen, $\boldsymbol{\rho \approx 0.1}$ g/cm$^{\mathbf{3}}$, with a nominal mass of seven tonnes. While the exact design parameters are not yet fixed, the proposed detector has been established as a design that would meet all the project goals. The ND has two broad goals:

Constrain the systematic uncertainties in the oscillation studies: First we want to quantify the precision of the ND measurements that will be essential for the neutrino oscillation studies ($\boldsymbol{\nu}$OSCL) in LBNE. Regardless of the process under study, the associated systematic error should be less than the corresponding statistical error. The required systematic precision in the ND will determine the detector parameters such as resolution, fiducial mass, and so on. To this end, we will pay particular attention to:

(1): Measurement of the relative abundance and energy spectrum of all **four** species of neutrinos in the LBNE beam: $\boldsymbol{\nu_\mu}$, $\boldsymbol{\overline{\nu}_\mu}$, $\boldsymbol{\nu_e}$ and $\boldsymbol{\overline{\nu}_e}$ via the ***in situ*** identification of their CC-interactions

(2): Determination of the absolute ν-flux using the ν-electron scattering

(3) Identification and precise measurement of π^0, photon, electron and positron yields in ν-induced neutral-current (NC) and charge-current (CC) interactions — the most important background to the ν_e-appearance

(4) Measurement of NC cross-section relative to CC as a function of the hadronic energy, E_{Had}, since NC processes constitute the largest background to the ν-CC identification

(5) Measurement of the $\pi^\pm$ content in CC and NC hadronic jets since the $\pi^\pm \rightarrow \mu^\pm$ are the principal background to the $\nu_\mu(\bar{\nu}_\mu)$-CC;

(6) Measurement of the differential cross section for various exclusive, semi-exclusive and inclusive channels relevant for the νOSCL studies, such as quasi-elastic (QE), resonance (Res) and deep-inelastic (DIS) interactions

(7) Quantification of nuclear-target material cross-section that might affect the ν-nucleus interactions when extrapolating the ND measurements to the FD

Precision neutrino physics: We propose to match the ND needs for the LBNE oscillation studies with a generational advance in the precision of Standard Model measurements. The measurements include isospin physics, sum-rules, QCD tests, baryon-spin, strange meson and baryon production, charm mesons and electroweak constants. As a case study, we propose to investigate the feasibility of a measurement of the weak-mixing angle, $\sin^2\theta_W$ in the $\nu(\overline{\nu})$-q (DIS) channel at a momentum transfer (Q) in the neighborhood of 4 GeV with a precision approaching 0.2%. The sought precision on $\sin^2\theta_W$ in this experiment will be comparable to that attained by the collider experiments. The HIRESMNU ND will also permit searches for new physics with unprecedented sensitivity; the searches include high-Δm^2 oscillations in $\nu_\mu \rightarrow \nu_e$, $\nu_\mu \rightarrow \nu_\tau$, $\bar{\nu}_\mu \rightarrow \bar{\nu}_e$, and $\nu_e \rightarrow \nu_\tau$ channels, rare resonances, heavy neutrinos, and exotic bosons.

HIRESMNU reinvents the concept of a near detector, providing powerful constraints on the systematics associated with the discovery of the PMNS mixing matrix elements. It promises an "Event-Generator" measurement for the LBNE FD including the hadronic multiplicity ($\pi^\pm$, $K^\pm$, π^0 & p) comprising topologies of CC and Neutral-Current (NC) events with a special focus on the identification of (semi)exclusive e^-, e^+, γ, relevant to the ν_e appearance. It concurrently offers a rich precision ν-physics program: questions/measurements that were speculative will be possible to address with the HIRESMNU. If realized, the detector will yield over 200 papers over a 10-year span and will rewrite the "textbook" on the Standard

Model neutrino physics.

3.2 Detector Components and Geometry

The HIRESMNU design has an active tracker with dimensions of about $\mathbf{350 \times 350 \times 750}$ cm$^{\mathbf{3}}$, surrounded by an ECAL embedded in a dipole magnet with $\mathbf{B \approx 0.4}$ T. The nominal fiducial volume (FV) corresponds to $\sim$5 tonnes of mass. A schematic of the detector concept is presented in Figure 3–1. The active target is composed of the straw tube tracker (STT) equipped with the transition radiation (TR) capability to distinguish electron/positron from muon/pions with high efficiency ($\geq$ **90%**) and purity ($\geq$ **0.999**). Taking advantage of the existing design and production details for the ATLAS Transition Radiation Tracker [19,20,21] and the COMPASS detector [22,23], the HIRESMNU design uses straw tube trackers. Figure 3–1 shows one module of the STT where two planes of straw tubes are glued together and held by an Al-frame. In front of each module a plastic radiator made of many thin foils provides 85% of the total mass of the detector and can be adjusted according to the required resolution and statistics. The STT module design is taken from the COMPASS experiment; the TR component follows the ATLAS-TRT. The accompanying figure, Figure 3–2, shows the layout with the external (downstream) muon-ID detector. The detector shall have Argon target at the upstream end of the tracker; the Argon target will have sufficient mass to provide $\simeq$ **5** times more neutrino interactions than those expected in the FD as discussed in Section-4.1 and in Chapter 7.

The HIRESMNU idea is a generational advance over the the most precise existing neutrino experiment. It offers an order-of-magnitude better statistical and systematic precision over NOMAD which has the most precise neutrino data in the energy range of $\mathbf{5 \leq E_\nu \leq 100}$ GeV to date [9], [10], [11], [12], [13]. NOMAD is a low-density tracking detector, $\boldsymbol{\rho} \leq$ **0.1** g/cm$^{\mathbf{3}}$, inside a B field with an ECAL at the downstream end, and outside the magnet, a muon-ID detector. In HIRESMNU, we propose an active target tracker with a factor of two more sampling points along the $\boldsymbol{z}$-axis ($\boldsymbol{\nu}$-direction) and a factor of six more sampling points in the plane transverse to the neutrino direction compared to NOMAD. Figure 3–3 juxtaposes the resolving power of a light active tracker (e.g. NOMAD) versus that of a calorimeter (CCFR/NuTeV) in relation to a neutral current event. One sees the contrast in resolution of the NC event in the active tracker vis-a-vis that of the calorimeter. Compared to NOMAD, the HIRESMNU will have an order-of-magnitude more hits along a typical hadronic track and will have, in addition, calorimetric coverage for the side-exiting neutrals. Section 3.3 summarizes the salient improvements over NOMAD.

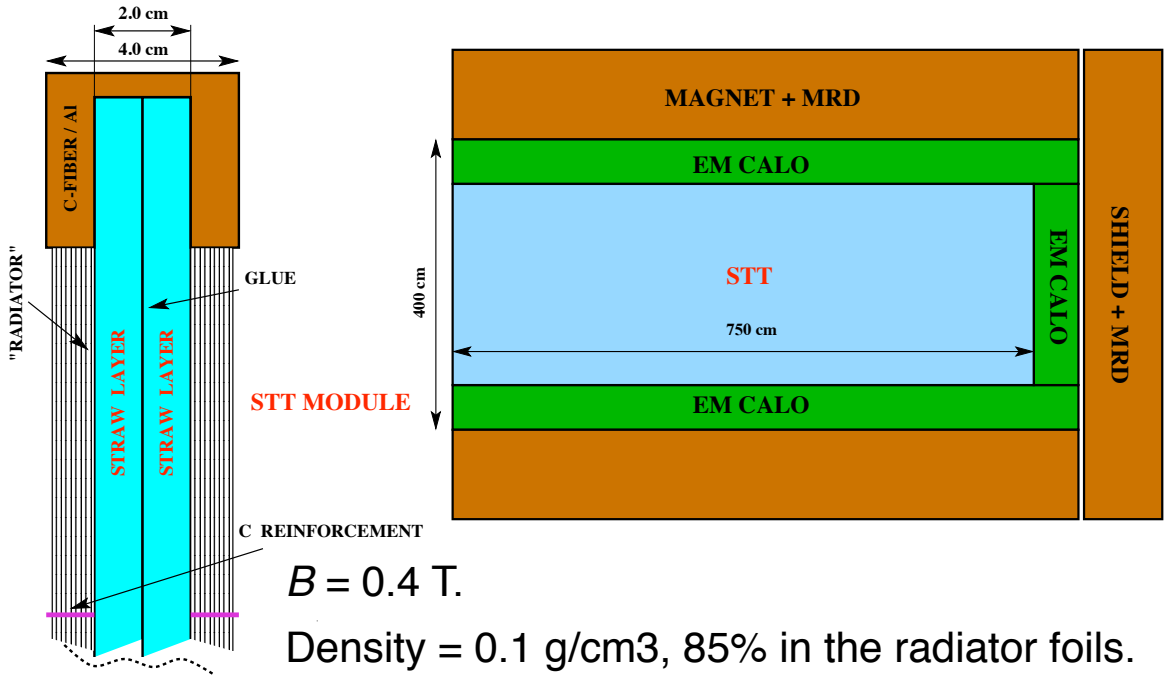

Figure 3–1: Sketch of the proposed HIRESMNU detector showing the inner STT and the 4π ECAL in the dipole magnet with the muon-ID detector (MRD). The internal magnetic volume is approximately 4.5m $\times$ 4.5m $\times$ 8m. Also shown is one module of the proposed STT.

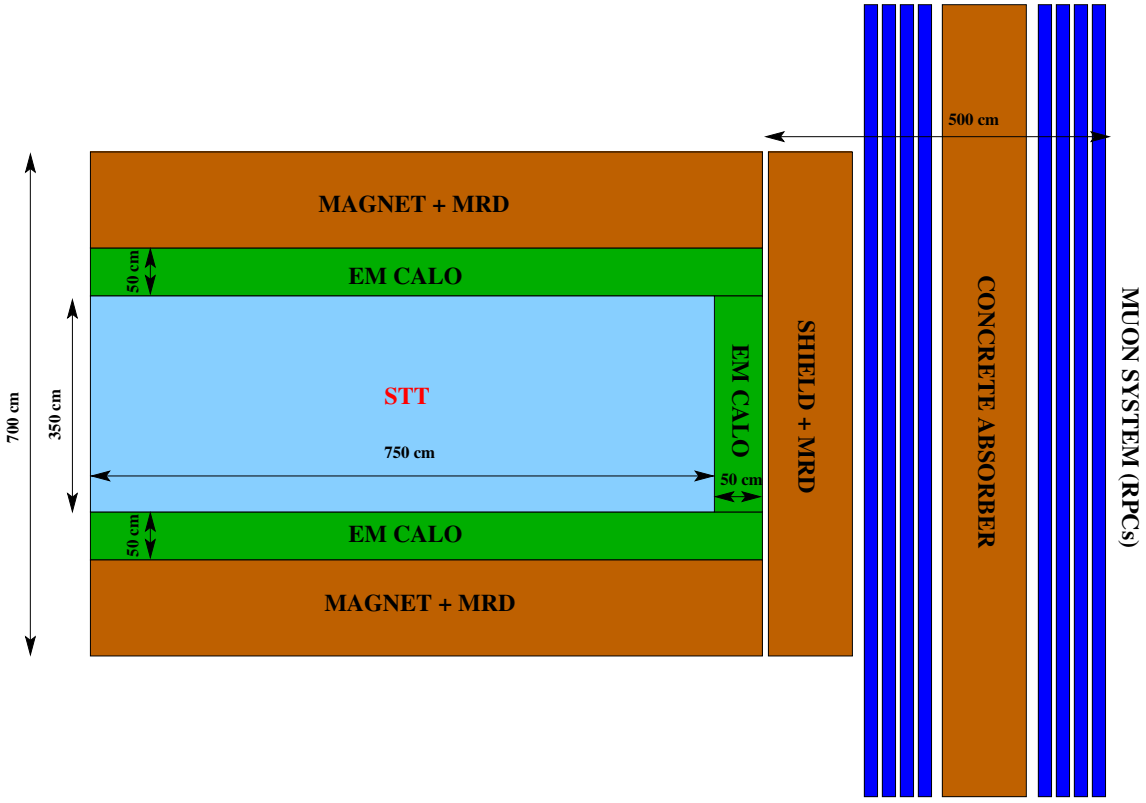

Figure 3–2: Layout of the HIRESMNU with downstream, external muon-ID detector (EMI) and shielding. The EMI specifications are preliminary; detailed simulation studies of EMI will yield a more robust design.

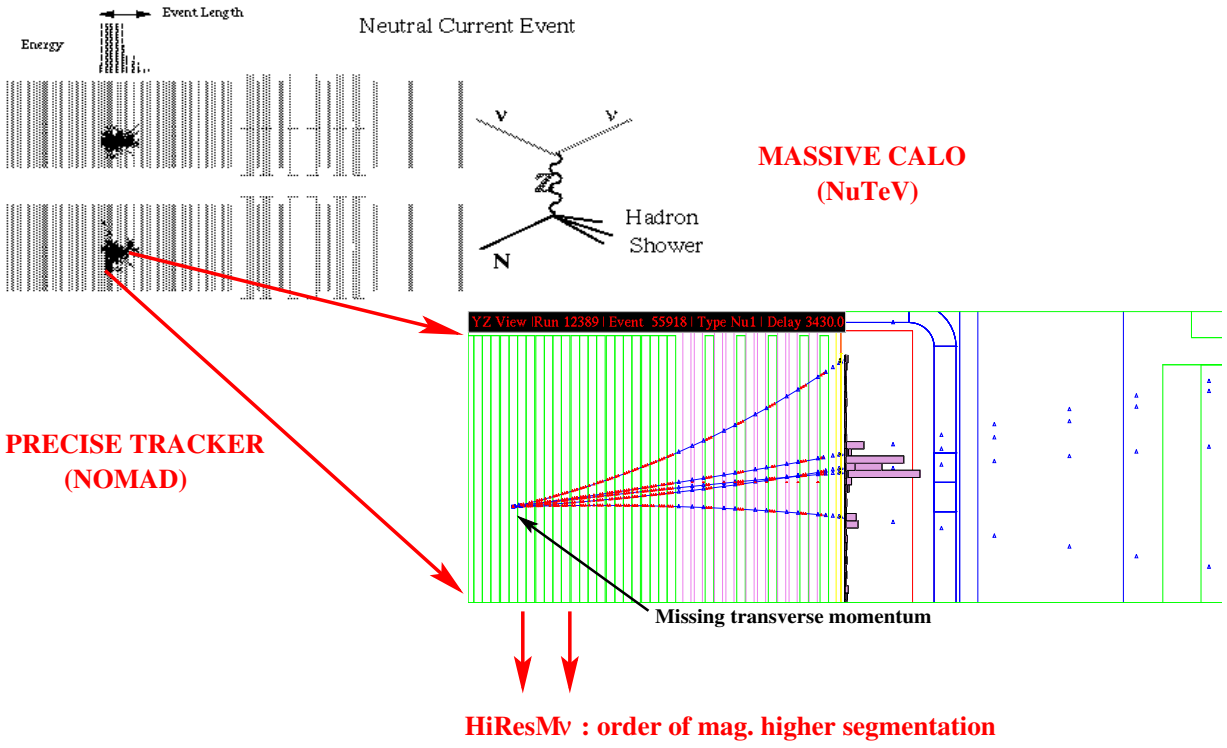

Figure 3–3: Candidate NC Event in a Calorimeter vs Active-Tracker: In tracking charged particles HIRESMNU will provide a factor of two higher segmentation along z-axis and a factor of six higher segmentation in the transverse-plane compared to NOMAD.

3.3 Salient Features of the Detector

The HIRESMNU offers a generational advance in the precision of the individual particle momenta measurements and their identification. The most precise neutrino detector to date is NOMAD whose energy range was $\mathbf{2.5 \leq E_\nu \leq 300}$ GeV; the energy range of interest in LBNE is $\mathbf{0.5 \leq E_\nu \leq 100}$ GeV. Thus, NOMAD offers a natural foil to contrast the capability of HIRESMNU. The advancement over the current precision measurements are:

(1) Enhanced Tracking Detector: The tracker will be composed of straw tubes with 1 cm diameter. Vertical ($\boldsymbol{Y}$) and horizontal ($\boldsymbol{X}$) straws will be alternated and arranged in modules – each module containing a double straw layer – as shown in Figure 3–2. An alternative with very similar cost is a module composed double layers of $\boldsymbol{Y}$ and $\boldsymbol{X}$ straws bracketed by transition radiation foil. We plan to have readout at both ends of the straws to resolve ambiguities in the hit assignment. In front of each module, plastic foils, the "radiators", provide 85% of the mass and allow a measurement of the transition radiation (TR), which will yield continuous identification of electrons through the tracking volume. Much of the active target is composed of carbon. We propose to use Xe-gas in the straw tubes (Xe/CO_2) to maximize the TR capability. Finally we shall measure $\boldsymbol{dE/dx}$, thereby enabling the identification of protons, charged pions and kaons. The identification of individual tracks as protons is especially important for the neutrino Quasi-Elastic (QE) and resonance ($\boldsymbol{\Delta}$) interactions.

(2) 4π Electromagnetic Calorimeter Coverage: In HIRESMNU, the tracking volume will be fully surrounded by electromagnetic calorimetry, ie., downstream (DS), sides (Barrel) and the upstream (US) ends of the detector. The $\mathbf{4\pi}$ ECAL coverage will enable complete detection of neutral particles, such as photons, neutrons and $\boldsymbol{K^0}$ produced in the $\boldsymbol{\nu}$ interactions. This arrangement provides a marked improvement over NOMAD which had an ECAL only at the downstream end of the detector. In HIRESMNU, the ECAL modules will have transverse and longitudinal segmentation. The default design of ECAL calls for a lead-scintillator calorimeter. A possible cost optimization could entail that in the first stage of construction, we construct only the downstream end of the ECAL and the last 4 m of the barrel. Later, we will instrument completely the sides making the ND fully hermetic.

(3) Improved Muon-Identification: HIRESMNU will tag 98% of the muons in the $\boldsymbol{\nu_\mu}$-CC sample, in contrast to the 85% efficiency of muon detection in most detectors, e.g., NOMAD. To accomplish this, the magnet yokes and the station downstream and outside of the magnet will be instrumented with external muon identifiers (EMI) made of resistive plate chambers (RPC), see Figure 3–2, enabling a $\mathbf{4\pi}$ muon coverage. We point out that the EMI is only meant to provide the identification of the muon — the momentum vector of the muon will be measured by the STT inside the B field.

Table 3–1: Improved subdetectors in HIRESMNU compared to NOMAD

Subdetector	NOMAD	HIRESMNU	Improvement
Tracking		$\times 6$ more hits in X-Y	$\times 2$ higher QE-Proton Eff.
			$e^{\pm}$ down to 80 MeV
		$\times 2$ more hits along Z	γ-Conv. Reconstruction
TR: Electron-ID	Downstream	Continuous	$\simeq \times 3$ $e^{\pm}$-Eff
Calorimetry	Downstream	4π Coverage	Much better coverage
Segmentation	No Long.	Fine Longitudinal	$e^{\pm}/\pi$ Separation
			Better miss-P_T
	Transverse	Finer Transverse	Powerful 'Dirt'-Veto
E-shower Resolution	$3\%/\sqrt{E}$	$6\%/\sqrt{E}$	Poorer resolution
μ-ID	Downstream $P_\mu \geq 2.5$ GeV	4π Coverage	P_μ down to 0.3 GeV
Trigger	Downstream	Continuous in STT	P down to 0.1 GeV
	No Cal. Trigger	Calorimetric Trigger	$E \simeq 0.3$ GeV

(4) Trigger: The trigger in HIRESMNU will have neither geometry bias nor charge bias (which was the case in NOMAD.) We aim to have $\approx$ 100% trigger efficiency for any event with $\geq$ **100** MeV of visible energy in the tracker or ECAL.

(5) Event Rate: The LBNE beam will enable HIRESMNU to accumulate about 60 million neutrino interactions in five years — a factor of 30 more events than NOMAD had. Combined with the terrific resolution, HIRESMNU will offer a generational advance in the precision neutrino physics.

Table 3–1 summarizes the improvements of HIRESMNU over NOMAD, currently the most precise neutrino detector.

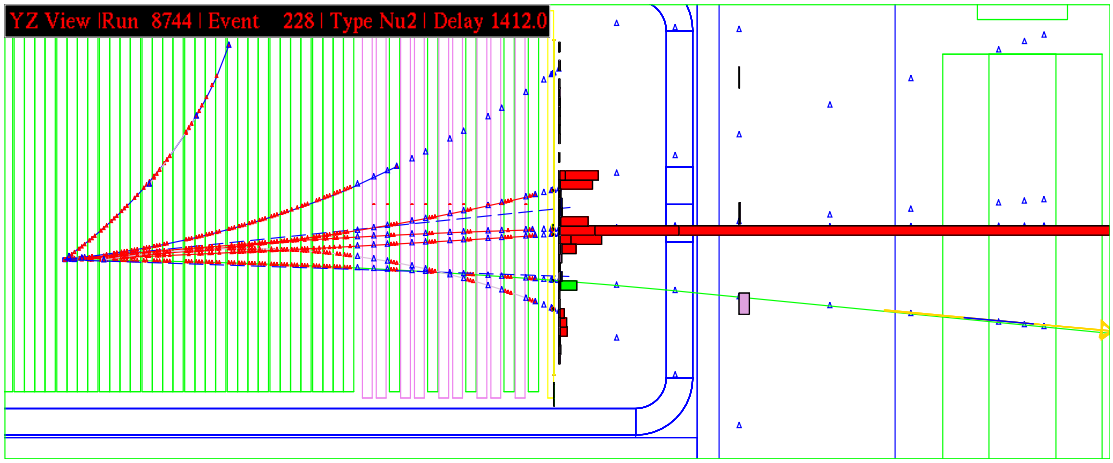

Figure 3–4: A ν_μ CC Event Candidate in NOMAD. HIRESMNU will have more sampling points and better muon coverage.

3.4 Neutrino Event Pictures as Expected in the Proposed Detector

HIRESMNU will measure all *four* neutrino species: the easily identified $\boldsymbol{\nu_\mu}$- and $\boldsymbol{\bar{\nu}_\mu}$-CC events with $\geq$ **95%** efficiency, and the more challenging $\boldsymbol{\nu_e}$- and $\boldsymbol{\bar{\nu}_e}$-CC with $\geq$ **50%** efficiency with a systematic precision $<<$ **1%**. Nothing summarizes the power of the proposed detector better than depictions of $\boldsymbol{\nu_\mu}$- and $\boldsymbol{\bar{\nu}_e}$-CC events. Figure 3–4 shows a $\boldsymbol{\nu_\mu}$-CC event in NOMAD where the $\boldsymbol{\mu^\pm}$ is easily measured in the tracker with a B field. The novel feature of a low-density detector is the capability for a clear measurement of the charged and neutral hadrons composing the accompanying hadronic jet. Figure 3–5 shows a $\boldsymbol{\bar{\nu}_e}$-CC event, the most difficult of the $\boldsymbol{\nu}$-species to measure, in NOMAD; the $\boldsymbol{e^+}$ is identified by the curvature, the dotted lines show the bremsstrahlung photons associated with the $\boldsymbol{e^+}$-track, the charged and neutral hadrons are also identified. The pictures lead to the following two conclusions:

(1): The $\boldsymbol{\nu_\mu}$-induced muon and and the $\boldsymbol{\bar{\nu}_e}$-induced positron both leave tracks measured in the B field, and as such are very similar.

(2): Leptons aside, the hadronic showers are indistinguishable between the two species. And to measure the low-energy, high-angle particles composing the hadronic shower, one needs a tracker with a large transverse coverage ($\geq$ 3m $\times$ 3m).

HIRESMNU will have substantially better tracking resolution than NOMAD and, unlike NOMAD, will have continuous TR capability. HIRESMNU will accurately determine the relative content and $\boldsymbol{E_\nu}$ spectrum of all four neutrino species.

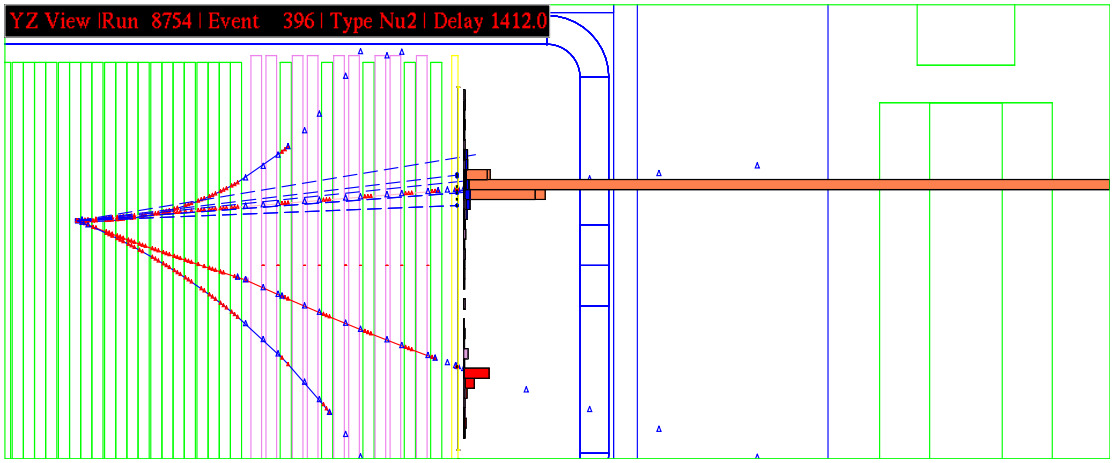

Figure 3–5: A $\bar{\nu}_e$ CC Event Candidate in NOMAD. The positron track with bremsstrahlung photons is clearly visible. HIRESMNU will have more sampling points, continuous TR, and and better γ acceptance.

3.5 Measurable Quantities

Figures 3–4 and 3–5 illustrate how the detector will measure the charge and momenta of all charged particles, the position and energy deposited in the ECAL, and hence the momenta of the neutral particles, the ID of $\boldsymbol{\mu^{\pm}}$ and the ID of $\boldsymbol{e^{\pm}}$. A less obvious feature of the tracker is the capability to measure energy loss per unit length ($\boldsymbol{dE/dx}$) of charged particles, providing ID of the low-energy protons, e.g., in quasi-elastic interactions. The photons that convert into $\boldsymbol{e^+e^-}$ pairs in the tracker are easily identified; furthermore, the photon-induced EM shower in ECAL is distinguished from neutral hadrons using the transverse and longitudinal profiles of the energy deposition. Finally, $\boldsymbol{K^0_S}$, $\boldsymbol{\Lambda}$ and $\boldsymbol{\bar{\lambda}}$ are identified via their decays into charged particles in the STT.

A most important kinematic measurable afforded by the HIRESMNU is the transverse momentum vectors ($\boldsymbol{P_T}$) of the neutrino-induced particles in the plane normal to the incident neutrinos. Neutrinos travel almost parallel to the detector axis, thus, in a CC event the lepton's $\boldsymbol{P_T}$ must balance the $\boldsymbol{P_T}$ of the recoiling hadronic system. It follows that the NC event is characterized by a large $\boldsymbol{P_T}$. The measurement of the missing-$\boldsymbol{P_T}$ vector ($\boldsymbol{p_T}$) provides a powerful constraint on the reconstruction and missing energy. Figure 3–6 shows the kinematic variables accessible in HIRESMNU. The $\boldsymbol{P^m_T}$-vector measurement allows a clean separation of NC (non-prompt) from CC (prompt) events.

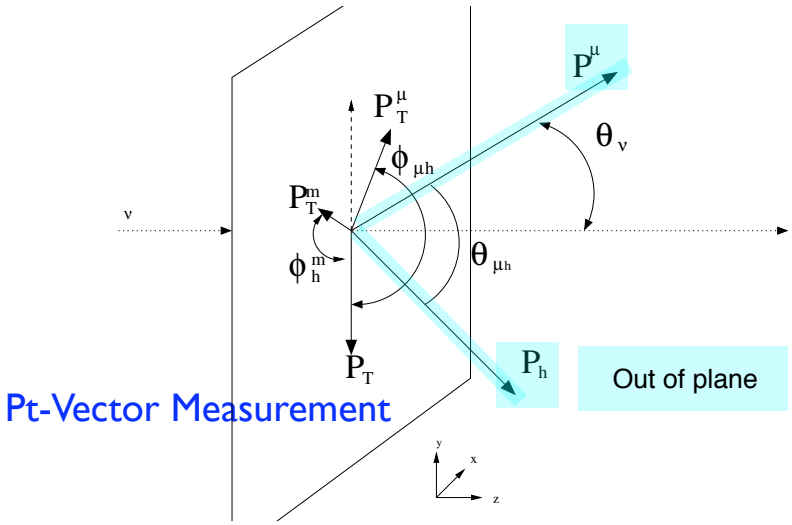

Figure 3–6: Reconstruction of the event kinematics from individual tracks and neutral clusters in the ECAL is a powerful tool to discriminate NC from CC events.

3.6 Expected Detector Resolutions

We expect that the space-point resolution of the STT will be $\mathbf{200}\boldsymbol{\mu}$ on individual hits with a time resolution of about 1 nanosecond. The test-beam measurements of both the ATLAS-TRT and COMPASS-STT have achieved better than $170\boldsymbol{\mu}$ resolution. The resolution of the coordinates of a $\boldsymbol{\nu_\mu}$-CC event, $\boldsymbol{\Delta(X,Y,Z)}$, is expected be $\boldsymbol{\mathcal{O}(100\mu)}$, a value commensurate with the space-point precision of the NOMAD experience. Figure 3–7 shows the superb longitudinal ($\boldsymbol{z}$-position of the $\boldsymbol{\nu}$-vertex) radiography of NOMAD, revealing the elements of the tracker such as the Kevlar skin, the Honeycomb and the Gas-gap within the tracking drift-chambers. The STT will afford vertex resolution at least a factor of two better than that achieved in Figure 3–7.

The energy resolution of the proposed ECAL will be $\boldsymbol{\approx 6\%/\sqrt{E}}$ and a time resolution of 1 ns for e/$\boldsymbol{\gamma}$ with energy $\boldsymbol{\geq 100MeV}$. The MRD, composed of RPCs, will have a space-point resolution of about $200\boldsymbol{\mu}$ and a time resolution of a few nanoseconds. The MRD in the magnet will permit muon identification down to 300 MeV. The momentum resolution of a $\boldsymbol{\nu_\mu}(\boldsymbol{\bar{\nu}_\mu})$-CC induced $\boldsymbol{\mu^-}$ ($\boldsymbol{\mu^+}$) is shown in Figure 5–1 for a 2-m-long track. It should be noted that the average length of a $\boldsymbol{\mu^-}$ ($\boldsymbol{\mu^+}$) from a CC is about 3.5 m. The energy resolution of a $\boldsymbol{\nu_e}(\boldsymbol{\overline{\nu_e}})$-CC induced $\boldsymbol{e^-}$ ($\boldsymbol{e^+}$) is also shown in Figure 5–1 where the electronic charge and direction are measured in the STT and the energy in the ECAL.

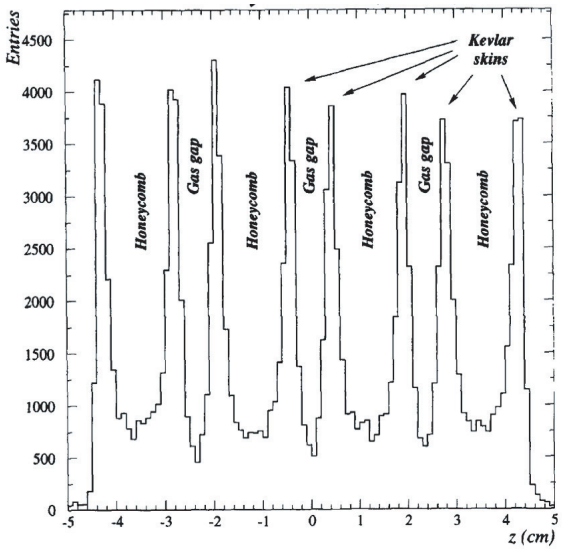

Figure 3–7: A neutrino radiograph of the NOMAD drift chambers shows the internal structure of the tracking volume. It illustrates the high resolution of the z-postion of the vertex.

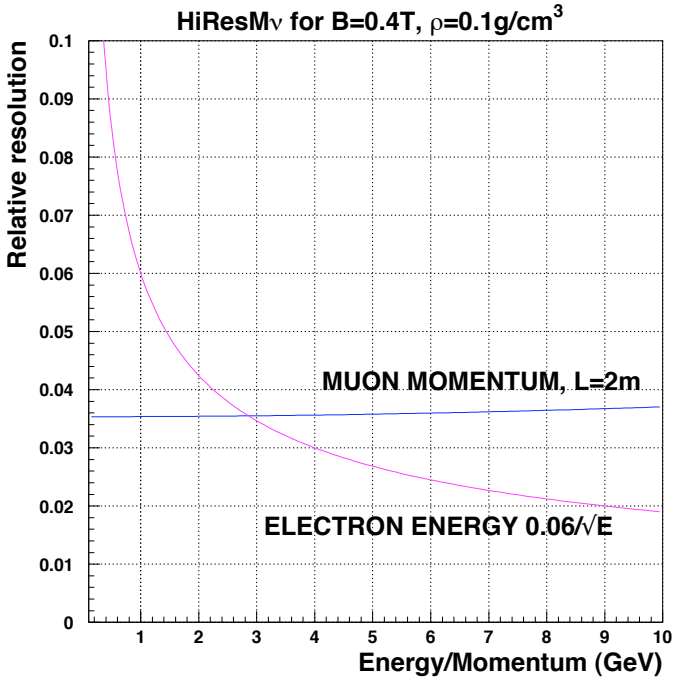

Figure 3–8: Momentum resolution of a $\nu_\mu(\bar{\nu}_\mu)$-CC induced μ^- (μ^+) is shown, in blue, as a function of the muon momentum. Also shown, in red, is the resolution of $\nu_e(\overline{\nu_e})$-CC induced e^- (e^+).

3.7 The LBNE Beam

The LBNE experiment will use a 700 kW proton beam at 120 GeV impinging upon a graphite target. The secondary mesons will be focused via horns and other beamline elements that make up the target hall, 49 m long. The focused charged particles, e.g., $\boldsymbol{\pi^{\pm}}$, $\boldsymbol{K^{\pm}}$ and protons, along with neutral particles, enter into a 4 m diameter and 204-m-long decay pipe. At the end of the decay pipe the hadrons are stopped by an absorber and the large number of muons are ranged out by a 210 m rock shield. The ND hall is at the end of the muon rock-shield, with the ND itself 459 m from the primary target. Figure 3–9 illustrates the beam layout. The neutrino flux are simulated using these beam parameters. We point out that the dimensions of the decay pipe are somewhat preliminary.

3.8 Expected Statistics

The expected event statistics assumes five years running in the neutrino (focusing positive particles) and five in the antineutrinos (focusing negative particles) modes (denoted "5+5"). Assuming $\mathbf{1.8 \times 10^7}$ seconds/year as the operational duration of the LBNE-beam employing 120 GeV protons from the Main Injector with 700 MW, a 5-year run will yield $\mathbf{3.2 \times 10^{21}}$ protons-on-target (PoT). The inclusive sample comprises quasi-elastic (QE), resonance (Res), and deep inelastic scattering (DIS) events. Table 3–2 presents the expected number of events in HIRESMNU induced by $\boldsymbol{\nu_\mu}$ in a 5-year run: Inclusive-CC, QE, NC, coherent-$\boldsymbol{\pi^0}$ and -$\boldsymbol{\pi^+}$, inverse-muon decay (IMD) and $\boldsymbol{\nu_\mu}$-e NC. Also included are the CC events induced by the inherent "contaminant" neutrinos in the beam: $\boldsymbol{\nu_e}$, $\boldsymbol{\overline{\nu}_e}$, and $\boldsymbol{\overline{\nu}_\mu}$.

3.9 Challenges of Precision Oscillation Studies at LBNE

Nothing better encapsulates the challenges of conducting precision oscillation studies at LBNE, or, indeed, at any long-baseline experiment with accelerator beam or atmospheric neutrino than Figure 3–10: a simple figure depicting channels that make up the inclusive $\boldsymbol{\nu_\mu}$-CC at the near location in the LBNE beam. The channels QE, single-pion Res, multi-pion Res, and DIS all have different energy spectra; not shown in the figure are processes having still smaller cross section and still different energy dependence — conveying the complexity of elucidating what one measures at the ND. What makes the precision oscillation study challenging at LBNE, or at any long-baseline experiment, is that the composition of the inclusive $\boldsymbol{\nu_\mu}$-CC at the FD is different from that at the ND. Furthermore, $\boldsymbol{\bar{\nu}_\mu}$-CC, $\boldsymbol{\nu_e}$-CC and $\boldsymbol{\bar{\nu}_e}$-CC will have still different compositions compared to the inclusive $\boldsymbol{\nu_\mu}$-CC, and these compositions at the FD will not be the same as at the ND. Finally, the neutral current spectra from all four neutrino species will be entirely distinct at the two locations.

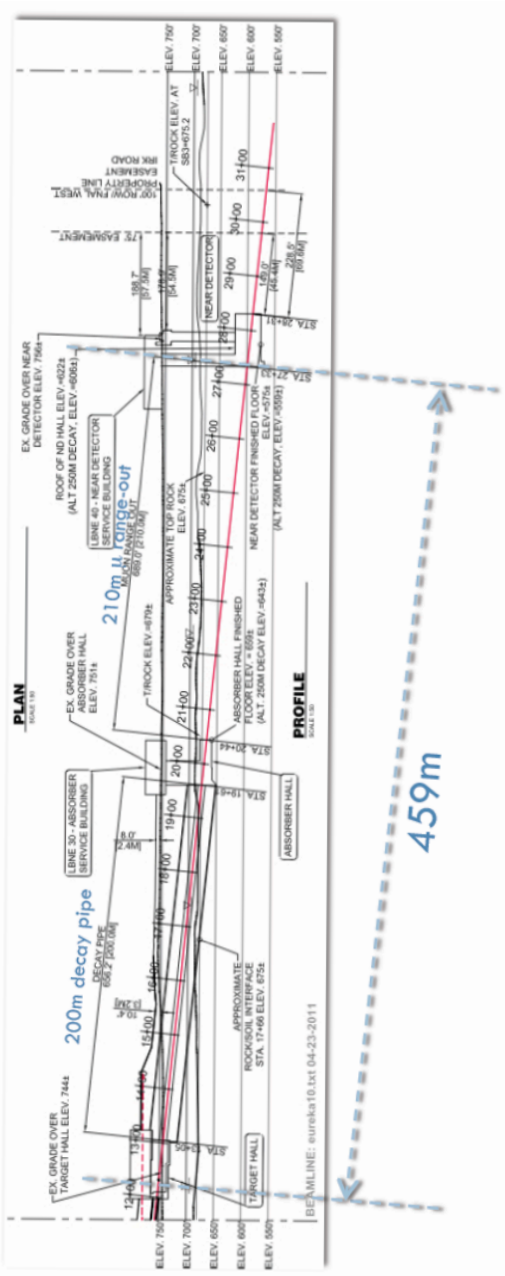

Figure 3–9: Schematic of the LBNE neutrino beamline

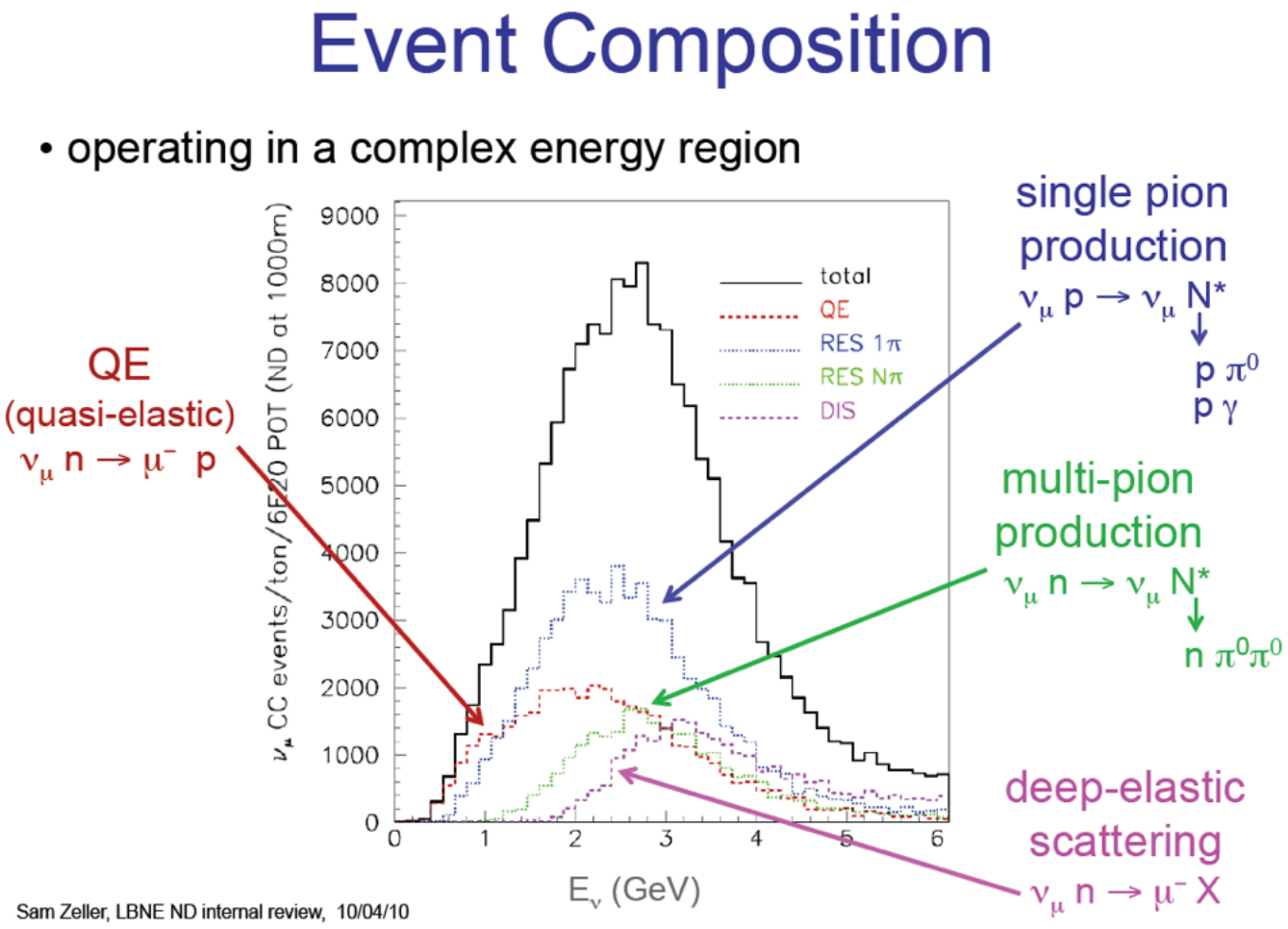

Figure 3–10: Composition of ν_μ-CC, $\mu^- X$, at a Near Location: QE, Single-pion resonance, multi-pion resonance, Coherent-pion, and DIS channels compose the inclusive ν_μ-CC in LBNE. Credit: G. Zeller, FNAL

Table 3–2: Expected Events in a 5-Year ν-Run: Events in the fiducial volume for various interactions are shown.

Interaction	Events	Cuts
Inclusive ν_μ-CC	38.2×10^6	FV
ν_μ-QE-CC	8.1×10^6	FV
ν_μ-Res-CC	11.0×10^6	FV
ν_μ Coherent-π^+	0.63×10^6	FV
Inclusive ν_μ-NC	4.1×10^6	FV & $E_{Had} \geq 3$ GeV
Coherent-π^0	0.32×10^6	FV
IMD	1944	FV ($E_\nu \geq 11$ GeV)
ν_μ-e NC	4700	FV
Contaminant CC's		
ν_e-CC	4.2×10^5	FV
$\bar{\nu}_e$-CC	4.2×10^4	FV
$\bar{\nu}_\mu$-CC	2.5×10^6	FV

Figure 3–10 illustrates that LBNE will be operating in a complex region, made the more inscrutable by the poorly known neutrino- and antineutrino-nucleon cross sections.

Neutrino-Nucleon Cross Section: Figure 3–11 presents a compilation of the inclusive ν_μ-nucleon cross section measurements as a function of neutrino energy (E_ν). It should be noted how poorly $\sigma(\nu_\mu N)$ is measured in the $0.5 \leq E_\nu \leq 10$ GeV region, the region that concerns all current and future long-baseline experiments.

Antineutrino-Nucleon Cross Section: If $\sigma(\nu_\mu N)$ is poorly measured, the antineutrino-nucleon cross section is still more poorly measured, as Figure 3–12 shows. Indeed, there are hardly any measurements below 10 GeV.

Neutrino Quasi-Elastic Interaction: The cross section data of the exclusive, seemingly 'simple' quasi-elastic interaction, $\nu_\mu + n \rightarrow \mu^- + p$, evinces a $\sim$30% discrepancy around $E_\nu \simeq 3$ GeV. Nuclear effects can significantly modify the visible final states. For example, in meson-exchange currents a much larger fraction of the incident neutrino energy goes into the hadronic sector [24]. Indeed, the nuclear effects could prove pernicious – meson-exchange currents could affect the neutrino and antineutrino interactions differently causing a spurious 'CP-violating' effect. Therefore, the ND must accurately measure the recoil proton.

Neutrino Neutral Current Cross-Section: Although the NC events make up 35% of all

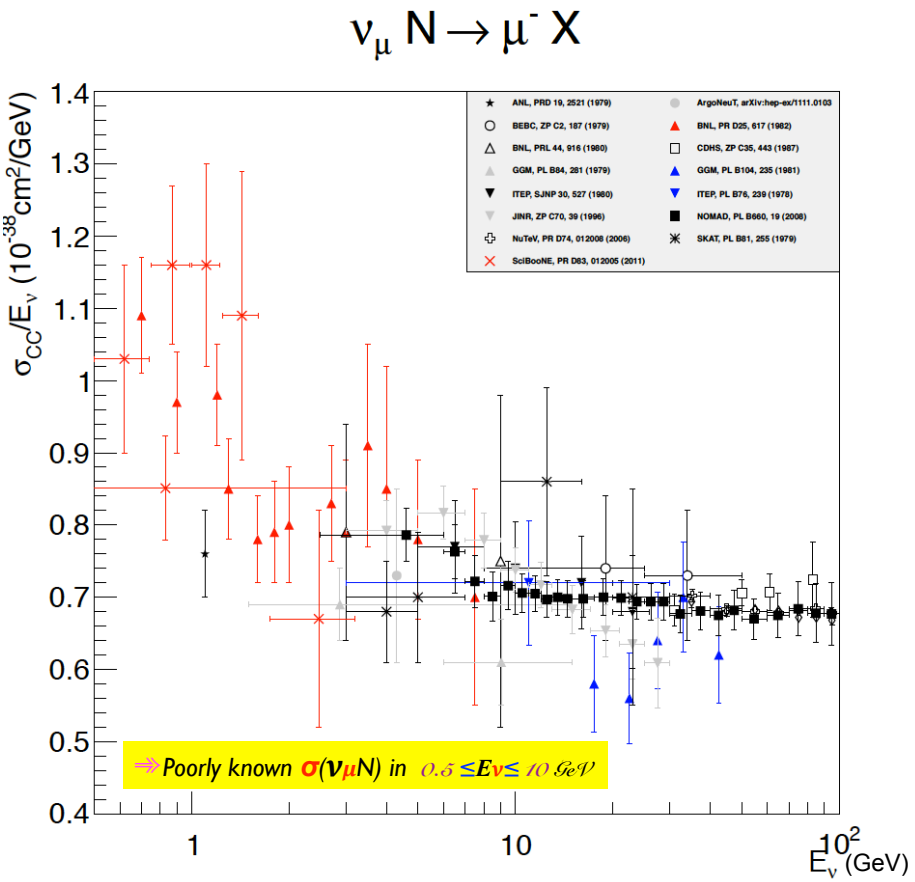

Figure 3–11: Compilation of the inclusive ν_μ-nucleon cross section measurements as a function of the neutrino energy (E_ν).

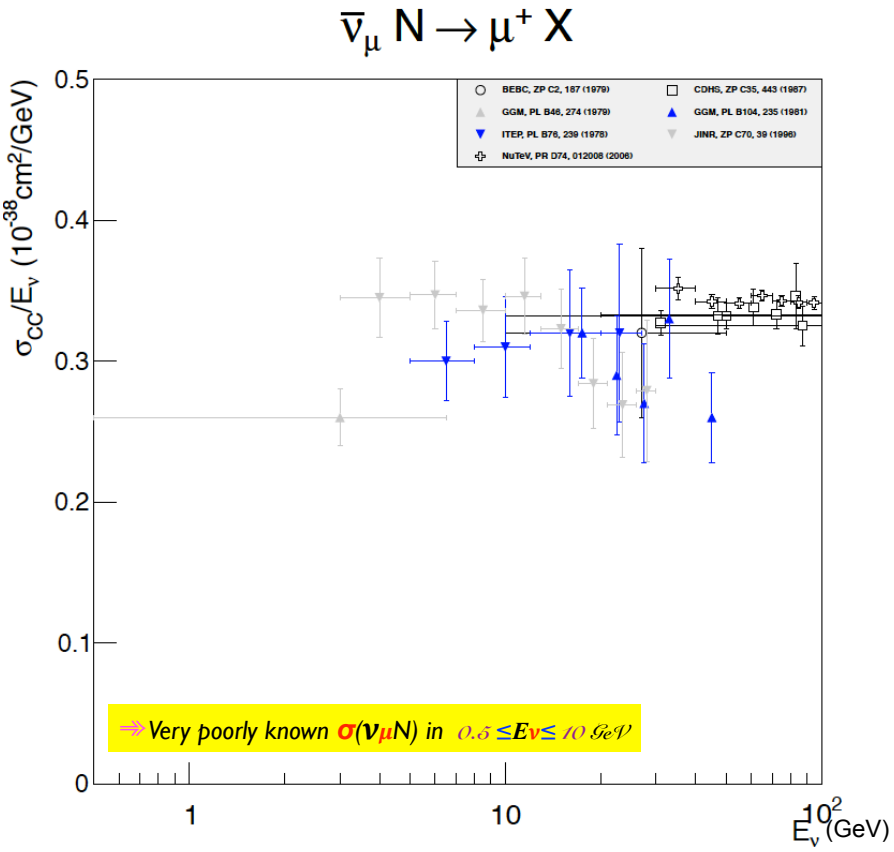

Figure 3–12: Compilation of the inclusive $\bar{\nu}_\mu$-nucleon cross section measurements as a function of the antineutrino energy (E_ν).

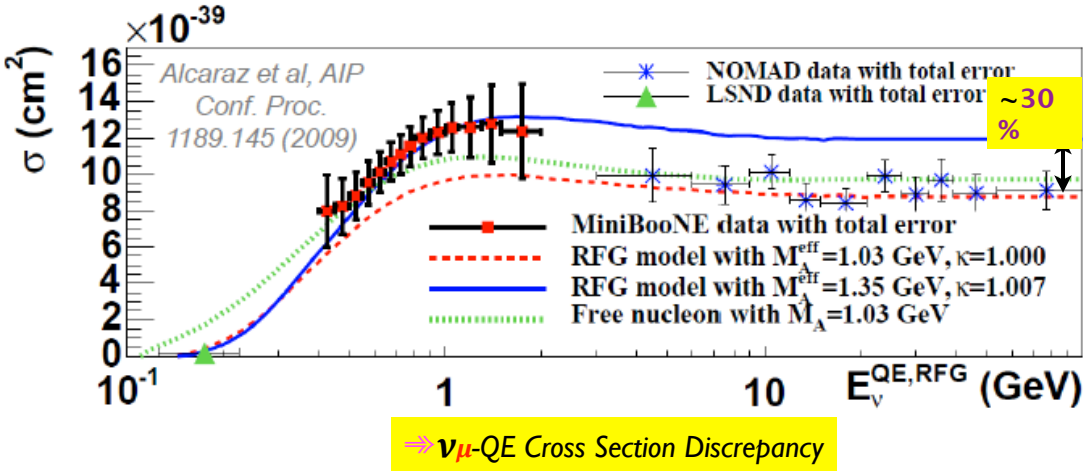

Figure 3–13: Neutrino quasi-elastic cross section by NOMAD and MiniBOONE experiments

ν-interactions, the cross-section of NC events at visible, or hadronic, energies below 5 GeV — where most of the LBNE events are — has not been reported. It should be pointed out that just like the inclusive ν_μ-CC cross section, the ratio NC/CC is measured to a very high precision at higher energies ($\geq$ **20** GeV). The low-energy NC region, however — all-important to the oscillation studies — remains unelucidated.

Returning to Figure 3–10, the experimental status of the one- and multi-pion resonance processes is worse than that of QE; and, as mentioned above, there are no published measurements of neutral current cross section in the visible energy range of 0.5–5 GeV.

Given the paucity of precise, composite data in the neutrino and antineutrino cross sections and the complexity of the processes composing the neutrino/antineutrino spectra, the task of the next generation near detector is to identify these channels, measure their cross-sections, and predict with high accuracy their spectra as a function of energy at the far location. As presented in Chapter 4, the HIRESMNU will meet these challenges.

3.10 Trigger and Rates

HIRESMNU will employ two triggers. The principal trigger will be STT-based, distributed throughout the detector. This avoids the geometric bias employed by NOMAD where a charged track is required to traverse the downstream end of the detector. The maximum drift time for a Xenon-CO_2 mixture is 125 ns over 5 mm (note that the straw tube has a 1 cm diameter), allowing the STT to resolve beam bunches that are 19 ns apart. We propose a self-triggering scheme in which hits are stored in pipelines awaiting a later decision. The ATLAS-TRT front-end readout has a pipeline of 256 ns. The secondary trigger will

based upon the energy deposition in the ECAL where a minimum energy deposited will be required, typically 0.25 or 0.5 GeV, consistent with the beam RF time. The two triggers are complementary, allowing a cross-calibration of the efficiency and dead time.

4 The Detector Design

The high-resolution near detector for LBNE, HIRESMNU, will comprise an active straw tube tracker (STT), surrounded by an electromagnetic calorimeter (ECAL), all embedded inside a dipole magnet, and instrumented with muon-ID detectors, see Figure 3–1. This chapter details the design parameters of these subdetectors. The low average density of the target, $\boldsymbol{\rho \simeq 0.1\ g/cm^3}$ (similar to that of liquid hydrogen), combined with the granularity of the STT, affords excellent momentum and angular resolutions for $\boldsymbol{\mu^{\pm}}$, $\boldsymbol{e^{\pm}}$, $\boldsymbol{\pi^{\pm}}$ and ***proton***, and via decay/conversion, for $\boldsymbol{\pi^0/\gamma}$ and $\boldsymbol{K^0_S}$ produced in $\boldsymbol{\nu}$-induced interactions. The volume of the tracker is $\boldsymbol{\sim 350 \times 350 \times 750}$ cm$^{\mathbf{3}}$. The $\boldsymbol{4\pi}$ ECAL coverage ensures accurate determination of the momentum vector of the hadronic shower. The dipole magnet yokes are instrumented with muon-ID detectors (called muon range detectors, MRD) to identify the low-energy, wide-angle muons; downstream and outside the magnet there are additional muon-ID detectors (called external muon identifiers, EMI) for high-energy, forward muons (see Figure 3–2). The STT will have nuclear targets, for example argon and iron, relevant to LBNE and INO experiments respectively, to provide sufficient statistics, i.e. about five times more than expected in FD, to quantitate the difference in $\boldsymbol{\nu}$-nuclei cross section.

4.1 Straw Tube Tracker

The STT is the heart of the detector. The design of the straw tube follows that of the COMPASS detector [22,23] whose dimensions are similar to ours. The conceptual transition-radiation measurement in $\boldsymbol{\nu}$-interactions is based upon NOMAD-TRD [10]; the design of the TR-detection follows that of the ATLAS Transition Radiation Tracker [19,20,21].

The straw tube will have a 9.53 mm diameter inner foil and 9.7 mm diameter outer foil. The inner foil will be made of 40-$\boldsymbol{\mu}$m-thick carbon-loaded Kapton film 160XC370. The outer foil will be made of 25-$\boldsymbol{\mu}$m-thick aluminium-laminated Kapton film 100HN. (A possible alternative is that both inner and outer foils be thick Kapton 100HN.) The foils would be aluminium laminated, and the inner strip coated with carbon during manufacturing to provide electrical conductivity. Although the alternative would reduce the M&S cost of STT

by ∼10%, it would entail additional labor and risk.)

Each straw will have a 30-μm diameter gold-plated tungsten wire positioned along the axis of the straw by spacers and end plugs. The active gas of the STT will be a mixture of Xenon (70%) and CO_2 (30%). Vertical (Y) and horizontal (X) planes of straws will be alternated and arranged in modules. Each module will consist of a double straw layer (either XX or YY), the second layer shifted by half the diameter with respect to the first layer as shown in Figures 3–1 and 4–1. Each layer will have 352 straw stubes; two layers will make a module. The STT will have a total of 160 modules, containing 112,640 straw tubes. Readout will occur from both ends of the straws to resolve ambiguities in the hit assignment.

An alternative design calls for a STT module containing four layers of straw tubes arranged as XX-YY. The two designs agree within 5% of the estimated cost; the physics sensitivity of the alternative design is under study.

At either side of the two straw layers in each module, there will be a set of hydrocarbon foils called "radiators" at the upstream and downstream ends of the STT module. As an electron traverses the radiators, it will generate transition radiation (TR) photons distinct from those generated by charged-pions or muons. Each radiator target is composed of two sections, with a total of 38 + 37 layers of 40-μm polypropylene (C3H6)n films alternating with 37 + 36 sheets of 250-μm tulle fabric spacers. Radiators not only generate TR but also constitute ∼82–85% of the nominal mass of the target. The mass of the radiator installed in each module is ∼35 kg. One radiation length (X_0) corresponds to about 5 m in the STT.

Nuclear targets will be positioned at the upstream end of the tracker, replacing the radiator module. Thin nuclear targets, of Fe or Ca, for example, could be installed in the upstream region of STT as shown in Figure 4–2 to provide a statistically robust sample (×5 the FD statistics) to quantitate differences in ν-nuclear interactions. Since the LBNE FD employs argon, we propose to use argon gas in pressurized tubes at the upstream end of the STT. An engineering drawing shows the Ar target in Figure 7–13. The STT resolution of the vertex position of a neutrino interaction with $\geq$ 2 charged tracks is sufficient to locate the interaction inside the nuclear target(s) as presented in Section 3.6 and further discussed below.

To enable the TR measurement, the STT will have a mixture of Xenon (70%) and CO_2 (30%) gas. The total active gas volume of STT is 39 m^3 and will be flushed with approximately one volume change/hour. The endplug for the STT will be similar to that for the ATLAS-TRT as shown in Figure 4–3. The gas distribution will be a closed recirculating system to minimize Xe losses; the exiting gas from the STT will be recovered, cleaned and recirculated. The gas pressure in the straws will be ∼1 mbar to minimize Xe losses, similar to the ATLAS criterion. The STT must be protected against humidity. To achieve this, CO_2 will be flushed through the straws throughout the outer envelope of the STT (78 m^3) at a forced-flow rate of ∼100 m^3/h.

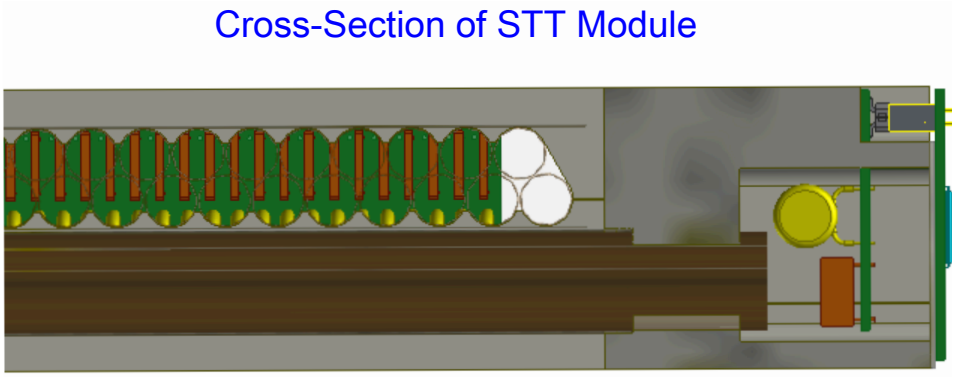

Figure 4–1: Layout of the straw layers and cross section of an STT Module.

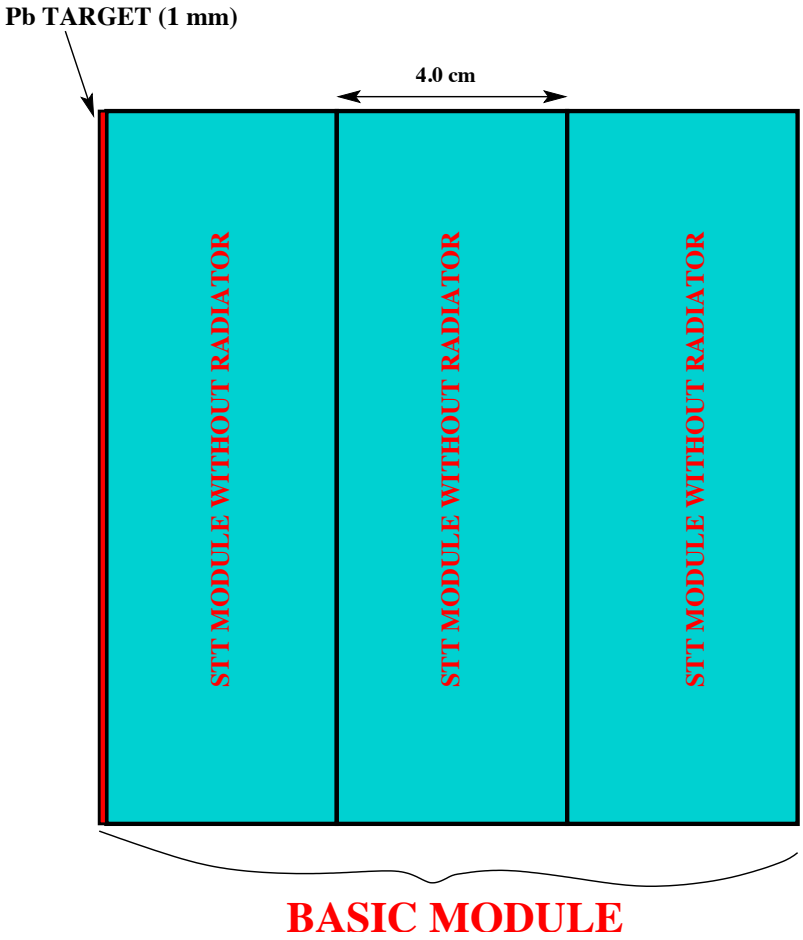

Figure 4–2: Sketch of a basic STT module for the measurement of nuclear effects. Several modules can be placed in the upstream magnetic volume with different target materials (Pb, Fe etc.) of the same thickness in radiation length.

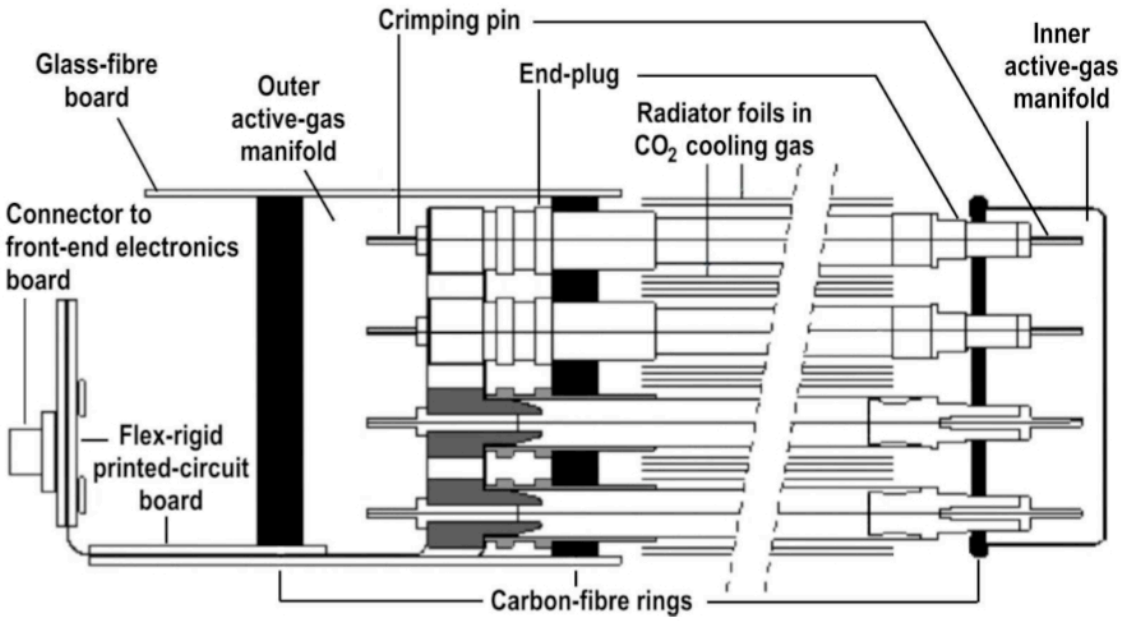

Figure 4–3: Schematic of the ATLAS STT Endplug

To minimize ambiguity in assigning hits to a track, the straw tubes will be read out at both ends. The readout electronics will be based upon the ATLAS design, (see Figure 4–4). Front-end (FE) boards, mounted on the STT frame, will provide amplification, shaping and baseline restoration. The FE will be based upon an 8-channel analogue ASIC. A subsequent 16-channel ASIC will perform the drift-time measurement ($\sim$3 ns binning). The TR and $\boldsymbol{dE/dx}$ measurements will be performed with an ADC connected to the FE-ASIC.

The following steps are envisioned in the construction of an STT module:

- Procure wires, end-plugs, spacers, pins, connectors, etc.
- Complete assembly of the straws
- Perform quality control on the straws
- Laminate plastic films into straws
- Connect and insulate straws
- Procure the mechanical frames of the modules
- Assemble the straws into STT modules

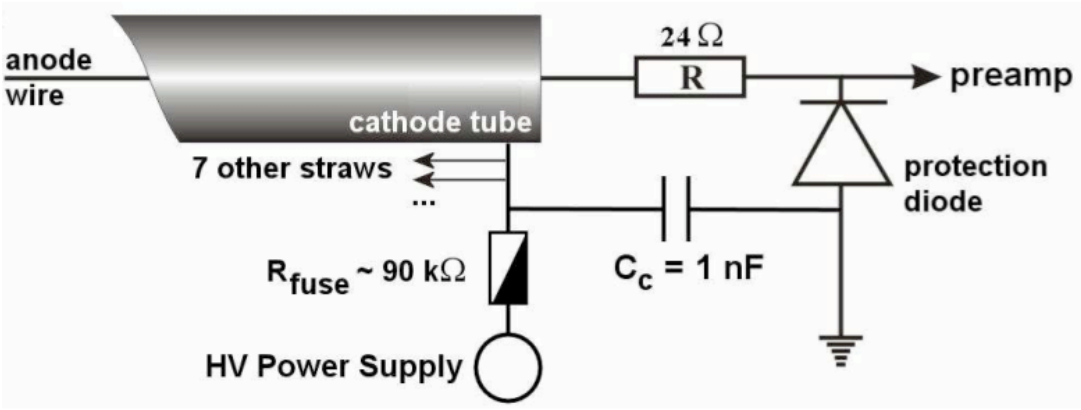

Figure 4–4: Schematic of the STT Readout.

- Procure Kapton films for straw construction
- Procure the radiators
- Assemble the radiators/targets in STT modules
- Procure the readout boards
- Assemble the readout boards
- Perform acceptance tests for the STT modules

The fabrication is described more fully in Chapter 7.

4.2 Electromagnetic Calorimeter

The tracking volume will be surrounded by an ECAL: the forward or downstream (DS) module, the four-sides (top-bottom and left-right) of the Barrel module, and the upstream (US) module. The ECAL will have transverse and longitudinal segmentation. The ECAL is a lead-scintillator calorimeter based upon the T2K-ECAL. The ECAL-surrounded STT will be embedded inside the dipole magnet.

The most important component of the ECAL is the forward, or DS, module composed of 58 layers of 10-mm-thick (along z-direction) scintillator (Sci) followed by 1.75-mm-thick lead, corresponding to 18 radiation lengths (X_0). The first layer will be composed of 160 horizontal

scintillator bars (providing $\boldsymbol{y}$-coordinate of particles), 400-cm long, 2.5-cm wide, and 1-cm thick; followed by the Pb sheet. The 2.5-cm width of the bar is informed by the Moliere-radius of a 2.5 GeV electron — typical of $\boldsymbol{\nu_e}$-induced CC — which is approximately 2 cm. The second layer will be composed of 160 vertical scintillator bars (providing X-coordinate), 400-cm long, 2.5-cm wide, and 1-cm thick; followed by the Pb sheet. The third layer will be a Y-plane of bars, vertically shifted by 1.25 cm; followed by Pb sheet; The fourth layer will be a X-plane of bars, horizontally shifted by 1.25 cm; followed by Pb sheet. This arrangement will repeat itself to complete the DS-ECAL module. Figure 4–5 shows a preliminary schematic of the DS-ECAL containing a total of 9280 Sci-bars with a total Sci-volume of 4.64 $\mathbf{m^3}$. Figure 4–6 shows the engineering details of the module.

At a national lab or fabrication center in India the scintillator bars will be extruded with Kuraray wavelength-shifting fibers and later threaded through the middle of the bars. The fibers will be read out at each end by silicon photomultiplier (SiPM) type photosensors. The two readings allow for a position determination. It follows that the number of readout channels will be twice the number of scintillator bars. In the DS-ECAL, there will be 18,560 SiPMs. The T2K-ECAL used the Hamamatsu photosensors called MPPC which will be adequate for our use. It must be noted that the SiPM technology has undergone a rapid improvement, driving the costs lower and offering better performance.

Since the Barrel-ECAL will surround the sides of STT, nominally there would be four modules, 8m $\times$ 4m area, corresponding to the top, bottom, left and right sides. The conceptual design of the Barrel-ECAL is similar to that of the DS-ECAL. A Barrel-ECAL module, Figure 4–7, will have eight layers of alternating horizontal and vertical scintillator strips every 7 mm of lead, or 10-$\mathbf{X_0}$ deep. The upstream (US) ECAL will be identical to one of the Barrel-ECAL modules (see Figure 4–8). For the scintillator bars, our default assumption is that the dimensions of the bars in the Barrel-ECAL and US-ECAL will remain similar to those in the DS-ECAL, i.e., 400-cm long, 2.5-cm wide, and 1-cm thick. The total number of bars in the eight modules of Barrel-ECAL and the one module of US-ECAL will be 11,520 (4-layers $\times$ 400cm/2.5cm $\times$ 9) corresponding to 30,000 readout channels.

We have given some thought to reducing the number of channels in the ECAL. Our preliminary optimization studies include (a) reducing the longitudinal granularity in the most important portion, the DS-ECAL; (b) reducing its transverse granularity; and (c) reducing the transverse granularity of the Barrel-ECAL. A detailed GEANT4 based MC will provide us with better guidance.

4.3 Dipole Magnet

The tracking detector and ECAL modules will reside inside a 0.4-T dipole magnet with inner dimensions of 4.5-m wide by 4.5-m high by 8.0-m long. The proposed dipole magnet is a larger version of the UA1 dipole magnet [9] which was used by NOMAD, and is currently in use by

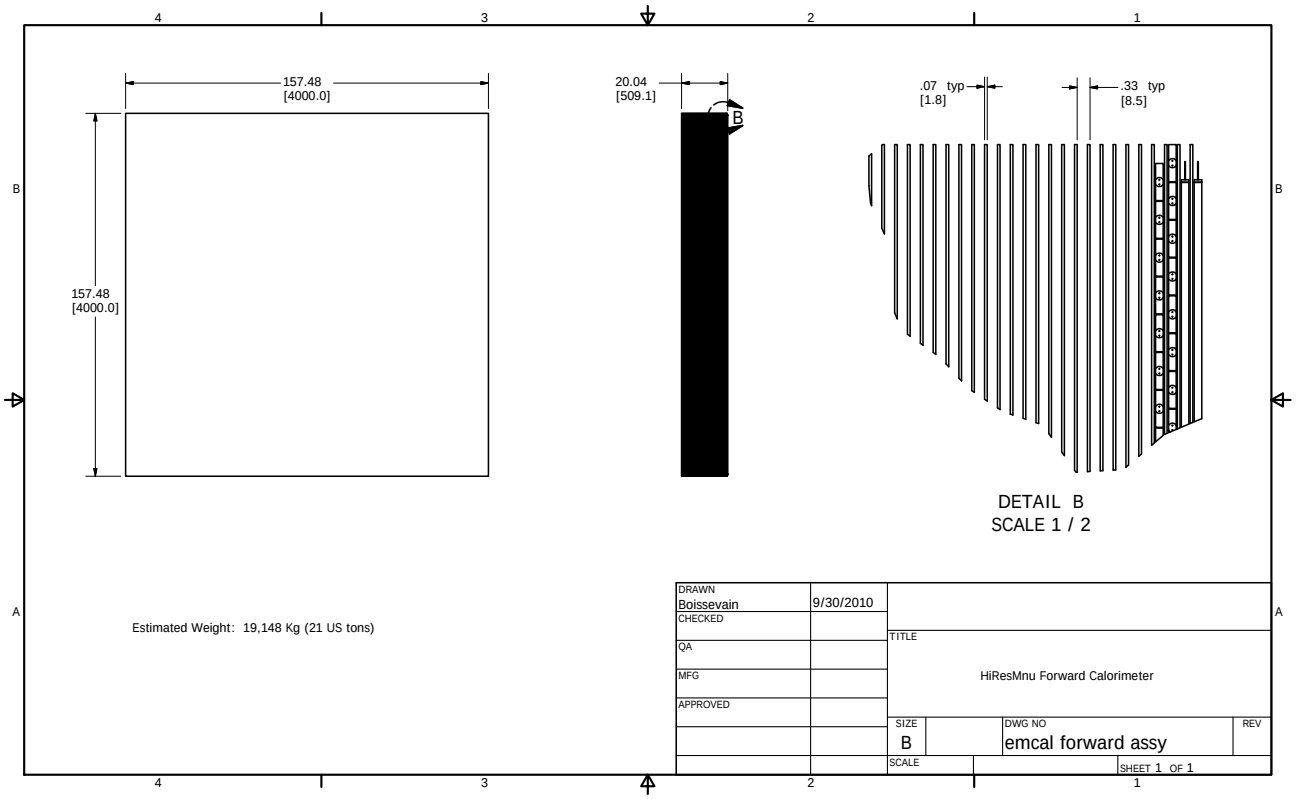

Figure 4–5: Preliminary Schematic of the DownStream or Forward ECAL.

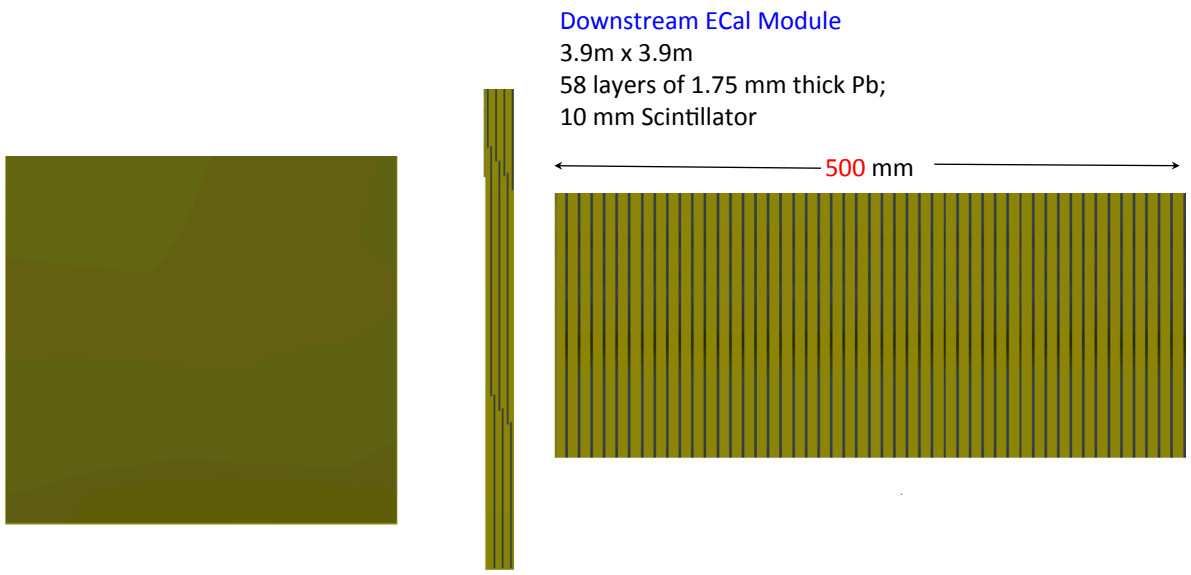

Figure 4–6: DownStream (DS) or Forward ECAL

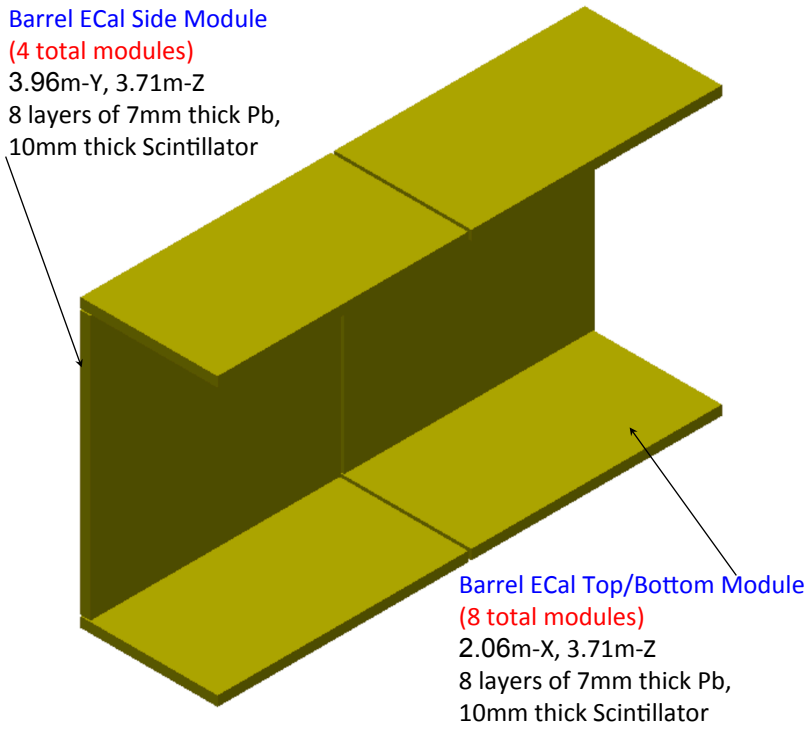

Figure 4–7: Specifications of the Barrel ECAL

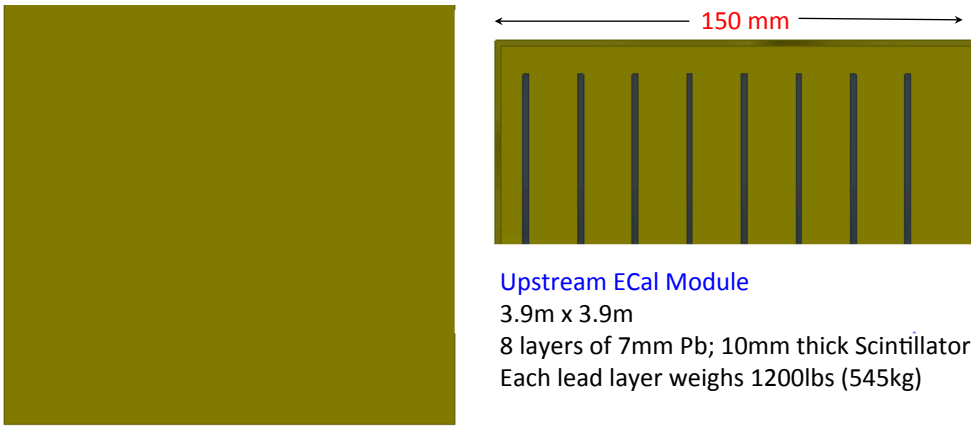

Figure 4–8: UpStream (UP) ECAL

the near detector at T2K. Because the dipole magnet for HIRESMNU is very similar to the UA1 magnet, we first present the design and parameters of the UA1 dipole. Figure 4–9 shows the UA1 magnet yoke assembly, Figure 4–10 shows its yoke & coils, Figure 4–11 presents the corresponding coil assembly, and Figure 4–12 shows a photograph of the specifications of the UA1 magnet during the NOMAD operation. Table 4–1 summarizes the salient parameters of this magnet at the maximum operating B field of 0.7 T. The HIRESMNU magnet will operate at 0.4 T.

Table 4–1: Parameters of the UA1/NOMAD dipole magnet. The quoted numbers are for Al-coil and the maximum B-field (0.7 T). The nominal B-field for HIRESMNU is 0.4 T.

Item	Cost ($)
Dimension	3.5 x 3.5 x 7 m^3
Maximum B-Field	0.7 T
Maximum Current	10,000 A
Resistance (40C)	0.0576
Voltage	576 V
Mass	900 T
Cooling water flow	50 liters/sec
Pressure gredient	15 atm (in .vs. out)
Temperature Diff	30 C

The principal differences between the UA1/NOMAD and the HIRESMNU magnets are: **(a):** Size; **(b):** Coil — UA1 used Al-coil (to minimize the degradation of the energy resolution of the outgoing jets) with resistivity $\boldsymbol{\rho_{Al} = 2.8 \times 10^{-8} \Omega m}$ whereas the HIRESMNU proposes to use Cu-coil whose resistivity is $\boldsymbol{\rho_{Cu} = 1.7 \times 10^{-8} \Omega m}$; and **(c):** HIRESMNU magnet does not need a hole in the coil to allow passage of the proton beam, as was the case with the UA1 magnet. The HIRESMNU dipole will be composed of 8 + 8 'C'-sections, the iron yokes. The coil will be made of copper, with aluminium as another option. Figure 4–13 shows a conceptual engineering drawing of the proposed magnet and 'C' section.

4.4 Muon-ID Detector

In the HIRESMNU design, the muon-ID detector will identify muon tracks which will then be matched with tracks in the STT with measured momenta and charges. Thus, the muon-ID detector is not required to furnish muon momentum, only the $\boldsymbol{\mu}$-ID. However, given the large rate of muons in the ND location, we need a muon-ID detector with such spatial and time resolutions as to precisely reconstruct $\boldsymbol{\mu}$-track segments and permit an unambiguous match with the muon track in the STT.

The muon-ID detector can be divided into two systems:

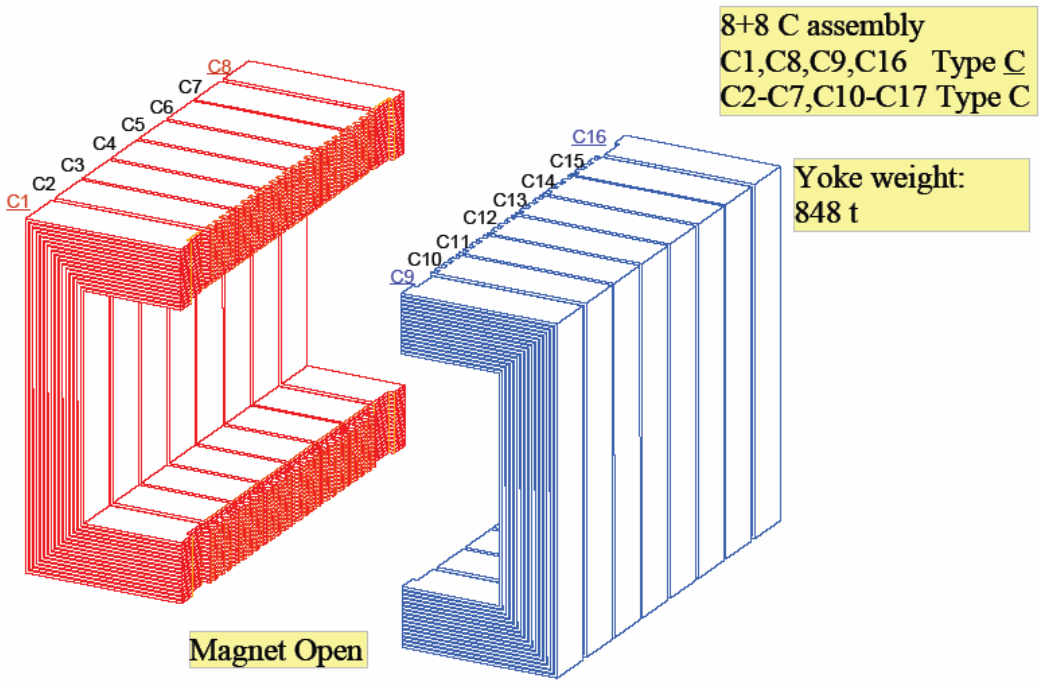

Figure 4–9: Magnet yoke assembly of the UA1/NOMAD dipole magnet.

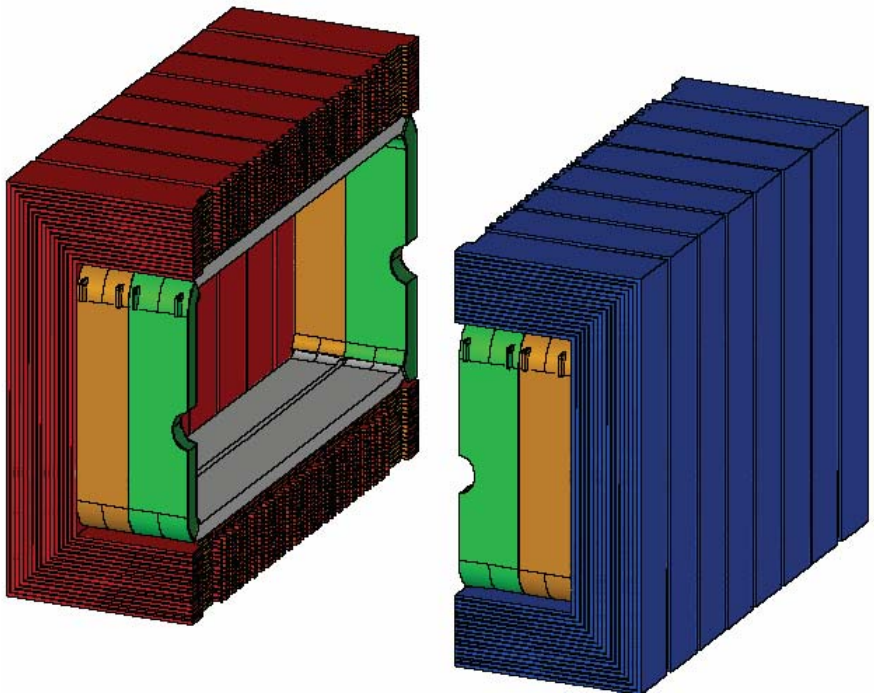

Figure 4–10: Yoke and coil of the UA1/NOMAD dipole magnet.

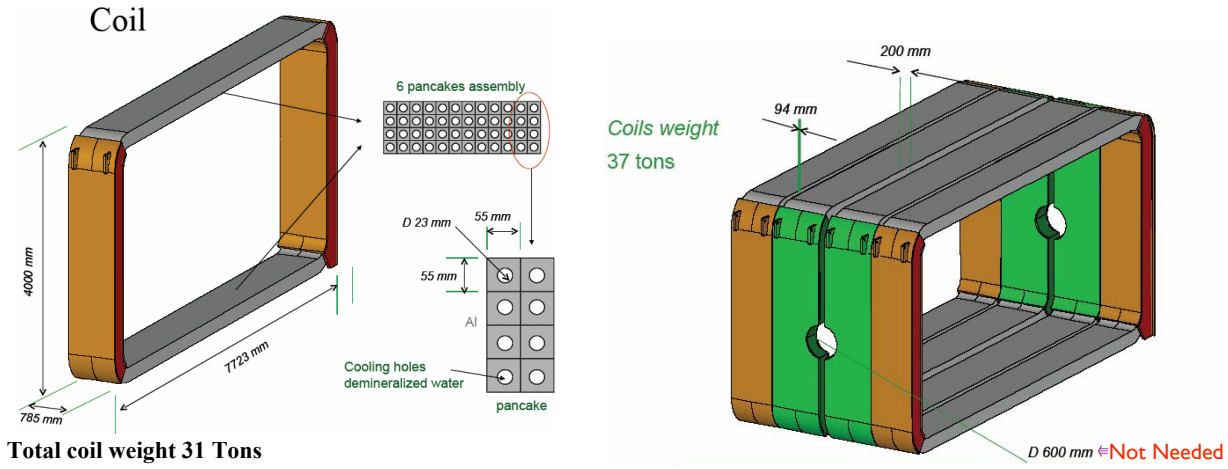

Figure 4–11: Coil and coil-assembly of the UA1/NOMAD dipole magnet.

Figure 4–12: Specs of the UA1/NOMAD dipole magnet.

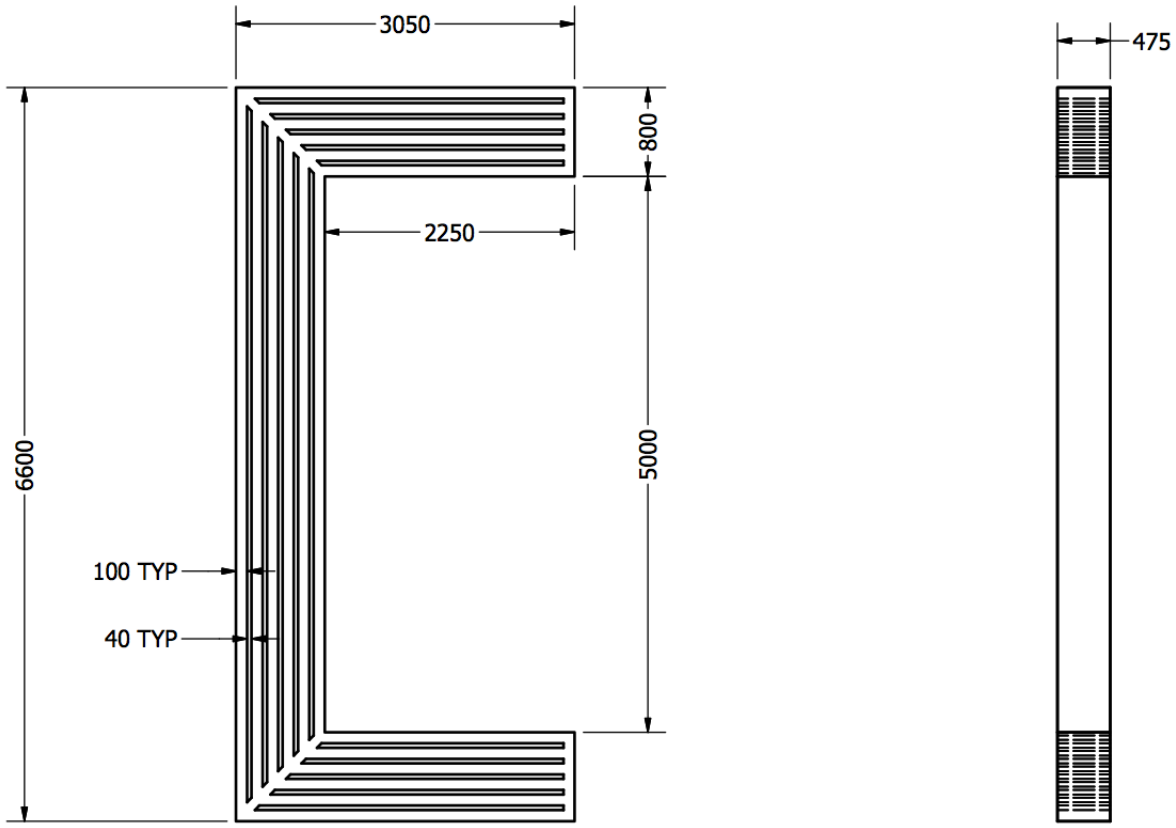

Figure 4–13: Conceptual sketch of one of the C-sections that constitute the magnet return yoke (dimensions are in mm). The vertical dimension is longer than the horizontal one in order to accommodate the magnet coil.

- **[I]** The Muon Range Detector (MRD) instruments the gaps between the plates of the magnet return yoke. The main task of the MRD is to identify muons at low momenta exiting the sides of the detector. The MRD will reconstruct track segments within the magnet return yoke, including those of the stopping (ranging-out) muons.
- **[II]** The External Muon Identifier (EMI) will identify high-energy forward muons. It is located outside the magnet, at the downstream end of the detector. The EMI will consist of two stations separated by a passive concrete/iron absorber. At each station, outside and downstream of the dipole magnet, it will reconstruct muon track segments to be matched with the STT tracks.

Due to multiple scattering in the material (mainly iron) crossed by the muon tracks reaching both the MRD and the EMI detectors, a space resolution in the range of $\simeq \mathbf{0.75}\ \boldsymbol{mm}$ will be adequate to accomplish the tracking task of the muon-ID detectors. For both the MRD and the EMI detectors we have selected the same Resistive Plate Chamber (RPC) technology as that developed for the LHC experiments, OPERA, BaBar and Argo. (An alternative under consideration is glass-based RPCs.) In particular, we follow the design of the RPC detectors used in the OPERA experiment to instrument the gaps within the magnet of the Muon Spectrometer. This type of application is similar to our MRD and has been operational for a few years in OPERA. A sketch of the detector is shown in Figure 4–14. Two electrodes, made of 2-$\boldsymbol{mm}$ Bakelite with lineseed oil and volume resistivity $\boldsymbol{\rho > 5 \times 10^{11}\ \Omega}$ cm at T = $20^{\mathbf{0}}$ C, are kept 2 $\boldsymbol{mm}$ apart by means of polycarbonate spacers in a 10-cm lattice configuration. The external surface of the electrodes is painted with graphite of high surface resistivity and protected with 190 $\boldsymbol{\mu m}$ thick polyethylene terephtalate (PET) insulating film. An additional 250 $\boldsymbol{\mu m}$ thick PET layer is applied during the installation on each side of the RPC to prevent high voltage discharge. The inner surface of the electrodes is coated with a few-micron-thick polymerized lineseed oil layer. The total thickness of an RPC is between 6 and 7 $\boldsymbol{mm}$.

The RPC counters will be operated in the streamer operation regime because of its large amplitude signals ($\sim$100 mV). The default gas mixture can be the one used in OPERA, which is argon, tetrafluoroethane and isobutane in the volume ratios 76/20/4 with the addition of 0.5 % of sulphur hexafluoride. Each RPC row is flushed separately at five refills/day, using an open-flow gas system. Copper and stainless steel pipes will be used throughout the system to avoid excessive humidification of the mixture, with the exception of the detector connections, where flexible plastic pipes will be used.

The double coordinate read-out is performed by means of 7-$\boldsymbol{mm}$ pitch strip panels. Between the strips and the RPC, on both detector sides, additional 200-$\boldsymbol{\mu}$-thick polyethylene thereph-thalate layers are added to ensure better insulation. To guarantee the strip adherence to the RPCs in the MRD, spacers made of polyester fibers will be used to fill the residual gap space between the iron slabs.

The high voltage (HV) difference across the gas gap is obtained by applying opposite polarity

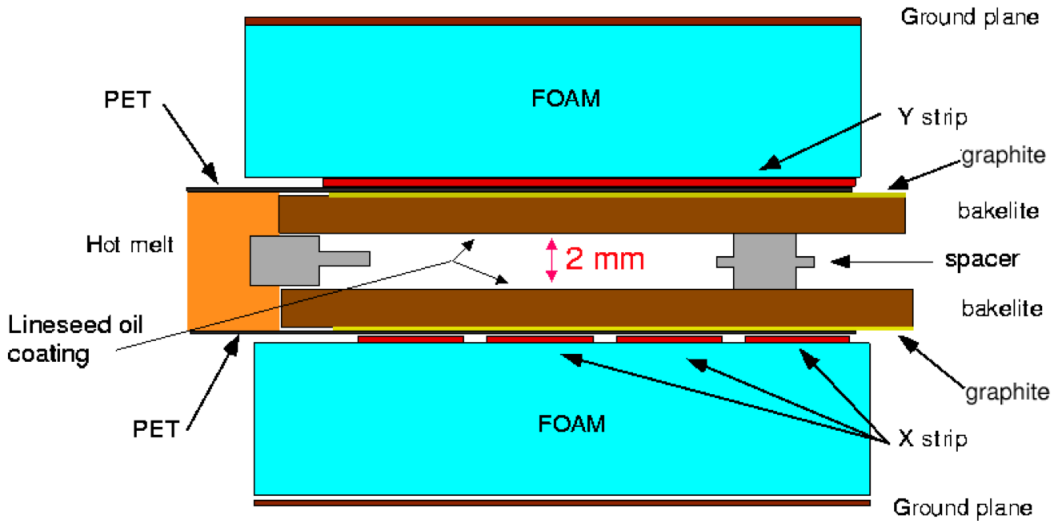

Figure 4–14: Cross section of a Resistive Plate Chamber with its associated strips for the readout of the induced signal.

voltages on the two electrodes. In the HV system we will use distributors measuring operating currents with nA precision. As temperature is a relevant parameter for RPC operation, ten thermistors will be placed on each RPC layer between the external side of the read-out strips and the filling material.

The design of the RPC detectors is based upon the extant models that have been successfully operated in the LHC experiments, and in the OPERA and Daya-Bay experiments for several years. Extensive aging tests were performed under high-rate conditions for the LHC experiments. The average RPC efficiency measured during the quality control tests for the OPERA experiment was 98%, with a non-uniformity over the RPC surface smaller than 2%.

The size of each RPC detector will be $\boldsymbol{3m \times 1m}$, which is very similar to those used in the OPERA and LHC experiments. Figure 4–13 shows a sketch of one of the C elements of the magnet return yoke. Each of the five gaps between consecutive steel plates will be instrumented with a plane of RPC detectors. In addition, one RPC plane will be located on the external surface of the magnet. Overall, the MRD will consist of a total of six RPC planes. The thickness of each steel plate is 10 $\boldsymbol{cm}$, with gaps 4-$\boldsymbol{cm}$ thick. The total area to be instrumented by RPC detectors within the MRD will be about 1,065 $\boldsymbol{m^2}$, corresponding to 355 RPC modules.

In order to guarantee a good acceptance for forward muons, the EMI must have a large transverse area. Currently an ambitious $\boldsymbol{10m \times 10m}$ EMI is assumed; realistically the dimensions will be closer to $\boldsymbol{7m \times 7m}$; the precise dimensions of the EMI will be determined after further simulations. We will instrument the EMI with two separate MRD stations, each

consisting of three layers of RPC detectors. Muons entering the first and second stations will have to cross an amount of material equivalent to five interaction lengths ($\boldsymbol{\lambda}$) and $\mathbf{8\lambda}$, respectively. Overall, the total area to be instrumented by RPC detectors within the EMI will be about 600 $\boldsymbol{m^2}$, corresponding to 200 RPC modules.

We plan to use different granularity for the positive and negative polarities applied to the two electrodes in order to maintain the high voltage difference across the gas gap. For the positive HV polarity we will connect three RPC chambers per HV channel. For the negative HV polarity we will connect 63 RPC chambers per HV channel. The total number of HV channels required will thus be 194, including both the MRD and the EMI.

Since we have chosen to operate the RPC detectors in streamer mode we will collect large signals from the strips and we will not need to use pre-amplifiers in the readout. In addition, the readout electronics can be installed on the top of the magnet and will be directly connected to the pick-up strips by means of twisted pair cables (typical length $\sim \mathbf{10}\boldsymbol{m}$). We plan to use the center of gravity of the charge collected by the strips within a cluster to improve the space resolution of the RPC detectors. The readout electronics will include one discriminator, one ADC and one TDC for each channel/strip.

Each RPC will have a double coordinate read-out by means of two orthogonal planes of strips. The maximal length of the pick-up strips will be $\sim \mathbf{4}\ \boldsymbol{m}$ in the MRD and $\sim \mathbf{5}\ \boldsymbol{m}$ in the EMI to avoid deterioration in the time resolution. The thickness of the strips will be $\mathbf{7}\ \boldsymbol{mm}$. Each plane of RPCs will be split into two independent halves in order to match the maximal strip length. Overall we will have 65,486 strips in the MRD and 34,286 strips in the EMI, for a total of 99,772 read-out channels.

With a strip width of $\mathbf{7}\ \boldsymbol{mm}$ and by exploiting the center of gravity of the charge in streamer mode, it should be possible to achieve a space resolution of the order of 700 $\boldsymbol{\mu m}$ in both the X and Y directions. Considering a maximal length of the strips of 4-5 $\boldsymbol{m}$ a timing resolution better than $\mathbf{4}\ \boldsymbol{ns}$ is expected. If needed, it should be possible to further improve the time resolution by tuning the gas mixture.

We plan to use industrial RPC modules, as were used to build large area detectors in the LHC experiments and in the OPERA experiment. The main labor needed will include the tests and quality controls at the participating institutions, as well as the installation of the final detector at Fermilab.

4.5 Detector Assembly

This section presents preliminary engineering drawings of the assembly of the subdetectors that make up HIRESMNU. Figure 4–15 and 4–16 picture the isometric and Y-Z views of the assembly of the STT and the DS- and US-ECAL modules; Figure 4–17 shows this

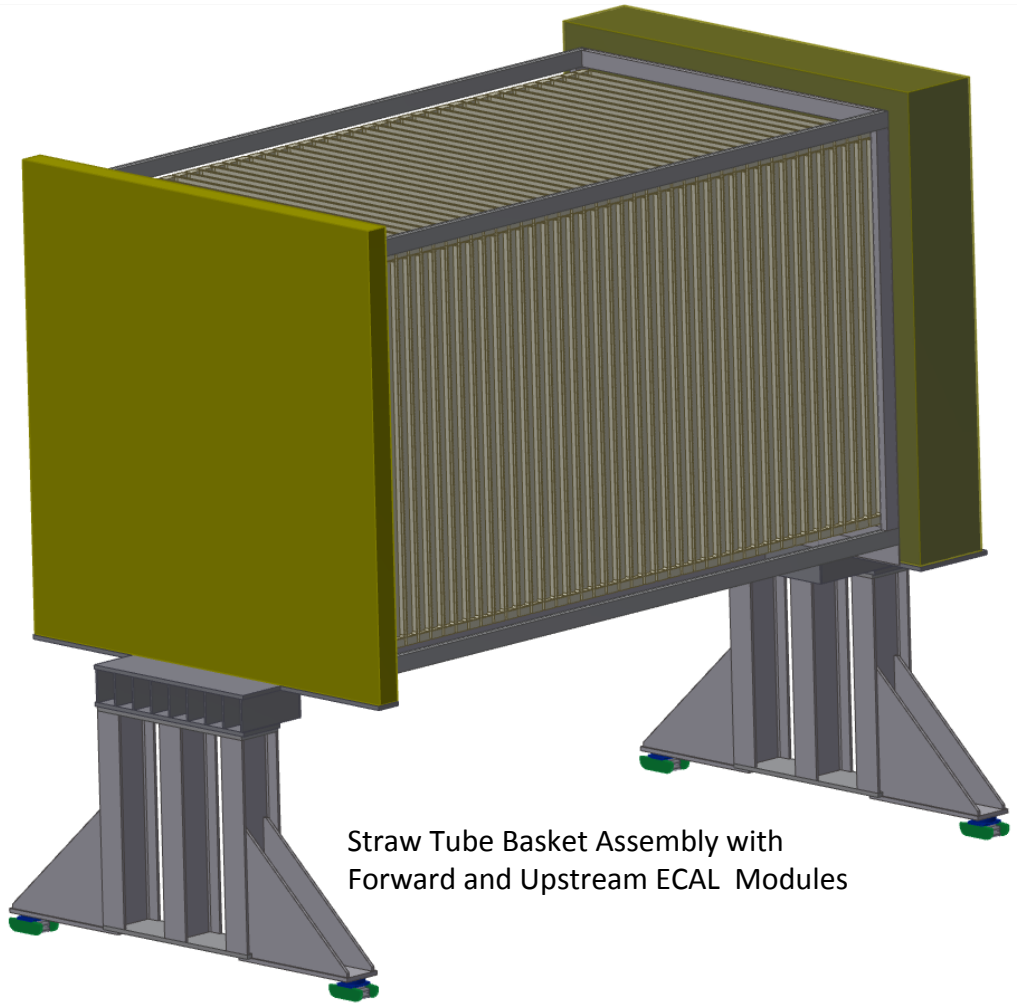

Figure 4–15: Preliminary engineering drawing of STT with the DS and US ECAL

assembly on the rack-tower. Figure 4–18 shows the addition of the muon-ID detector. Finally, Figure 4–19 shows the isometric and Y-Z views of the fully assembled detector; Figure 4–20 presents the Top and X-Y views. Chapter 5 presents physics sensitivity studies with the complete HIRESMNU.

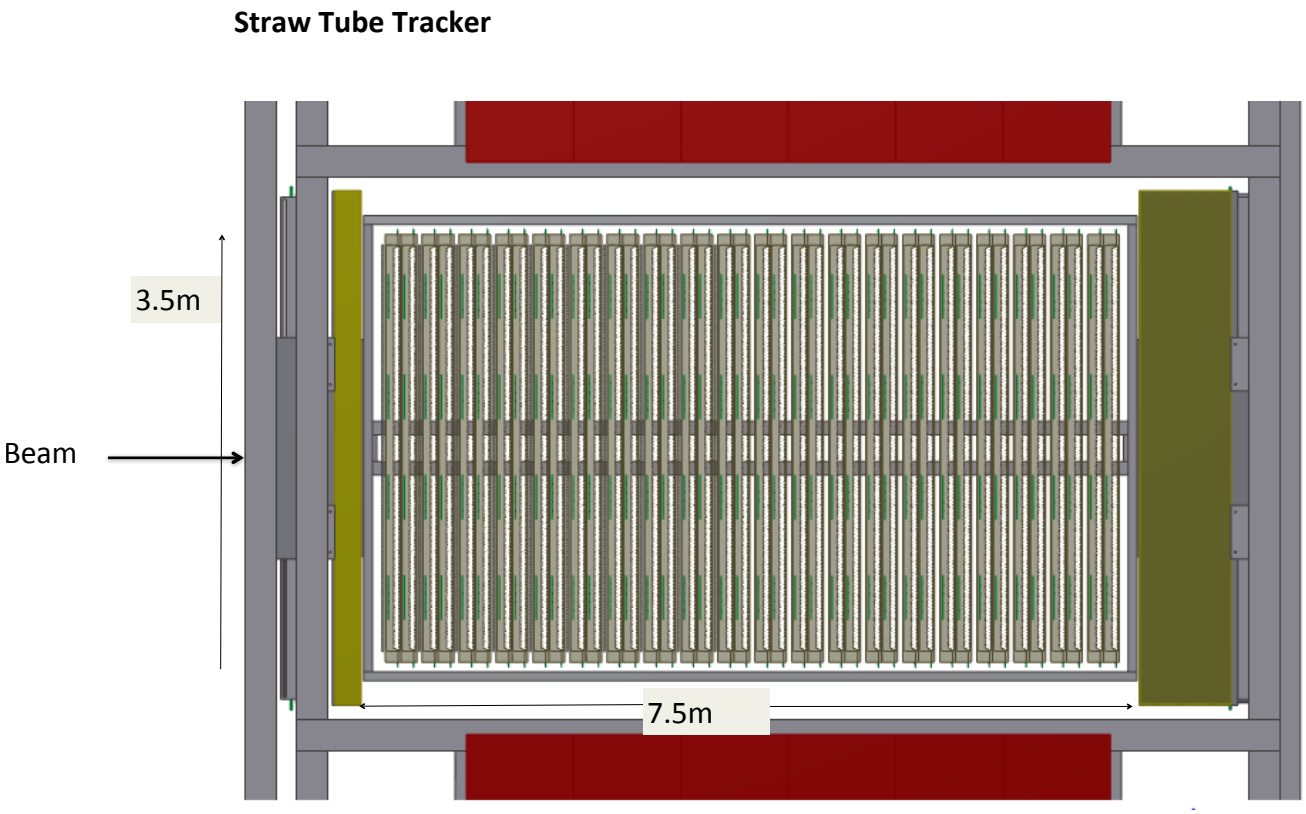

Figure 4–16: STT with the DS and US ECAL: YZ View

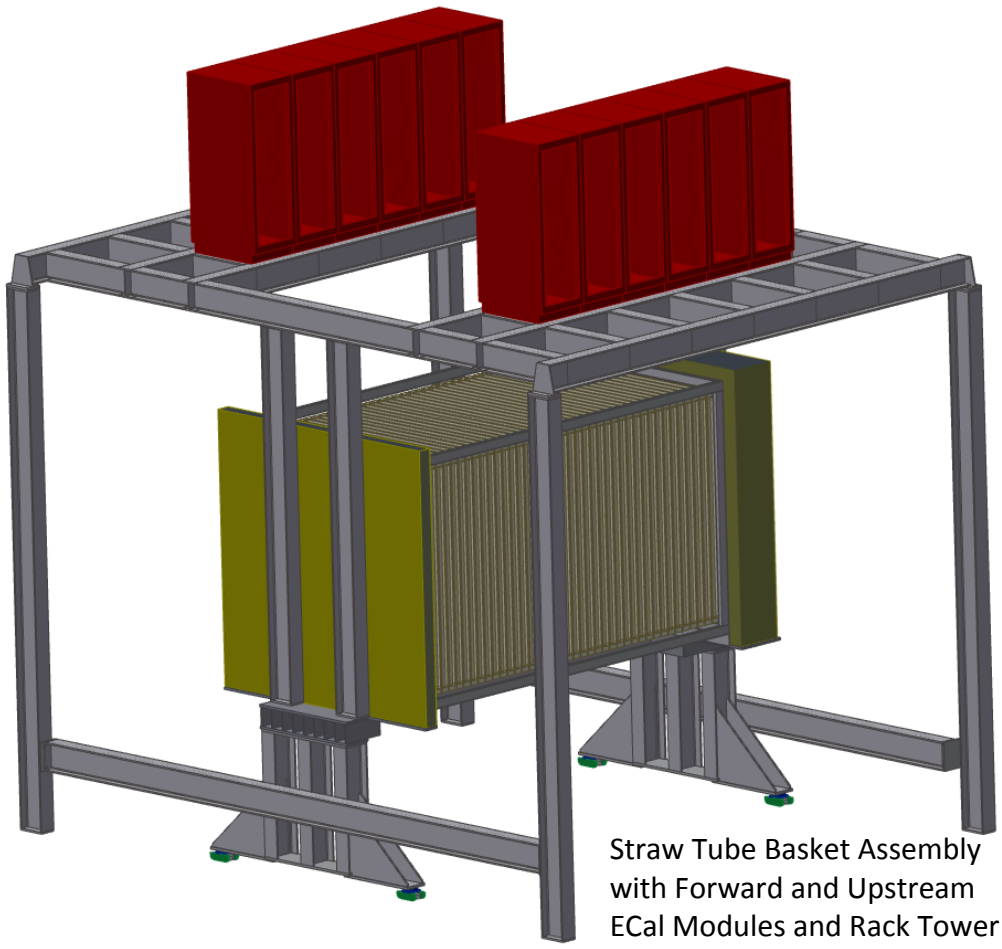

Figure 4–17: STT with the DS and US ECAL on the rack

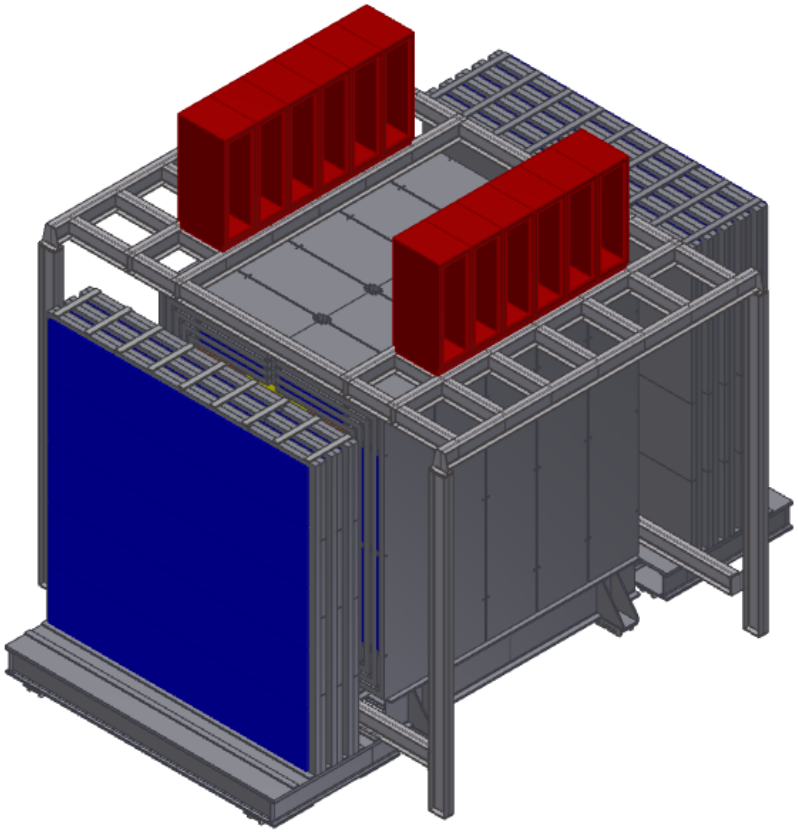

Figure 4–18: STT with the DS and US ECAL with muon-ID detector

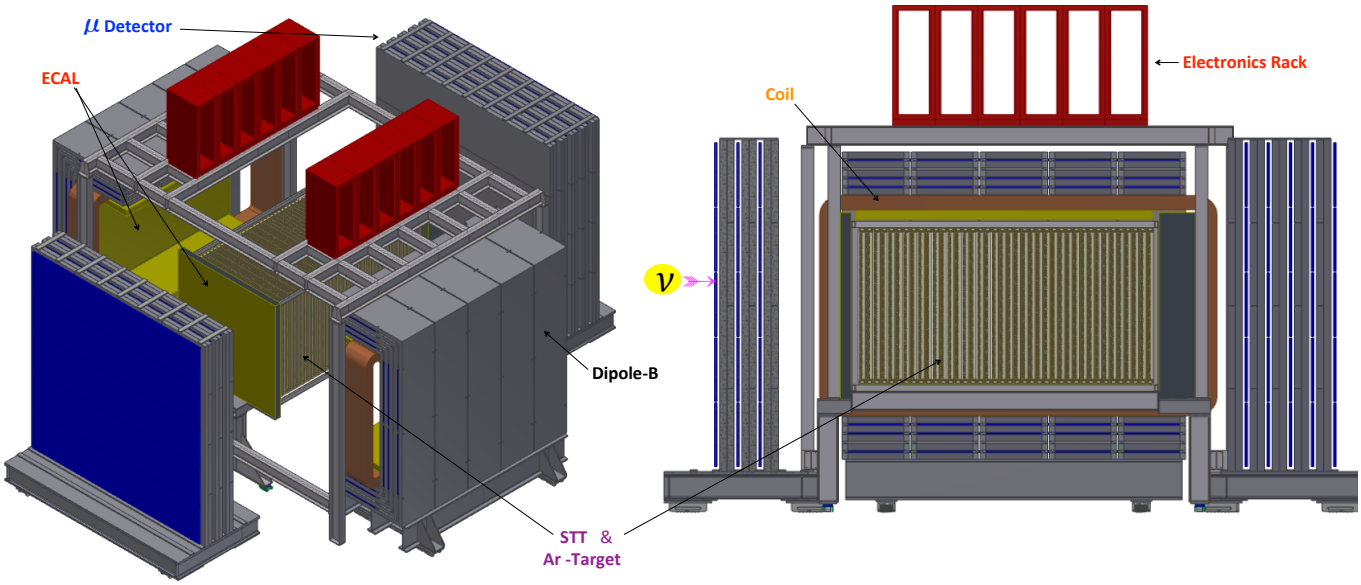

- Best performance among the 4-options
- ~3.5m x 3.5m x 7.5m STT (ρ=0.1gm/cm^3)
  - 4π-ECAL in a Dipole-B-Field (0.4T)
  - 4π-μ-Detector (RPC) in Dipole and Downstream
- Pressurized Ar Target (≃x5 FD-Stat) ⇛ *LAr-FD*

Transition Radiation ⇛ e-/e+ ID ⇒ γ
dE/dx ⇛ Proton, π+/-, K+/-
Magnet/Muon Detector ⇛ μ+/-
{ν-e ⇒ Absolute Flux measurement}

Figure 4–19: Isometric and YZ views of a half-size detector; the neutrino is incident from the right in the YZ view.

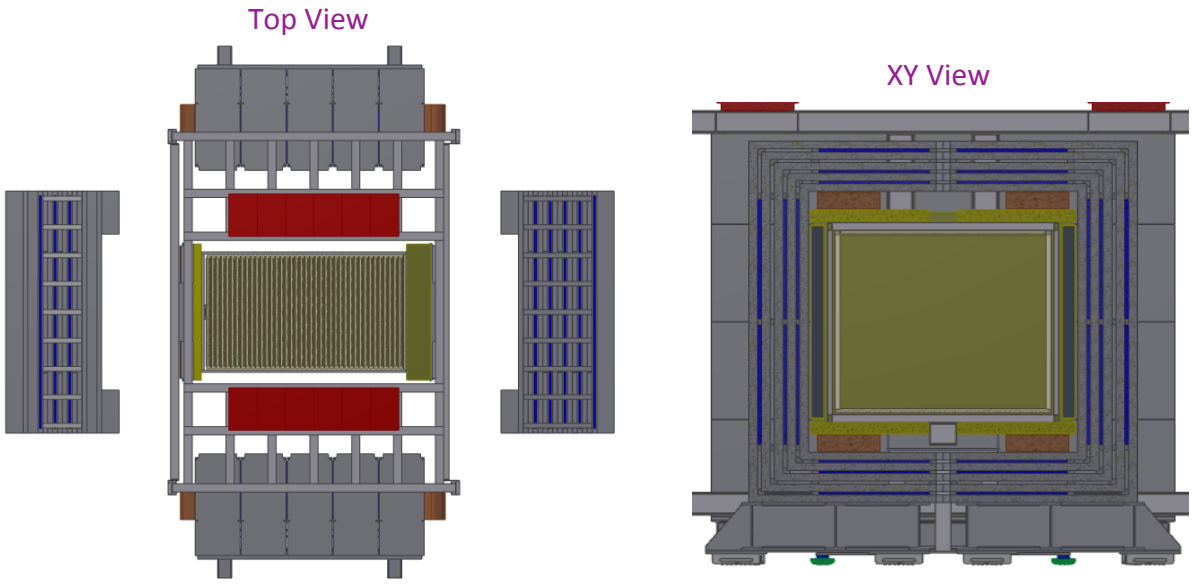

Figure 4–20: Top and XY views of the fully assembled half-size detector.

5 Physics Sensitivity Studies

This chapter presents a synopsis of physics sensitivity studies conducted with HIRESMNU. The studies include momentum measurements and ID of particles produced in neutrino interactions, charged particles, electron vs pion/muon, photons, protons and kaons. Topics important for oscillation measurements include the all important relative and absolute flux measurements, quasi-elastic interactions, $\boldsymbol{\nu_e}$ and $\boldsymbol{\bar{\nu}_e}$ CC interactions, NC interactions, and the $\boldsymbol{\pi^0/\gamma}$ yields in neutrino interactions. Studies pertaining precision Standard Model (SM) processes include strangeness content of the nucleon, weak mixing angle, isospin physics and sum-rules, nucleon and nuclear structure, and QCD tests. Finally, sensitivity to new physics searches include topics such as heavy neutrinos and short baseline oscillations.

5.1 Momentum-Measurement of Particles and Particle-ID

The $\boldsymbol{\nu_\mu}$-CC (Figures 3–4)and $\boldsymbol{\bar{\nu}_e}$-CC (3–5) events reconstructed in the active tracker of NOMAD show a clean measurements of the momentum vectors of the charged particles produced in these interaction. Similarly, momenta of the neutral particles can be easily determined where they manifest as charged particles such as photon-conversion ($\boldsymbol{\gamma \rightarrow e^+e^-}$) and neutral-kaon decay ($\boldsymbol{K^0_S \rightarrow \pi^+\pi^-}$). For the remaining neutrals, the energy will be determined by the energy deposited in the calorimeter and the momentum direction cosines by joining the vertex position with the position in the calorimeter.

5.2 Charged Particle Measurement

We expect that the space-point resolution of the STT will be $\boldsymbol{200\mu}$ on individual hits with a time resolution of about 1 nanosecond. The test-beam measurements of both the ATLAS-TRT and COMPASS-STT have achieved a better than $170\boldsymbol{\mu}$ resolution. The resolution of the coordinates of a $\boldsymbol{\nu_\mu}$-CC event, $\boldsymbol{\Delta(X,Y,Z)}$, is expected be $\boldsymbol{\mathcal{O}(100\mu)}$, a value commensurate with the space-point precision and the NOMAD experience. Figure 3–7 shows the longitudinal (Z-position of the $\boldsymbol{\nu}$-vertex) radiography of NOMAD revealing the elements of

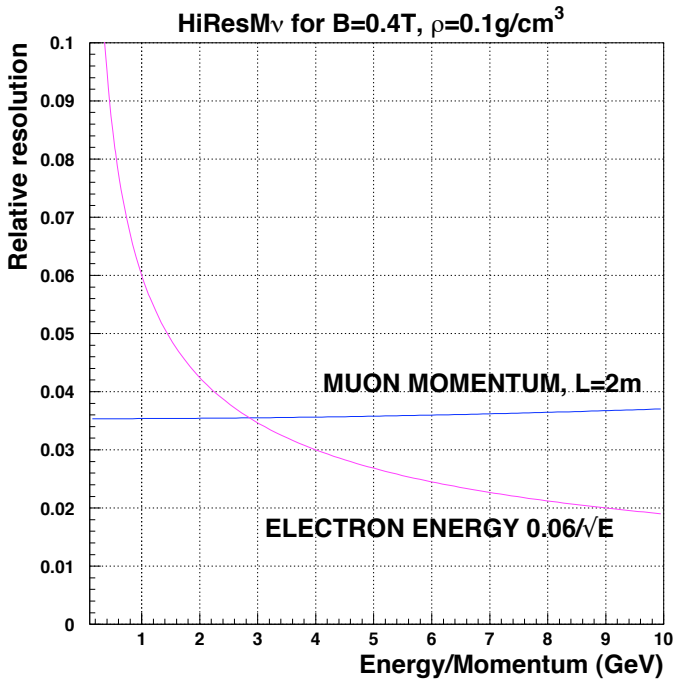

Figure 5–1: Momentum resolution of a $\nu_\mu(\bar{\nu}_\mu)$-CC induced μ^- (μ^+) is shown, in blue, as a function of the muon momentum. Also shown, in red, is the resolution of $\nu_e(\overline{\nu_e})$-CC induced e^- (e^+).

the tracker such as the Kevlar skin, the Honeycomb, and the Gas-gap within the tracking drift-chambers. The STT will enable a better vertex resolution by a factor of two, or more, than that of NOMAD. The charged tracks in the STT will be measured with an approximate momentum (p) resolution of $\sigma_p/p = 0.05/\sqrt{L} \oplus 0.008p/\sqrt{L^5}$ (p in GeV/c and L in meters) with unambiguous charge separation in the energy range of interest, 0.1–50 GeV. The momentum resolution of a $\nu_\mu(\bar{\nu}_\mu)$-CC induced μ^- (μ^+) is shown in Figure 5–1 for a 2-m-long track. It should be noted that the average length of a μ^- (μ^+) from a CC is about 3.5 m.

5.3 Electron-ID: Transition Radiation

In addition to providing the trajectory of a charged particle, the active STT also provides transition radiation (TR) providing a powerful discriminant for electron/positrons from the muons and charged pions. The TR detection is fashioned after the transition-radiation tracker (TRT) of the ATLAS experiment. Its transverse dimension is similar to that used by the NOMAD experiment. Figure 5–2 compares the TR for a 5 GeV muon with a 2 GeV electron as measured by the NOMAD TR subdetector. Figure 5–3 shows the electron TR efficiency as a function of electron momentum for a 10^{-3} rejection of charged pions. The figure shows

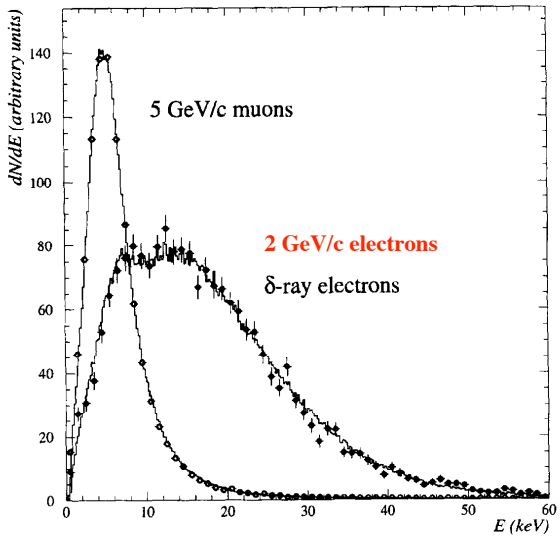

Figure 5–2: Comparison of the TR of a 5 GeV muon and a 2 GeV electron.

that the TR affords a 90% (70%) efficiency for an electron of 1 (0.6) GeV while rejecting 1000 charged pions. GEANT simulation of the proposed STT confirms these efficiencies for a 1/1000 pion rejection. The TR capability of the subdetector provides a high-purity $\boldsymbol{\nu_e}$- and $\boldsymbol{\bar{\nu}_e}$-CC signal as described below.

5.4 Electromagnetic Shower Measurement in ECAL

The energy resolution of the proposed ECAL will be $\boldsymbol{\approx 6\%/\sqrt{E}}$ and the time resolution will be $\sim$1 ns for e/γ with energy $\boldsymbol{\geq 100MeV}$. The energy resolution of a $\boldsymbol{\nu_e(\overline{\nu_e})}$-CC induced $\boldsymbol{e^-}$ ($\boldsymbol{e^+}$) is also shown in Figure 5–1 where the electronic charge and direction are measured in the STT and the energy in the ECAL. The longitudinal and transverse profiles of the energy deposited in the ECAL provide a powerful discriminant for EM versus hadronic shower, independent of the TR measurements. For example, the calorimetric energy profile of a 3 GeV electron will have $\boldsymbol{\geq 95\%}$ efficiency while rejecting hadronic showers by a factor of 100.

5.5 Proton ID and Charged-Kaon ID

The tracker is designed to have high efficiency for the low-energy protons needed to measure the quasi-elastic (QE) and resonance interactions of neutrinos. The STT will record not only the position but also the energy of the particle providing the $\boldsymbol{dE/dx}$ pattern associated with

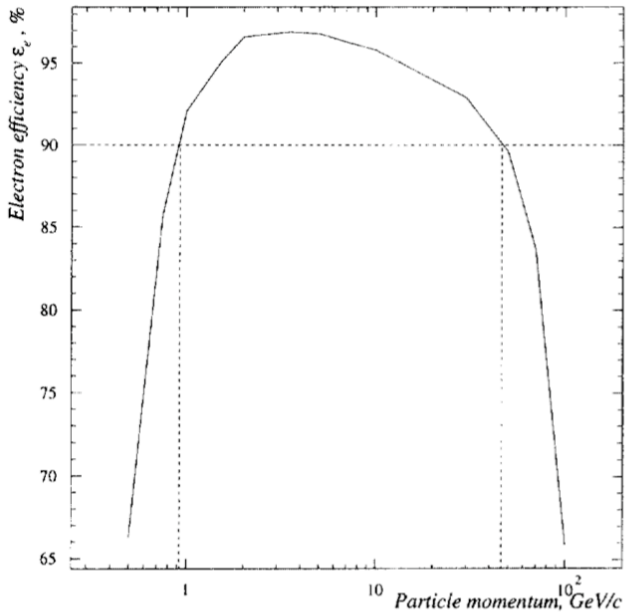

Figure 5–3: Electron TR-ID Efficiency as a function of the electron momentum for a 1/1000 rejection of pions

charged tracks. Figure 5–4 contrasts the energy loss from a proton produced in $\boldsymbol{\nu_\mu}$ quasi-elastic (QE) with that of a charged hadron produced in the background due to resonance (Res) and deep inelastic scattering (DIS) processes. We point out that the background events displayed in the figure might contain protons in addition to pions. We also point out that in the data there will be a statistically large sample of ultra-pure ($\geq$ **95%**) protons, from Lambda-decays, with momenta similar to those of QE-protons as discussed in Section 5.11.

We are conducting $\boldsymbol{dE/dx}$ studies to identify charged kaons, especially in the kinetic energy range of 200 to 500 MeV; another tack under investigation is tagging the charged kaons that decay in-flight to muons or to three charged pions.

5.6 Neutrino and Antineutrino Flux Measurement

A most important task of the ND is the measurement of the flux as a function of neutrino energy for each of the four neutrino species ($\boldsymbol{\nu_\mu, \bar{\nu}_\mu, \nu_e, \bar{\nu}_e}$), and prediction of the ratio of far-to-near detector flux (FD/ND). We have developed several independent methods to determine the (anti)neutrino fluxes from the HIRESMNU data at LBNE. The combination of the large statistics expected at LBNE with the finely segmented detector at the near site allows comparable precision from different techniques. Table 5–1 presents a conspectus of methods, the corresponding expected precision, and the salient detector requirements to achieve the precision. This redundancy of measurements is necessary for the validation of

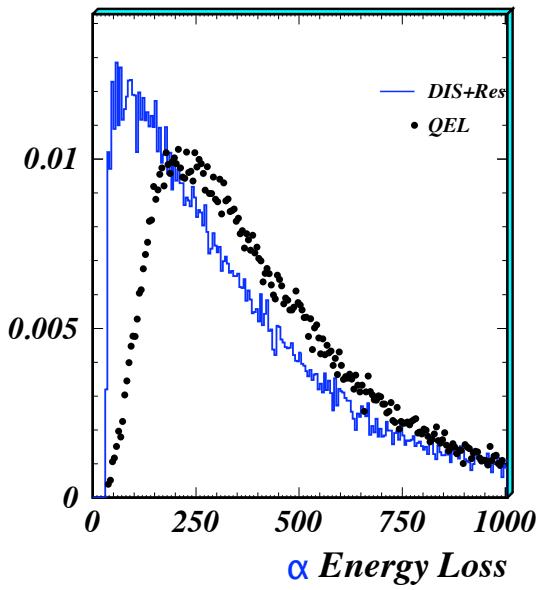

Figure 5–4: The dE/dx plot for ν_μ-induced QE and background proceses

the flux extraction at the level of precision needed for the oscillation searches.

The in situ determination of neutrino fluxes is not only a service measurement crucial for the oscillation studies in the FD, but also is critical for a panoply of precision measurements of fundamental interactions discussed below. Indeed, the possibility of making discoveries with the short-baseline physics program depends critically upon the knowledge of the neutrino source. The uncertainty on the fluxes has been a limiting factor for all past neutrino scattering experiments. The high intensity of the LBNE beam and the excellent granularity in HIRESMNU allows a substantial reduction on the flux uncertainty. Additionally, the extraction of the fluxes themselves relies upon the knowledge of specific physics processes requiring an understanding of the theoretical and experimental issues related to their measurements.

As summarized in Table 5–1, the proposed HIRESMNU will offer an ***insitu*** absolute $\boldsymbol{\nu}$ flux measurement using **(a)** $\boldsymbol{\nu}$-electron neutral current elastic scattering with a precision of $\boldsymbol{\approx 2.5\%}$ for $\boldsymbol{E_\nu \leq 10}$ GeV; **(b)** $\boldsymbol{\nu_\mu}$-electron charged current scattering with an accuracy of $\boldsymbol{\approx 3\%}$ for $\boldsymbol{E_\nu \geq 11}$ GeV (average-$\boldsymbol{E_\nu}$ $\approx$25 GeV); and (c) the slope of $\boldsymbol{d\sigma(\nu_\mu - QE)/dQ^2}$ on a deuterium target and for the $\bar{\boldsymbol{\nu}}_{\boldsymbol{\mu}}$ mode, using the hydrogen target. The three methods are systematically independent. We have studied the first two methods and summarize our findings in Sections 5.7 and 5.8; the feasibility of the last method is being investigated.

Table 5–1: Precisions achievable from in situ ν_μ and ν_e flux measurements in the fine-grained ND with different techniques.

Flavor	Technique	Relative abundance	Absolute normalization	Relative flux $\Phi(E_\nu)$	Detector requirements
ν_μ	$\nu_\mu e^- \to \nu_\mu e^-$	1.00	2.5%	$\sim 5\%$	e ID θ_e Resolution e^-/e^+ Separation
ν_μ	$\nu_\mu e^- \to \mu^- \nu_e$	1.00	3%		μ ID θ_μ Resolution 2-Track (μ+X) Resolution μ energy scale
ν_μ	$\nu_\mu n \to \mu^- p$ $Q^2 \to 0$	1.00	$3-5\%$	$5-10\%$	D target p Angular & Energy resolution Back-Subtraction
$\bar{\nu}_\mu$	$\bar{\nu}_\mu p \to \mu^+ n$ $Q^2 \to 0$	0.70	5%	10%	H target Back-Subtraction
ν_μ	Low-ν_0	1.00		2.0%	μ^- vs μ^+ E_μ-Scale Low-E_{Had} Resolution
$\bar{\nu}_\mu$	Low-ν_0	0.70		2.0%	μ^- vs μ^+ E_μ-Scale Low-E_{Had} Resolution
$\nu_e/\bar{\nu}_e$	Low-ν_0	0.01	1-3%	2.0%	e^-/e^+ Separation (K^0_L)

5.7 Low-Energy Absolute Flux: Neutrino-Electron Neutral Current Scattering

Neutrino neutral current interaction with the atomic electron in the target, $\nu_\mu e^- \to \nu_\mu e^-$ (NuElas), provides an elegant measure of the absolute flux. The total cross section for NC elastic scattering off electrons is given by [25]:

$$\sigma(\nu_l e \to \nu_l e) = \frac{G_\mu^2 m_e E_\nu}{2\pi}\left[1 - 4\sin^2\theta_W + \frac{16}{3}\sin^4\theta_W\right], \quad (5.1)$$

$$\sigma(\bar{\nu}_l e \to \bar{\nu}_l e) = \frac{G_\mu^2 m_e E_\nu}{2\pi}\left[\frac{1}{3} - \frac{4}{3}\sin^2\theta_W + \frac{16}{3}\sin^4\theta_W\right], \quad (5.2)$$

where θ_W is the weak mixing angle (WMA). For $\sin^2\theta_W \simeq 0.23$ the above cross sections are very small $\sim 10^{-42}(E_\nu/\mathrm{GeV})$ cm^2. The NC elastic scattering off electrons can be used to determine the absolute flux normalization since the cross section only depends upon the knowledge of $\sin^2\theta_W$. Within the SM the value of $\sin^2\theta_W$ at the average momentum transfer expected at LBNE, $Q \sim 0.07$ GeV, can be extrapolated down from the LEP/SLC measurements with a precision of $\leq 1\%$. Precision electroweak measurements with HIRESMNU data should be able to determine the value of $\sin^2\theta_W$ to better than

0.3%. Therefore, the theoretical uncertainty on the absolute flux normalization can eventually be substantially improved by a combined analysis with the electroweak measurements. In the present analysis, however, we assume the 1% error in the WMA. The signature of the process $\boldsymbol{\nu_l(\bar{\nu}_l)e \rightarrow \nu_l(\bar{\nu}_l)e}$ is a single electron in the final state, emitted almost collinearly with the beam direction ($\boldsymbol{\theta \sim}$ mrad). The dominant backgrounds are from NC $\boldsymbol{\pi^0}$ production and single photon production, in which one photon mimics a single electron. It should be noted that the $\boldsymbol{\pi^0}$ background is charge symmetric. A much smaller background contribution is given by $\boldsymbol{\nu_e}$ quasi-elastic scattering events in which the proton is not visible. This measurement requires a detector that can efficiently distinguish photons from electrons, and electrons from positrons, and that provides an excellent angular resolution for the electron in the final state.

The $\boldsymbol{\nu_\mu e^- \rightarrow \nu_\mu e^-}$ (NuElas) will produce a single $\boldsymbol{e^-}$ collinear with the $\boldsymbol{\nu}$-beam ($\boldsymbol{\leq}$ **40** mrad). The background, dominated by the asymmetric conversion of a photon in an ordinary $\boldsymbol{\nu}$-N neutral current event, will produce $\boldsymbol{e^-}$ and $\boldsymbol{e^+}$ in equal measure with much broader angular distribution. The key to this is measuring the angle, energy, and charge of the electron or positron: the ability to make these measurements exemplifies the strength of the HIRESMNU design. The analysis proceeds in two steps. First, we require a single $\boldsymbol{e^-}$ or $\boldsymbol{e^+}$ passing the TR-ID and, second, we require that the 'forwardness' variable, $\boldsymbol{\zeta = P_e(1 - \cos\Theta_e)}$ be $\boldsymbol{\leq 10^{-3}}$. Table 5–2 shows the reduction of events, signal and background, leading to the efficiency of the signal of about 61%, with a large reduction in background. The background, though small, is symmetric in charge and will be measured in the detector.

Table 5–2: NuElas Selection Cuts

		$\boldsymbol{\nu_\mu}$-E	$\boldsymbol{\nu_\mu}$-CC	$\boldsymbol{\nu_\mu}$-NC
	Fiducial Volume	1,500	100,000	34,000
	$\boldsymbol{p_\mu} < 0.5$ GeV	1,500	8,273	34,000
	≥ 20 Mod (-Ve)	1,228	1,738	11,213
$\boldsymbol{e}$ Selection against Hadrons	$\boldsymbol{P_{-Ve} > 0.5}$ GeV	1,192	1,319	8,662
	TR-Cut	911	1.3	8.7
	$\boldsymbol{\gamma \rightarrow e^+e^-}$	-	5.5	24.1
$\boldsymbol{\pi^0}$ Background	TR-Cut	-	5.0	21.7
$\boldsymbol{e}$ sample	-	911	6.3	30.4

Figure 5–5 presents a comparison of the angular distributions of NuElas signal (symbol) with those of the hadronic background (histos) where a single charged track is reconstructed. The figure shows that the background is benign.

The measurement of NuElas will be dominated by the statistical error. We estimate that the absolute flux of the LBNE neutrinos will be determined to a $\boldsymbol{\simeq 2.5\%}$ precision. Since NuElas

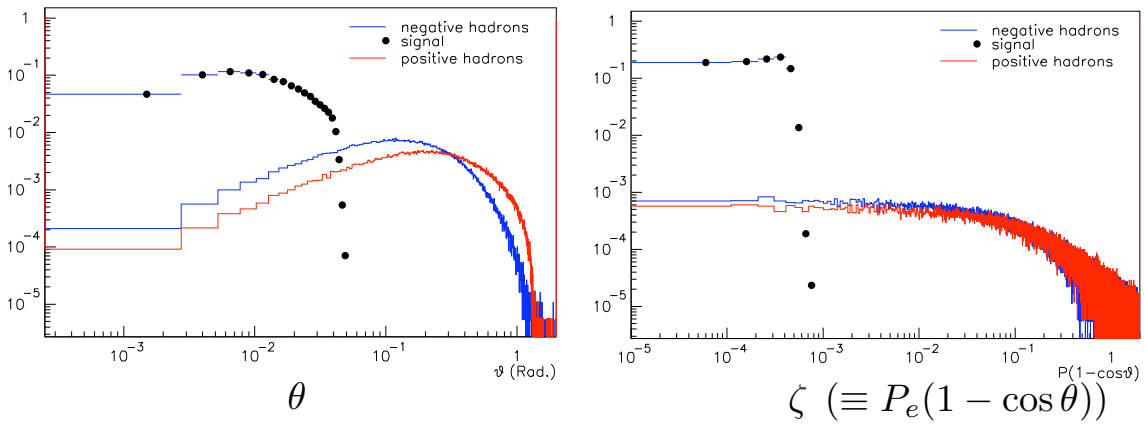

Figure 5–5: Comparison of Θ and ζ distributions of NuElas signal and background

is a two-body interaction, the incident neutrino energy can be calculated using the measured momentum and angle of the final electron. Figure 5–6 contrasts the E_ν distribution derived from P_e, Θ_e with the incident E_ν. The figure shows that in the $E_\nu \leq 5$ GeV range not only the absolute flux can be determined to $\simeq 3\%$ but also the shape of the ν spectrum can be determined to about 7% precision.

The measurement of NC elastic scattering off electrons can only provide the integral of all neutrino flavors, which, for the neutrino mode, includes about 92% ν_μ, 7% $\bar{\nu}_\mu$ and 1% $\nu_e + \bar{\nu}_e$. In order to determine the individual ν_μ and $\bar{\nu}_\mu$ components we need to measure the ratio $\bar{\nu}_\mu/\nu_\mu$ from CC interactions to better than 10%. This requirement is relatively loose since with a magnetized detector we can measure $\bar{\nu}_\mu/\nu_\mu$ to a few percent. It must be noted that the reactions $\nu_e e \rightarrow \nu_e e$ and $\bar{\nu}_e e \rightarrow \bar{\nu}_e e$ result from combined W and Z boson exchange. The corresponding cross section for $\nu_e(\bar{\nu}_e)$ is enhanced by a factor of about six (three) with respect to $\nu_\mu(\bar{\nu}_\mu)$. The relative ν_e contributions to the measured NC elastic scattering sample are therefore increased to about 6% of the total, requiring an additional measurement of the ratio ν_e/ν_μ from CC interactions to $10 - 15\%$.

5.8 High-Energy Absolute Flux: Neutrino-Electron Charged Current Scattering

The ν_μ-e^- CC interaction, $\nu_\mu + e^- \rightarrow \mu^- + \nu_e$ — the inverse muon decay (IMD) — offers an elegant way to determine the absolute flux. Given the threshold due to the massive-muon, IMD requires a minimum $E_\nu \geq 10.8$ GeV. Over a three-year period, the HIRESMNU detector should see ≥ 1900 IMD events. The reconstruction efficiency of the single, energetic and forward μ^- will be $\geq 98\%$; the angular resolution of the IMD-μ is ≤ 1 mrad. The background, primarily from the ν_μ-QE, can be precisely constrained using control samples.

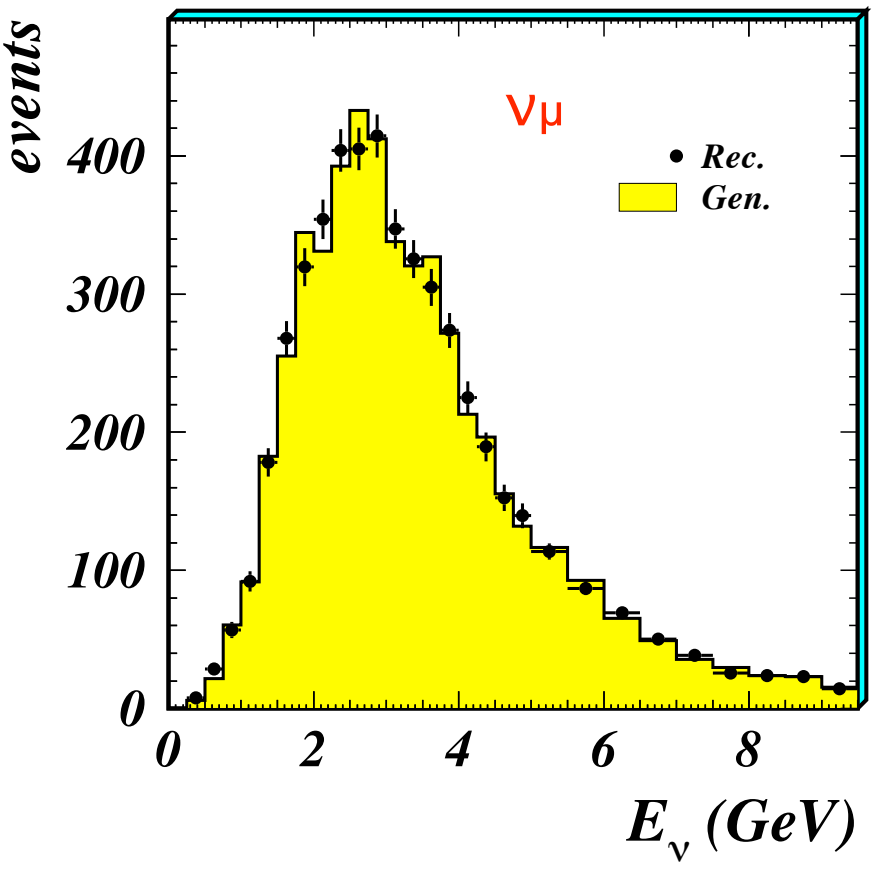

Figure 5–6: Comparison of derived E_ν using the reconstructed momentum and angle of the electron and the incident E_ν (histo).

In particular, the systematic limitations of the CCFR [26] and [27] and and those of the CHARM-II [28] IMD measurements will be substantially alleviated in HIRESMNU. Table 5–3 shows the salient steps of the analysis. The signal efficiency is $\simeq \mathbf{60\%}$ with $\sim \mathbf{6 \times 10^{-6}}$ of the background events surviving. Figure 5–7 shows the discriminant, $\boldsymbol{\zeta = E_\mu(1 - \cos\theta_\mu)}$, clearly separating the signal from the background.

Table 5–3: IMD selection and backgrounds

	ν_μ-IMD	ν_μ-CC	ν_μ-NC
	1,095	21,503,975	7,853,890
1 negative Track	1,095	3,254,740	86,305
Neutral Veto ($E_\gamma > 0.05$ GeV)	1,095	2,628,530	45,777
Neutral Veto ($E_{neutron} > 0.5$ GeV)	1,095	2,164,990	23,998
Neutral Veto ($E_{K_S,K_L} > 0.25$ GeV)	1,095	2,160,640	21,344
$E > 11$ GeV	1,080	176,616	240
$z < 0.001$ GeV	1,068	5,131	0
$z < 0.00005$ GeV	622	133	0

We anticipate that the IMD events will allow the absolute flux at high energies to be determined to $\approx 3\%$ precision.

5.9 Low-Energy Absolute Flux: QE in Water and Heavy-Water Targets

A third independent method to extract the absolute flux is through the Quasi-Elastic (QE) CC scattering $\boldsymbol{\nu_\mu n(p) \rightarrow \mu^- p(n)}$. Neglecting terms in $\boldsymbol{(m_\mu/M_n)^2}$, at $\boldsymbol{Q^2 = 0}$ the QE cross section is independent of neutrino energy for $\boldsymbol{(2E_\nu M_n)^{1/2} > m_\mu}$:

$$\frac{\boldsymbol{d\sigma}}{\boldsymbol{dQ^2}} \mid \boldsymbol{Q^2 = 0} \mid = \frac{\boldsymbol{G_\mu^2 \cos^2\theta_c}}{\boldsymbol{2\pi}} \left[\boldsymbol{F_1^2(0) + G_A^2(0)}\right] = \mathbf{2.08 \times 10^{-38}\ cm^2 GeV^{-2}}, \quad (5.3)$$

which is determined by neutron β decay and has a theoretical uncertainty $< 1\%$. The flux can be extracted experimentally by measuring low $\boldsymbol{Q^2}$ QE interactions ($\mathbf{0 - 0.05}$ GeV) and extrapolating the result to the limit of $\boldsymbol{Q^2 = 0}$. The measurement requires a deuterium or hydrogen (for antineutrino) target to minimize the smearing due to Fermi motion and other nuclear effects. This requirement can only be achieved by using both H_2O and D_2O targets embedded in the fine-grained tracker and extracting the events produced in deuterium by statistical subtraction of the larger oxygen component. The experimental resolution on the muon and proton momentum and angle is crucial. Dominant uncertainties of the method

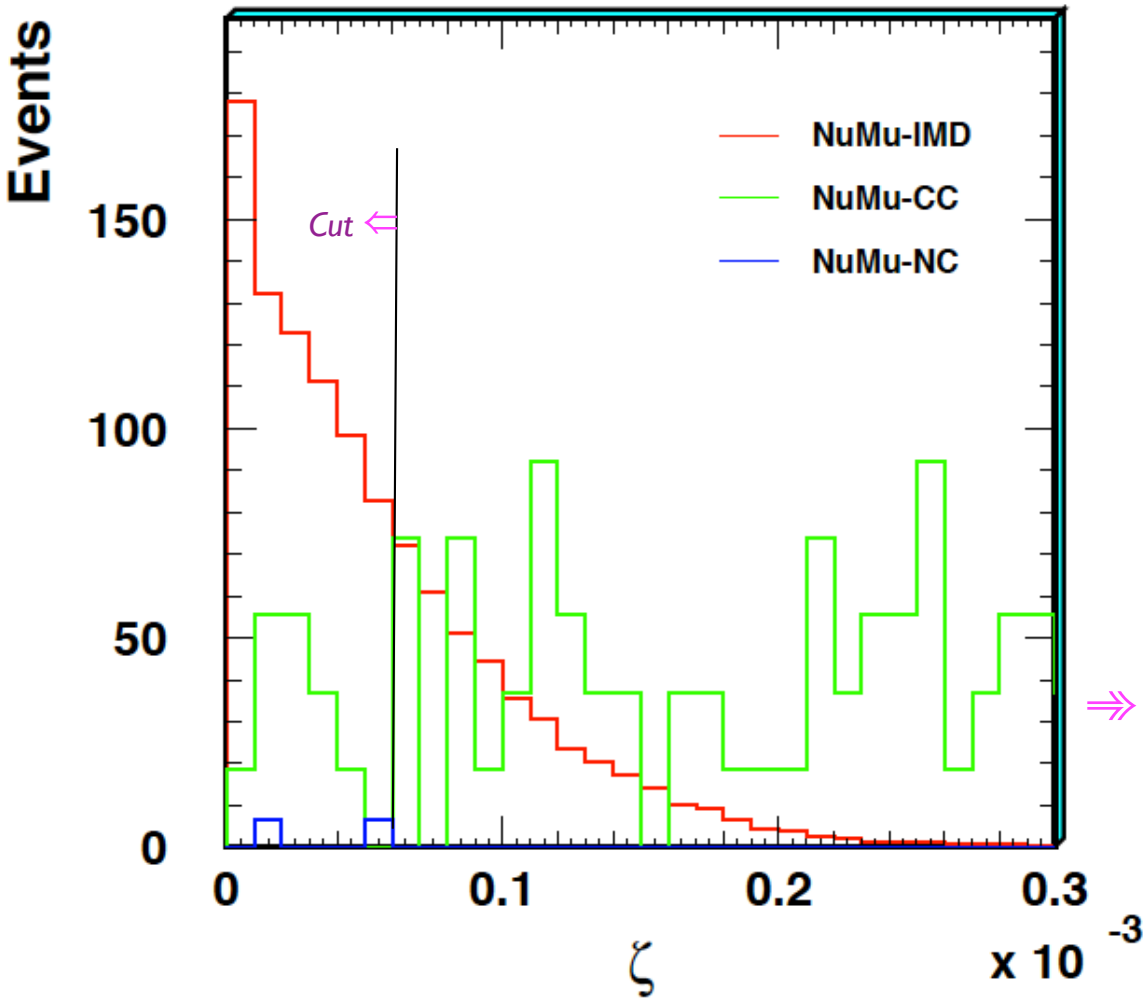

Figure 5–7: The ζ distribution of the μ^- from IMD and the background

are related to the extrapolation to $Q^2 = 0$, to the theoretical cross section on deuterium, the experimental resolution, and to the statistical subtraction. Sensitivity studies and the experimental requirements are under study.

5.10 Relative Neutrino and Antineutrino Flux Measurement and the FD/ND Ratio

The most promising method of determining the shape of the ν_μ and $\bar{\nu}_\mu$ flux is by measuring the low-hadronic (low-ν) charged current events: the Low-ν_0 method of relative flux determination [73]. The dynamics of neutrino-nucleon scattering implies that the number of events in a given energy bin with hadronic energy $E_{\rm had} < \nu_0$ is proportional to the neutrino (antineutrino) flux in that energy bin up to corrections $\mathcal{O}(\nu_0/E_\nu)$ and $\mathcal{O}(\nu_0/E_\nu)^2$. The method follows from the general expression of the ν-nucleon differential cross section:

$$\mathcal{N}(\nu < \nu_0) = C\Phi(E_\nu)\nu_0 \left[\mathcal{A} + \left(\frac{\nu_0}{E_\nu}\right)\mathcal{B} + \left(\frac{\nu_0}{E_\nu}\right)^2 \mathcal{C} + \mathcal{O}\left(\frac{\nu_0}{E_\nu}\right)^3\right], \qquad (5.4)$$

where the coefficients $\mathcal{A} = \mathcal{F}_2$, $\mathcal{B} = (\mathcal{F}_2 \pm \mathcal{F}_3)/2$, $\mathcal{C} = (\mathcal{F}_2 \mp \mathcal{F}_3)/6$ and $\mathcal{F}_i = \int_0^1 \int_0^{\nu_0} F_i(x)dxd\nu$ is the integral of structure function $F_i(x)$. The number $\mathcal{N}(\nu < \nu_0)$ is proportional to the flux up to correction factors of the order $\mathcal{O}(\nu_0/E_\nu)$ or smaller, which are not significant for small values of ν_0 at energies $\geq \nu_0$. It should be pointed out that the coefficients $\mathcal{A}, \mathcal{B}, \mathcal{C}$ are determined for each energy bin and neutrino flavor within the ND data themselves. Since our primary interest is the relative flux determination, i.e., neutrino flux in an energy bin relative to another energy bin, variations in the coefficients do not affect the relative flux.

The prescription for the relative flux determination is simple: we count the number of ν-CC events below a certain small value of hadronic energy (ν_0). The observed number of events, up to the correction of the order $\mathcal{O}(\nu_0/E_\nu)$ due to the finite ν_0, in each total visible energy bin is proportional to the relative flux. The smaller the factor ν_0/E_ν, the smaller is the correction. Furthermore, the energy of events passing the low-ν_0 cut is dominated by the corresponding lepton energy — a quantity which can be measured with very high precision in HIRESMNU. It is apparent from the above discussion that this method of relative flux determination is not very sensitive to nucleon structure, QCD corrections or types of ν-interactions such as scaling or non-scaling. With the excellent granularity and resolution foreseen in the low-density magnetized tracker it will be possible to use a value of $\nu_0 \sim 0.5$ GeV or lower, thus allowing flux predictions down to $E_\nu \sim 0.5$ GeV.

The key measurable quantities in the Low-ν_0 analysis are the resolution for hadronic energy and the systematic precision and resolution of the muon momentum. The $\nu_\mu(\bar{\nu}_\mu)$-CC flux at the ND provides a measure of the $\pi^+/K^+/\mu^+(\pi^-/K^-/\mu^-)$ content of the beam. The

analysis proceeds as follows. First, we obtain the relative $\nu_\mu(\bar{\nu}_\mu)$ flux using the Low-ν_0 method at the ND. Second, we fit the $d^2\sigma/dx_F dP_T^2$ of the parent mesons to the ν_μ flux with a simple parametrization:

$$\frac{d^2\sigma}{dx_F dP_T^2} = f(x_F)g(P_T)h(x_F, P_T). \tag{5.5}$$

The ingredients to this empirical fit to the meson production cross section (EP) are the following:

- Trace parent mesons through a simulation of the beam elements
- Decay the parent mesons
- Predict ν_μ and $\bar{\nu}_\mu$ fluxes by folding experimental acceptance
- Add external constraints on π/K from hadro-production experiments (MIPP)
- Compare predictions to the measured spectra at the ND and minimize the corresponding χ^2

It must be noted that the simple smoothness requirement on the functional form in Equation 5.5 allows extending the flux predictions down to $E_\nu \sim \nu_0$. In order to evaluate the sensitivity that can be achieved at LBNE with the low-ν_0 method we performed the flux analysis for the neutrino beam mode (positive focusing) using $\nu_\mu + \bar{\nu}_\mu$ CC mock data from the low-density magnetized detector and $\nu_0 < 0.5$ GeV. Figure 5–8 shows the ν_μ mock data and the corresponding fitted flux with the ND positioned at 500 m from the target. Having constrained the $d^2\sigma/dx_F dP_T^2$ of the pions/kaons, we can predict the flux at the ND location. The figure also contrasts the predicted flux at FD with the true value. Finally, the lower-right graph shows the most important double ratio: predicted-(FD/ND) divided by true-(FD/ND) as a function of neutrino energy. Overall we achieved a precision $\leq 2\%$ on the relative ν_μ flux with the low-ν_0 method in the energy region $1 \leq E_\nu \leq 30$ GeV in the fit with $\nu_0 < 0.5$ GeV. Similar uncertainties are expected for the $\bar{\nu}_\mu$ component (the dominant one) in the antineutrino beam mode (negative focusing). Figure 5–9 shows the subdominant $\bar{\nu}_\mu$ relative flux determination and the FD/ND prediction.

Analyses of several systematic errors on the Low-ν_0 flux was conducted. The analyses included the following effects:

- Variation of quasi-elastic, resonance and DIS cross sections by $\pm 10\%$: Figure 5–10 shows that a change of 10% in the QE and Res composition of the CC has $<< 1\%$

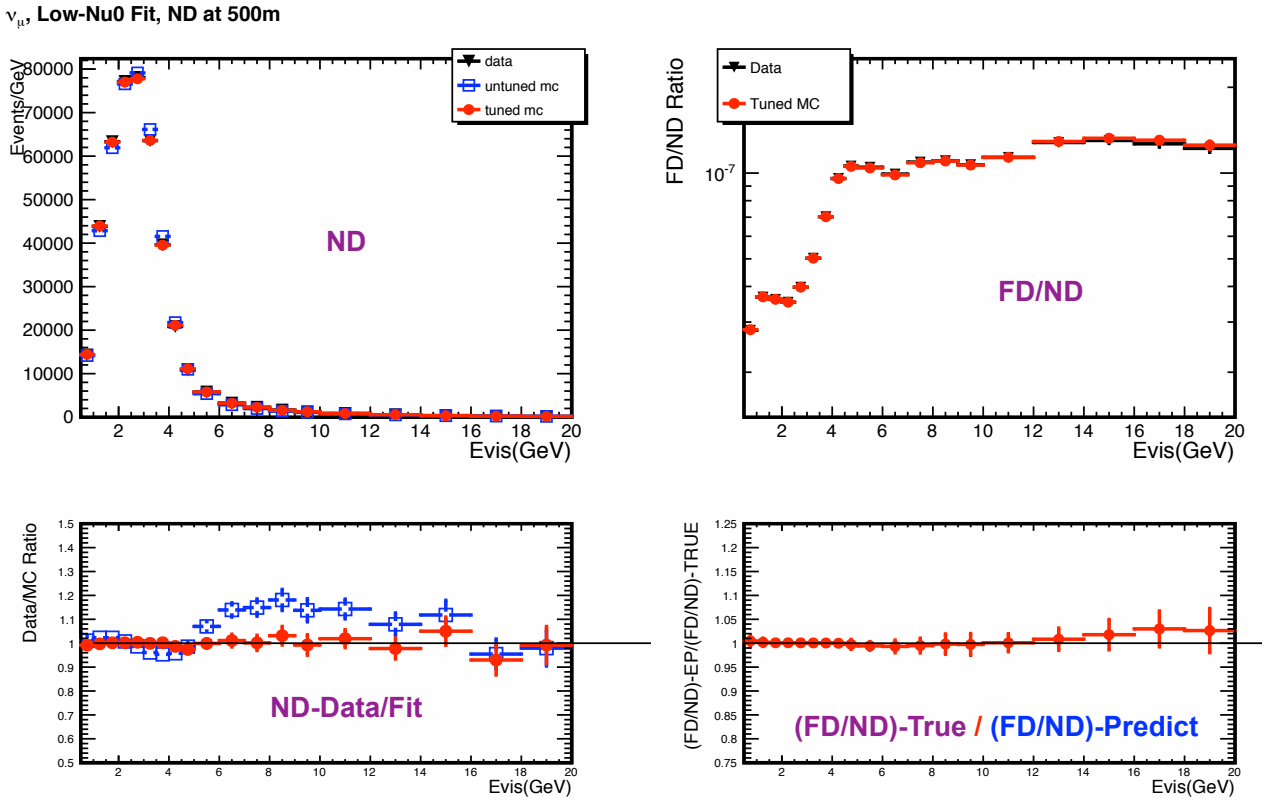

Figure 5–8: Relative ν_μ flux using Low-ν_0 method: The 'measured' low-ν_0 and the fitted EP flux at ND (left panels) and the FD/ND comparison (right panels).

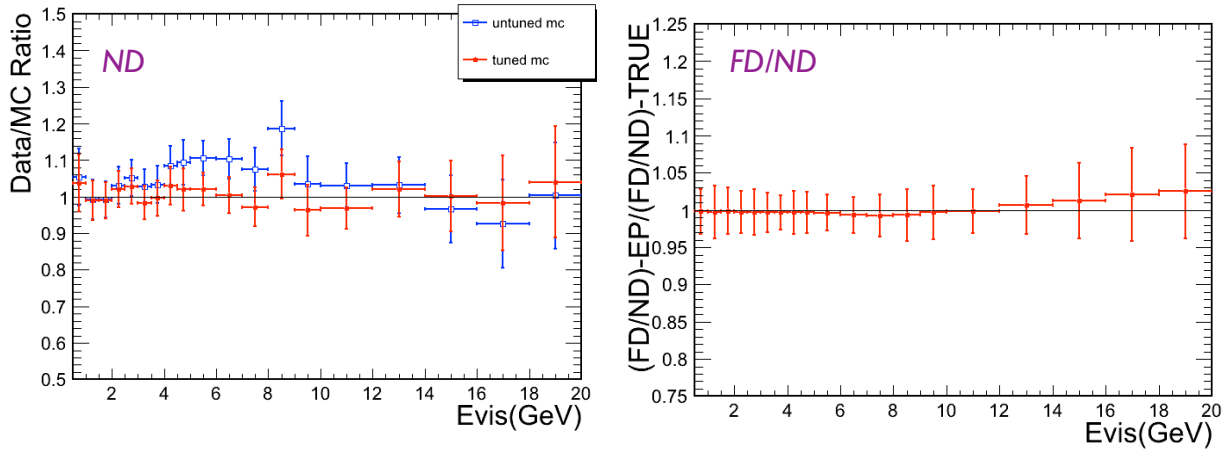

Figure 5–9: Relative $\bar{\nu}_\mu$ flux using Low-ν_0 method: The ratio of 'measured' low-ν_0 and the fitted EP flux at ND (left) and the FD/ND comparison (right).

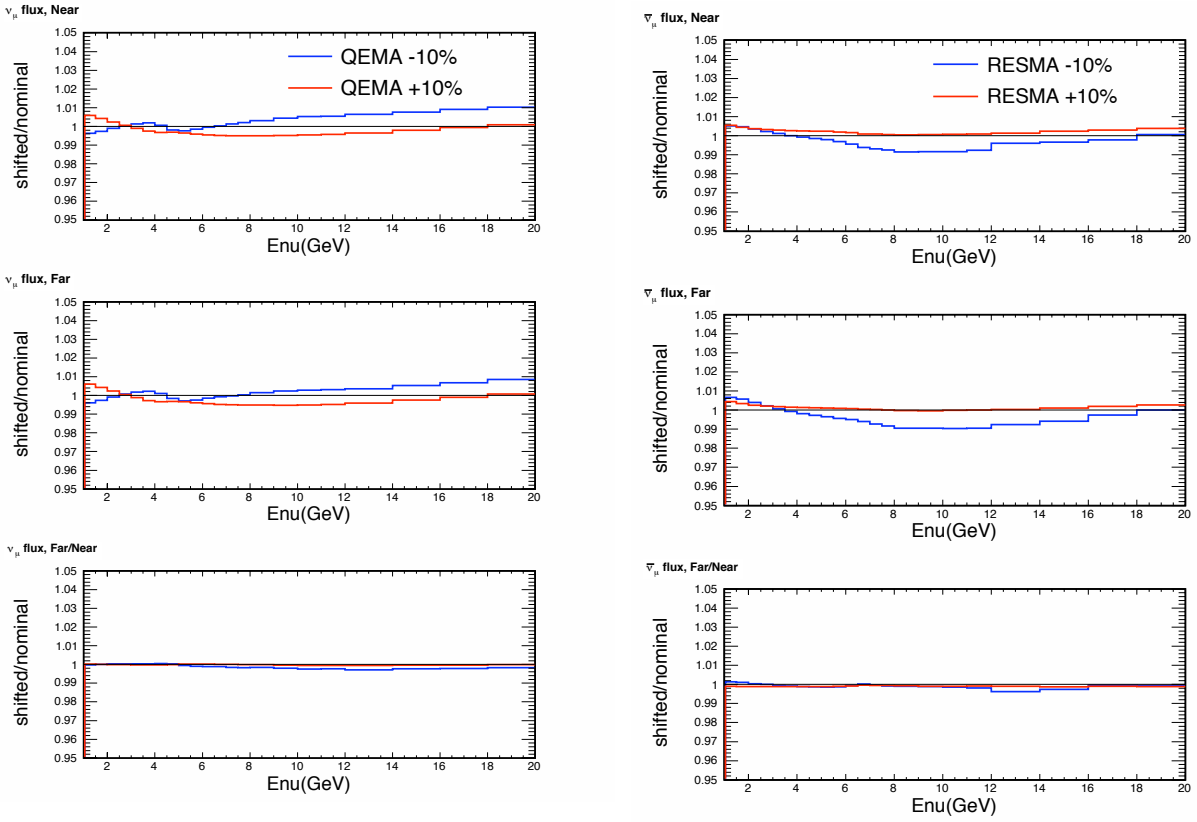

Figure 5–10: Effect of QE and Res variations on the relative ν_μ flux using Low-ν_0 method

effect on the FD/ND ratio. (It should be noted that these exclusive channels will be measured to $\simeq$ **3%** precision in HIRESMNU.) In a recent publication, Bodek *et al.* [74] conclude that theoretical error in the ν_μ ($\bar{\nu}_\mu$) flux is about $<$ **2%** for $E_\nu \geq$ **1** GeV; and that the flux error will be dominated by detector effects.

- Variation of muon and hadron energy scales: The most sensitive quantity controlling the precision of the Low-ν_0 flux is the muon energy. Figure 5–12 shows the variation in the ν_μ-flux when the muon (hadron) energy is shifted by $\pm$**0.2%** ($\pm$**0.5%**), the expected systematic precision in HIRESMNU.

- Variation of the functional form in Equation 5.5

- Systematic shift of the ν_0 values by $\pm$**20%**

- Effect of the beam-transport elements.

The beam-transport uncertainty will require additional studies after completing the design of the beamline since it depends on the precise beam elements and on the inert material that the hadrons encounter. Depending upon our knowledge of $p/\pi/K$ nuclear collisions,

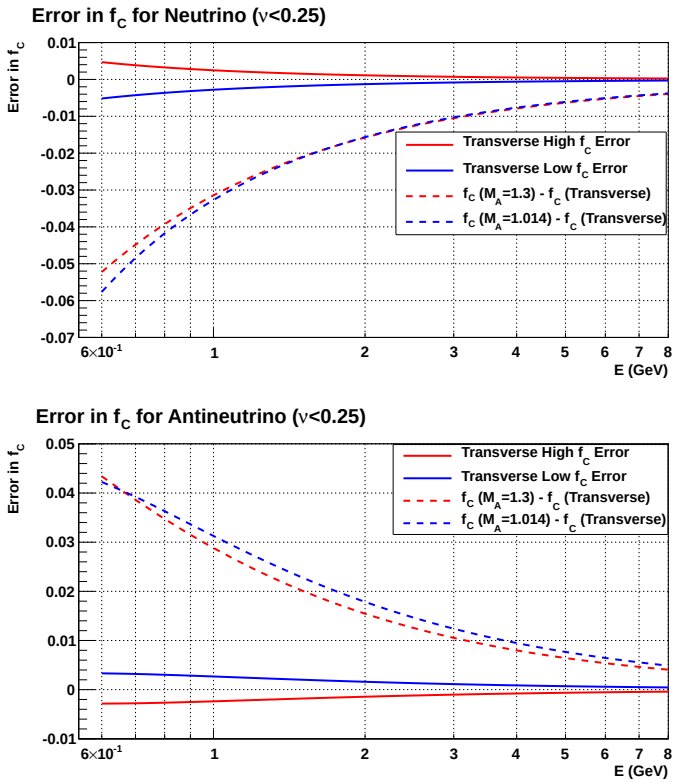

Figure 5–11: Model errors estimated in the relative ν_μ and $\bar{\nu}_\mu$ flux using Low-ν_0 method by Bodek *et al.*

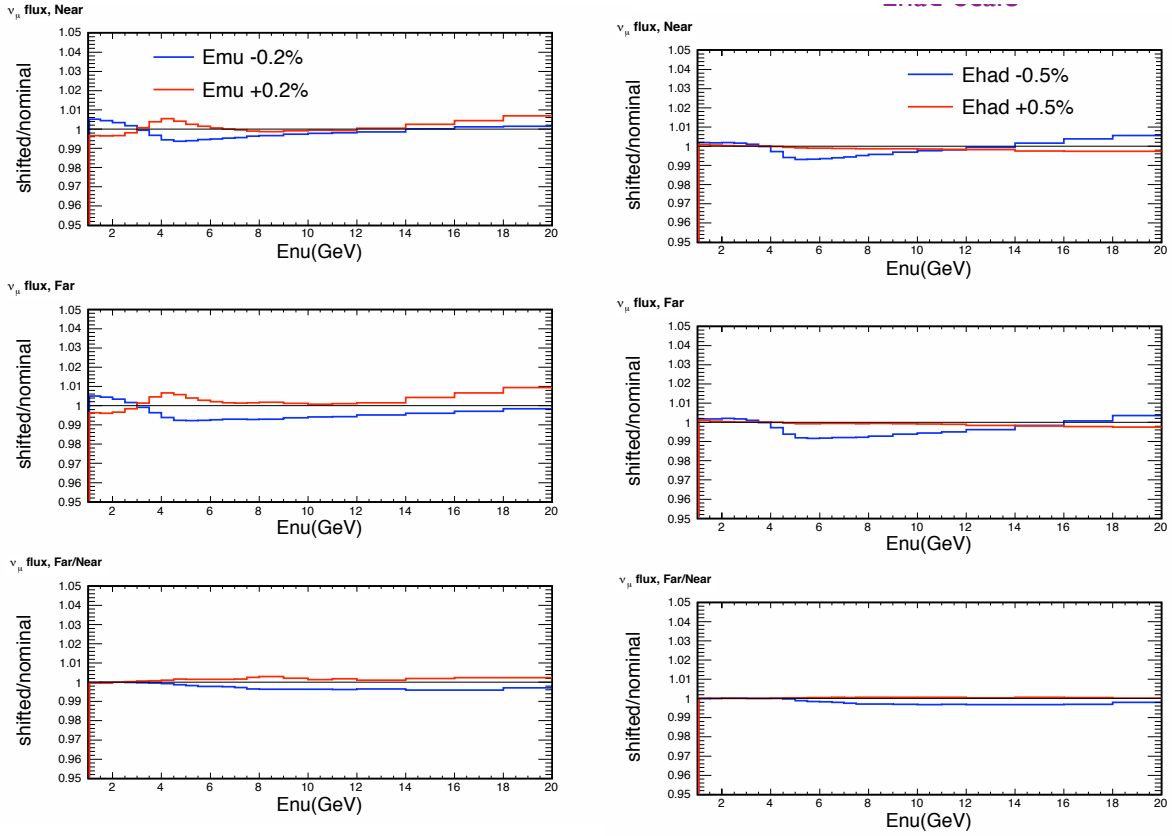

Figure 5–12: Effect of E_μ- and E_{Had} energy scale variation on the ν_μ flux using Low-ν_0 method

this uncertainty can become dominant for $\bar{\nu}_\mu$ production in the neutrino beam mode at low energy.

The relative flux as a function of energy could be also determined from NC elastic scattering off electrons, which is a two-body process with the initial electron being at rest. The calculation of the incoming neutrino energy requires a resolution of few milliradians on the angle of the outgoing electron as well as a good energy resolution. The low-density magnetized tracker can in principle fulfill such requirements. However, the limited statistics does not allow a precision better than $\sim \mathbf{7-10\%}$ on the relative flux.

5.10.1 Flavor Content of the Beam: $\nu_\mu, \bar{\nu}_\mu, \nu_e, \bar{\nu}_e$

The empirical parametrization (EP) of the pions and kaons, determined from the low-ν_0 flux at ND, allows one to predict the ν_μ and $\bar{\nu}_\mu$ flux at the FD location. The EP provides a measure of the $\pi^+/K^+/\mu^+(\pi^-/K^-/\mu^-)$ content of the beam at the ND. Additionally, with an ND capable of identifying $\bar{\nu}_e$ CC interactions, one can directly extract the elusive K^0_L content of the beam. Therefore, an accurate measurement of $\nu_\mu, \bar{\nu}_\mu$ and $\bar{\nu}_e$ CC interactions provides an absolute prediction of the ν_e content of the beam, which is an irreducible background for the ν_e appearance search in the FD:

$$\nu_e \equiv \mu^+(\pi^+ \to \nu_\mu) \oplus K^+(K^+ \to \nu_\mu) \oplus K^0_L \quad (5.6)$$

$$\bar{\nu}_e \equiv \mu^-(\pi^- \to \bar{\nu}_\mu) \oplus K^-(K^- \to \bar{\nu}_\mu) \oplus K^0_L \quad (5.7)$$

The μ component is well constrained from $\nu_\mu(\bar{\nu}_\mu)$ CC data at low energy, while the $K^\pm$ component is only partially constrained by the $\nu_\mu(\bar{\nu}_\mu)$ CC data at high energy and requires external hadro-production measurements of $K^\pm/\pi^\pm$ ratios at low energy from MIPP. Finally, the K^0_L component can be constrained by the $\bar{\nu}_e$ CC data and by external dedicated measurements at MIPP. The approximate relative contributions to the ν_e spectrum are 85% (55%) from μ^+, 10% (30%) from K^+ and 3% (15%) from K^0_L in the energy range $\mathbf{1(5)} \leq E_\nu \leq \mathbf{5(15)}$ GeV. Based on the NOMAD experience, we expect to achieve a precision of $\leq \mathbf{0.1\%}$ on the flux ratio ν_e/ν_μ. Taking into account the projected precision of the ν_μ flux discussed in the previous section, this translates into an absolute prediction for the ν_e flux at the level of $\mathbf{2\%}$.

Finally, the fine-grained ND can directly identify ν_e CC interactions from the LBNE beam. The relevance of this measurement is twofold: a) it provides an independent validation for the flux predictions obtained from the low-ν_0 method and b) it can further constrain the uncertainty on the knowledge of the absolute ν_e flux.

The flux ratio $\bar{\nu}_\mu/\nu_\mu$ as a function of energy can be determined with the low-ν_0 method

with an accuracy of $\leq \mathbf{2\%}$ in the region $\mathbf{1.5 < E_\nu < 30}$ GeV and of $\sim \mathbf{3\%}$ in the region $\mathbf{0.5 < E_\nu < 1.5}$ GeV. These numbers refer to the neutrino beam mode (positive focusing) and are obtained from a fit to mock data from the low density magnetized detector to extract the parent $\boldsymbol{\pi/K}$ distributions. The beam-transport uncertainty can become dominant for $\boldsymbol{\bar{\nu}_\mu}$ production (contamination) in the neutrino beam mode.

5.10.2 Effects of High Δm^2 Oscillations on the Flux Extraction

The results described in the previous sections were obtained under the assumption that the events observed in the ND originate from the same (anti)neutrino flux produced by the decay of the parent mesons. The recent results from the MiniBooNE experiment might suggest the possibility of relatively high $\boldsymbol{\Delta m^2}$ antineutrino oscillations consistent with the LSND signal. This effect, if confirmed, seems to indicate a different behavior between neutrinos and antineutrinos, which would imply CP or CPT violation.

The presence of high $\boldsymbol{\Delta m^2}$ oscillations with characteristic oscillation length comparable with the ND baseline at the LBNE energies, would imply the spectra observed in the ND could be already distorted by neutrino oscillations. Two main effects are expected on the flux extraction from a MiniBooNE/LSND oscillation:

- The $\boldsymbol{\nu_e}$ and $\boldsymbol{\bar{\nu}_e}$ CC spectra cannot be directly used to extract the $\boldsymbol{K^0_L}$ content in Equation (5.6) nor can they predict event rates in the FD;
- A deficit is induced in the $\boldsymbol{\bar{\nu}_\mu}$ CC spectrum due to a large disappearance rate.

Any in situ determination of the fluxes would then require the unfolding of the oscillation effect from the measured spectra. The measurement strategy in the ND should necessarily include a combined oscillation and flux analysis. Since the ND cannot be easily moved, different complementary measurements are needed. A requirement then for the ND is the ability to accurately determine the energy spectra of all four species $\boldsymbol{\nu_\mu}$, $\boldsymbol{\nu_e}$, $\boldsymbol{\bar{\nu}_\mu}$, and $\boldsymbol{\bar{\nu}_e}$. A MiniBooNE/LSND signal imposes stringent constraints on the ND design, as described in a following section.

Several follow-up experiments have been proposed to investigate the MiniBooNE/LSND effects: move MiniBooNE to a near detector location [75], OscSNS at the ORNL neutron spallation source [76] and a two-detector LAr experiment at the CERN PS [77]. The proposed experiments are expected to cover the region in the oscillation parameters consistent with MiniBooNE/LSND data, so that by the time LBNE will take data we might have a confirmation or a refutation of the high $\boldsymbol{\Delta m^2}$ oscillation hypothesis. However, the precision

that will be ultimately achieved in the determination of the fluxes at LBNE is directly connected to the high $\boldsymbol{\Delta m^2}$ oscillation parameters. If the oscillation is confirmed, we will need dedicated precision measurements in the ND at LBNE.

5.10.3 External Constraints from Hadro-production Measurements

A key points for an accurate determination of the fluxes is to exploit different complementary techniques providing the redundancy necessary to reach precision of the order of few percent. In the previous sections we have studied the measurements to be performed in situ. However, in order to fully exploit the power of the ND data, some external measurements will be needed to constrain the yields of the parent mesons decaying into (anti)neutrinos:

- $\boldsymbol{K^+/\pi^+}$ as a function of $\boldsymbol{P(2 \leq P \leq 20}$ GeV) and $\boldsymbol{P_T(\leq 0.4}$ GeV) of $\boldsymbol{K^+}$ and $\boldsymbol{\pi^+}$;
- $\boldsymbol{K^-/\pi^-}$ as a function of $\boldsymbol{P(2 \leq P \leq 20}$ GeV) and $\boldsymbol{P_T(\leq 0.4}$ GeV) of $\boldsymbol{K^-}$ and $\boldsymbol{\pi^-}$;
- $\boldsymbol{K^0/K^+}$ ratio.

This can be achieved with a dedicated hadro-production experiments (e.g. MIPP at Fermilab or NA-61 at CERN). The accuracy in the external measurements must be comparable to the precision of the ND data. The program must include separate measurements of the above quantities off different targets:

- The LBNE neutrino target;
- All the thin/thick Al, Cu, etc. targets that compose the horn and the beam elements;
- Air (N).

The external hadro-production measurements, which provide a constraint on the $\boldsymbol{\nu_e(\bar{\nu}_e)}$ flux, when combined with the $\boldsymbol{\nu_e}$ and $\boldsymbol{\bar{\nu}_e}$ CC measurement in the ND will provide the necessary redundancy to allow a systematically robust prediction of the flavour composition of the LBNE beam, and hence enable for the LBNE $\boldsymbol{\nu_e}$ appearance search.

5.11 Quasi-Elastic Interaction

In any long-baseline neutrino oscillation program, including LBNE, the quasi-elastic (QE) interactions are special. First, the QE cross section is substantial because the energy is low. Second, a measurement of $\boldsymbol{\nu_\mu}$-QE provides, to first oder, a direct measurement of flux. Third,

because of the simple topology — a $\boldsymbol{\mu^-}$ and a proton — the interaction provides, to the first order, a close approximation to the neutrino energy ($\boldsymbol{E_\nu}$). In the context of a fine-grained tracker, precise measurement of QE will impose direct constraints on neutrino interaction associated with Fermi-motion and final state interaction (FSI) dynamics: processes that must be determined empirically since they affect the entire oscillation program.

The key to $\boldsymbol{\nu_\mu}$-QE is the two-track topology, $\boldsymbol{\mu^-}$ and $\boldsymbol{p}$. It is difficult to reconstruct the recoiling proton, causing most experiments to only measure QE using one-track ($\boldsymbol{\mu}$-only) topology. Thus, the experimental challenge is the reconstruction of the emergent proton. Figure 5–13 shows NOMAD $\boldsymbol{\nu_\mu}$-QE candidate events where the muon and proton are reconstructed; the momentum of the proton is similar to that expected in the LBNE beam. HIRESMNU is designed to accurately and efficiently identify the proton and measure its momentum vector. Additionally, the STT will have the ability to measure the $\boldsymbol{dE/dx}$ of the recoil proton, see Section 5.5. The salient features of the detector include a larger acceptance for wide-angle protons, i.e., track reconstruction normal to the neutrino direction, and the $\boldsymbol{dE/dx}$ measurement. These features allowing the proton-reconstruction efficiency to be about twice that of NOMAD.

To estimate the $\boldsymbol{\nu_\mu}$-QE sensitivity in HIRESMNU, we follow the NOMAD analysis of QE [17]. Large samples of $\boldsymbol{\nu_\mu}$-induced QE, Res, DIS events were simulated in HIRESMNU using the LBNE spectra. First, require that there be a muon identified by the muon-ID detector; next, require that there be two tracks in the event; next, veto events where photons (neutral hadrons) deposit more than 0.1 GeV (0.5 GeV) energy; finally, the remaining event sample, composed of muon and proton, is subjected to a multivariate analysis using artificial neural network that maximizes the signal (QE) efficiency while keeping the Res/DIS backgrounds low by exploiting the kinematic relation between the muon and proton vectors. Figure 5–14 illustrates that the QE signal is well separated from the background. Figure 5–15 shows the efficiency and purity of reconstructing $\boldsymbol{\nu_\mu}$-QE induced $\boldsymbol{\mu^- p}$ events as a function of $\boldsymbol{E_\nu}$ in LBNE. The energy-averaged efficiency (purity) is **52%** (**82%**).

By contrasting the 2-track topology with 1-track (which is what most experiments measure), one can obtain ***in situ*** constraints on the Fermi-motion and on the final-state interaction (FSI) parameters. As regards the constraint on Fermi-motion: because QE is a two-body interaction, by using the energy and angle of the muon, ($\boldsymbol{E_\mu}$ and $\boldsymbol{\theta_\mu}$), one can derive the energy of the incident neutrino, $\boldsymbol{E_\nu}$, and compare it with the total visible energy of the two tracks, i.e., $\boldsymbol{E_{Vis} = E_\mu + E_{Pr}}$; the difference between the $\boldsymbol{E_{Vis}}$ and $\boldsymbol{E_\nu}$ is, to a first approximation, the Fermi-motion. Figure 5–16 shows that the NOMAD data, within a statistical sampling of several thousand events, provide a good description of the Fermi motion. The ND data in LBNE will provide an accurate, empirically determined measure of the Fermi-motion. Furthermore, the two topologies are very sensitive to the FSI parameters. By demanding consistency in the cross section between the two topologies, as shown in Figure 5–17 for the NOMAD data, we will empirically constrain the nuclear motion and the FSI parameters.

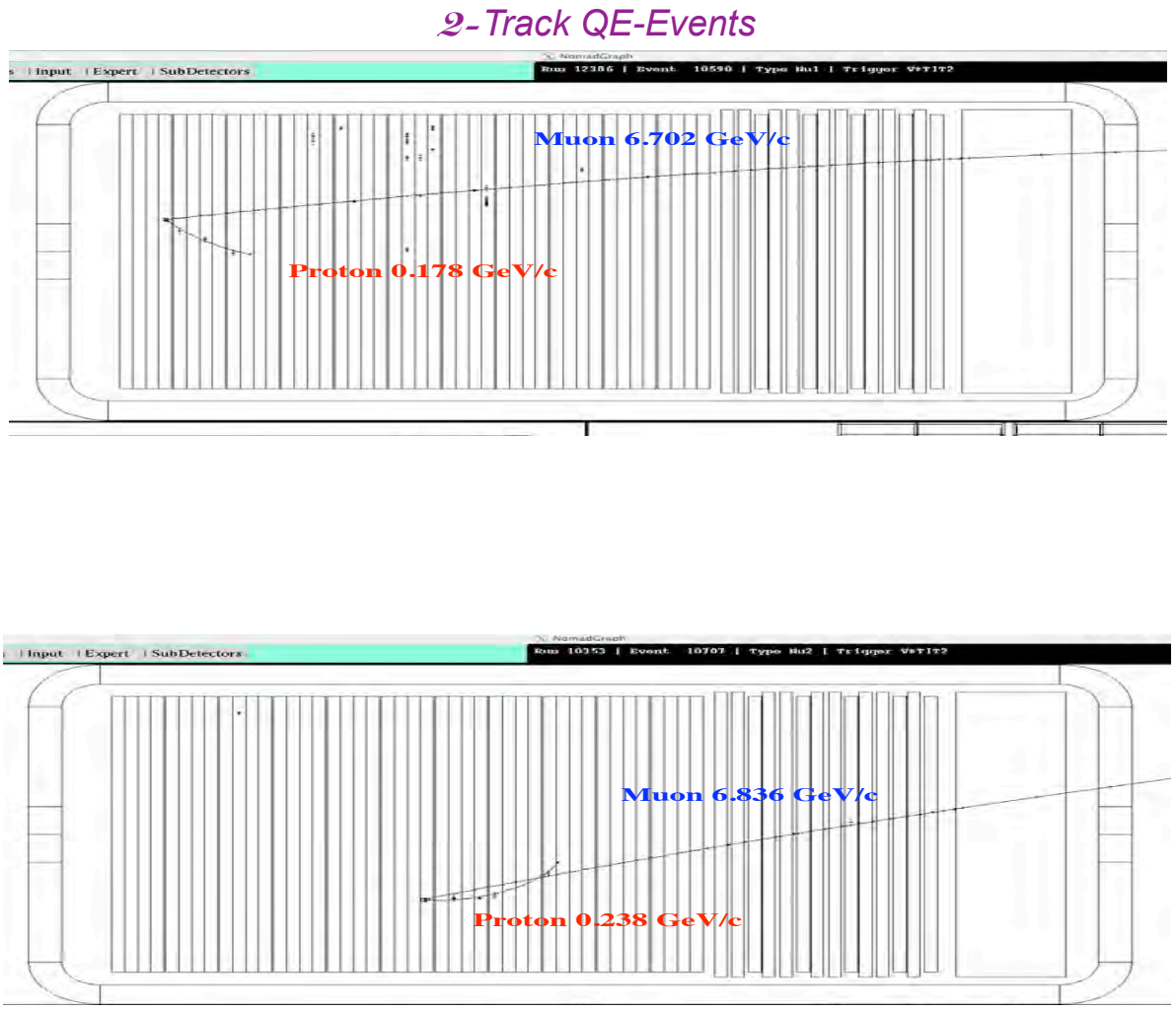

Figure 5–13: The ν_μ-QE events where μ^- and p are reconstructed, the 2-Track QE topology

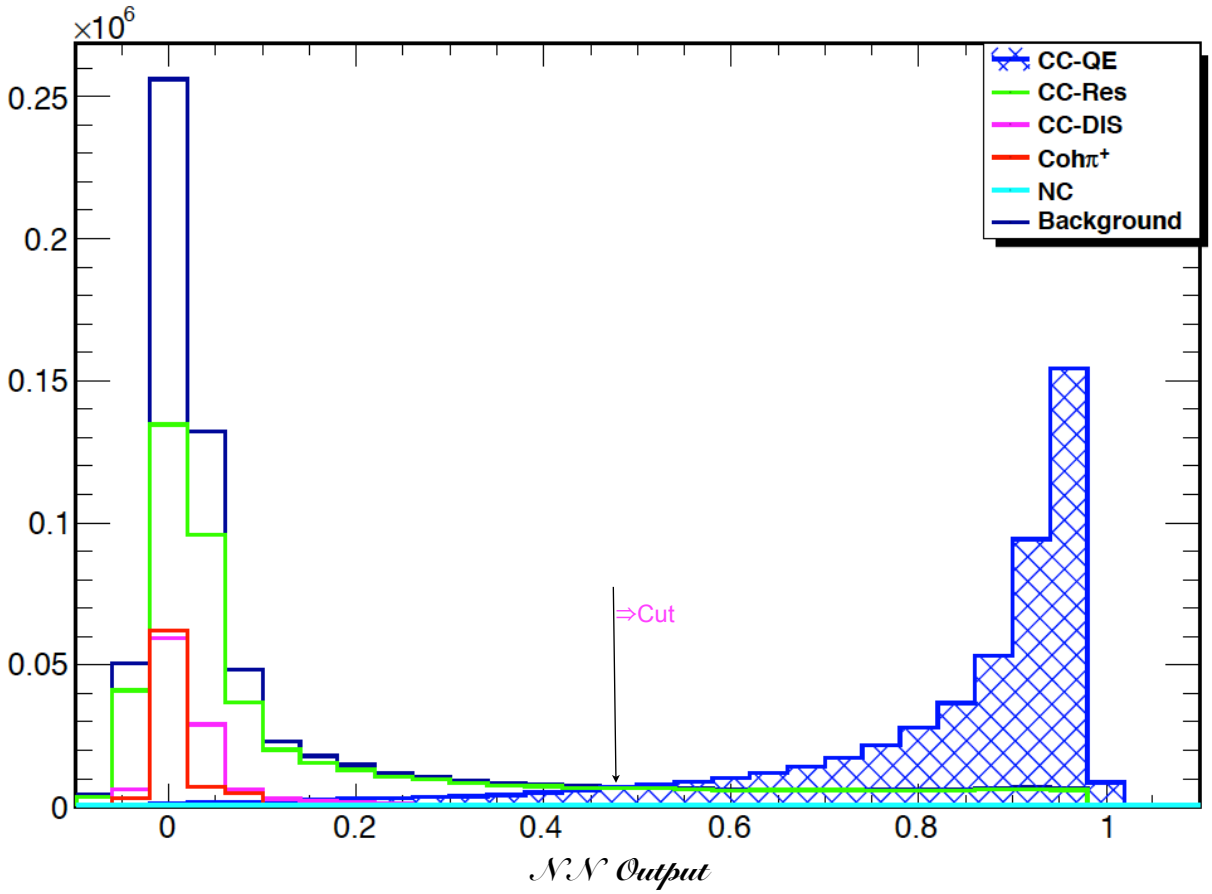

Figure 5–14: Multivariate (NN) separation of the QE-signal from the Res/DIS-background for 2-track, $\mu^- p$, topology passing the pre-selection.

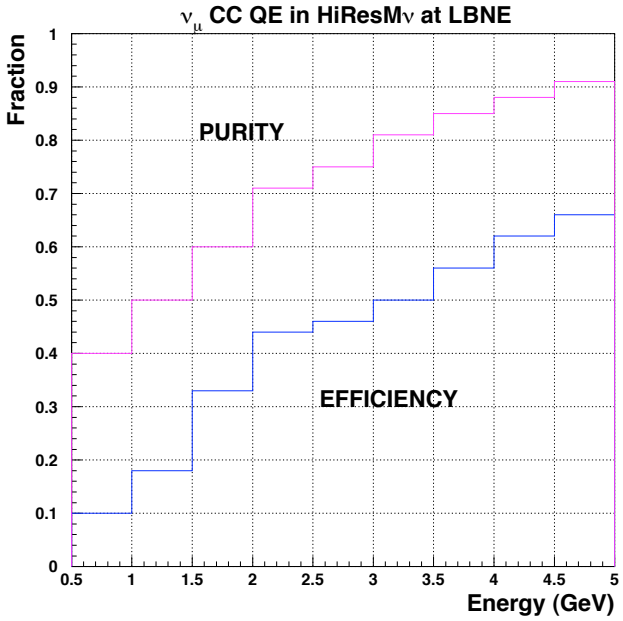

- *Protons easily identified by the large dE/dx in STT & range*

  $\Longrightarrow$ *Minimal range to reconstruct p track parameters 12cm* $\Rightarrow 250\ MeV$

- *Analize BOTH 2-track and 1-track events to constrain FSI, Fermi motion and nuclear effects*

- *Use multi-dimensional likelihood functions incorporating the full event kinematics to reject DIS & Res backgrounds*

  $\Longrightarrow$ *On average* $\varepsilon = 52\%$ *and* $\eta = 82\%$ *for CC QE at LBNE*

Figure 5–15: The efficiency and purity of $\boldsymbol{\nu_\mu}$-QE induced $\boldsymbol{\mu^- p}$ topology in HIRESMNU.

5.12 Sensitivity Studies of ν_e-CC and $\bar{\nu}_e$-CC

The goal of this study is to determine the efficiency of $\boldsymbol{\nu_e}(\overline{\boldsymbol{\nu_e}})$-CC signal and the reduction of the much larger NC and $\boldsymbol{\nu_\mu}$-CC samples, i.e., the purity. The relative abundance of $\boldsymbol{\nu_\mu}$-CC:NC:$\boldsymbol{\nu_e}$-CC is about 1:0.35:0.01; the $\bar{\boldsymbol{\nu}}_e$-CC is a factor of 10 smaller than $\boldsymbol{\nu_e}$-CC. The $\boldsymbol{\nu_e}$-CC analysis proceeds in two steps.

In the first step, we require that there be a negatively charged particle consistent with the electron-TR identification in the event as presented above. The TR selects electron with a 90% efficiency while affording a $\mathbf{10^3}$ rejection of charged pions/muons. The surviving background events are completely dominated by an asymmetric photon conversion producing an actual $\boldsymbol{e^-/e^+}$ near the event vertex. But such an $\boldsymbol{e^-}$ ($\boldsymbol{e^+}$) is emitted 'along' the hadronic shower. Figure 5–18 demonstrates a very interesting consistency, as expected from the $\boldsymbol{\nu_e}$ and $\boldsymbol{\nu_\mu}$ universality, in NOMAD data: a kinematic distribution of the measured $\boldsymbol{e^-}$ sample is compared to that of the measured $\boldsymbol{\mu^-}$-sample (normalized) plus the MC estimation of the non-prompt contribution to the $\boldsymbol{e^-}$-sample; the two are completely consistent. The figure shows that the non-prompt contribution to the electron sample can be very well measured in HIRESMNU.

In the second step, we require that the TR-identified electron be kinematically isolated from the hadronic jet. An outstanding feature of HIRESMNU is the capability for the measurement of momentum vectors in the plane transverse to the $\boldsymbol{\nu}$-direction, which can lead to an event-

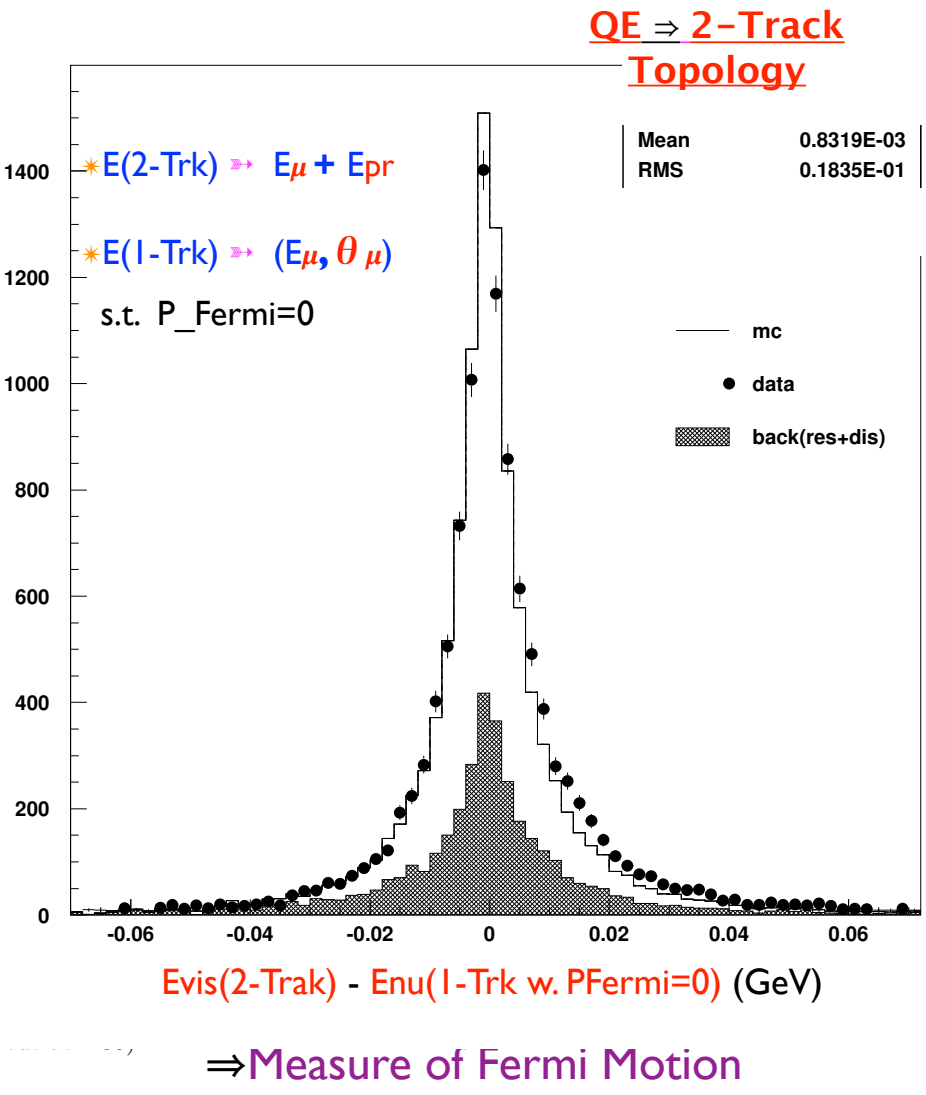

Figure 5–16: Histogram of $E_{Vis} - E_{\nu}$ for the 2-Track QE-candidates in NOMAD; the MC estimates of the QE-signal and the Res/DIS-background are also shown.

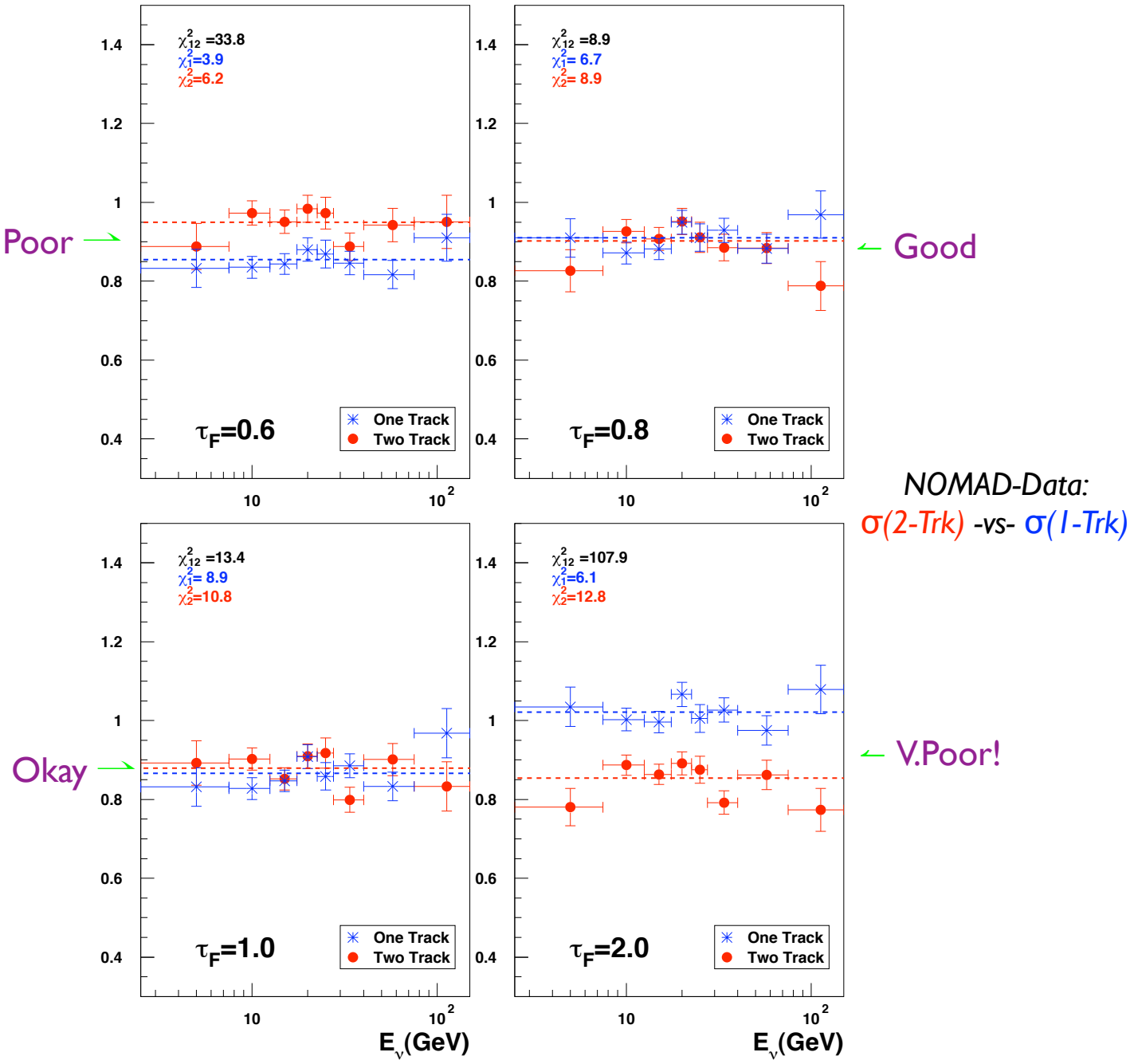

Figure 5–17: Cross-section of QE vs E_ν for 1-Track and 2-Track topologies in NOMAD.

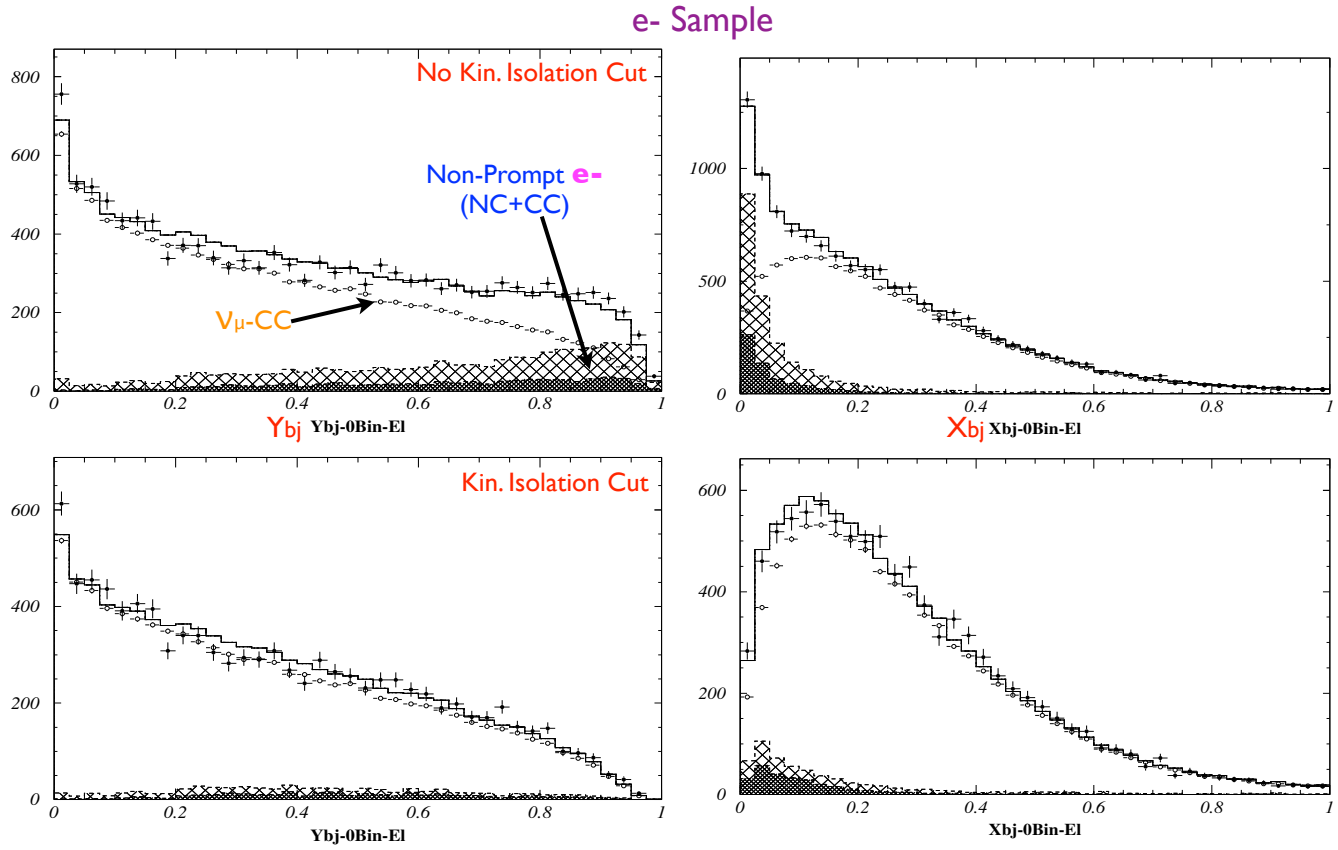

Figure 5–18: Comparison of kinematic quantities between the e^- events (cross) and μ^- events (Open circles) before (upper graphs) and after (lower graphs) the kinematic-isolation cuts.

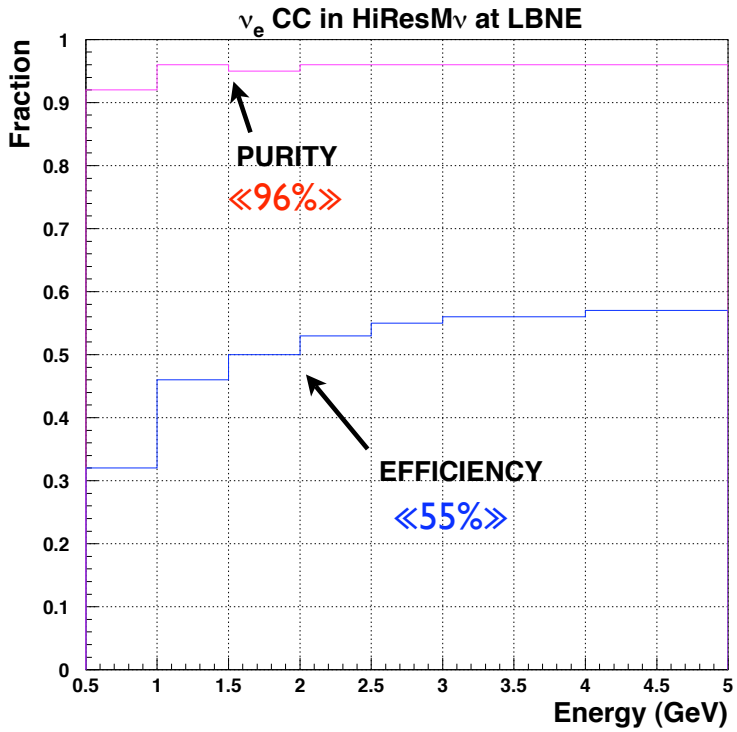

Figure 5–19: Efficiency and purity of the ν_e-CC sample as a function of the ν_e-energy

by-event determination of the missing transverse-momentum ($\boldsymbol{P_T^m}$) vector. The $\boldsymbol{P_T^m}$-vector measurement allows a clean separation of the NC-electrons (non-prompt) from the CC-electrons. To isolate the $\boldsymbol{\nu_e}$-CC induced prompt-$\boldsymbol{e^-}$ from the NC-induced photon-conversion, we use a multivariate likelihood function built using the momentum vector information of the lepton and the hadron. A mild cut on the lepton versus hadron isolation diminishes the signal efficiency by 10% while reducing the background by 80%. The consistency between the $\boldsymbol{e^-}$ and $\boldsymbol{\mu^-}$ data after the isolation-cut is shown in Figure 5–18. The final efficiency (55% average) and the purity (96% average) of the $\boldsymbol{\nu_e}$-CC is shown in Figure 5–19 as a function of the $\boldsymbol{\nu_e}$-energy. The $\overline{\boldsymbol{\nu_e}}$-CC analysis is conducted in a similar fashion. For the $\overline{\boldsymbol{\nu_e}}$-CC, if we choose to keep the average efficiency at 50% then the average purity will be 88%.

HIRESMNU will measure about 200,000 $\boldsymbol{\nu_e}$-CC and 20,000 $\bar{\boldsymbol{\nu}}_e$-CC over a 5-year neutrino run enabling one to fully characterize the LBNE neutrino source — the most important challenge for an ND in an oscillation program.

5.13 Measurement of Neutral Pions, Photons, and $\pi^{\pm}$ in Neutral and Charged Current Events

The principal background to the ν_e and $\bar{\nu}_e$appearance comes from the NC-events where a photon from the π^0 decay produces a signature identical to that produced by ν_e-induced electron; the second source of background is due to π^0s from ν_μ-CC where the μ^- evades identification — typically at high-y_{BJ}. Since the energy spectra of NC and CC are different, it is critical for ND to measure π^0s in NC and CC in the full kinematic phase space.

The proposed ND is designed to measure π^0s with high accuracy in three topologies: (a) both photons convert in the tracker ($\simeq$ **25%**), (b) one photon converts in the tracker and the other in the calorimeter ($\simeq$ **50%**), and (c) both photons convert in the calorimeter. The first two topologies afford the best resolution because the tracker provides precise γ-direction measurement. The third topology also suffers from non-π^0 backgrounds caused by energy deposition by neutral hadrons in the ECAL. In the following, we only use the first two topologies.

What sort of photon reconstruction resolution do we expect in the proposed detector? Figure 5–20 and Figure 5–21 display the exclusive two-photon events in NOMAD. The figures demonstrate the ability to reconstruct low-energy photons in a detector with $\rho = 0.1\text{g/cm}^3$. The proposed HIRESMNU is designed to have substantially improved photon reconstruction ability in the STT where e^+/e^- can be reconstructed down to 80 MeV.

To estimate the π^0 reconstruction efficiency, we focused on events where at least one photon converts in the STT. Figure 5–22 shows the π^0 reconstruction efficiency as a function of π^0 energy in NC events. If we include photons that reach the ECAL, the reconstruction efficiency is expected to be $\geq$ **75%**, but will have higher systematic error. Figure 5–23 shows the invariant mass distribution of the reconstructed photons in the ν_μ-CC sample of NOMAD; Figure 5–24 shows the invariant mass distribution of the reconstructed photons in the NC sample of NOMAD. Improvements in the π^0 reconstruction in HiResMν comes from two considerations: first, 50% more photons will convert in the tracker; second, the e^-/e^+ track will have a factor of 12 more track points than that in NOMAD, enabling more efficient reconstruction of low-momenta e^- and e^+. Finally the combinatorial background will be much smaller in LBNE than in NOMAD.

Immanent in the discussion above is that the reconstruction of events with quasi-exclusive single photon will be straight forward in HIRESMNU. Exclusive photon events occur rarely since to the first order in ν-interactions photons appear in pairs from π^0 decay. If processes exist that produce single photons, then 50% of these will be cleanly reconstructed in HIRESMNU. Figure 5–25 shows NOMAD events where a single photon was reconstructed, leading them to impose stringent limits on such processes [18]. The proposed detector will have better resolution to reconstruct a γ and will empirically constrain with high purity

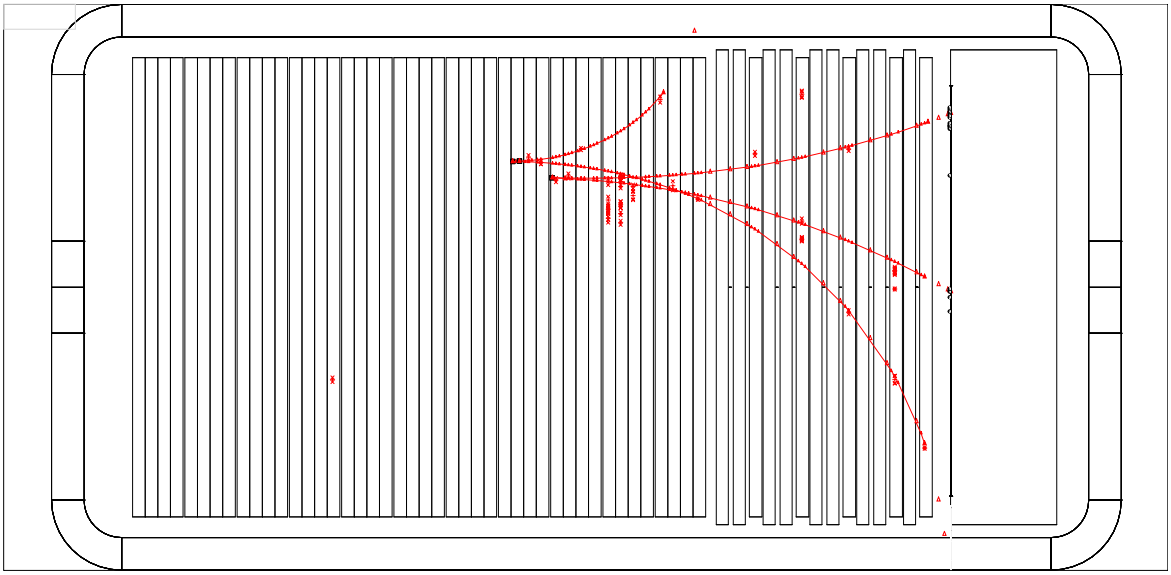

Figure 5–20: An exclusive two-photon event in NOMAD.

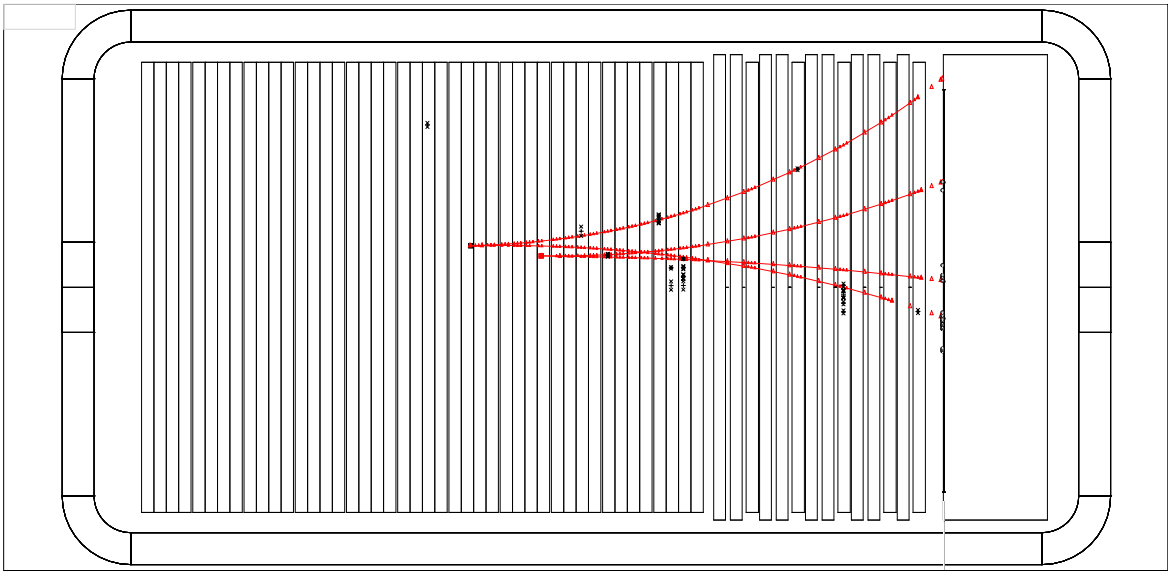

Figure 5–21: Another exclusive two-photon event in NOMAD.

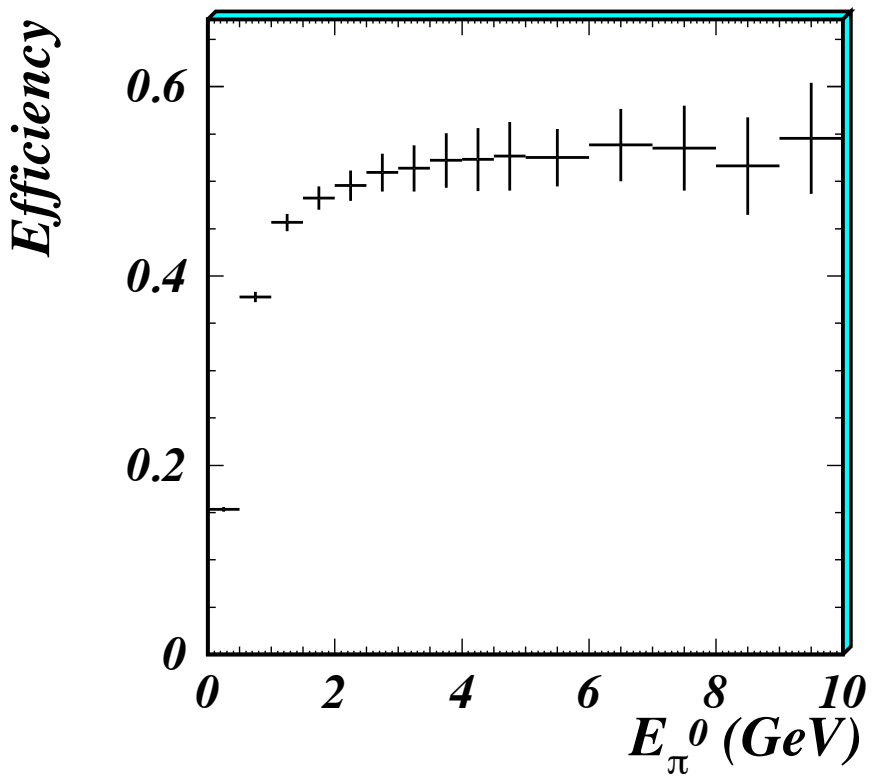

Figure 5–22: The π^0 reconstruction efficiency as a function of π^0 energy in NC events in HIRESMNU.

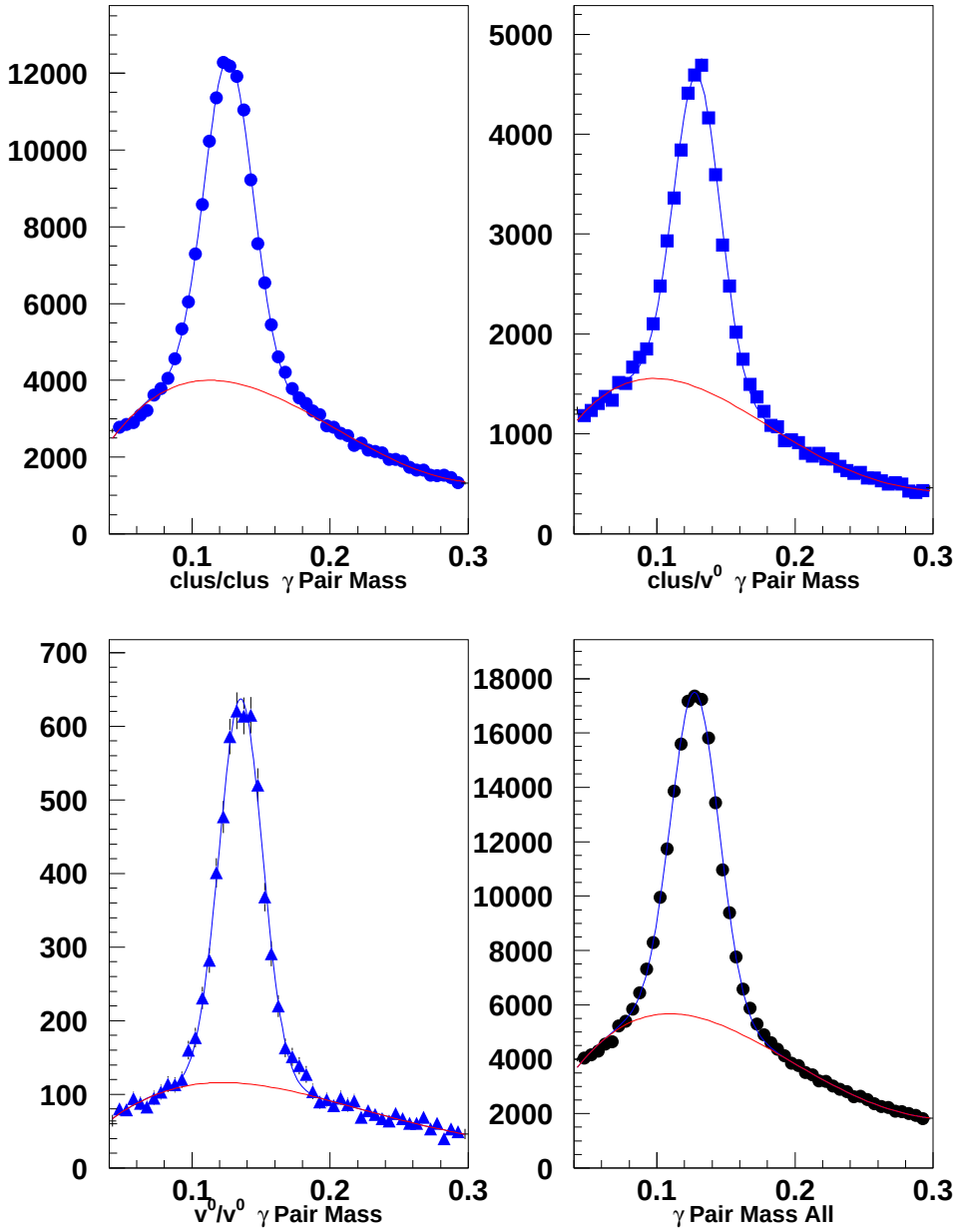

Figure 5–23: Reconstruction of π^0 in inclusive ν_μ-CC events in NOMAD (preliminary).

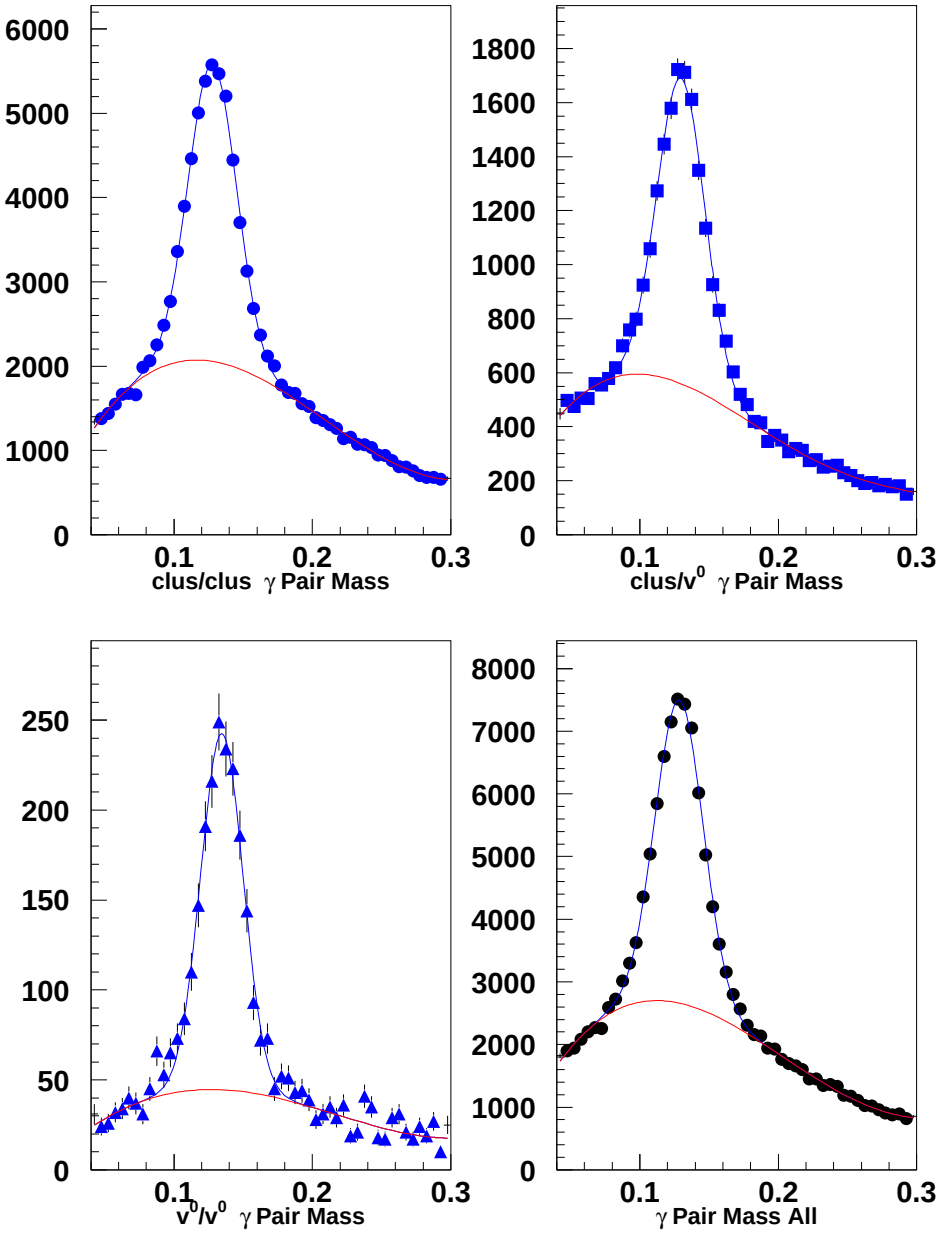

Figure 5–24: Reconstruction of π^0 in inclusive NC events in NOMAD (preliminary).

the ν_μ-CC- and ν-NC-induced photons, exclusive and semi-exclusive, as a function of E_{Vis} and angle. By contrasting the π^0 mass in the tracker versus in the calorimeter, the relative efficiencies of photon reconstruction will be well constrained.

Finally, the $\pi^\pm$ will be measured by the tracker including the dE/dx information. An *in situ* determination of the charged pions in the $\nu_\mu(\bar{\nu}_\mu)$-CC — with μID and without μID — and the ν-NC is crucial to constrain the systematic error associated with the $\nu_\mu(\bar{\nu}_\mu)$-disappearance, especially at low E_ν. The HIRESMNU determination of the charged pion production in non-μID-CC and NC will all but eliminate this error in the disappearance analysis. The NOMAD event pictures of ν_μ-CC, $\bar{\nu}_e$-CC and NC show that the measurement of the charged hadrons in HIRESMNU will be a routine task.

5.14 Measurement of Strange Mesons and Hyperons in ν-Interactions

A sample of ∼50 Million ν_μ-CC and attendant NC, $\bar{\nu}_\mu$-CC, etc., with an experiment capable of conducting measurements with a precision such as outlined above, offers an entire programme of text-book physics: from exclusive cross sections of QE and resonance, coherent-π, -ρ, Charmed mesons/baryons, to J/ψ-production in NC, to inclusive cross sections, to strange mesons, to hyperons and polarization measurements of hyperons. To illustrate the power of this experiment, we show a NOMAD event with three reconstructed K^0_S in Figure 5–26. Figure 5–27 shows a data *vs* MC comparison of the reconstructed K^0_S mass in NOMAD ($E_{K^0_S} \geq 1$ GeV). In the proposed experiment, we expect to reconstruct over 0.5 million K^0_S in the ν-mode.

The large K^0_S sample provides a powerful calibration of the momentum scale of charged particles, directly affecting the precision of the muon-energy scale. Another important service is provided by the large number of Λ baryons, $\Lambda \rightarrow p\pi^-$, which provides a very clean source of protons with momenta similar to that expected in the QE and resonance interactions. Figure 5–28 presents NOMAD's Armenteros plot where clear bands of K^0_S, Λ and $\overline{\Lambda}$ are seen.

5.15 Constraining the Neutrino-Induced Background to Proton Decay

In addition to background measurements for the long-baseline oscillation program, HIRESMNU can provide an estimate of the ν-induced background to the search for proton (nucleon) decay. Two generic proton decay modes are under study [61]: the π^0-mode, $e^+(\mu^+) + \pi^0$ and the kaon-mode, $\nu + K^+$ and $e^+(\mu^+) + K^0$.

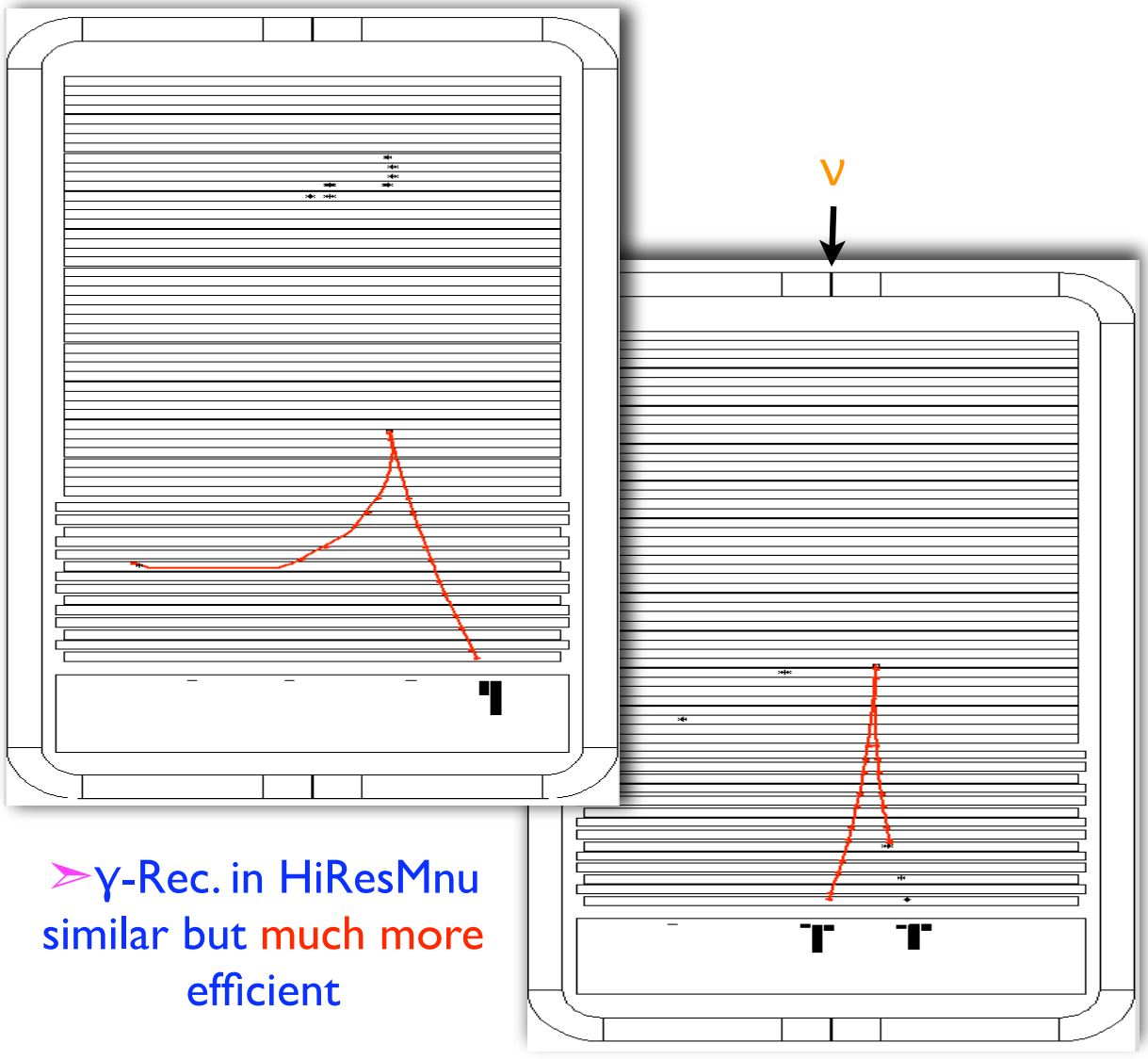

Figure 5–25: NOMAD events with a single visible photon

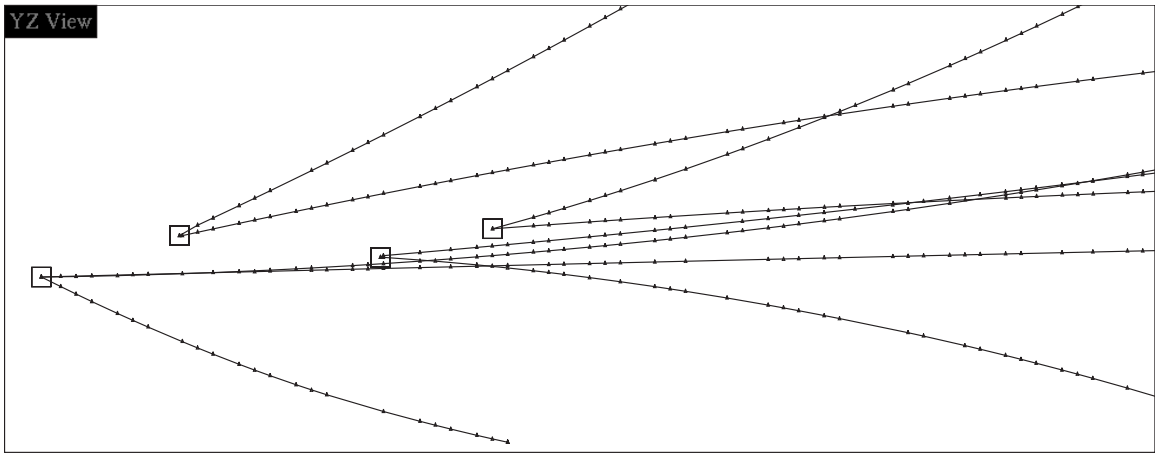

Figure 5–26: A reconstructed $\boldsymbol{\nu_\mu}$ CC event candidate in NOMAD containing 3 $\boldsymbol{V^0}$ vertices identified as $\boldsymbol{K^0_S}$. The scale on this plot is given by the size of the vertex boxes ($\boldsymbol{3 \times 3}$ cm^2). The HIRESMNU will have a much finer resolution.

The atmospheric neutrino spectrum is different from that of the LBNE beam. However, an accurate determination of exclusive channels induced by the LBNE neutrino beam at $\boldsymbol{E_\nu \simeq 2}$ GeV will provide empirical constraints for the atmospheric-neutrino background to proton decay at the FD, thus reducing the corresponding systematic uncertainty.

The K2K-ND has provided a definitive measurement of $\boldsymbol{e^+ + \pi^0}$ [62]. The ND at LBNE will have an efficient $\boldsymbol{\pi^0}$ and $\boldsymbol{e^+}$ identification with purity exceeding 95% and the identification of $\boldsymbol{\mu^+}$-mode will be straightforward. In addition, and importantly, the ND aims to measure the exclusive first-generation mesons such as $\boldsymbol{\eta}$, $\boldsymbol{\rho^0}$, etc., besides $\boldsymbol{\pi^0}$ accompanied by an $\boldsymbol{e^+}$ or a $\boldsymbol{\mu^+}$.

Supersymmetric models favor the proton-to-kaon decay mode. The main focus of the ND measurements at LBNE is the exclusive $\boldsymbol{K^0}$ production, i.e., $\boldsymbol{e^+/\mu^+ + K^0}$. There is an existence proof of precise determination of $\boldsymbol{K^0_S}$ in $\boldsymbol{\nu}$ CC and NC interactions [14], [15]. The ND at LBNE will extend the $\boldsymbol{K^0}$ measurement to lower energy. The $\boldsymbol{\nu + K^+}$ is a challenge, however, it should be pointed out that if the $\boldsymbol{K^0}$ mode is precisely measured then the $\boldsymbol{K^+}$ channel can be accurately predicted.

5.16 Measurement of Neutral Current Events

In most neutrino experiments, a neutral-current-like event is one with no identifiable muon. The NC-like events thus include not only true NC but also $\boldsymbol{\nu_\mu}$-CC and $\boldsymbol{\bar{\nu}_\mu}$-CC where the muon evades detection and $\boldsymbol{\nu_e}$-CC and $\boldsymbol{\bar{\nu}_e}$-CC where the leading lepton ($\boldsymbol{e^-/e^+}$) is part

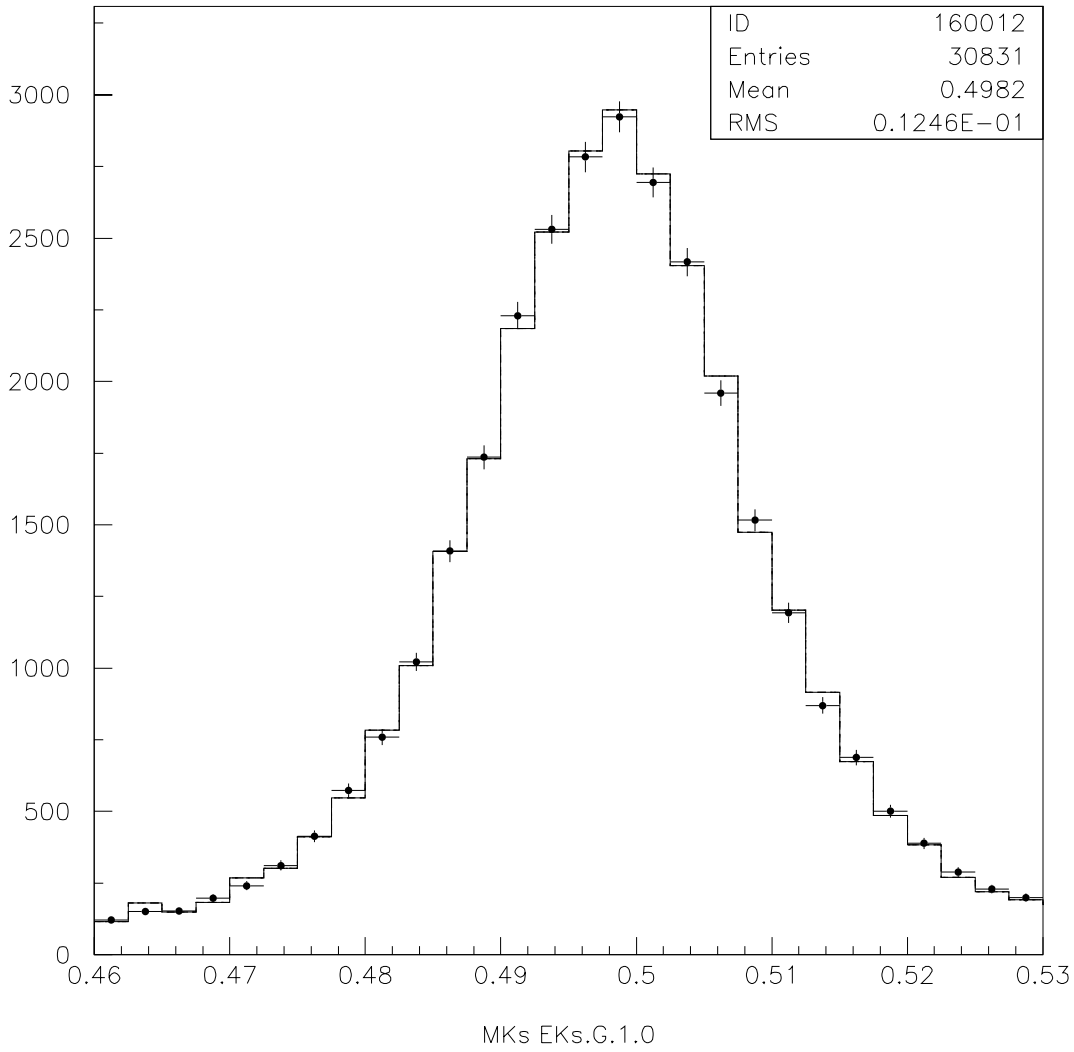

Figure 5–27: Reconstructed K_S^0 in NOMAD.

of the visible hadronic shower. Even the precision electroweak measurements conducted by CCFR [29] and NuTeV [30] had to deal with the large impurity of the NC-like sample and to conduct a large 'statistical-subtraction' of the attendant CC-background. However, for a precision oscillation study such as LBNE aims to make, it is critical to quantify the NC content of the neutrino event as a function of visible energy, and to predict the NC-spectra at the far location for all four species of neutrinos. HIRESMNU detector enables this crucial capability with very high precision. This comes about due to the following reasons:

Identification of ν_e-CC and $\bar{\nu}_e$-CC: HIRESMNU is designed to identify the ν_e-CC and $\bar{\nu}_e$-CC with high efficiency ($\simeq$ **55%**) and high purity ($\simeq$ **97%**); and, to the first order, these processes do not contaminate the NC-sample.

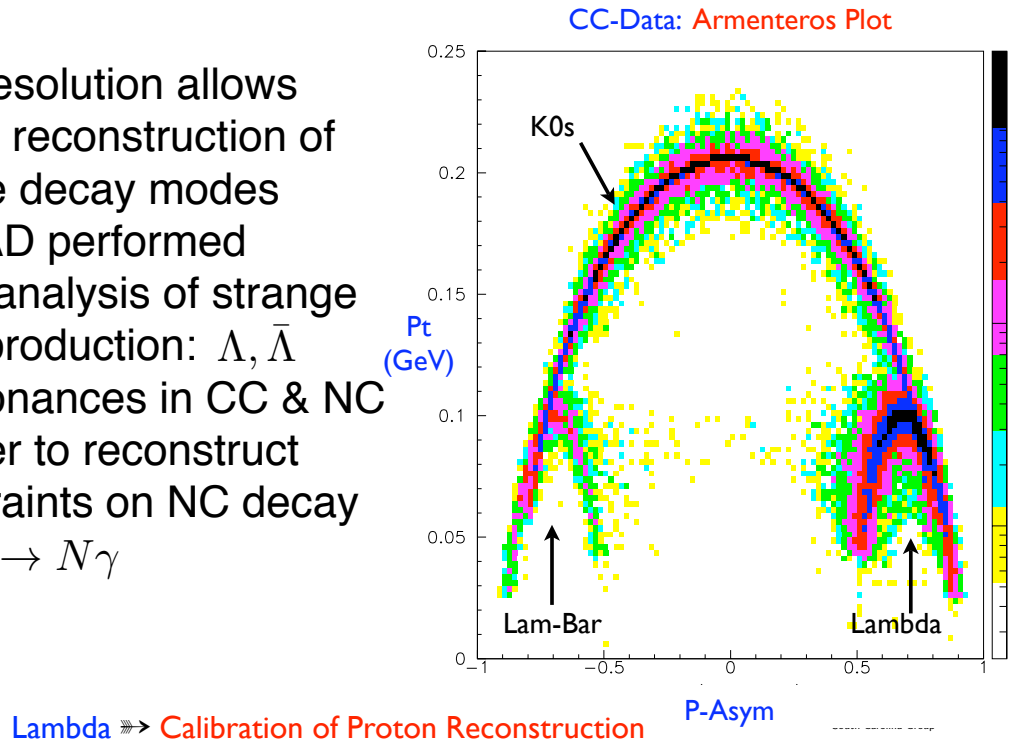

Figure 5–28: The measured Armenteros plot of detached vertices in NOMAD.

Kinematic Separation of High-y_{BJ} ν_μ-CC and $\bar{\nu}_\mu$-CC: A CC event in HIRESMNU, as in NOMAD, is an event where the $\boldsymbol{P_T}$ of the lepton balances the $\boldsymbol{P_T}$ of the hadron, i.e., miss-$\boldsymbol{P_T}$ is consistent with zero. Figure 3–3 depicts that an NC will have a large miss-$\boldsymbol{P_T}$ as illustrated in Figure 3–6.

Measurement of the miss-$\boldsymbol{P_T}$ vector in a detector like HIRESMNU affords a much richer separation of NC from CC events than simply identifying $\boldsymbol{\mu}$. For example, Figure 5–29 demonstrates that, for events where there is no identifiable muon, the kinematic correlations in CC are quite distinct from those of NC. NOMAD has conducted a measurement of NC events in the visible energy ($\boldsymbol{E_{Had}}$) range of 1–100 GeV. HIRESMNU should be able to measure the NC spectra in the neutrino and the antineutrino modes down to 0.5 GeV in visible energy.

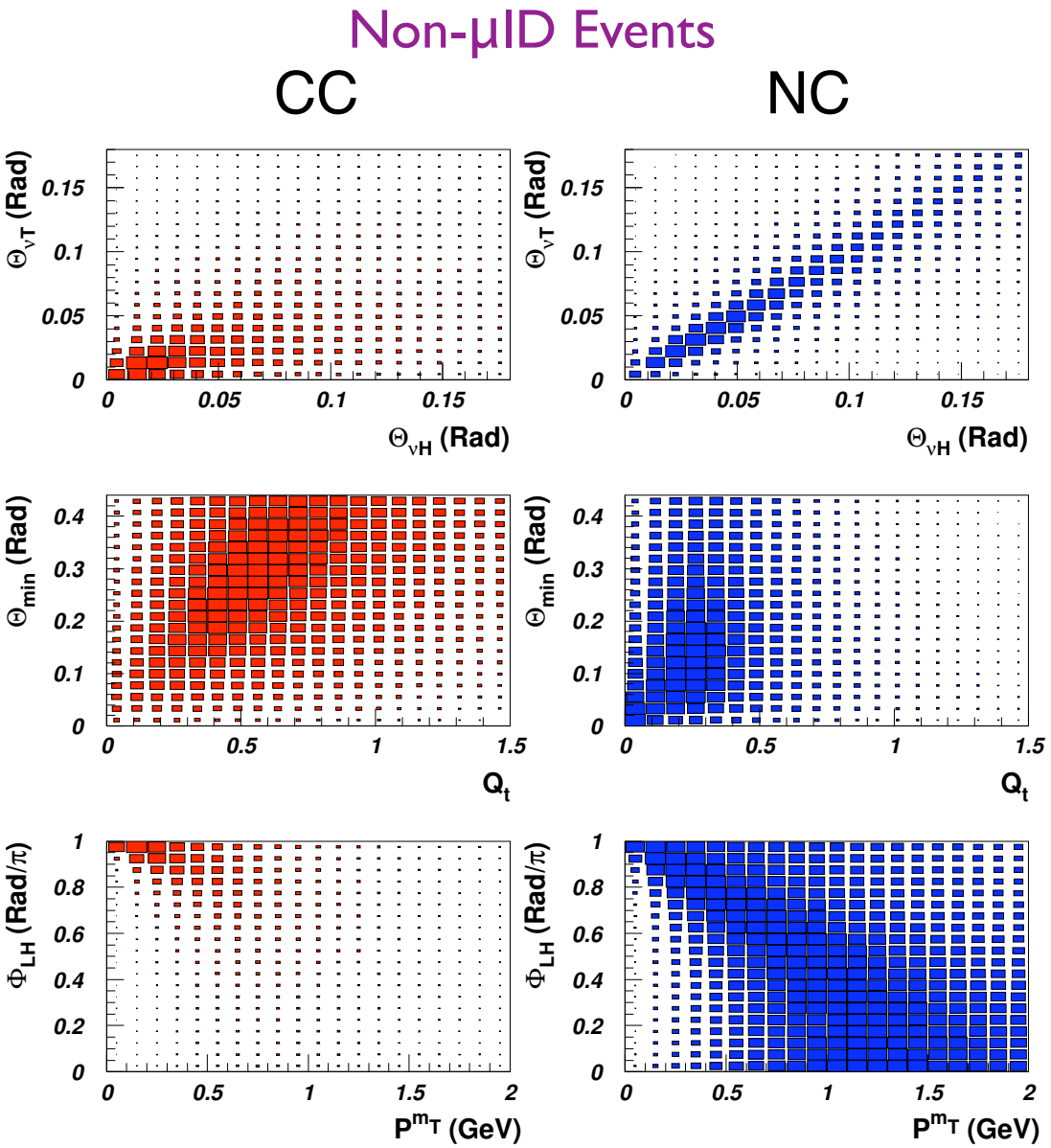

Figure 5–29: No-Muon Sample: Kinematic correlations in CC and NC events

5.17 Electroweak Precision Measurment: Weak Mixing Angle

Neutrinos are a natural probe for the investigation of electroweak physics. Interest in a precise determination of the weak mixing angle ($\sin^2\theta_W$) at LBNE energies via neutrino scattering is twofold: (a) it provides a direct measurement of neutrino couplings to the Z boson and (b) it probes a different scale of momentum transfer than LEP by virtue of not being on the Z pole. The weak mixing angle can be extracted experimentally from three main NC physics processes:

1. Deep Inelastic Scattering off quarks inside nucleons: $\nu N \rightarrow \nu X$;
2. Elastic Scattering off electrons: $\nu e^- \rightarrow \nu e^-$;
3. Elastic Scattering off protons: $\nu p \rightarrow \nu p$.

Figure 5–30 shows the corresponding Feynman diagrams for the three processes.

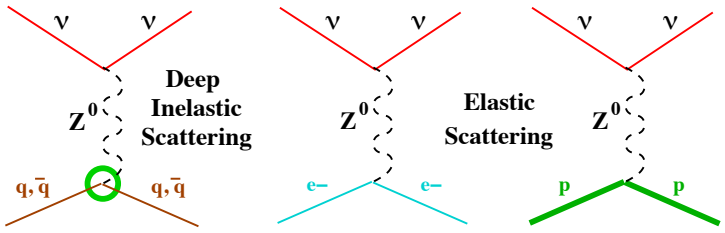

Figure 5–30: Feynman diagrams for the three main Neutral Current processes which can be used to extract $\sin^2\theta_W$ with the LBNE Near Detector complex.

The most precise measurement of $\sin^2\theta_W$ in neutrino deep inelastic scattering (DIS) comes from the NuTeV experiment which reported a value that is 3σ from the standard model [30]. The LBNE ND can perform a similar analysis in the DIS channel by measuring the ratio of NC and CC interactions induced by neutrinos:

$$\mathcal{R}^\nu \equiv \frac{\sigma^\nu_{\rm NC}}{\sigma^\nu_{\rm CC}} \simeq \rho^2 \left(\frac{1}{2} - \sin^2\theta_W + \frac{5}{9}\,(1+r)\sin^4\theta_W \right). \tag{5.8}$$

Here ρ is the relative coupling strength of the neutral-to-charged current interactions ($\rho = 1$ at tree-level in the Standard Model) and r is the ratio of antineutrino to neutrino cross section ($r \sim 0.5$). The absolute sensitivity of $\mathcal{R}^\nu$ to $\sin^2\theta_W$ is 0.7, which implies that a measurement of $\mathcal{R}^\nu$ of 1% precision would provide $\sin^2\theta_W$ with a precision of 1.4%. Contrary to the NuTeV experiment, the antineutrino interactions cannot be used for this

analysis at LBNE due to the large number of ν_μ DIS interactions in the $\bar{\nu}_\mu$ beam compared to the $\bar{\nu}_\mu$ DIS interactions.

The measurement of $\sin^2\theta_W$ from DIS interactions can be only performed with the low-density magnetized tracker since an accurate reconstruction of the NC event kinematics and of the ν CC interactions are crucial to keep the systematic uncertainties on the event selection under control. The analysis selects events in the ND after imposing a cut on the visible hadronic energy of $E_{\rm had} > 3$ GeV, as in the NOMAD $\sin^2\theta_W$ analysis (the CHARM analysis had $E_{\rm had} > 4$ GeV). With the reference 700 kW primary beam we expect about 3.3×10^6 CC events and 1.1×10^6 NC events, giving a statistical precision of 0.11% on $\mathcal{R}^\nu$ and 0.15% on $\sin^2\theta_W$ (Table 5–4).

The use of a low-density magnetized tracker can substantially reduce systematic uncertainties compared toa massive calorimeter. Table 5–4 shows a comparison of the different uncertainties on the measured $\mathcal{R}^\nu$ between NuTeV and LBNE. The largest experimental systematic uncertainty in NuTeV is related to the subtraction of the ν_e CC contamination from the NC sample. Since the low-density tracker at LBNE can efficiently reconstruct the electron tracks, the ν_e CC interactions can be identified on an event-by-event basis, reducing the corresponding uncertainty to a negligible level. Similarly, uncertainties related to the location of the interaction vertex, noise, counter efficiency and so on are removed by the higher resolution and by changing the analysis selection. The experimental selection at LBNE will be dominated by two uncertainties: the knowledge of the $\bar{\nu}_\mu$ flux and the kinematic selection of NC interactions. The former is relevant due to the larger NC/CC ratio for antineutrinos. The total experimental systematic uncertainty on $\sin^2\theta_W$ is expected to be about 0.14%.

The measurement of $\mathcal{R}^\nu$ will be dominated by model systematic uncertainties on the structure functions of the target nucleons. The estimate of these uncertainties for LBNE is based upon the extensive work performed for the NOMAD analysis and includes a NNLO QCD calculation of structure functions (NLO for charm production) [34,35,36], parton distribution functions (PDFs) extracted from dedicated low-Q global fits, high twist contributions [34], electroweak corrections [55] and nuclear corrections [38,39,40]. The charm quark production in CC, which has been the dominant source of uncertainty in all past determinations of $\sin^2\theta_W$ from νN DIS, is reduced to about 2.5% of the total ν_μ CC DIS with $E_{\rm had} > 3$ GeV with the low-energy beam spectrum at LBNE. This number translates into a systematic uncertainty of 0.13% on $\mathcal{R}^\nu$ (Table 5–4), assuming a knowledge of the charm production cross section to 5%. It is worth noting that the recent measurement of charm dimuon production by the NOMAD experiment allowed a reduction of the uncertainty on the strange sea distribution to $\sim 3\%$ and on the charm quark mass m_c to ~ 60 MeV [41]. The lower neutrino energies available at LBNE reduce the accessible Q^2 values with respect to NuTeV, increasing in turn the effect of non-perturbative contributions (High Twists) and R_L. The corresponding uncertainties are reduced by the recent studies of low-Q structure functions and by improved modeling with respect to the NuTeV analysis (NNLO vs. LO). The total model systematic uncertainty on $\sin^2\theta_W$ is expected to be about 0.29% with the reference beam configuration. The corresponding total uncertainty on the value of $\sin^2\theta_W$ extracted

Table 5–4: Comparison of uncertainties on the $\mathcal{R}^{\nu}$ measurement between NuTeV and LBNE with the reference beam. The corresponding relative uncertainties on $\sin^2\theta_W$ must be multiplied by a factor of 1.4, giving for LBNE a projected overall precision of 0.36%.

	$\delta R^{\nu}/R^{\nu}$	
Source of uncertainty	NuTeV	LBNE
Data statistics	0.00176	0.00110
Monte Carlo statistics	0.00015	
Total Statistics	0.00176	0.00110
$\nu_e, \bar{\nu}_e$ flux ($\sim 1.7\%$)	0.00064	0.00010
Energy measurement	0.00038	0.00040
Shower length model	0.00054	n.a.
Counter efficiency, noise	0.00036	n.a.
Interaction vertex	0.00056	n.a.
$\bar{\nu}_{\mu}$ flux	n.a.	0.00070
Kinematic selection	n.a.	0.00060
Experimental systematics	0.00112	0.00102
d,s$\rightarrow$c, s-sea	0.00227	0.00130
Charm sea	0.00013	n.a.
$r = \sigma^{\bar{\nu}}/\sigma^{\nu}$	0.00018	n.a.
Radiative corrections	0.00013	0.00013
Non-isoscalar target	0.00010	N.A.
Higher twists	0.00031	0.00070
R_L (F_2, F_T, xF_3)	0.00115	0.00140
Nuclear correction		0.00020
Model systematics	0.00258	0.00206
TOTAL	0.00332	0.00255

from νN DIS is 0.36% with the 700 kW beam.

Most of the model uncertainties will be constrained by in situ dedicated measurements using the large CC samples and employing improvements in theory that will have evolved over the course of the experiment. In the low-density tracker we shall collect about 80,000 neutrino-induced inclusive charm events with the 700 kW beam. The precise reconstruction of charged tracks will allow measurement of exclusive decay modes of charmed hadrons (e.g. D^{*+}) and measurement of charm fragmentation and production parameters. The average semileptonic branching ratio $B_{\mu} \sim 5\%$ with the low-energy LBNE beam. The most precise sample of 15,400 dimuon events is collected by the NOMAD experiment [41]. Finally, precision measurements of CC structure functions in the fine-grained tracker would further reduce the uncertainties on PDFs and on High Twist contributions.

The precision that can be achieved from νN DIS interactions is limited by both the event rates and by the energy spectrum of the reference 700 kW beam configuration. The high-statistics beam exposure combined with a dedicated run with the high-energy beam option would increase the statistics by more than a factor of 20. This major step forward would not only reduce the statistical uncertainty to a negligible level, but would provide large control samples and precision auxiliary measurements to reduce the systematic uncertainties on structure functions. The two dominant systematic uncertainties, charm production in CC interactions and low Q^2 structure functions, are essentially defined by the available data at present. Overall, the use of a high-energy beam with an upgraded intensity can potentially improve the precision achievable on $\sin^2\theta_W$ from νN DIS to about 0.2%. It is worth mentioning that the high-energy beam is also required for the determination of the fluxes in case high Δm^2 oscillations are present.

A second independent measurement of $\sin^2\theta_W$ can be obtained from NC $\nu_\mu e$ elastic scattering. This channel has lower systematic uncertainties since it does not depend upon the knowledge of the structure of nuclei, but has limited statistics due to its very low cross section. The value of $\sin^2\theta_W$ can be extracted from the ratio of neutrino to antineutrino interactions [25]:

$$\mathcal{R}_{\nu e}(Q^2) \equiv \frac{\sigma(\bar{\nu}_\mu e \to \bar{\nu}_\mu e)}{\sigma(\nu_\mu e \to \nu_\mu e)}(Q^2) \simeq \frac{1 - 4\sin^2\theta_W + 16\sin^4\theta_W}{3 - 12\sin^2\theta_W + 16\sin^4\theta_W}, \tag{5.9}$$

in which systematic uncertainties related to the selection and electron identification cancel out. The absolute sensitivity of this ratio to $\sin^2\theta_W$ is 1.79, which implies a measurement of $\mathcal{R}_{\nu e}$ of 1% precision would provide $\sin^2\theta_W$ with a precision of 0.65%.

The event selection was described earlier since the NC elastic scattering off electrons is also used for the absolute flux normalization. The WMA analysis can be performed only with the low-density magnetized tracker in conjunction with a large LAr detector. In the former case the total statistics available is limited to about a few thousand $\nu(\bar{\nu})$ events. These numbers do not allow a competitive determination of $\sin^2\theta_W$ by using the magnetized tracker alone. However, if we consider a 100 ton LAr detector in the ND complex, we expect to collect about 20,000 (12,000) $\nu(\bar{\nu})$ events; and a factor of four more with a high-intensity beam.

A combined analysis of both detectors can achieve the optimal sensitivity: the fine-grained tracker is used to reduce systematic uncertainties (measurement of backgrounds and calibration), while the LAr ND provides the statistics required for a competitive measurement. Overall, the use of the massive LAr detector can provide a statistical accuracy on $\sin^2\theta_W$ of about 0.3%. However, the extraction of the weak mixing angle is dominated by the systematic uncertainty on the $\bar{\nu}_\mu/\nu_\mu$ flux ratio in Equation (5.9). We evaluated this uncertainty with the low-ν_0 method for the flux extraction and we obtained a systematic uncertainty of about 1% on the ratio of the $\bar{\nu}_\mu/\nu_\mu$ flux integrals. Therefore, the overall precision on $\sin^2\theta_W$ achievable from NC elastic scattering off electrons is limited to about 0.9%.

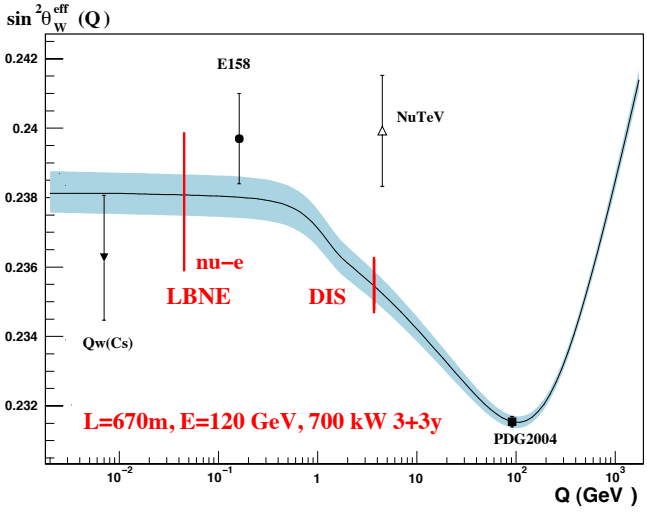

Figure 5–31: Expected sensitivity to the measurement of $\sin^2\theta_W$ from the LBNE ND with the reference 700 kW beam. The curve shows the Standard Model prediction as a function of the momentum scale [49]. Previous measurements from Atomic Parity Violation [50,51], Moeller scattering (E158 [52]), ν DIS (NuTeV [30]) and the combined Z pole measurements (LEP/SLC) [51] are also shown for comparisons. The use of a high-energy beam can reduce the LBNE uncertainties by almost a factor of two.

Together, the DIS and the NC elastic scattering channels involve substantially different scales of momentum transfer, providing a tool to test the running of $\sin^2\theta_W$ in a single experiment. To this end, the study of NC elastic scattering off protons can provide additional information since it occurs at a momentum scale which is intermediate between the two other processes. Figure 5–31 summarizes the target sensitivity from the LBNE ND, compared with existing measurements as a function of the momentum scale.

5.18 Strangeness Content of the Nucleon

The strange quark content of the proton and its contribution to the proton-spin remain enigmatic. The question is whether the strange quarks contribute substantially to the vector and axial-vector currents of the nucleon. A large observed value of the strange quark contribution to the nucleon spin (axial current), Δs, would change our understanding of the proton structure. The spin structure of the nucleon also affects the couplings of axions and supersymmetric particles to dark matter. The salient topics in this section include:

- Neutral Current Elastic Scattering and Measurement of Δs
- Strange Form Factors

- Charm Production and (anti)strange Parton Distribution Function
- Strange Particle Production in NC and CC

The strange *vector* elastic form factors of the nucleon have been measured to high precision in parity-violating electron scattering (PVES) at Jefferson Lab, Mainz and elsewhere. A recent global analysis [42] of PVES data finds a strange magnetic moment $\boldsymbol{\mu_s = 0.37 \pm 0.79}$ (in units of the nucleon magneton), so that the strange quark contribution to proton magnetic moment is less than 10%. For the strange electric charge radius parameter $\boldsymbol{\rho_s}$, defined in terms of the Sachs electric form factor at low $\boldsymbol{Q^2}$ as $\boldsymbol{G_E^s = \rho_s Q^2 + \rho_s' Q^4 + \mathcal{O}(Q^6)}$, one finds a very small value, $\boldsymbol{\rho_s = -0.03 \pm 0.63}$ GeV$^{\boldsymbol{-2}}$, consistent with zero.

Both results are consistent with theoretical expectations based on lattice QCD and phenomenology. [43]. In contrast, the strange *axial vector* form factors are poorly determined. A global study of PVES data [42] finds $\boldsymbol{\widetilde{G}_A^N(Q^2) = \tilde{g}_A^N \left(1 + Q^2/M_A^2\right)^2}$, with the effective proton and neutron axial charges $\boldsymbol{\tilde{g}_A^p = -0.80 \pm 1.68}$ and $\boldsymbol{\tilde{g}_A^n = 1.65 \pm 2.62}$.

The strange axial form factor at $\boldsymbol{Q^2 = 0}$ is related to the *spin* carried by strange quarks, $\boldsymbol{\Delta s}$. Currently the world data on the spin-dependent $\boldsymbol{g_1}$ structure function constrain $\boldsymbol{\Delta s}$ to be $\boldsymbol{\approx -0.055}$ at a scale $\boldsymbol{Q^2 = 1}$ GeV$^{\boldsymbol{2}}$, with a significant fraction coming from the region $\boldsymbol{x < 0.001}$. In addition, the HERMES collaboration [44] extracted the strange quark spin from semi-inclusive DIS data over the range $\boldsymbol{0.02 \leq x \leq 0.6}$, yielding a *negative* central value, $\boldsymbol{\Delta s = 0.037 \pm 0.019 \pm 0.027}$, although still consistent with the above global average.

Table 5–5: Coefficients entering Equation 5.10 for NC elastic scattering and CC QE interactions, with $\boldsymbol{\tau = Q^2/4M_p}$.

A	B	C
$\frac{1}{4}\left[G_1^2(1+\tau) - \left(F_1^2 - \tau F_2^2\right)(1-\tau) + 4\tau F_1 F_2\right]$	$-\frac{1}{4} G_1 (F_1 + F_2)$	$\frac{1}{16}\frac{M_p^2}{Q^2}\left(G_1^2 + F_1^2 + \tau F_2^2\right)$

An independent extraction of $\boldsymbol{\Delta s}$, which does not rely on the difficult measurements of the $\boldsymbol{g_1}$ structure function at very small $\boldsymbol{x}$ values, can be obtained from (anti)neutrino NC elastic scattering off protons, see Figure 5–32. Indeed, this process provides the most direct measurement of $\boldsymbol{\Delta s}$. The differential cross section for NC elastic and CC QE scattering of (anti)neutrinos from protons can be written as:

$$\boldsymbol{\frac{d\sigma}{dQ^2} = \frac{G_\mu^2}{2\pi}\frac{Q^2}{E_\nu^2}\left(A \pm BW + CW^2\right); \quad W = 4E_\nu/M_p - Q^2/M_p^2,} \tag{5.10}$$

where the positive (negative) sign is for (anti)neutrino scattering and the coefficients $\boldsymbol{A, B,}$ and $\boldsymbol{C}$ contain the vector and axial form factors as listed in Table 5–5.

The axial-vector form factor for NC scattering can be written as the sum of the known axial form factor G_A plus a strange form factor G_A^s:

$$G_1 = \left[-\frac{G_A}{2} + \frac{G_A^s}{2} \right], \tag{5.11}$$

while the NC vector form factors can be written as:

$$F_{1,2} = \left[\left(\frac{1}{2} - \sin^2\theta_W \right) \left(F_{1,2}^p - F_{1,2}^n \right) - \sin^2\theta_W \left(F_{1,2}^p + F_{1,2}^n \right) - \frac{1}{2} F_{1,2}^s \right], \tag{5.12}$$

where $F_1^{p(n)}$ is the Dirac form factor of the proton (neutron), $F_2^{p(n)}$ is the corresponding Pauli form factor, and $F_{1,2}^s$ are the strange vector form factors. These latter are expected to be small from the PVES measurements summarized above. In the limit $Q^2 \to 0$, the differential cross section is proportional to the square of the axial-vector form factor $d\sigma/dQ^2 \propto G_1^2$ and $G_A^s \to \Delta s$. The value of Δs can therefore be extracted experimentally by extrapolating the NC differential cross section to $Q^2 = 0$.

Previous neutrino scattering experiments have been limited by the statistics and by the systematic uncertainties on background subtraction. The only information available comes from the analysis of 951 NC νp and 776 NC $\bar{\nu} p$ collected by the experiment BNL E734. [45,46,47]. The LBNE neutrino beam will be sufficiently intense that a measurement of NC elastic scattering on proton in the fine-grained ND can provide a definitive statement on the contribution of the strange sea to either the axial or vector form factor.

Systematic uncertainties can be reduced by measuring the NC/CC ratios for both neutrinos and antineutrinos:

$$\mathcal{R}_{\nu p}(Q^2) \equiv \frac{\sigma(\nu_\mu p \to \nu_\mu p)}{\sigma(\nu_\mu n \to \mu^- p)}(Q^2); \qquad \mathcal{R}_{\bar{\nu} p}(Q^2) \equiv \frac{\sigma(\bar{\nu}_\mu p \to \bar{\nu}_\mu p)}{\sigma(\bar{\nu}_\mu p \to \mu^+ n)}(Q^2), \tag{5.13}$$

as a function of Q^2. Figure 5–32 shows the absolute sensitivity of both ratios to Δs for different values of Q^2. The sensitivity for $Q^2 \sim 0.25$ GeV^2 is about 1.2 for neutrinos and 1.9 for antineutrinos, which implies that a measurement of $\mathcal{R}_{\nu p}$ and $\mathcal{R}_{\bar{\nu} p}$ of 1% precision would enable the extraction of Δs with an uncertainty of 0.8% and 0.5%, respectively.

The design of HIRESMNU includes several different nuclear targets. Therefore, most of the neutrino scattering is from nucleons embedded in a nucleus, requiring nuclear effects to be taken into account. Fortunately, in the ratio of NC/CC the nuclear corrections are expected to largely cancel out. The Δs analysis requires a good proton reconstruction efficiency as well as high resolution on both the proton angle and energy. To this end, the low-density magnetized tracker at LBNE can increase the range of the protons inside the ND, allowing the reconstruction of proton tracks down to $Q^2 \sim 0.07$ GeV^2. This capability will reduce the uncertainties in the extrapolation of the form factors to the limit $Q^2 \to 0$.

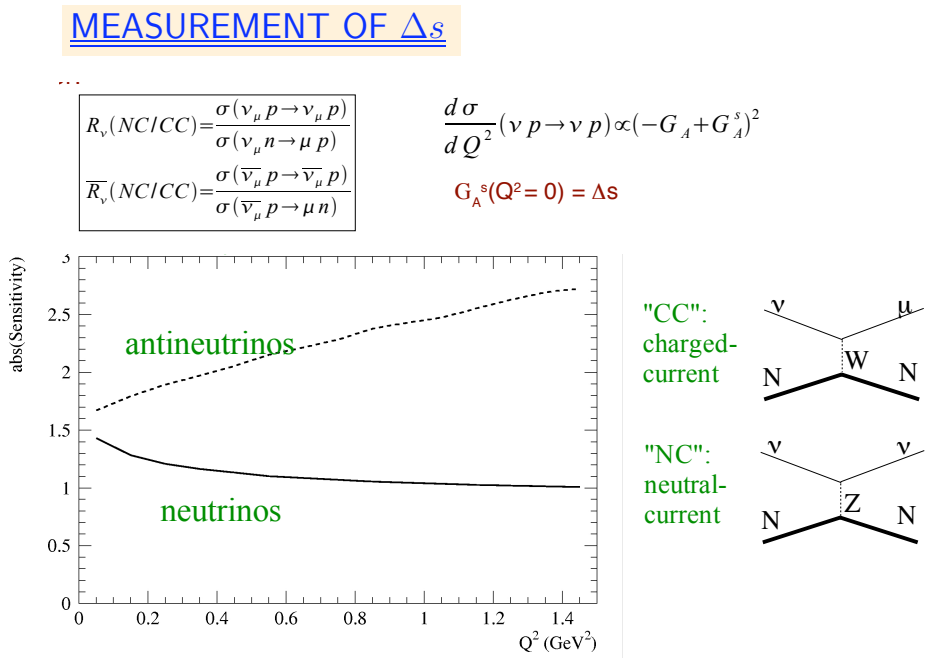

Figure 5–32: Absolute sensitivity of the ratios $\mathcal{R}_{\nu p}$ (solid) and $\mathcal{R}_{\bar{\nu}p}$ (dashed) to the strange contribution to the spin of the nucleon, Δs, as a function of Q^2.

Table 5–6 summarizes the expected proton range for the low-density ($\rho \sim 0.1\ g/cm^3$) STT. We expect about $1 \times 10^5\ \nu p(\bar{\nu}p)$ events after the selection cuts in the low-density tracker, yielding a statistical precision of the order of 0.3%.

Table 5–6: Expected proton range for the low density ($\rho \sim 0.1\ g/cm^3$) tracker. The first column gives the proton kinetic energy and the last column the proton momentum. The Q^2 value producing T_p is calculated assuming the struck nucleon was initially at rest.

T_p MeV	Q^2 GeV$^2/c^2$	Range STT cm	P_p GeV/c
20	0.038	4.2	0.195
40	0.075	14.5	0.277
60	0.113	30.3	0.341
80	0.150	50.8	0.395
100	0.188	75.7	0.445

We follow the analysis performed by the FINeSSE collaboration [48] and in the SciBooNE experiment for the determination of Δs. In particular, based upon the latter, with the scintillator tracker we expect a purity of about 50%, with background contributions of 20% from neutrons produced outside of the detector, 10% νn events and 10% NC pion backgrounds. The dominant systematic uncertainty will be related to the background subtraction. The low-energy beam spectrum at LBNE provides the best sensitivity for this measurement since the external background from neutron-induced proton recoils will be reduced by the strongly

suppressed high-energy tail. The low-density magnetized tracker is expected to increase the purity by reducing the neutron background and the NC pion background. We point out that the outside neutron background can be determined using the $n \rightarrow p + \pi^-$ process in the STT. In summary, we are believe that we can achieve a precision on Δs of about $0.02 - 0.03$. The sensitivity analysis is in progress.

5.19 Isospin Physics and Sum-Rules

One of the most compelling physics topics accessible to the HIRESMNU detector in the LBNE is the isospin physics using neutrino and antineutrino interactions. The salient topics are:

- Adler Sum Rule
- Tests of Isospin (Charge) Symmetry in Nucleons and Nuclei

The Adler sum rule relates the integrated difference of the antineutrino and neutrino F_2 to the isospin of the target:

$$\mathcal{S}_A(Q^2) = \int_0^1 dx \left[F_2^{\bar{\nu}}(x, Q^2) - F_2^{\nu}(x, Q^2)\right] / (2x) = 2\, I_z, \tag{5.14}$$

where the integration is performed over the entire kinematic range of the Bjorken variable x and I_z is the projection of the target isospin vector on the quantization axis (z axis). For the proton $\mathcal{S}_A^p = 1$ and for the neutron $\mathcal{S}_A^n = -1$.

In the quark parton model the Adler sum is the difference between the number of valence u and d quarks of the target. The Adler sum rule survives the strong interaction effects because of the conserved vector current (CVC) and provides an exact relation to test the local current commutator algebra of the weak hadronic current. We note that in the derivation of the Adler sum rule the effects of both non-conservation of the axial current and heavy quark production are neglected.

Experimental tests of the Adler sum rule require the use of a hydrogen target to avoid nuclear corrections to the bound nucleons inside nuclei. The structure functions $F_2^{\bar{\nu}}$ and F_2^{ν} have to be determined from the corresponding differential cross sections and must be extrapolated to small x values in order to evaluate the integral. The only test available is limited by the modest statistics and was performed in bubble chambers by the BEBC collaboration using about 9,000 $\bar{\nu}$ and 5,000 ν events collected on hydrogen [60].

The LBNE program can provide the first high precision test of the Adler sum rule. To this end, the use of the high-energy beam configuration, although not essential, would increase

the sensitivity allowing us to reach higher Q^2 values. Since the use of a liquid H_2 bubble chamber is excluded in the ND hall due to safety concerns, the (anti)neutrino interactions off a hydrogen target can only be extracted with a subtraction method from the composite materials of the ND targets. Using this technique to determine the position resolution in the location of the primary vertex is crucial to reducing systematic uncertainties. For this reason a precision test of the Adler sum rule can be only performed with the low-density magnetized ND.

Two different targets are used resulting in a fiducial hydrogen mass of about 1 tonne: the polypropylene $(C_3H_6)_n$ foils placed in front of the STT modules and pure carbon foils. The statistical subtraction increases the statistical uncertainty by a factor of four. With the LBNE fluxes from the standard exposure we would collect about 1×10^6 inclusive $\nu(\bar{\nu})$ CC events on the hydrogen target. This level of precision will open up the possibility of making new discoveries in the quark and hadron structure of the proton.

5.20 Nucleon Structure, Parton Distribution Functions, and QCD Studies

Precision measurements of (anti)neutrino structure functions and differential cross sections would directly affect the oscillation measurements by providing accurate simulation of neutrino interaction and offer an estimate of all background processes that are dependent upon the angular distribution of the outgoing particles in the FD. Furthermore, QCD analyses within the framework of global fits to extract parton distribution functions (PDF) by using the differential cross sections measured in ND data provide a crucial step by constraining systematic error in precision electroweak measurements not only in neutrino physics but also in hadron-collider measurements.

Under the rubric of nucleon-structure, the topics include:

- Measurement of Form Factors and Structure Functions
- QCD Analysis of Parton Distribution Functions
- d/u Parton Distribution Functions at Large x
- GLS Sum Rule and α_s
- Non-perturbative Contributions and High Twists
- Quark-hadron Duality
- Generalized Parton Distributions

For quantitative studies of inclusive deep-inelastic lepton-nucleon scattering, it is vital to have precise F_3 structure functions, which can only be measured with neutrino and antineutrino beams, as input into global PDF fits. Because it depends on weak axial quark charges, the F_3 structure function is unique in its ability to differentiate between the quark and antiquark content of the nucleon. On a proton target, for instance, the neutrino and antineutrino F_3 structure functions (at leading order in α_s) are given by

$$xF_3^{\nu p}(x) = 2x\left(d(x) - \bar{u}(x) + \bar{s}(x) + \cdots\right), \quad (5.15)$$

$$xF_3^{\bar{\nu} p}(x) = 2x\left(u(x) - \bar{d}(x) - \bar{s}(x) + \cdots\right). \quad (5.16)$$

In contrast, electromagnetic probes are sensitive only to a sum of quark and antiquark PDFs. Unfortunately, the neutrino scattering cross sections have considerably larger uncertainties than the electromagnetic inclusive cross sections at present. The proposed HIRESMNU offers a promise to reduce the gap between the uncertainties on the weak and electromagnetic structure functions, and would have a major impact on global PDF analyses.

Recent experiments at JLab have collected high-precision data on the individual F_1 and F_2 (or F_T and F_L) structure functions at large x from Rosenbluth-separated cross sections. This avoids the need for model-dependent assumptions about the ratio $R = \sigma_L/\sigma_T$ of the longitudinal to transverse cross sections in the extraction of the structure functions from the measured cross sections. Similar quality data on the individual F_T and F_L structure functions from neutrino scattering would be available from the ND at Fermilab to maximally complement and facilitate the flavor decomposition of these functions.

In addition to data in the DIS region, there is considerable interest in obtaining data at low Q^2 (down to $Q^2 \sim 1$ GeV^2) and low W ($W < 2$ GeV), to complement data from JLab. Unpolarized structure functions can be expressed in terms of powers of $1/Q^2$ (power corrections):

$$F_{2,T,3}(x, Q^2) = F_{2,T,3}^{\tau=2}(x, Q^2) + \frac{H_{2,T,3}^{\tau=4}(x)}{Q^2} + \frac{H_{2,T,3}^{\tau=6}(x)}{Q^4} + \ldots\ldots \quad (5.17)$$

where the first term ($\tau = 2$), expressed in terms of PDFs, represents the Leading Twist (LT), which describes the scattering off a free quark, and is responsible for the scaling of SF via perturbative QCD $\alpha_s(Q^2)$ corrections. The Higher Twist (HT) terms ($\tau = 4, 6$) reflect instead the strength of multi-parton correlations (qq and qg). The ND data at LBNE would allow a good separation of target mass and higher twist corrections, both of which are $1/Q^2$ suppressed at high Q^2, from leading twist contributions [53], [54].

Global PDF fits show that at large values of x ($x > 0.5 - 0.6$) the d quark distribution (or the d/u ratio) is very poorly determined. The main reason for this is the absence of free neutron targets. Because of the larger electric charge on the u quark than on the d, the electromagnetic proton F_2 structure function data provide strong constraints on the u quark distribution, but are relatively insensitive to the d quark distribution.

To constrain the d quark distribution a precise knowledge of the corresponding neutron F_2^n structure functions is required, which in practice is extracted from inclusive deuterium F_2 data. At large values of x the nuclear corrections in deuterium become large and, more importantly, strongly model-dependent, leading to large uncertainties on the resulting d quark distribution.

Several planned experiments at JLab with the energy upgraded 12 GeV beam will measure the d/u ratio up to $x \sim 0.85$ using several different method to minimize the nuclear corrections. One method will use semi-inclusive DIS from deuterium with a low-momentum ($|\vec{p}| < 100$ MeV) spectator proton detected in the backward center-of-mass hemisphere, to ensure scattering on an almost free neutron (the "BoNuS" experiment [59]). Preliminary results have confirmed the feasibility of this method at the current 6 GeV energies, and a proposal for the extension at 12 GeV has been approved.

Perhaps the cleanest and most direct method to determine the d/u ratio at large x is from neutrino and antineutrino DIS on hydrogen. Existing neutrino data on hydrogen have relatively large errors and do not extend beyond $x \sim 0.5$. A new measurement of neutrino and antineutrino DIS from *hydrogen* at LBNE with significantly improved uncertainties would therefore make an important discovery about the d/u behavior as $x \to 1$. This measurement might be possible with a statistical subtraction of pure-carbon from the hydro-carbon target with negligible systematic errors due to acceptance. To well complement the proposed JLab 12 GeV experiments, the kinematical reach would need to be up to $x \sim 0.85$ and with as large a Q^2 range as possible to control for higher twist and other sub-leading effects in $1/Q^2$.

5.21 Neutrino-Nuclear Interactions and Nuclear Effects

An integral part of the physics program envisioned in this proposal involves detailed measurements of (anti)neutrino interactions in a variety of nuclear targets. The standard target of the proposed ND is hydro-carbon, largely due to the mass of the the STT radiators. Among the additional nuclear targets, the most important is the argon-target which composes the LBNE FD. We propose to have argon gas in pressurized aluminium tubes with sufficient mass to provide $\simeq$5 times the ν_μ-CC and NC statistics as expected in the LBNE FD. Equally important nuclear targets are iron, which is used in the ICAL of INO, and carbon. Indeed the modularity of the STT provides for successive measurements using thin nuclear targets such as lead, calcium, etc. An arrangement of nuclear targets positioned upstream of the detector, as shown in Figure 4–2 and Figure 7–13, provides the desired sample in (anti)neutrino interactions. For example, a single 1-mm-thick Pb sheet, at the upstream end of the detector, will provide about 2×10^5 ν_μ-CC interactions in one year.

The topics in nuclear effects include the following studies:

- Nuclear Modifications of Form Factors
- Nuclear Modifications of Structure Functions
- Mechanisms for Nuclear Effects in Coherent and Incoherent Regimes
- A Dependence of Exclusive and Semi-exclusive Processes
- Effect of Final-State Interactions
- Effect of Short-Range Correlations
- Two-Body Currents

The study of nuclear effects in (anti)neutrino interactions off nuclei is directly relevant for the oscillation studies. The use of argon or iron in the LBNE FD requires a measurement of nuclear cross sections on the same targets in the ND. In addition to the different $\boldsymbol{p/n}$ ratio in argon or iron or water, nuclear modifications of cross sections can differ from 5% to 15% between oxygen and argon, while the difference in the final state interactions could be larger. Additionally, nuclear modifications can introduce a substantial smearing of the kinematic variables reconstructed from the observed final-state particles. Detailed measurements of the $\boldsymbol{A}$ dependence of different processes are then required in order to understand the absolute energy scale of neutrino events and to reduce the corresponding systematic uncertainties on the oscillation parameters.

Furthermore, an important question in nuclear physics is how the structure of a free nucleon is modified when said nucleon is inside a nuclear medium. Studies of the ratio of structure functions of nuclei to those of free nucleons (or in practice, the deuteron) reveal nontrivial deviations from unity as a function of $\boldsymbol{x}$ and $\boldsymbol{Q^2}$. These have been well explored in charged lepton scattering experiments, but little empirical information exist from neutrino scattering. Another reason to investigate the medium modifications of neutrino structure functions is that most neutrino scattering experiments are performed on nuclear targets, from which information on the free nucleon is inferred by performing a correction for the nuclear effects. In practice this often means applying the same nuclear correction as for the electromagnetic structure functions, which introduces an inherent model dependence in the result. In particular, significant differences between photon-induced and weak boson-induced nuclear structure functions are predicted, especially at low $\boldsymbol{Q^2}$ and low $\boldsymbol{x}$, which have not been tested. A striking example is offered by the ratio $\boldsymbol{R}$ of the longitudinal-to-transverse structure functions [58]. While the electromagnetic ratio tends to zero in the photoproduction limit, $\boldsymbol{Q^2 \to 0}$, by current conservation, the ratio for neutrino structure functions is predicted to be *finite* in this limit. Thus significant discovery potential exists in the study of neutrino scattering from nuclei. Finally, the extraction of (anti)neutrino interactions on deuterium from the statistical subtraction of H_2O from D_2O, which is required to measure the fluxes (Section 5.9), would allow the first direct measurement of nuclear effects in deuterium. This measurement can be achieved since the structure function of a free isoscalar

nucleon is given by the average of neutrino and antineutrino structure functions on hydrogen ($F_2^{\nu n} = F_2^{\bar{\nu} p}$). A precise determination of nuclear modifications of structure functions in deuterium would play a crucial role in reducing systematic uncertainties from the global PDF fits.

5.22 Search for Heavy Neutrinos

The most economic way to handle the problems of neutrino masses, dark matter and baryon asymmetry of the Universe in a unified way may be to add to the SM three Majorana singlet fermions with masses roughly on the order of the masses of known quarks and leptons. The appealing feature of this theory (called the νMSM for "Neutrino Minimal SM") is the fact that there every left-handed fermion has a right-handed counterpart, leading to an equal way of treating quarks and leptons. The lightest of the three new leptons is expected to have a mass from 1 keV to 50 keV and play the role of the dark matter particle. Two other neutral fermions are responsible for giving masses to ordinary neutrinos via the see-saw mechanism at the *electroweak scale* and for creation of the baryon asymmetry of the Universe (for a review see [84]). The masses of these particles and their coupling to ordinary leptons are constrained by particle physics experiments and cosmology. They should be almost degenerate, thus nearly forming Dirac fermions (this is coming from the requirement of successful baryogenesis). Different considerations indicate that their mass should be in $\mathcal{O}(1)$ GeV region [85].

The νMSM is described by the most general renormalizable Lagrangian containing all the particles of the SM and three singlet fermions. For the purpose of the present discussion we take away from it the lightest singlet fermion N_1 (the "dark matter sterile neutrino"), which is coupled extremely weakly to the ordinary leptons. In addition, we take N_2 and N_3 degenerate in mass, $M_2 = M_3 = M$. Then the convenient parametrization of the interaction of $N's$ with the leptons of SM is:

$$L_{\text{singlet}} = \left(\frac{\kappa M m_{atm}}{v^2}\right)^{\frac{1}{2}} \left[\frac{1}{\sqrt{\epsilon e^{i\eta}}} \bar{L}_2 N_2 + \sqrt{\epsilon e^{i\eta}} \bar{L}_3 N_3\right] \tilde{H} - M \bar{N_2}^c N_3 + \text{h.c.}\,, \quad (5.18)$$

where L_2 and L_3 are the combinations of L_e, L_μ and L_τ

$$L_2 = \sum_\alpha x_\alpha L_\alpha\,, \qquad L_3 = \sum_\alpha y_\alpha L_\alpha\,. \quad (5.19)$$

with $\sum_\alpha |x_\alpha|^2 = \sum_\alpha |y_\alpha|^2 = 1$.

In Equation (5.18) $v = 246$ GeV is the vacuum expectation value of the Higgs field H, $\tilde{H}_i = \epsilon_{if} H_j^*$, $m_{atm} \simeq 0.05$ eV is the atmospheric neutrino mass difference, and $\kappa = 1$ (2) for normal (inverted) hierarchy of neutrino masses. The x_α and y_α can be expressed through the parameters of the active neutrino-mixing matrix (explicit relations can be found in [85]).

The parameter ϵ (by definition, $\epsilon < 1$) and the CP-breaking phase η cannot be fixed by using neutrino masses and mixings.

If the mass of N is fixed, smaller ϵ yields stronger interactions of singlet fermions to the SM leptons. This would have led to equilibration of these particles in the early Universe above the electroweak temperatures, and, therefore, to erasing of the baryon asymmetry. In other words, the mixing angle U^2 between neutral leptons and active neutrinos must be small, explaining why these new particles have not been seen previously. For small ϵ,

$$U^2 = \frac{\kappa m_{atm}}{4M\epsilon} \ . \tag{5.20}$$

The most efficient mechanism of sterile neutrino production is through weak decays of heavy mesons and baryons, as can be seen from the left panel of Figure 5–33, showing some examples of relevant two- and three-body decays. Heavy mesons can be produced by energetic protons scattering off the target material.

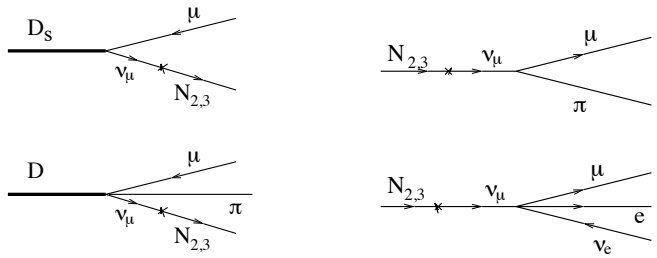

Figure 5–33: Left panel: Feynman diagrams of meson decays producing heavy sterile neutrinos. Right panel: Feynman diagrams of sterile neutrino decays.

Several experiments have conducted searches for heavy neutrinos, for example BEBC [86], CHARM [87], NuTeV [88] and the CERN PS191 experiment [89,90] (see also discussion of different experiments in [91]. In the search for heavy neutrinos, the strength of the proposed high-resolution ND, compared to earlier experiments, lies in reconstructing the exclusive decay modes including electronic, hadronic and muonic. Furthermore, the detector offers a means to constrain and measure the backgrounds using control samples. Preliminary investigations suggest that HIRESMNU will have an order of magnitude higher sensitivity in exclusive channels than previous experiments. We are actively advancing the sensitivity evaluation.

5.23 Search for Non-Standard Interactions: High Δm^2 Neutrino Oscillations

The evidence for neutrino oscillations obtained from atmospheric, long-baseline accelerator, solar and long-baseline reactor data from different experiments consistently indicates two different scales with $\boldsymbol{\Delta m^2_{32} \sim 2.4 \times 10^{-3}}$ eV^2 defining the atmospheric oscillations and $\boldsymbol{\Delta m^2_{21} \sim 7.9^{-5}}$ eV^2 defining the solar oscillations. The only way to accommodate oscillations with relatively high $\boldsymbol{\Delta m^2}$ at the eV^2 scale is therefore to add one or more sterile neutrinos to the conventional three light neutrinos.

Recently, the MiniBooNE experiment reported that their antineutrino data might be consistent with the LSND $\boldsymbol{\bar{\nu}_\mu \rightarrow \bar{\nu}_e}$ oscillation with $\boldsymbol{\Delta m^2 \sim}$ eV^2 [93]. Contrary to the antineutrino data, the MiniBooNE neutrino data seem to exclude high $\boldsymbol{\Delta m^2}$ oscillations, possibly indicating a a different behavior between neutrinos and antineutrinos.

Models with five (3+2) or six (3+3) neutrinos can potentially explain the MiniBooNE results. In addition to the cluster of the three neutrino mass states accounting for "solar" and "atmospheri" mass splitting two (or three) states at the eV scale are added, with a small admixture of $\boldsymbol{\nu_e}$ and $\boldsymbol{\nu_\mu}$ to account for the LSND signal. One distinct prediction from such models is a significant probability for $\boldsymbol{\bar{\nu}_\mu}$ disappearance into sterile neutrinos, of the order of 10%, in addition to the small probability for $\boldsymbol{\bar{\nu}_e}$ appearance.

Since the ND at LBNE is located at a baseline of 460 m and uses the LE beam, it can reach the same value $\boldsymbol{L/E_\nu \sim 1}$ of MiniBooNE and LSND. The large fluxes and the availability of fine-grained detectors make the LBNE program well suited to search for oscillations at the eV^2 scale. Due to the potential differences between neutrinos and antineutrinos four possibilities have to be considered in the analysis: $\boldsymbol{\nu_\mu}$ disappearance, $\boldsymbol{\bar{\nu}_\mu}$ disappearance, $\boldsymbol{\nu_e}$ appearance and $\boldsymbol{\bar{\nu}_e}$ appearance. As discussed in Section 5.10.2, the search for high $\boldsymbol{\Delta m^2}$ oscillations has to be performed simultaneously with the in situ determination of the fluxes.

To this end, we need to obtain an independent prediction of the $\boldsymbol{\nu_e}$ and $\boldsymbol{\bar{\nu}_e}$ fluxes starting from the measured $\boldsymbol{\nu_\mu}$ and $\boldsymbol{\bar{\nu}_\mu}$ CC distributions since the $\boldsymbol{\nu_e}$ and $\boldsymbol{\bar{\nu}_e}$ CC distributions could be distorted by the appearance signal. The low-$\boldsymbol{\nu_0}$ method can provide such predictions if external measurements for the $\boldsymbol{K^0_L}$ component are available from hadro-production experiments (Section 5.10.1).

We will follow an iterative procedure:

1. Extract the fluxes from $\boldsymbol{\nu_\mu}$ and $\boldsymbol{\bar{\nu}_\mu}$ CC distributions assuming no oscillations are present
2. Comparison with data and determination of oscillation parameters (if any)
3. New flux extraction after subtraction of the oscillation effect

4. Iterate until convergence

The analysis has to be performed separately for neutrinos and antineutrinos due to potential CP or CPT violation according to MiniBooNE/LSND data.

We measure the ratio of electron-to-muon CC events:

$$\mathcal{R}_{e\mu}(L/E) \equiv \frac{\#\ of\ \nu_e N \to e^- X}{\#\ of\ \nu_\mu N \to \mu^- X}(L/E); \qquad \bar{\mathcal{R}}_{e\mu}(L/E) \equiv \frac{\#\ of\ \bar{\nu}_e N \to e^+ X}{\#\ of\ \bar{\nu}_\mu N \to \mu^+ X}(L/E) \tag{5.21}$$

which is then compared with the predictions obtained from the low-ν_0 method. Deviations of $\mathcal{R}_{e\mu}$ or $\bar{\mathcal{R}}_{e\mu}$ from the expectations as a function of L/E would provide evidence for oscillations. It must be noted that this procedure only provides a relative measurement of $\nu_e(\bar{\nu}_e)$ vs. $\nu_\mu(\bar{\nu}_\mu)$. Actually, since the fluxes are extracted from the observed ν_μ and $\bar{\nu}_\mu$ CC distributions, an analysis of the $\mathcal{R}_{e\mu}(\bar{\mathcal{R}}_{e\mu})$ ratio cannot distinguish between $\nu_\mu(\bar{\nu}_\mu)$ disappearance and $\nu_e(\bar{\nu}_e)$ appearance.

The process of NC elastic scattering off protons (Section 5.18) can provide the complementary measurement needed to disentangle the two hypotheses of $\nu_\mu(\bar{\nu}_\mu)$ disappearance into sterile neutrinos and $\nu_e(\bar{\nu}_e)$ appearance. In order to cancel systematic uncertainties, we will measure the NC/CC ratio with respect to quasi-elastic scattering:

$$\mathcal{R}_{NC}(L/E) \equiv \frac{\#\ of\ \nu p \to \nu p}{\#\ of\ \nu_\mu n \to \mu^- p}(L/E); \qquad \bar{\mathcal{R}}_{NC}(L/E) \equiv \frac{\#\ of\ \bar{\nu} p \to \bar{\nu} p}{\#\ of\ \bar{\nu}_\mu p \to \mu^+ n}(L/E) \tag{5.22}$$

We can reconstruct the neutrino energy from the proton angle and momentum under the assumption of neglecting the nuclear smearing (the same for the neutrino CC sample). In the oscillation analysis we are only interested in relative distortions of the ratio $\mathcal{R}_{NC}(\bar{\mathcal{R}}_{NC})$ as a function of L/E and not in the absolute values of the ratios. For $Q^2 > 0.2$ GeV^2 the relative shape of the total cross sections is not very sensitive to the details of the form factors. To improve the energy resolution we can use events originating from the deuterium inside the D_2O target embedded into the fine-grained tracker.

An improved oscillation analysis is based on a simultaneous fit to both $\mathcal{R}_{e\mu}(\bar{\mathcal{R}}_{e\mu})$ and $\mathcal{R}_{NC}(\bar{\mathcal{R}}_{NC})$. The first ratio provides a measurement of the oscillation parameters while the latter constrains the $\nu_e(\bar{\nu}_e)$ appearance vs. the $\nu_\mu(\bar{\nu}_\mu)$ disappearance. This analysis results in two main requirements for the ND:

- e^+/e^- separation to provide an unambiguous check of the different behavior between neutrinos and antineutrinos suggested by MiniBooNE
- Accurate reconstruction of proton momentum and angle

In order to validate the unfolding of the high $\boldsymbol{\Delta m^2}$ oscillations from the in situ extraction of the (anti)neutrino flux, we would also need to change the beam conditions, since the ND cannot be easily moved. To this end, it will be important to have the possibility of a short run with a high energy beam and to change/switch off the beam focusing system.

6 The R&D Plans for Near Detector

This chapter presents the R&D plans for the HIRESMNU proposal. The R&D work will involve (a) detailed simulation studies aimed at quantifying subdetector parameters and choices, (b) building small prototypes of STT and ECAL subdetectors and using them to conduct calibration measurements using known particles of precise momenta at a test beam facility at Fermilab or CERN, and (c) building one-module prototypes of the full-scale STT, ECAL and muon-ID detectors. The anticipated time scale for the R&D work is about five years, of which the last two years will be increasingly devoted to streamlining the M&S procurement and setting up the fabrication facilities.

6.1 Simulation Studies

We need a detailed GEANT4-based simulation of the proposed detector to examine various options and alternatives, and to evaluate the physics sensitivity for various oscillation and precision-measurement topics. The principal tasks include the following:

- **Configuring the GEANT4 Simulation Package:** Set up the geometry of the STT, the ECAL, the magnetic field model of the dipole magnet and the muon-ID detector.
- **Generating Simulation Samples:** Generate sets of exclusive and inclusive CC and NC events for all four species of neutrinos. The MC data will be produced in a format agreed to by all, and disseminated to the group. It will provide an excellent initiation for young students and post-docs.
- **Determining Data Framework:** Determine the framework and format for the data files. Establish broad principles for conducting various analyses.
- **Analysis of Simulation Samples:** Conduct analysis of the MC samples to reach a refined sensitivity to various processes, in particular $\boldsymbol{\nu_\mu}(\boldsymbol{\bar{\nu}_\mu})$-QE, $\boldsymbol{\nu_\mu}$-Res, inclusive $\boldsymbol{\nu_e}$ $(\boldsymbol{\bar{\nu}_e})$ CC, $\boldsymbol{\pi^0}$-reconstruction, NC events and neutrino $\boldsymbol{\nu s}$ antineutrino interactions. For analysis, we will use existing neutrino data to cross-check and calibrate our simulation results.

- **Simulating Salient Options and Alternatives:** Quantify the effects of different STT and ECAL parameters, the two critical detectors in HIRESMNU.

The duration of the simulation studies will be about two years. The deliverable will be a firm defense of the projected sensitivities and the subdetector parameters of HIRESMNU. It is anticipated that in 1.5 years, this project will be externally reviewed. Post-review, our group's effort will be focused on building the prototypes for the STT and ECAL.

6.2 R&D for the Straw Tube Tracker

Having optimized the detector parameters and established consensus within the collaboration, we plan to build a prototype straw tube tracker (STT) module. We envision undertaking this task in the second year of this proposal. As argued in earlier chapters, the STT technology is well established and our model closely resembles those of the ATLAS and COMPASS experiments, currently in operation at CERN.

The STT prototype is intended to test and optimize the actual module design and the readout chain for HIRESMNU, and to measure the corresponding performance in terms of tracking capability and particle identification. We plan to calibrate the STT prototype to a beam of electrons, muons, pions and protons of well known momenta at either Fermilab's or CERN's test beam facility. This prototype will have a smaller transverse dimension, 1.8 m $\times$ 1.8 m, but otherwise it will follow the specifications of the full STT. We plan to build four STT modules, each composed by a double layer of straws, a radiator module and the electronic readout. The arrangement will provide a total of eight space-points, sufficient to to reconstruct track parameters. We anticipate that this STT R&D work will take three years from the start date.

Another goal of the STT R&D is to build one full-size module, equip it with $Xe/CO_{\mathbf{2}}$ gas, and operate it with cosmic-ray muons. The task will include engineering design of the tracker, radiator and readout electronics for STT. We propose to establish, follow and debug the complete set of steps for full-scale STT module construction in order to understand and overcome any issues that arise, set up the M&S procurement chain, and establish the production factory or factories. We plan to undertake this task in the last year and a half of the allotted 3 years. The total budget for the design work is about \$600 k; the full-scale prototype is estimated at \$800 k.

6.3 R&D for the Electromagnetic Calorimeter

The R&D work for the ECAL follows steps very similar to the STT. We propose to build a small DS-ECAL module, 1.5 m $\times$ 1.5 m across, and about 10 $\boldsymbol{X_0}$ deep. The module will be calibrated in a test beam. The total cost of ECAL prototype is estimated to be \$780 k which includes engineering design (\$190 k), procurement & construction (\$490 k) and test-beam exposure (\$100 k).

6.4 R&D for the Muon-ID Detector

The R&D work for the muon-ID detector is less demanding. There is no need for test-beam exposure. We propose to build two full-size modules of RPCs and conduct measurements using cosmic rays. The cost for this R&D work is about \$680 k.

6.5 Prototyping

The duration for the construction and calibration of the prototypes of the STT, ECAL, and muon-ID detectors will be about three years, after the simulation studies and the ND review have concluded. A most important task associated with R&D is the calibration of the small STT and ECAL modules in a test beam of particles, including electron, muon, charged pion, neutral pion, and proton, of well defined momenta at Fermilab or CERN. In addition, one full-size module of each of the three subdetectors will be built at the production site in India. The prototypes will have the same specification as the complete detector.

7 Near Detector Fabrication and Manufacturing Infrastructure

We present the steps involved in the fabrication of the subdetectors. The required laboratories and associated infrastructure are described.

7.1 Fabrication of the Straw Tube Tracker

7.1.1 Fabrication Steps

The construction of the straw tube tracker (STT) will proceed in the following steps:

- **Procure Kapton films for the straw construction:** The plastic films will be bought from industry, for example, DuPont. The material is 40 μm thick carbon-loaded Kapton film 160XC370 for the inner foil and 25 μm thick aluminium-laminated Kapton film 100HN for the outer foil of the straw tubes. Alternatively, the same Kapton 100HN ($\mathbf{25}\mu m$ thick) could be used for both the inner and outer foils, as in the ATLAS TRT. In this case, the inner foil must be Aluminum-laminated and coated with carbon during the manufacturing process of the straws to provide electrical conductivity.

- **Lamination of the plastic films into straws:** The inner and outer Kapton foils are laminated and reinforced externally with carbon fiber bundles. The straws will be molded by Lamina Dielectrics Ltd (UK), which is the same factory used for the ATLAS TRT. The straws have an inner diameter of 9.53 mm and an outer diameter of 9.7 mm. This is a highly specialized and critical procedure and we lean toward this option.

- **Procure wires, end-plugs, spacers, pins, connectors, etc.:** The materials needed to complete the straw assembly and to make them electrically functional will be bought from different sources. The gold-plated tungsten wires (30 μm diameter) must not have deviations from wire diameter and circularity greater than 1% and 2% respectively. The wire can be bought from Toshiba, in Japan, as was done for the ATLAS TRT. All the

small parts including end-plugs, spacers to support the wire internally, crimping pins for the wire, HV and readout connectors can be bought in the US.

- **Complete assembly of the straws:** The straws produced by Lamina Dielectrics Ltd are basically empty Kapton tubes that have not yet been cut to their final length. They must be cut and assembled to form the complete straw tubes at the production sites. The first step is to pre-cut the straws to the approximate length needed and test them for inner-surface conductivity. After that the plastic end-plugs are glued to the straws. These provide electric insulation of the straws from the support frame, the gas distribution into the straw, the wire attachment and the attachment of the straw to the support frame. The final step to get the precise straw length is to cut the outer end-plug.

- **Quality control of the straws:** The fully equipped straws must pass through several quality tests. First each is checked for gas leaks. Then they are simultaneously checked for straightness and proper length with a CCD camera moving along the straw, which will be rotating on its axis. Finally, visual inspection checks will be conducted on each straw for any damage, bubbles in glued parts, excess glue, etc.

- **Connecting and insulating straws:** The next step is to add the connecting elements to the straws. These elements include three types of end pieces, namely the inner insulation socket, the outer insulation socket and high voltage connector, all made of precision plastic parts. The connecting plastic elements of the detector must be manufactured to a precision of tens of microns.

- **Procure the mechanical frames of the modules:** Two support bars are the key elements of the mechanical strucure of the STT modules. In order to achieve the required position accuracy and lightness of weight, the support bars are made of Carbon Fiber Reinforced Plastic (CFRP) with specific tolerances of tens of microns. The CFRP provides low mass, good mechanical strength and low gas permeability. The bar matrix is made of epoxy resin that must have a low coefficient of thermal expansion ($\leq \mathbf{4} \times \mathbf{10^{-6}}$) and a polymerization degree $\geq \mathbf{95\%}$. The CFRP bars are electrically conductive and should be at ground potential. Because the bars have a direct capacitance coupling to the signal connectors of the straws, it is necessary to make a low-impedance electrical connection between the bars and the detector-signal return ground. This connection is made by gluing special contact pins into holes drilled in the bars. The CFRP bars will be industrially produced and must undergo quality controls before shipping. The following measurements are required:

    - bar dimensions
    - bar deflection under load
    - percentage amount of fibers and resin in the bar material
    - Young's modulus under traction and bending

- coefficient of thermal expansion
- visual inspection

The support bars delivered to the assembly sites shall pass through Input Quality Control procedures at each site for bar flatness, dimensions, hole diameter, bar deflection and visual inspection.

The CFRP bars are inserted into external mechanical frames that provide the overall mechanical structure for the STT modules. These frames can be made of either aluminum or carbon fiber and are produced industrially with the required specifications. The frames undergo the same quality controls as the CFRP bars both before leaving the factory and at the production assembly sites.

- **Assembly of the straws into STT modules:** Assembly requires flat ($< \mathbf{200}\ \boldsymbol{\mu}$m) tables with precision holes (better than $\mathbf{100}\ \boldsymbol{\mu}$m) to position the various items during assembly. The precision of the overall assembly is defined by the precision of these holes, the flatness of the assembly tables, the precision of the tooling used to fix the STT modules to the table and by environmental factors such as temperature and humidity. Each component, either received from a manufacturer or produced in-house, has to be checked for conformance to specifications and cleaned before assembly. Furthermore, quality control has to be performed after each step of the assembly.

  The STT module assembly starts with the installation of the CFRP support bars on the precision assembly table. The bars are installed using precisely positioned tooling rods connecting the two bars. Particular care has to be taken for the alignment of the holes in the bars, since the accuracy and precision of the positioning will determine the straightness of the straws once they are inserted into the bars.

  The straws are then inserted through the holes in the top bar towards the bottom bar. Each straw must be inspected after insertion, both visually and using optical tools. Bent straws are replaced before gluing. After the installation and the straightness inspection of the first plane of straws, the straws in that plane are glued into position. After glue polymerization, which takes 24 hours, another plane of straws is inserted and glued to the previous plane. The reinforced straws themselves become part of the mechanical structure of the STT module. Each STT module contains 1,408 straws, divided into four layers of 352 straws each (XX and YY). Figure 7–1 shows one layer of the straw tubes.

  After gluing all the straw planes the assembled STT layers can be removed from the assembly table using custom transfer tools. The transfer tooling shall maintain the flatness of the partially assembled STT modules and allow a high-precision smooth lift from one assembly table to another. The STT double layers are moved to a second flat table on which the external mechanical frame is positioned. The STT double layers are then inserted into the mechanical frame and glued to the frame. The mechanical frames are designed to lock the support bars and are fixed by screws.

  Finally, the internal anode wires are installed and fastened by crimp tubes on both sides. A wire tension of about 90 g is expected to be appropriate. Because of the large

number of wires needed, a special wiring machine has to be used. The basic working principle of the wiring machine is to float the anode wire in a moving stream of air along the axis of the straw. After wiring, a global wire-tension measurement has to be performed to identify and replace wires with a tension below specification.

A series of preliminary engineering drawings depict the STT module fabrication steps: Figure 7–1, Figure 7–2, Figure 7–3, Figure 7–4 and Figure 7–6. Figure 7–5 shows the gluing and sealing of the straw tubes in a layer.

- **Procure radiators:** Radiators are stacks of alternating 37 layers of thin plastic film and separated by 36 sheets of a tulle fabric spacer. The radiator foils are made of commercially available polypropylene film of **15** μm thickness and are perforated with one 2 mm$^{\mathbf{2}}$ hole per 100 cm$^{\mathbf{2}}$ of film, in order to breathe easily in response to pressure or composition changes of the environmental gas. A synthetic net (tulle fabric) is used as spacer between successive film layers. The tulle fabric layer is made from multi-fiber threads composed of 22 dtex polyamid fibers and is characterized by a mesh size of 6 mm $\times$ 7 mm and a density of $\sim$ 2 g/m$^{\mathbf{2}}$. The average spacing between films provided by the tulle is 250 μm. Both polypropylene films and tulle fabric can be bought commercially in large rolls.

- **Assembly of the radiators/target in the STT modules:** The stacks of 37 radiator foils and 36 spacers can be pre-assembled by the industrial contractor. All foils and spacers are first cut into the required size of the STT modules and then stacked together by pinning them in their locating holes on a flat table. The tulle fabric has to be stretched during the assembly. A laser telemeter mounted on a rotating arm must be used to measure the thickness of the radiatior stacks in different points along the surface. During storage and transport the radiators must be attached to a flat, semi-rigid support plate with pins inserted in all the locating holes in order to accurately maintain their proper geometry at all times.

  Radiators are mounted at both sides of each STT module at the production sites. The radiator stacks are in contact with the straws and are kept in place by locating pins in the external frame of the STT module, which are inserted in the corresponding mounting holes located 10 mm inwards from the outer perimeter of the radiators. For the STT modules requiring nuclear targets, the radiator section in front of the STT module is replaced by the corresponding nuclear target.

- **Procure the readout board:** The active STT board (STTB) is the interface between the straws on one side and the readout electronics and high voltage on the other side. The active STTB is a printed circuit board consisting of two flex Kapton multi-layers sandwiched between two rigid printed FR-4 boards. A single board connects 64 straws to their readout channels and supplies two groups of 32 straws with the necessary high voltage. Overall there are 22 STTBs in each STT module. The main parts of the STTB are a baseplate containing HV protection capacitors, HV connectors and fuses, three flaps each containing protection resistors and a connector, and finally two Kapton flex parts for signal and HV connection. The STTBs will be developed by a participating

academic/research institution in collaboration with an industrial contractor who will produce the final STTBs for the detector construction.

In addition to the standard quality control steps at the production company, the reliability and quality of the bare STTBs are subject to quality controls at the production sites for: geometry and mechanical tolerances, and mechanical stability of the multilayers. In addition there will be visual inspection of the flexible layers and samples tested to withstand multiple bends of the flexible Kapton flaps, all foils and connectors tested for conductivity and connectivity. HV lines must withstand 3,000 V with respect to ground with current $< \mathbf{1}$ nA.

- **Assembly of the readout board:** After quality tests the the flex-rigid printed circuit boards (STTB) are glued to the top CFRP support bar holding the straws. To glue the STTBs, they must first be vacuum-clamped to a special assembly table. Then the resin is applied to the STTBs and the STT module is lifted onto the active STTBs using the transfer tooling. After a period of 24 hours the vacuum pump is switched off and the STT module can be moved. The quality of the glue joints must be inspected and faulty glue joints must be repaired with additional resin.

  Figure 7–7, Figure 7–8, and Figure 7–9 picture the front-end, HV board and the connector boards for the STT module.

- **Acceptance tests for the STT modules:** After the assembly, the STT modules have to pass a number of quality controls and strict acceptance tests both at the production sites and at the installation site(Fermilab) before the final installation in the ND hall. First a visual inspection of the STT modules is performed. All critical dimensions of the STT modules are then checked and compared to the specifications.

  • Because the wire tension is critical for the stability of the straw operation, the wire tension has to be measured at each step to ensure that no major tension loss has occurred due to slippage of the wire inside the crimping pin, partially inserted HV plugs, transportation, measuring errors during the STT assembly or other factors. The wire tension is measured by applying a potential ($\sim \mathbf{500}$ V) between the anode and the cathode, then vibrating or mechanically shocking the whole detector to set the anode wire vibrating. The tension can be determined from the resulting resonance curves.

  • The gas tightness test of the assembled STT modules is carried out by measuring the pressure drop in the closed detector gas volume filled with argon 20 mbar over atmosphere for a few hours. Internal pressure, atmospheric pressure and temperature are recorded during the gas-tightness test. The leak rate can be evaluated by fitting the pressure-drop trend measured. In order to avoid substantial losses of the expensive $\boldsymbol{Xe}$ gas we require that the leak rate be limited to 1 mbar/min/bar.

  • A short-term high-voltage test already would have been performed during the assembly of the STT modules with straws filled with $CO_{\mathbf{2}}$, to detect leakage currents or shorts. A six-day long high-voltage test is then performed to identify faulty channels (discharge or large leakage current) in an active gas mixture of $Ar/CO_{\mathbf{2}}$ at a higher

voltage ($\sim$ **1500** V). During the long-term high-voltage test the current and the number of electrical trips are monitored. In the case of large currents or repeated trips on a particular high voltage channel, that channel is investigated to identify the faulty straw.

- The final test is the straw straightness measurement. Uniform gas gain along the straw tube is important for the safety of the detector and for optimal performance. We need to check for possible deformations of the straws that show up as non-straightness along the length, non-circularity in diameter or wire offset from the axis of the straw. The measurement of the gas gain along the straws and of the wire offset with respect to its nominal position within the straw are the most critical tests for acceptance.

We will decide upon a primary production center(s) for the STT modules. To this end India will benefit from the technical collaboration with the JINR laboratory in Dubna, Russia, which was one of the production centers for both the ATLAS TRT detector and the COMPASS straw tracker. The JINR laboratory in Dubna, Russia, one of the production centers for both the ATLAS TRT detector and the COMPASS straw tracker, has agreed to collaborate and provide technical expertise.

Although an exacting detector, it must be emphasized that the STT technology does not require any major R&D since it is well tested technology as evidenced by the operational ATLAS-TRT and COMPASS detectors. An additional production site for the STT modules would be useful to reduce the time required for the construction of the STT. Furthermore, specific items like the readout electronics, the gas circulating system and the cooling system can be allocated to different institutions. Based on the ATLAS experience we expect to complete the STT construction, testing and installation in a period of about four years.

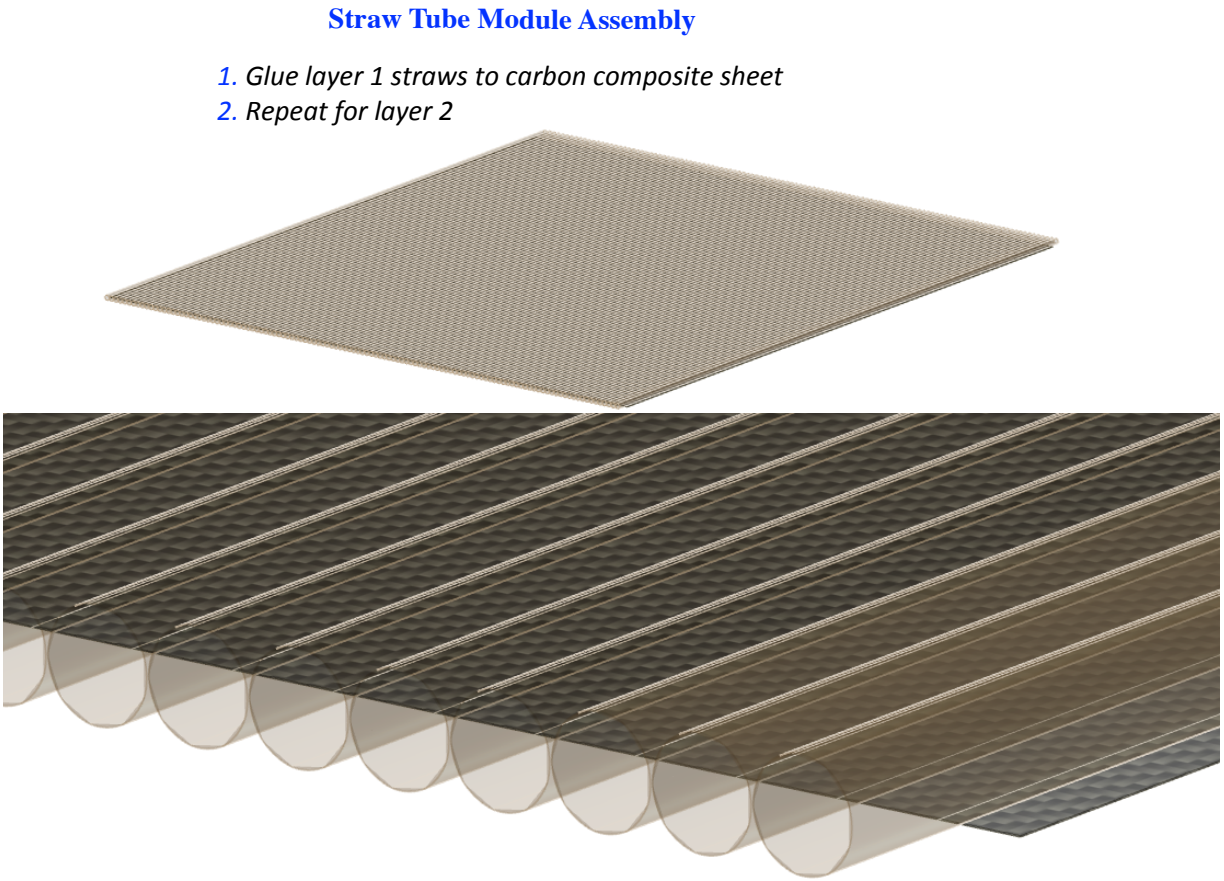

Figure 7–1: Preliminary engineering drawing of Straw Tube Tracker Module Assembly: Steps 1 and 2.

3. *Glue carbon composite ends A to layer 1*

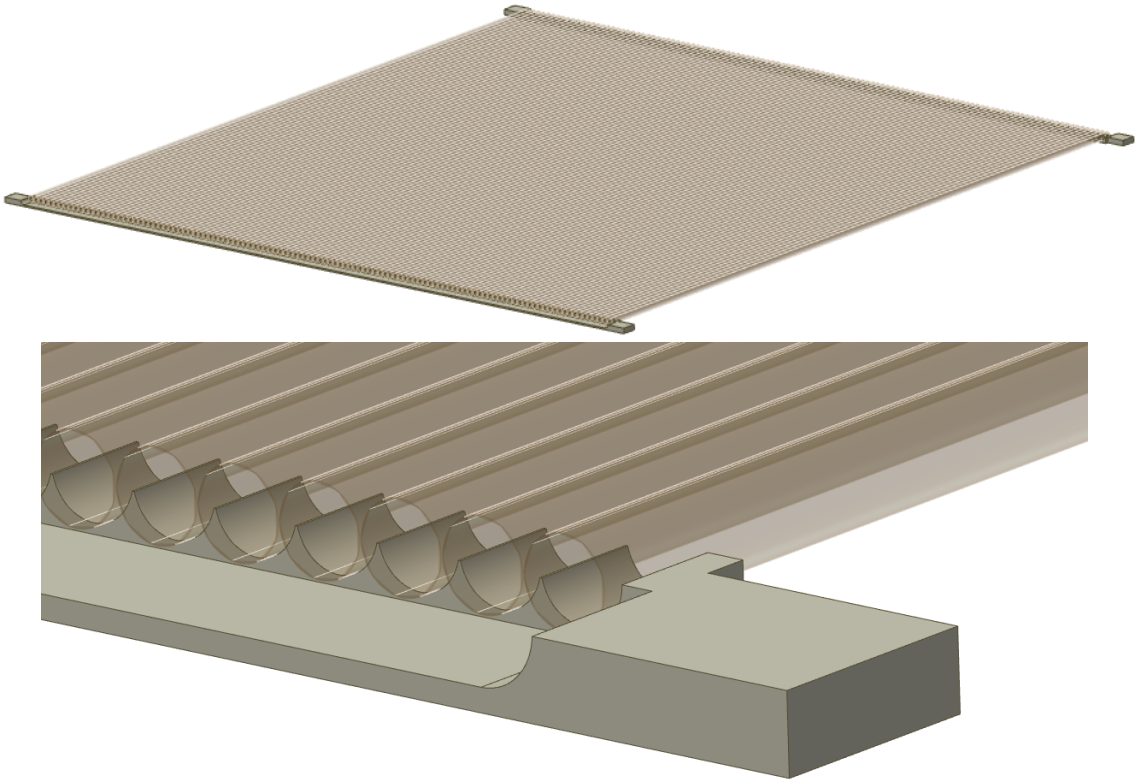

Figure 7–2: (Preliminary engineering drawing) Straw Tube Tracker Module Assembly: Step 3.

4. Repeat for layer 2 and ends B

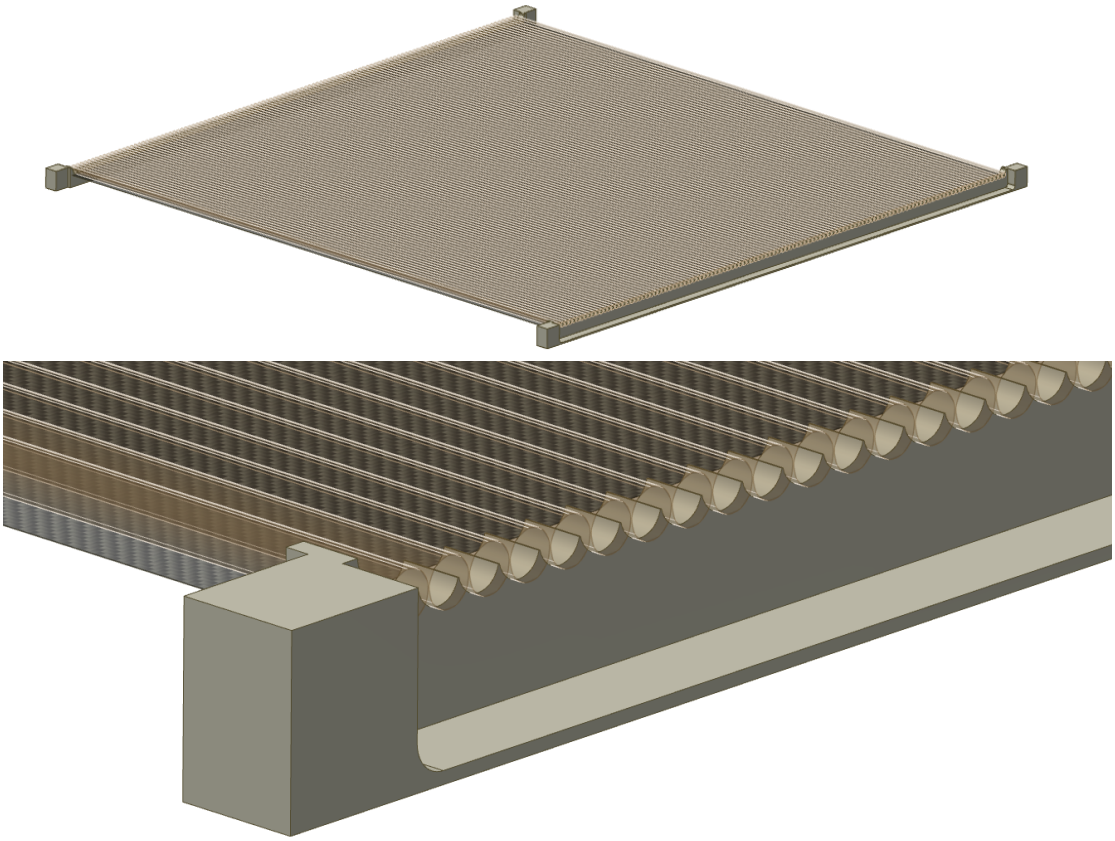

Figure 7–3: Straw Tube Tracker Module Assembly: Step 4.

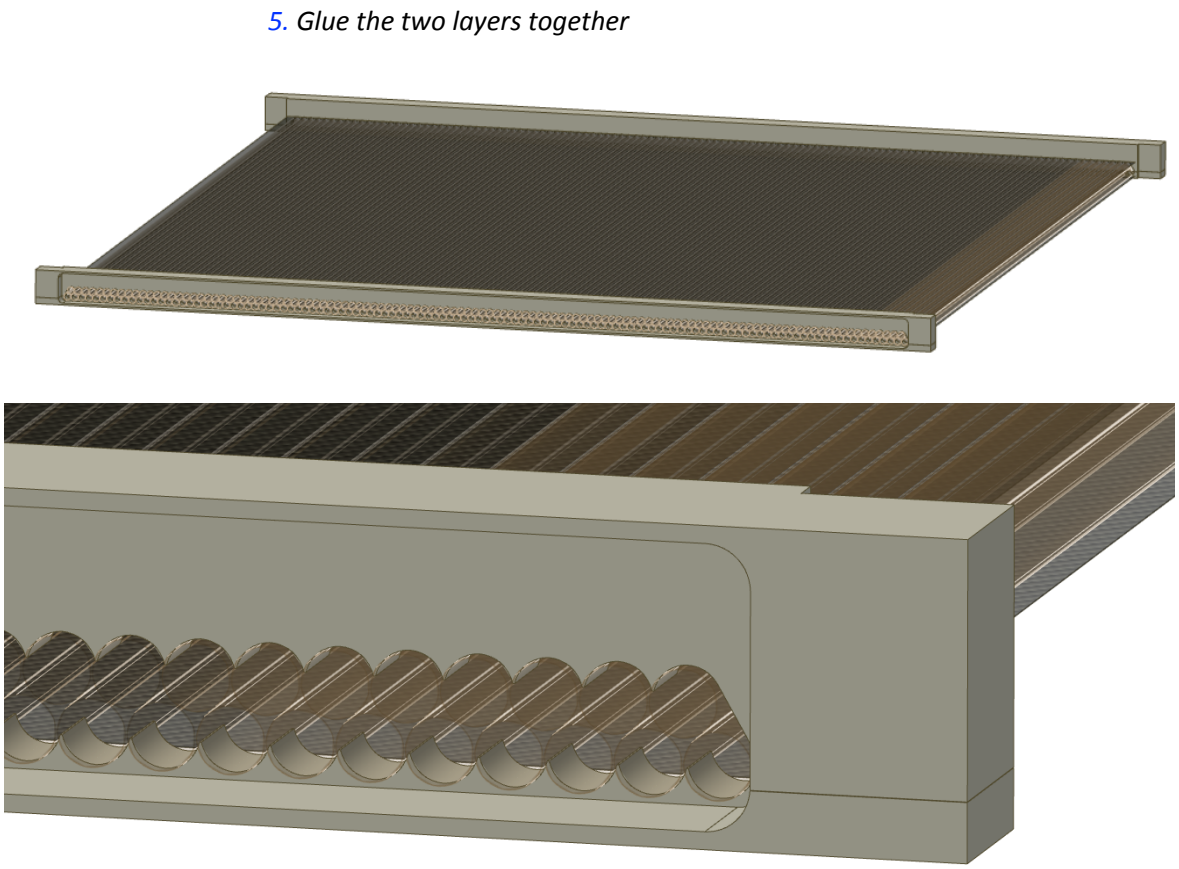

Figure 7–4: Straw Tube Tracker Module Assembly: Step 5.

We conclude this section with engineering drawings illustrating the steps involved in the assembly of the STT modules, which will be done at Fermilab. Preliminary engineering drawings show the full STT assembly in See Figure 7–11 and Figure 7–12.

7.1.2 Nuclear Targets

Instrumenting solid targets made of Fe, Ca or Pb is relatively easy as sketched in Figure 4–2. Instrumenting the Ar-target is more challenging. LBNE engineers have a good solution at hand that we plan to adopt: provide argon gas in pressurized tubes, as depicted in Figure 7–13, and station the argon modules in the upstream region of STT.

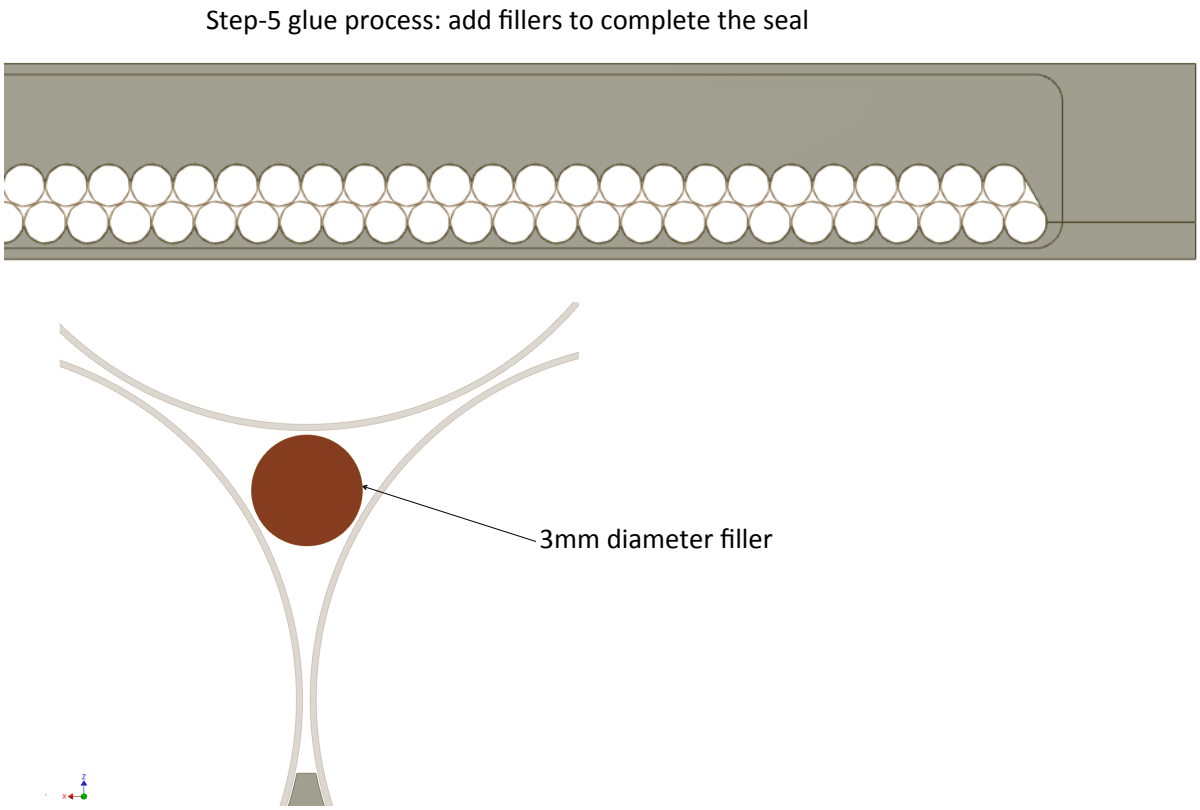

Figure 7–5: Straw Tube Tracker Module Assembly: Layout and sealing the module.

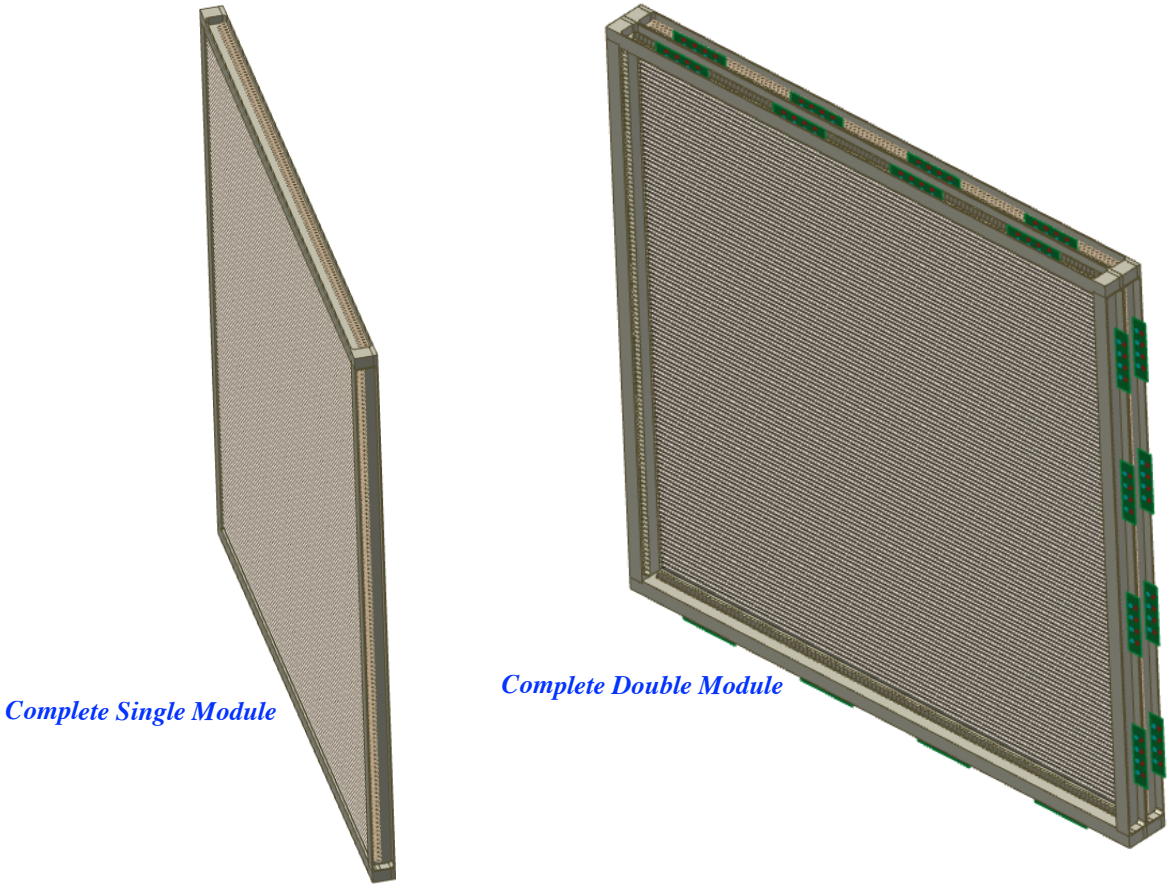

Figure 7–6: Straw Tube Tracker Module Assembly: Step 6.

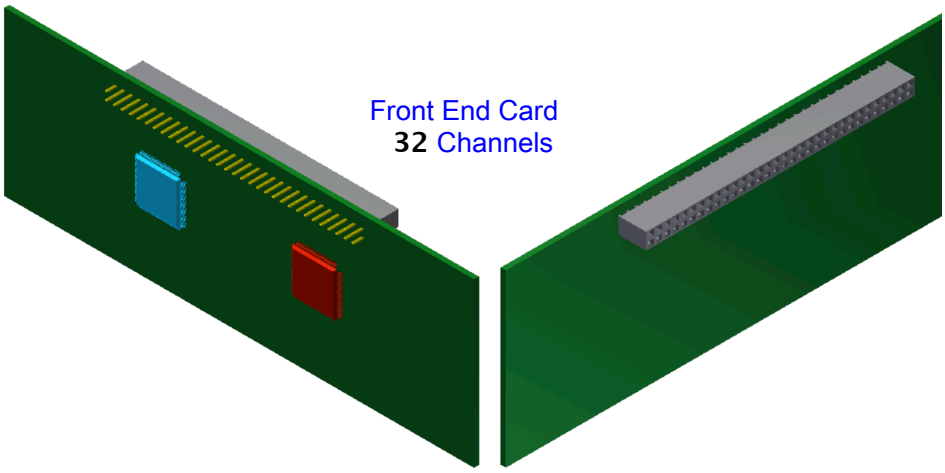

Figure 7–7: Straw Tube Tracker front-end board

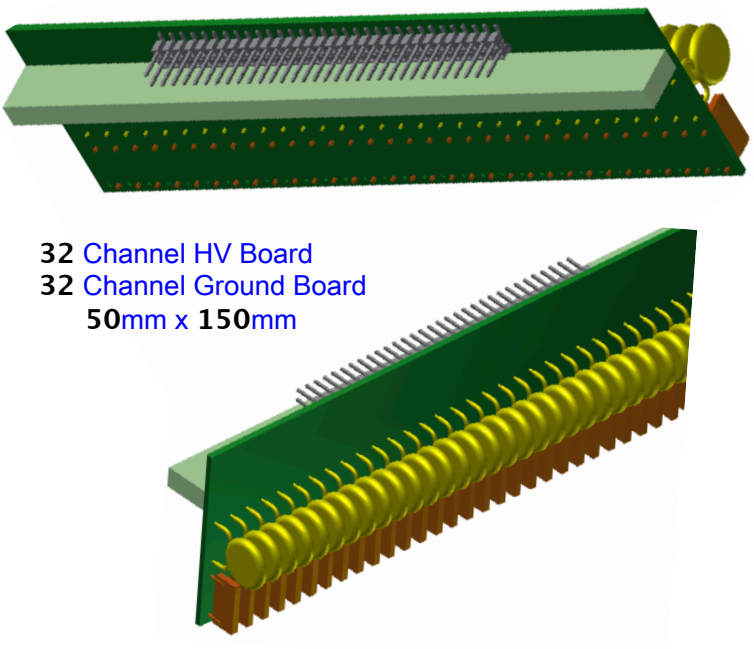

Figure 7–8: Straw Tube Tracker high-voltage and ground board

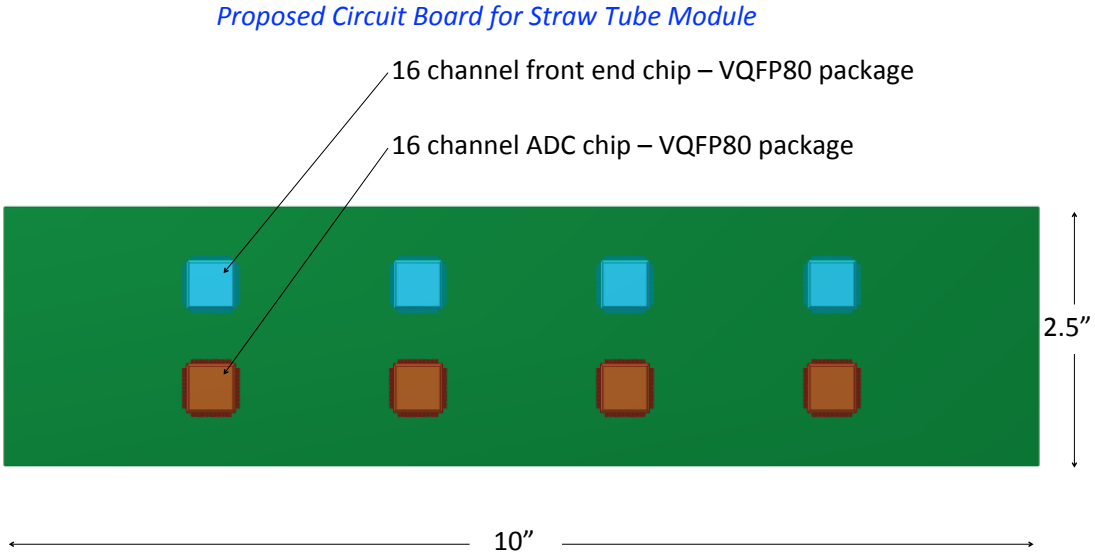

Figure 7–9: Straw Tube Tracker Circuit Board

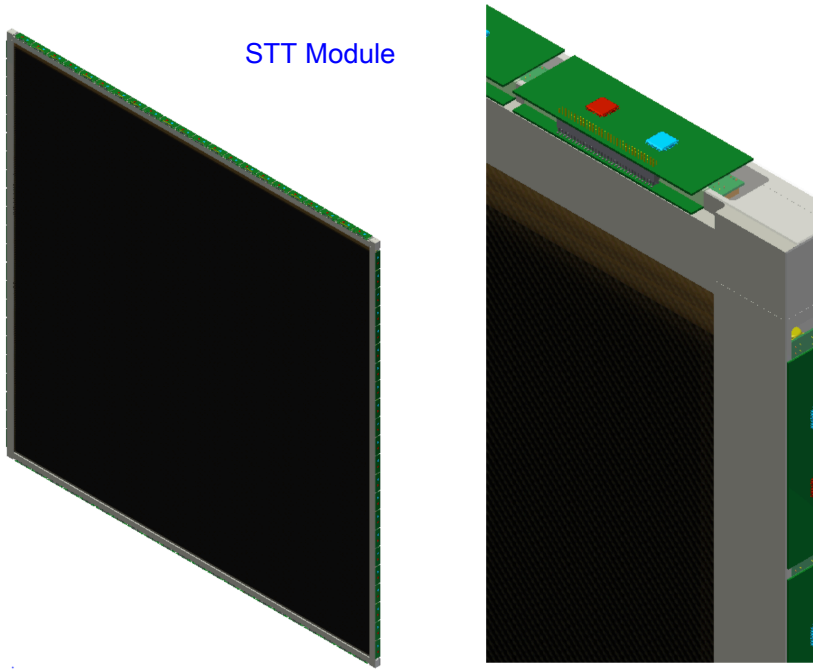

Figure 7–10: Straw Tube Tracker module

7.1.3 STT Fabrication Laboratories/Factories

This section describes the assumptions and requirements of the laboratories/factories that will produce the STT.

We foresee at least 2 (two) Indian institutions to act as production centers for the STT subsystem. A factory will be created at each production center, consisting of multiple assembly lines. The minimal number of assembly lines required for each factory is two, which is defining the Basic Production Unit (BPU).

Our starting assumption is that it would be possible for one BPU to produce 25 straw tubes per day using both assembly lines. Each BPU will thus produce 20000 to 25000 straws in about 800 days. We define the number of BPUs needed by this required throughput; therefore the large STT with 130000 straws will need five BPUs, which will be shared between two institutions acting as production centers. Each BPU is assumed to operate for a single eight hour shift, five days a week. The 3.5 m $\times$ 3.5 m final straw tube panel is planned to consist of subassemblies, each 1/3 the width of the entire panel, for ease of construction and handling. The full panel is assembled from the subassemblies outside the clean area where an overhead crane is available. The XX and YY assemblies are assumed to be identical. The target and radiators are assumed to be separate modules that are attached to the XX and YY panels to form a "super assembly." This concept forms the basis for the cost, resources and schedule — the Resource Loaded Schedule, or RLS — presented in the following section.

Figure 7–11: Straw Tube Tracker Basket

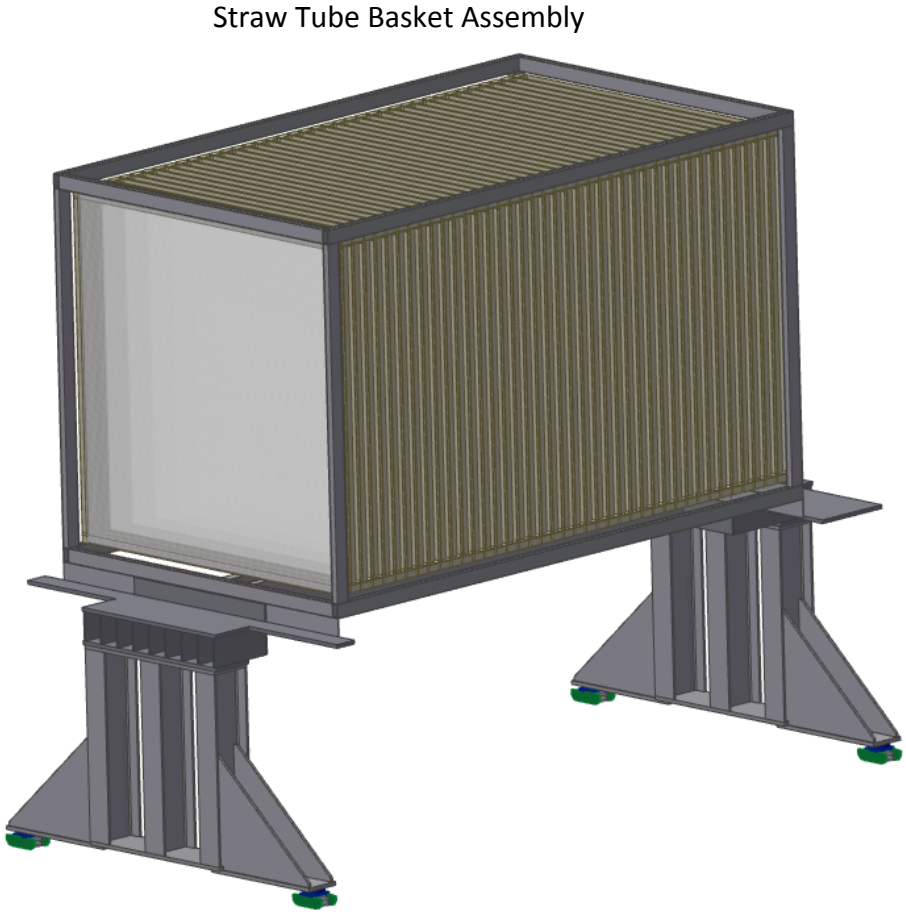

Figure 7–12: Straw Tube Tracker Basket Assembly

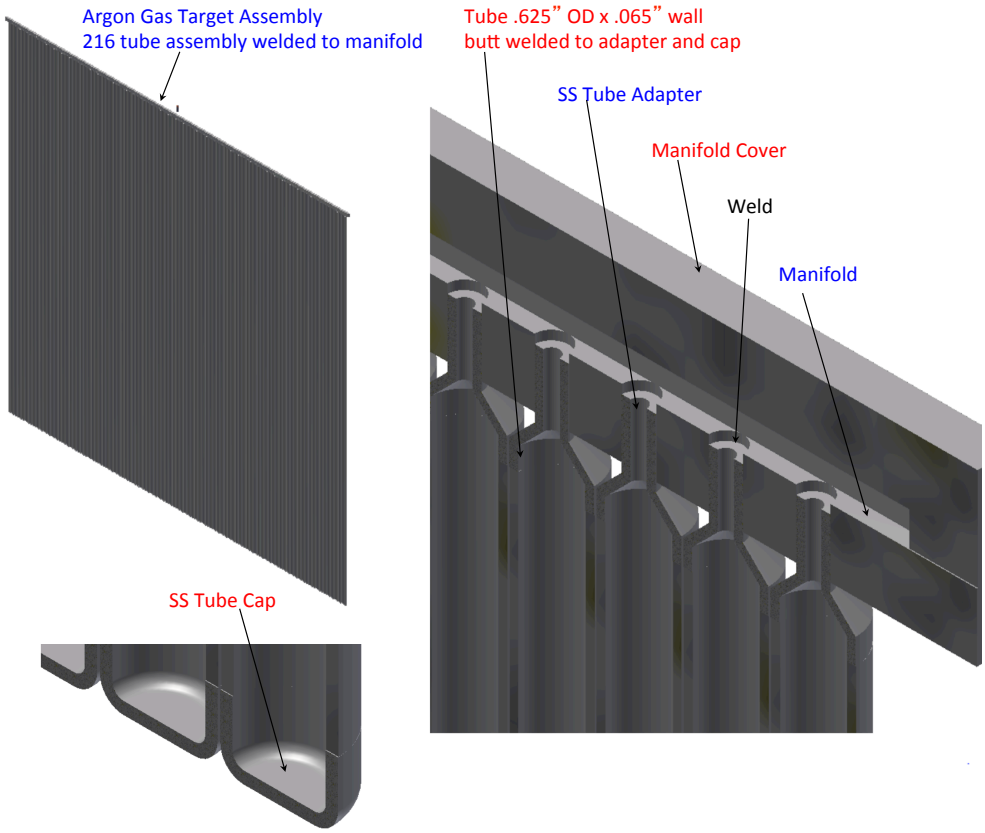

Figure 7–13: Engineering Drawing of Ar Target: Shown is a module of Ar gas in pressurized tube, positioned upstream of the STT.

Below, we present the requirements for the STT production factory, subject to change once detailed engineering designs are produced.

- Each factory / production center will be equipped with a class 1000 clean tent with HEPA filters, outfitted with sufficient power for the test equipment and plumbed with gas lines for testing the straw tubes. The area covered by the clean tent will depend upon the number of BPU active in the factory, each BPU requiring about 1,800 sq ft. The gas supply is outside of the clean tent. The gas for testing straws is Ar/CO_2 (70/30). Electronic equipment is inside the tent. Outside of the clean tent is a comparable area in size for assembly, testing and storage of the 3.5 m $\times$ 3.5 m modules. The target and radiators are assembled outside of the clean tent.

- Each straw tube assembly line has two large flat tables (100 μm flatness) to support the subassemblies, one for gluing and the other for testing. Optical tables (12 ft $\times$ 4 ft) are adequate for this purpose and have been costed in the RLS. A flat aluminum jig plate could be attached to the top of the table to slightly expand the flat surface area. Jigs are fabricated to sit on the flat tables to hold the straw tubes during the assembly and gluing processes and are fabricated to a tolerance of 50 μm. The jigs can be larger than the table. We envision that the jigs will be similar to those used in COMPASS. For each assembly line, one table is for gluing and one table is for testing.

- The 1/3 subassembly is tested after five gas purges and left under HV bias for three days as the tubes are flushed and the gas becomes more pure.

STT Manpower: Assuming 812 working day operation, we envision a total of about 111 FTE years for the STT fabrication ans test, where a FTE is defined as 1,600 labor hours (i.e. 200 days of 8 hours each). Each BPU will require 7 technicians/physicists to operate two assembly lines, for a total of 35 technicians/physicists. Taking into account the production schedule the manpower requirement is about 27 FTE/year.

7.2 Fabrication of the Electromagnetic Calorimeter

The construction of the ECAL is presented in this section.

7.2.1 Fabrication Steps

First, we present the steps for fabrication of one layer.

- **Procure Sci-bars, Fibers, Pb, Epoxy, etc.** A procedure must be in place to quality control the sci-bars, fibers, Pb, etc. If the extrusion of scintillator with in situ wavelength-shifter fiber is available then it will not only lower the ECAL cost and time but also will make it easier to maintain a better quality control.
- **Frame:** Affix the aluminium frame to the table.
- **Positioning of Sci-Bars:** Lay the bars inside the frames, using the locator pins through the frame to position them.
- **Adhesive for Pb:** Apply Araldite epoxy adhesive to the surface of the bars.
- **Positioning of Pb:** Lay the lead on top of the bars, ensuring that it overlaps the lip at the edge of the frame.
- **Curing:** Use a vacuum curing process overnight to cure the adhesive.

Next, we present the steps in the construction of one module of ECAL.

- Affix the bulkheads to the worktable.
- Lay the carbon-fiber outer skin inside the bulkheads.
- Affix the LI system LEDs to the carbon-fiber.
- Lay the (first) layer inside the bulkheads.
- Insert the WLS fiber into the bars, attach SiPM (MPPCs) and scanning electronics.
- Scan the layer using the 2D scanner and a 3mCi 137 Cs source.
- Repeat last three steps until finished with layers.
- Affix the LI system LEDs to the top carbon-fiber skin.
- Put the top carbon-fiber skin in place.
- Put all MPPCs (SiPM) in place, attach cables, group cables.
- Put cooling plates in place, feeding MPPC cables through.
- Attach busbars, electronic cards, cooling pipes, covers and structural supports.
- Cool the modules using dry nitrogen and water; electronic cards are all inside the module.

7.2.2 ECAL Fabrication Laboratories/Factories

We assume that the scintillator bars will be extruded with coating and delivered to the factory, as will the Pb-sheets, WLS fibers, frames and other sundry items. The factory will have a receiving area, fabrication area and testing area. Fabrication will involve assembling the scintillator and lead sheets into a module. Pre-fabricated ECAL frames will house each of the ECAL subassemblies.

The requirements of the ECAL production factory are presented below. These are subject to change once detailed engineering designs are produced.

- The factory requires lifting capability for an ECAL module. A 15-tonne crane would be adequate. The ECAL module subassembly must be of a size that can be transported easily and does not require capabilities greater than 15 tonnes for a crane or forklift.
- The factory should be clean with adequate ventilation since gluing and cleaning materials will be used.
- Lead and scintillator will be assembled into frames in place and moved to storage. A 3000 sq ft open floor space will be needed with floor loading capability for the modules (the required capacity is to be determined later).
- Workspace tables will be needed but no special tables are required, as in the STT case. Electronic test equipment will be available at each assembly area.

ECAL Manpower: For the ECAL, assuming a 270 work day duration, we anticipate the need for a total of about 8.3 FTE years for the ECAL fabrication and test. Taking into account the production schedule the manpower requirement is about 6 FTE/year.

7.3 Fabrication of the Dipole Magnet

The dipole magnet will closely follow the UA1 design, and does not require extensive R&D. It will require a careful examination and design effort by engineers and physicists. We anticipate having the iron-yokes (“C’s”) and Al-coil fabricated by commercial industries. The dipole magnet will be assembled at Fermilab.

It must be pointed that the Dipole must be the first deliverable since the installation of all other subdetectors depend upon the availability of the dipole because the subdetector are affixed to the magnet in one way or the other.

7.4 Fabrication of the the Muon-ID Detector

The muon-ID detectors are RPCs, for which many indigenous RPC-related efforts are already underway (CMS, ICAL-INO). Compared to these, the requirements for the HIRESMNU are modest. The Bakelite-based CMS model for fabricating the RPCs is sufficient for our needs.

The factory requirements are similar to those for the ECAL. The muon-ID detector factory must have a 15-tonne crane coverage. The RPCs are of a size that will be easily transportable using a crane or a forklift. The factory should be clean with humidity and temperature control. The factory will require a 3,000 sq ft open floor space with loading capability (to be determined). Workspace tables will be needed, as will electronic test equipment.

The manpower need is expected to be about half of what the ECAL fabrication requires, i.e. about 3.5 FTE years for an overall schedule of about one year.

7.5 Role of Industries

We expect to involve commercial industries in manufacturing straw tubes, scintillators/WLS-fiber, SiPMs, iron-yokes for the magnet and elements for RPCs.

7.6 Schedule for the Fabrication

The fabrication will begin in the fourth year of project, T0$\oplus$4-Years, while the construction of the prototypes is being concluded. One year will be devoted to the setting up of the factories including all the tooling, assembly, and storage needs. The streamlining of the procurement of the materials will also be in place. Next, the fabrication will commence lasting four to five years. All the subdetectors will be fabricated in parallel; the Dipole will be completed first, being the critical path item in the assembly of the ND. Finally, the subdetectors will be assembled in the LBNE beam at Fermilab. The assembly and testing will be completed in one year.

7.7 Preliminary Engineering Drawings (STT, ECAL, Assembled Detector)

We conclude the chapter with some preliminary engineering drawings for the STT and Barrel-ECAL in Figure 7–14 and the fully assembled detector in the open dipole in Figure 7–15.

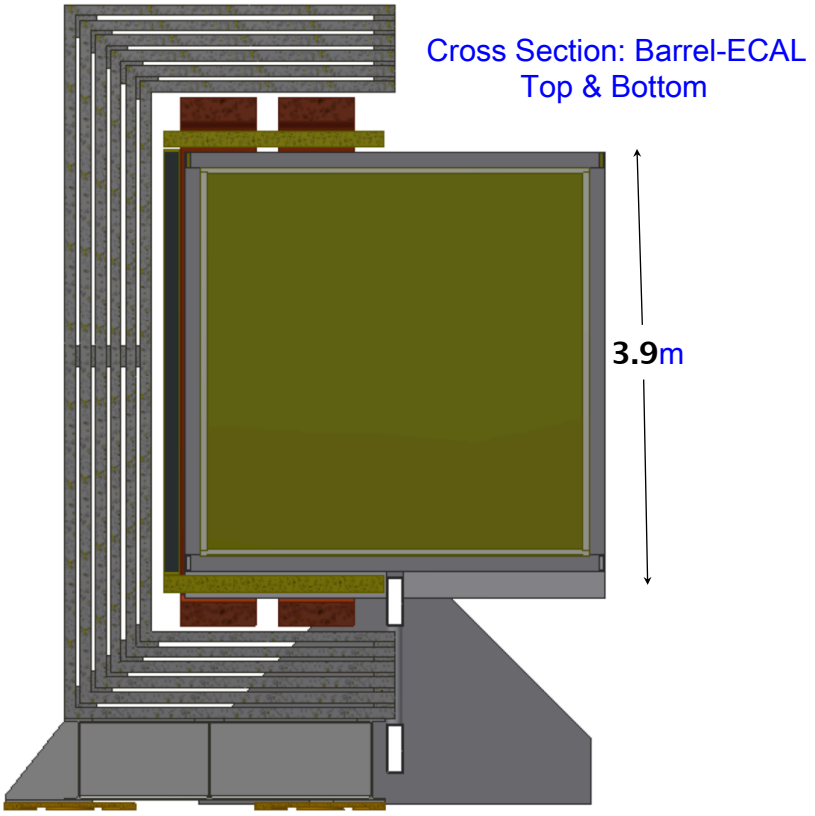

Figure 7–14: (Preliminary engineering drawing) Assembly of STT and Barrel-ECAL embedded in the dipole.

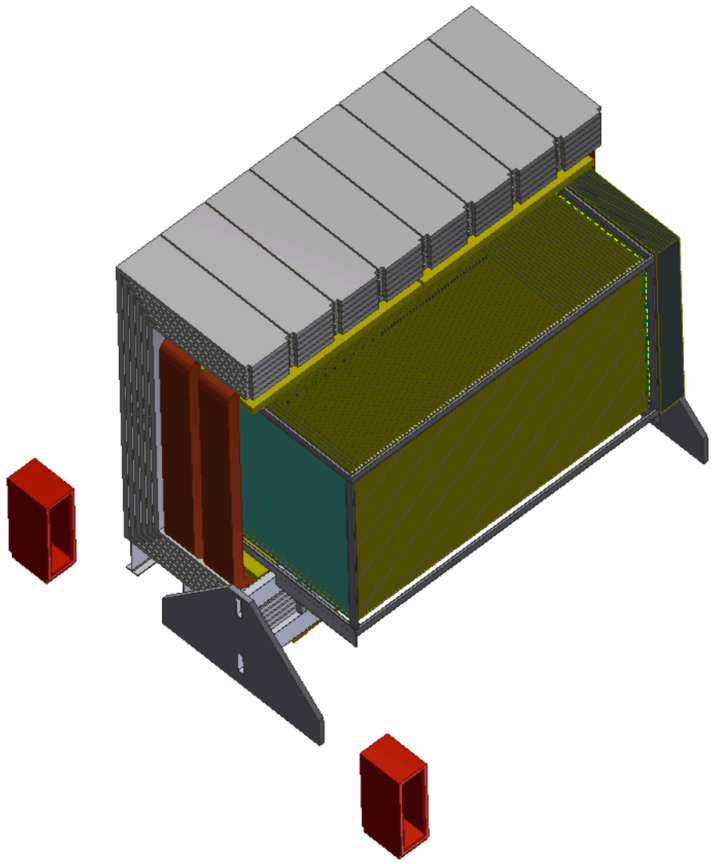

Figure 7–15: (Preliminary engineering drawing) Assembly of the complete HIRESMNU.

8 Proposed Contribution to the Liquid Argon Far Detector

Liquid argon time projection chamber (LArTPC) detectors provide superb resolution for particle detection, are relatively inexpensive, and the technology has come to be regarded as a promising candidate for large neutrino experiments. The LBNE Collaboration and Project have chosen this technology for their Far Detector (FD). In phase 1 of LBNE, there will be a 10-kilotonne fiducial mass detector sited on the surface at SURF, 1,300 km from Fermilab. Given the promise of the LArTPC technology, its complex cryogenic instrumentation and its physics potential, the LBNE FD offers opportunities for Indian institutions to both make a significant contribution to the LBNE project and to champion this promising new technology at home. LBNE is seeking to expand the design and construction of its FD into a fully global collaboration, in which India would be a leading participant. The specific areas of contribution by India will be determined in negotiations between Fermilab and DAE in the context of the development of this global collaboration over the next year or two. In this chapter we give an overview of the FD conceptual design, and point out several potential areas of Indian contributions to LBNE.

8.1 Overview of the Liquid Argon Far Detector

The Far Detector conceptual design for LBNE is a liquid argon (LAr) time projection chamber (TPC). The basic components of this type of detector include a cryostat to contain the LAr, a TPC detection mechanism immersed in the LAr, readout electronics and a cryogenic system to keep the LAr temperature at 87 K and maintain the required purity.

The LBNE Far Detector, referred to simply as the FD, consists of two large cryostats as shown in Figure 8–1, each of which holds a total of 9.4 kiltonnes of LAr. The active (instrumented) LAr mass of each is 6.7 kilotonnes and its fiducial mass, as defined for neutrino oscillation studies, is 5 kilotonnes.

A uniform electric field is created within the LArTPC volume between cathode planes and anode wire planes. The anode planes have three wire layers oriented at different angles to

allow 3D reconstruction of particle trajectories. Charged particles passing through the TPC ionize electrons that drift to the anode wire planes. The bias voltage is set on the anode plane wires so that ionization electrons drift between the first several (induction) planes and are collected on the last (collection) plane. Readout electronics amplify and continuously digitize the induced waveforms on the sensing wires at 2 MHz, and transmit these data to the data acquisition (DAQ) system for processing. In addition to these basic components, a photon-detection system provides a trigger for non-beam events, and helps distinguish the beam neutrino events from cosmic ray background.

The FD concept is designed for assembly from smaller-sized, independent unit cells that can be repeated almost indefinitely in any dimension to form the entire assembly within a large cryostat. Each of the standalone unit cells includes an independent mechanical structure to support the elements it contains. To a large extent, scaling from detector volumes containing anywhere from a few to several hundred such unit cells is straightforward with small and predictable risk.

The FD will be located on the site of the Sanford Underground Research Facility (SURF) at the former Homestake Mine in Lead, South Dakota. The detectors are built in a pit that will be excavated in the surface rock. A detector hall will be built above it to house electronics and cryogenic services and to allow access to the detectors. Rock excavated from the pit will be placed on top of the roof to provide a minimum of 3 m of solid-rock-equivalent shielding to absorb the hadronic and electromagnetic components of cosmic ray showers. The configuration is illustrated in Figure 8–2 and Figure 8–3.

8.1.1 Cryostat Construction

The cryostat construction uses commercial stainless-steel-membrane technology engineered and produced by industry. These vessels are widely deployed in liquefied natural gas (LNG) tanks and tanker ships, and are typically manufactured in sizes much larger than that required for the FD. The side walls consist of a series of membranes, foam insulation and reinforced concrete poured against the shotcrete covered rock. The inner (primary) membrane liner, made of stainless steel, is corrugated to provide strain relief from temperature-related expansion and contraction. The two FD membrane cryostats are hermetically sealed containers supported by the surrounding rock. This “in-ground” configuration offers access only from the top and protects against possible cryogen leaks out of the tank.

8.1.2 Cryogenic and LAr Purification Systems

The LAr requires infrastructure for transfer, cooling and purification. The LAr must be initially transferred to the cryostats and must be kept cold, pure and circulating smoothly during operations in order to maintain a sufficiently long drift lifetime for the ionization

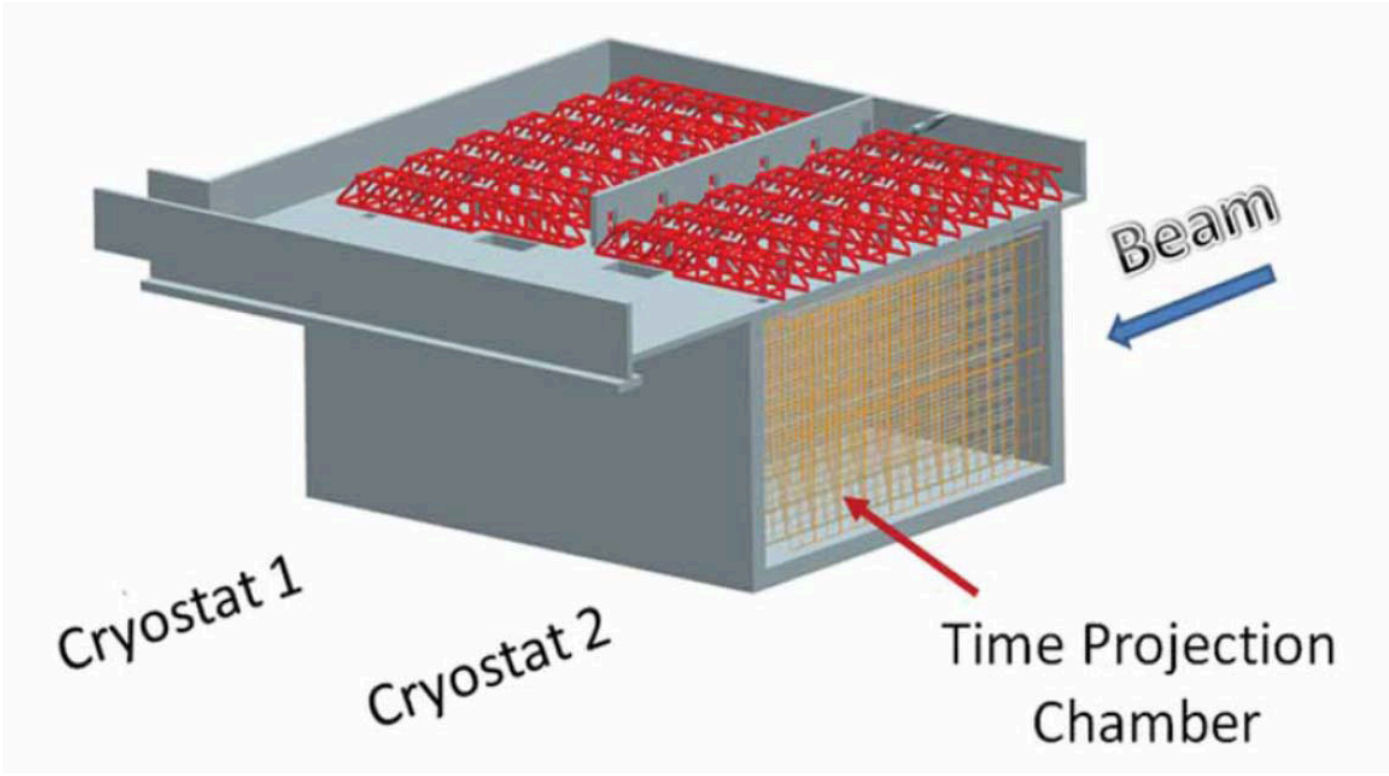

Figure 8–1: FD Configuration: The beam enters from the east, placing Detector (cryostat) 1 north of Detector 2.

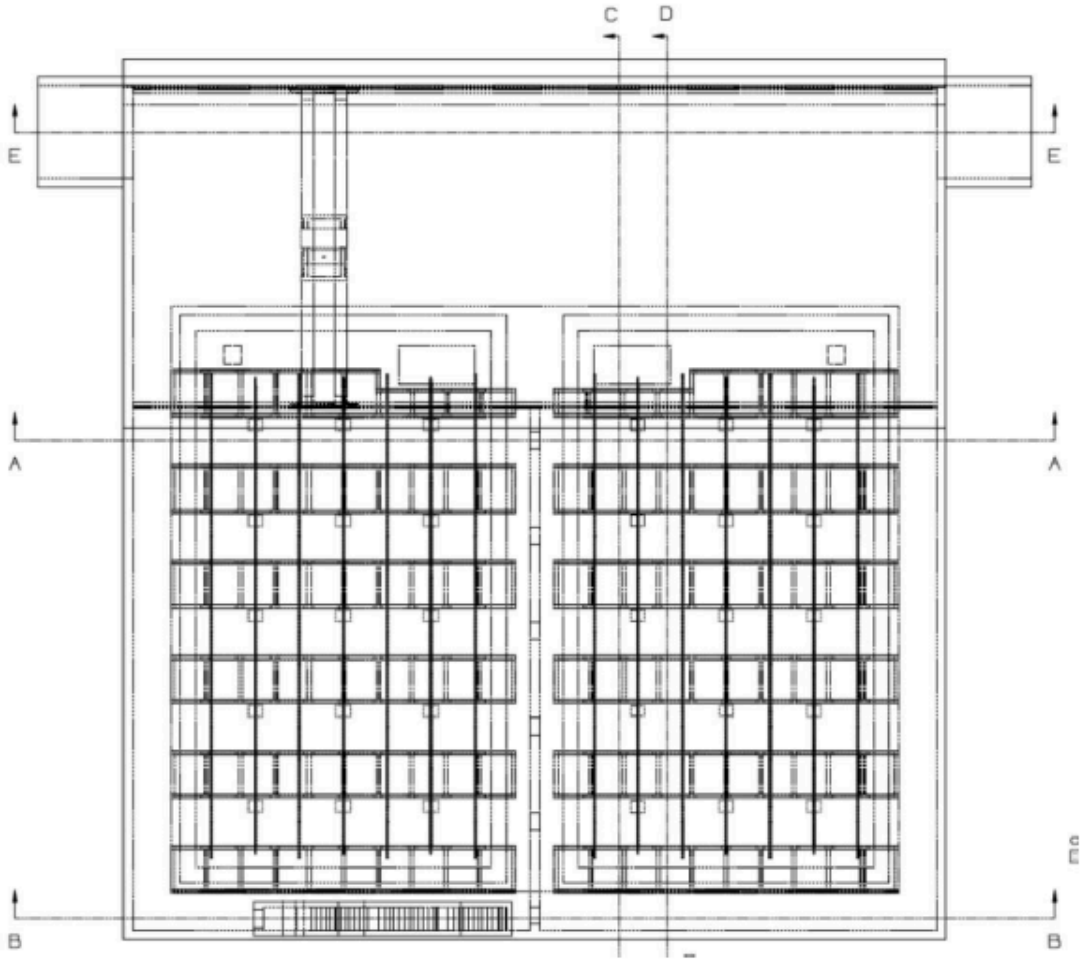

Figure 8–2: Plan view of the two-cryostat detector showing trusswork on top of detector; beam enters at bottom of the illustration; high bay is from the A-A line upwards.

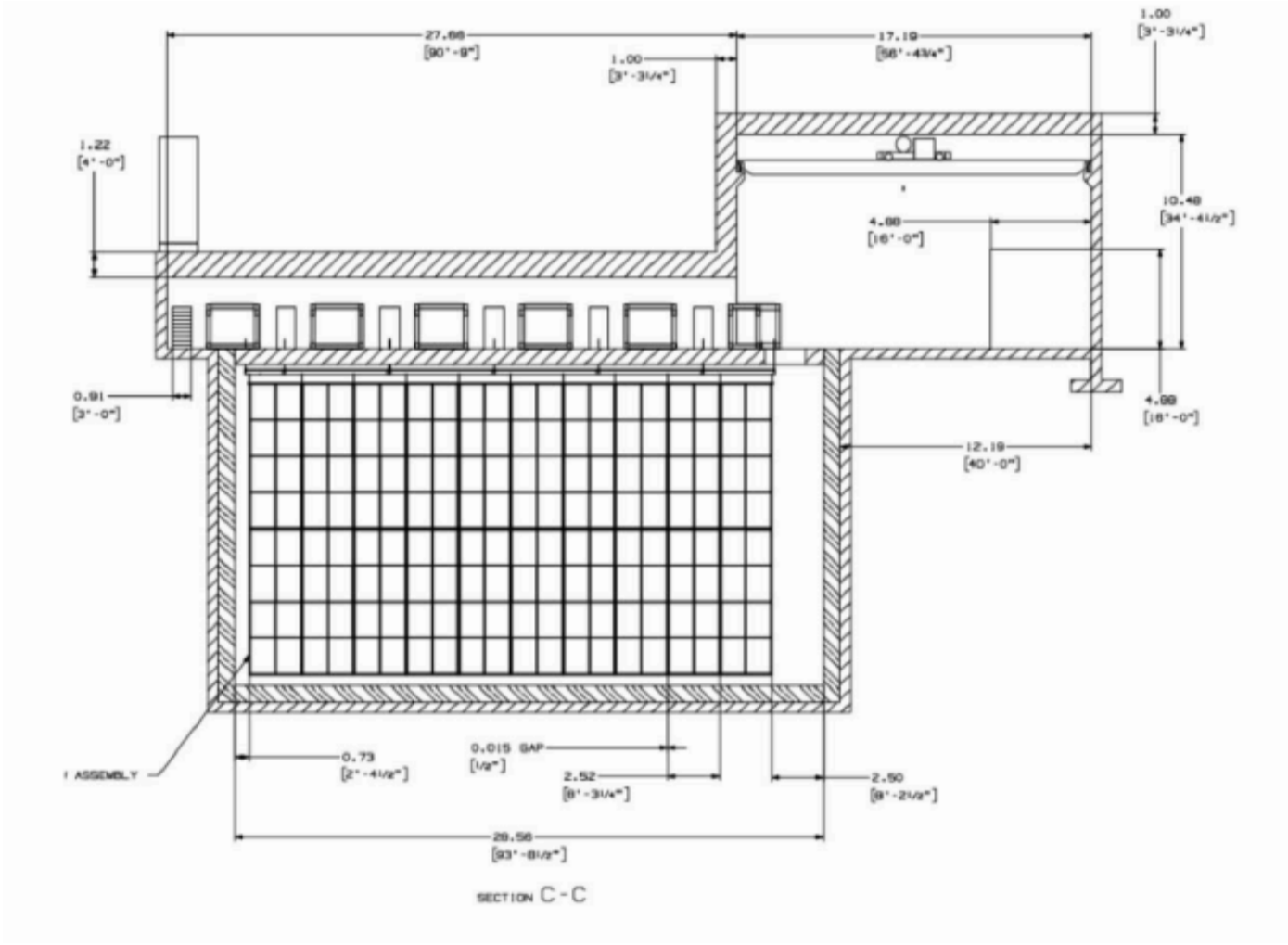

Figure 8–3: Vertical slice of detector (cross section C-C in Figure 8–4). Detector elements are shown in the cryostat, trusswork is above in the Detector Hall, and the high bay is to the right. The beam enters from the left in this view.

electrons. The major cryogenic systems used to perform these functions include the cryogen supply for cool-down and fill, gas filtration, argon condensing, liquid filtration and circulation and argon purity analysis. Three liquid nitrogen (LN) refrigerators (two operating and one spare) will provide a cooling capacity of 165 kW. Two 50-m^3 dewars provide LN and LAr storage. To allow the ionization electrons to be collected efficiently, the LAr must be purified of electronegative contaminants, principally oxygen, to below the 10^{-10} level. The purification of LAr is accomplished using molecular sieves and chemically reducing materials, a system that is scalable within the contemplated purity range to accommodate the estimated irreducible material-outgassing from warm materials in the vapor space above the LAr.

8.1.3 Time Projection Chamber

The Time Projection Chamber (TPC) is the active detection element of the FD. The construction concept is shown schematically in Figure 8–4. The TPC is located inside the cryostat vessel and is completely immersed in LAr at 87 K. The dimensions of its active volume are 14 m high, 14 m wide and 25 m long (in the beam direction). It has four rows of Cathode Plane Assemblies (CPA) interleaved with three rows of Anode Plane Assemblies (APA) that are oriented vertically, parallel to the beamline, with the electric field applied perpendicular to the planes. The maximum electron-drift distance between a cathode and an adjacent anode is 2.3 m. Both the cathode and anode plane assemblies are 2.5 m wide by 7 m high, a reasonable size for fabrication, handling and shipping. Two 7-m modules (either APA or CPA) stack vertically to instrument the 14-m active depth. In each row, 10 such stacks are placed edge-to-edge along the beam direction, forming the 25-m active length of the detector. Each cryostat houses a total of 60 APAs and 80 CPAs. A "field cage" surrounds the top, bottom and ends of the detector to ensure uniformity of the electric field. The field cage is assembled from panels of FR-4 sheets with parallel copper strips connected to resistive divider networks.

Each APA has three wire planes that are connected to readout electronics; two induction planes (labeled U and V in Figure 8–4) and one collection plane (X). A fourth wire plane, grid plane (G), is held at a bias voltage but is not instrumented with readout electronics. The grid plane improves the signal-to-noise ratio on the U plane and provides electrostatic discharge protection for the readout electronics. At a nominal wire pitch (center-to-center separation) of 4.5 mm, the total number of readout channels in an APA is 2560. With 60 APAs in each module, this comes to a total of 153,600 channels in each cryostat.

8.1.4 Electronics, Readout and Data Acquisition

Requirements for low noise and for extreme purity of the LAr motivate locating the front-end electronics directly in the LAr (hence "cold electronics"). CMOS electronics, which has

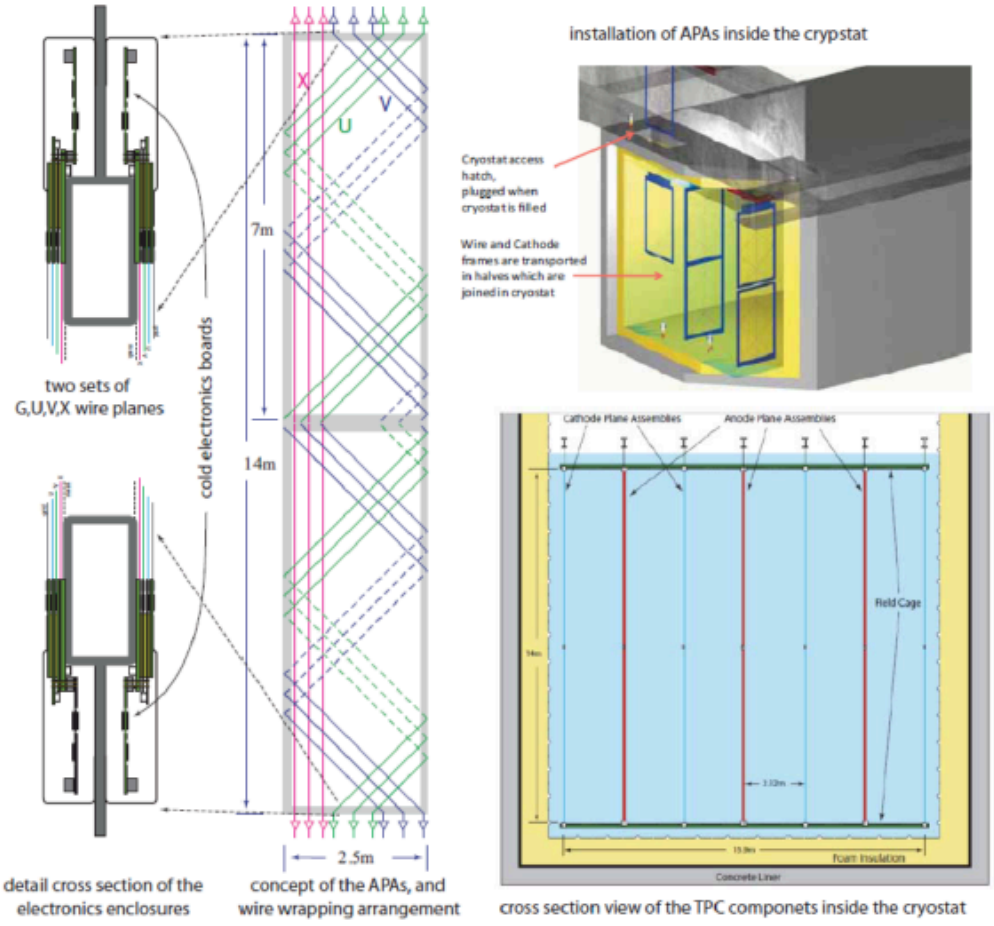

Figure 8–4: TPC modular construction concept

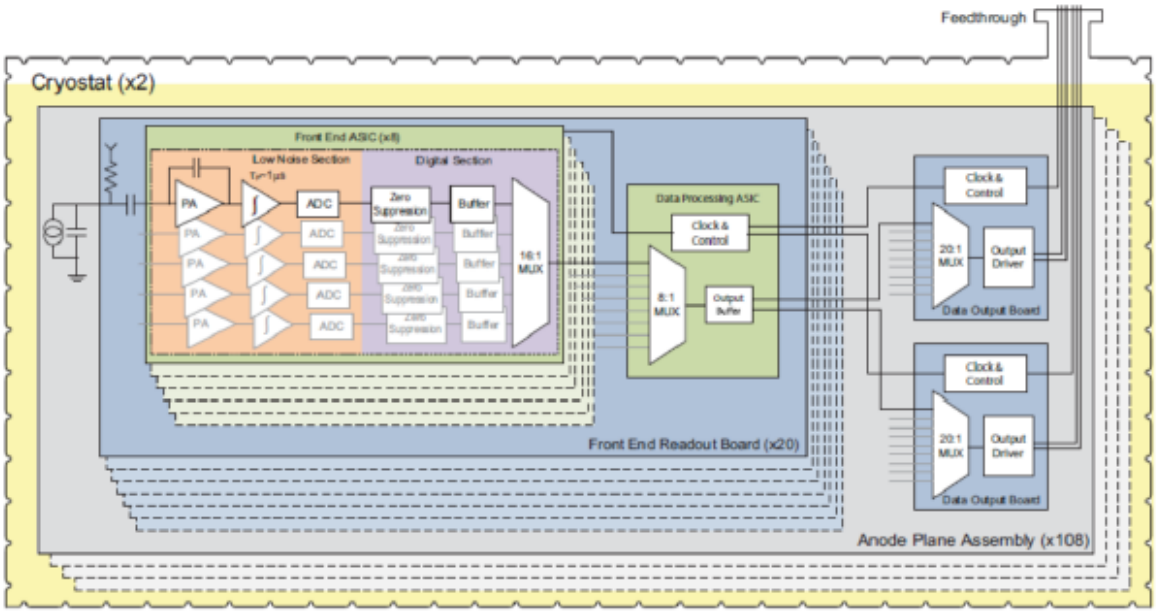

Figure 8–5: Conceptual front-end electronics architecture

a series noise minimum near 87 K, is used. Signal zero-suppression and multiplexing will be implemented, minimizing the number of cables and feedthroughs in the vapor space above the LAr, therefore reducing contamination from cable outgassing. Figure 8–5 shows the conceptual architecture of a front-end electronics design that meets the requirements for the FD. The entire electronics chain is immersed in the LAr. All signal feedthroughs will be placed at the top of the cryostat, where they are easily installed, always accessible, maintained at low hydrostatic pressure and where they pose no risk of LAr leakage. The cold electronics system will include digitization, buffering, and some level of digital output multiplexing. Output data links will include redundancy to eliminate the effect of any single-point failure. The data acquisition (DAQ) system is illustrated in Figure 8–6, including components in the cryostat, those on the detector just outside the cryostat, and those in a local counting room. Altogether, there will be 307,200 channels read out every 0.5 μsec.

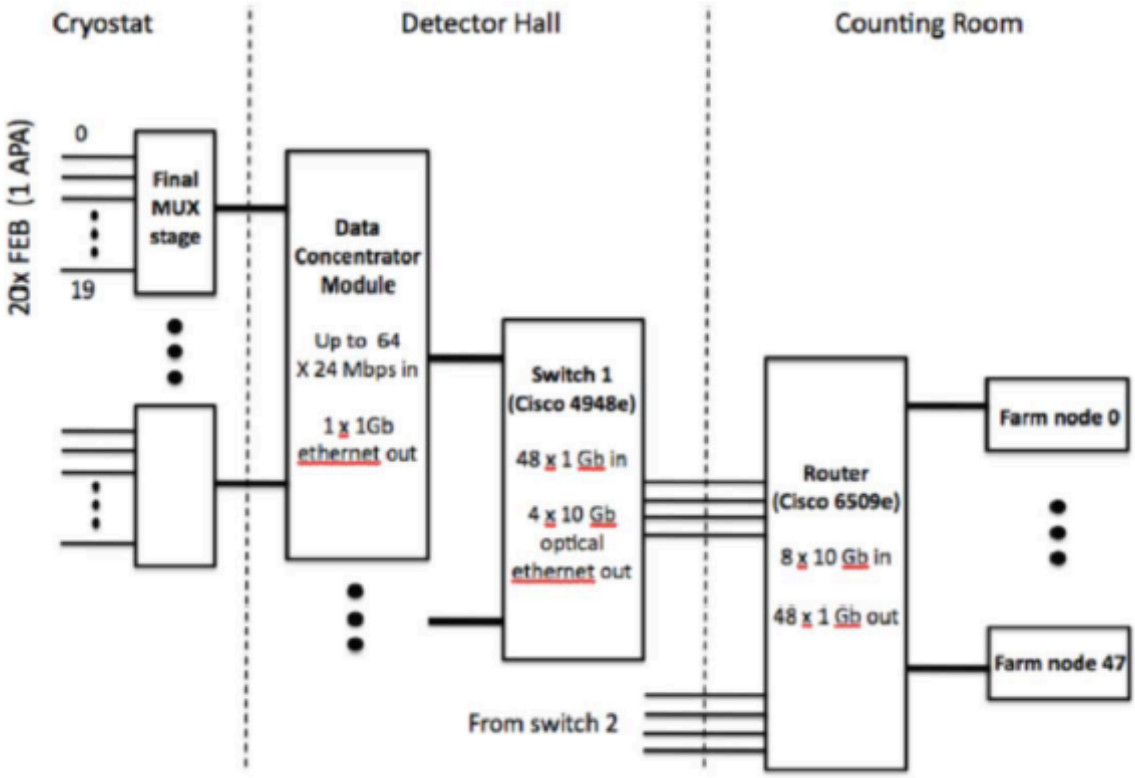

Figure 8–6: Block diagram of the DAQ conceptual architecture

8.1.5 Photon-Detection System

Identification of the different possible charged-particle types depends on accurate measurements of ionization along tracks. This requires accurate determination of the time of interaction, or event time, t_e, which leads to the absolute location of the event along the drift axis, and allows correction for attenuation of the ionization charge during the drift time and thereby the determination of Q_0, the true ionization charge. For beam-induced events, t_e is determined from the known time of the accelerator beam spill, but for non-accelerator physics events, t_e is not known a priori. However, LAr is an excellent scintillator, generating of the order 10^4 128-nm photons per MeV of deposited energy. Detection of scintillation photons provides a prompt signal that allows unambiguous location of particle positions along the drift axis. Photon detection is also important for mitigating the effects of the significant cosmic ray backgrounds expected for a surface detector by allowing events out-of-time with the 10 μsec long beam spill to be rejected.

The photon-detection system consists of acrylic light-guides that lead to small photomultiplier tubes (PMTs) or silicon photomultipliers (SiPM), as shown in Figure 8–7. A wavelength shifting coating on the light guides efficiently converts the scintillation photon wavelength from 128 nm to 428 nm where the PMT is most sensitive. Approximately 5% of the converted photons are captured within the light guide and travel to the PMT. The fast PMT signals will be routed out of the cryostat to standard readout electronics. Ten light-guide and PMT assemblies, or "paddles", will be installed within each APA frame prior to wire winding, between the left- and right-facing wire planes.

8.2 Potential Areas of Indian Contribution to the LBNE Far Detector

The LAr Far Detector presents many opportunities for India to make significant contributions to LBNE while also advancing domestic capabilities in this cutting edge detector technology. Indian involvement in almost any aspect of the detector design and construction is possible, although for the moment the discussions center on the Time Projection Chamber (TPC), which is the active detector element and the heart of the FD. This would involve the design, construction and testing of 120 Anode Plane Assemblies, 160 Cathode Plane Assemblies, and the associated field cage modules. This task is critical to the success of the LBNE, represents a standalone task that can be accomplished by two or three DAE and DST institutions, and offers a fitting complementarity to our contribution to the ND complex. It would constitute a major accomplishment by our institutions. In addition, there may be opportunities for Indian contribution to the photon detection system or the cold electronics, which are attached to the APA, or to the cryogenics and liquid argon purification systems, which could involve Indian industry in this advanced project. Due to budgetary limitations in the US the only prototype detector currently planned by the LBNE project is a cryostat containing 35 t of

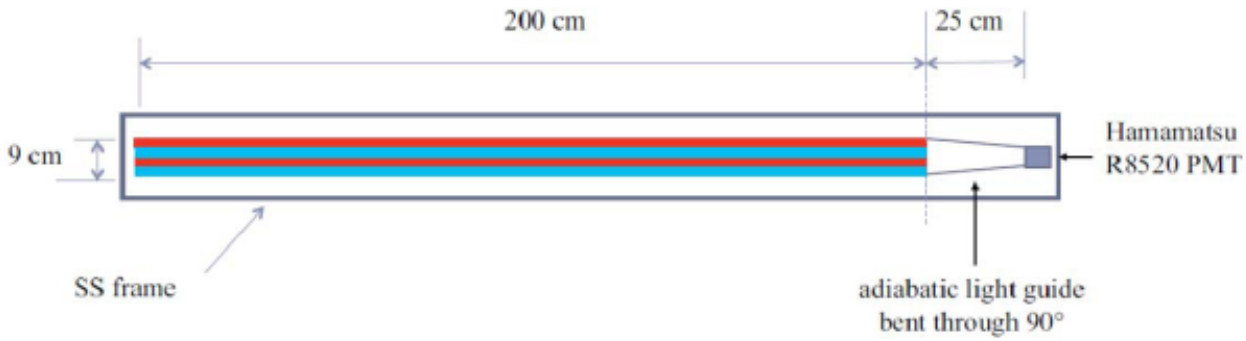

Figure 8–7: Photon detection system, consisting of wavelength shifter coated guides read out by standard or silicon PMTs.

LAr, which is too small to hold a full-size TPC module. It would be desirable for the LBNE program to include a larger-scale prototype which would include at least one full-size APA-CPA pair with associated field cage and a drift distance of up to the 2.3 m. Construction of such a prototype, including a dewar large enough to hold a full TPC module with associated cryogenic and argon purification systems, could be a significant contribution by India to demonstrate the engineering design of the LBNE Far Detector, and would put India at the heart of the project.

As we pointed out in the introduction to this chapter these proposed LArTPC research areas of contribution are preliminary and open to further negotiations between Fermilab and DAE. The actual work that we would do will be established in the context of this developing collaboration.

9 LBNE-India: Project Management and Execution

9.1 Management

The LBNE-India Project will be under the management of the larger Indian Institutions and Fermilab Collaboration (IIFC). The entire IIFC governance will adhere to the joint recommendations by the DAE and DOE. The LBNE-India Project will be managed by Indian and US counterparts. Similarly the ND project will have project managers from India and the US. As the project evolves into designing and building of the subdetectors, each subdetector will have an Indian leader and a corresponding US scientist. Throughout this project, there will be a close working collaboration and equal partnership between the Indian and US scientists.

9.2 Timeline

R&D Simulation and Design: 2 Years: The simulation and design studies will take two years. It is anticipated that the ND project will be reviewed by Fermilab about 18 months after the start.

R&D Prototype Construction and Factory Design: 3 Years After the simulation studies, the prototype construction of the STT, ECAL and muon-ID subdetectors will begin. The prototypes will include smaller versions of these subdetectors; the STT and ECAL prototypes will be calibrated in a test beam at Fermilab. While the test-beam measurements are underway, we propose to build one module each of the full-scale subdetectors. The last year of this phase will be devoted to the setting up of production factories for the subdetectors, building the necessary tooling, and streamlining the material procurement from industries. The R&D phase will end after three years.

Full Scale Detector Fabrication: 4–5 Years: Next the full-scale production of all the subdetectors will begin. The Magnet is the critical-path item which must be ready before other subdetectors can be assembled. The production will last for four to five years.

Assembly and Test: 1 year: The subdetectors will be shipped to Fermilab, assembled in the ND hall, and tested. The task will take about one year, i.e., the LBNE ND will be ready to take data starting in 2023–2024.

9.3 Near Detector Technology Selection and Review

This document describes a design for a Near Detector for LBNE. The proposed design will meet the scientific goals of LBNE and satisfy the mandate given to the IIFC-nP by DAE. The LBNE collaboration will continue to fine-tune the design based on the R&D that we propose to carry over the next several years. The proposed design will undergo the standard joint US-India review procedures of the LBNE collaboration and the funding agencies.

The DAE mandated a program:

1. Which is rich in physics, capable of producing 50-100 PhDs from Indian Institutions;

2. Which builds India's scientific infrastructure;

3. Which constitutes a significant contribution to the Fermilab project with a DAE/DST ownership; and

4. Which shares synergy with the ongoing research programs in India including the INO program.

The scientific goals of the ND are described in Chapters 2 and 3 of this document.

The LBNE Collaboration, of which IIFC-nP's Indian institutions are an integral part, may propose modifications of the design to Fermilab and the funding agencies (DAE/DST and DOE). If requested by the funding agencies, the LBNE-USA and LBNE-India Project Managers will establish review committee(s), in consultation with the LBNE spokesperson(s), LBNE Project Director, LBNE Executive Committee and with the concurrence of the Fermilab Director and the DOE-DAE Principal and Technical Coordinators. The review committee(s) will be charged to evaluate the modifications in light of the DAE mandates, the LBNE scientific goals, technical feasibility, cost and schedule. The LBNE Project Director

would evaluate these recommendations and submit the final recommendation to the Fermilab Director. The ultimate decision is made by the DAE/DST and DOE Principal Coordinators.

A Expected Physics Papers from HIRESMNU

We enumerate physics papers expected to come out of the proposed Near Detector for LBNE, HIRESMNU. The topics/papers are motivated by the published results by NOMAD, CCFR, NuTeV, MiniBOONE and other experiments.

Criteria for choosing the topics is as follows:

(A) Best Measurement: If the topic deals with a Standard Model measurement, then it should be the most precise measurement to date.

(B) Most Sensitive Search: If the topic involves a search, then it should be the most sensitive search to date.

(C) New Method: Where (A) and (B) are not applicable, the topic should include a novel measurement technique.

The list of topics is not complete. For example, it does not include topics involving detector development, R&D measurements or engineering efforts that typically are published in journals such as NIM and IEEE. The list is intended to illustrate the power of the high-resolution detector based on past experiments and on the outstanding physics potential of HIRESMNU. Over the duration of the project, expected to be ∼10 years, the number of theses/papers will be more than twice as many as the number of topics.

Neutrino Beam and Service to Long-Baseline Neutrino Experiments

1: The energy scale and relative flux of the muon-neutrino in the beam

2: The AntiNuMu to NuMu ratio as a function of neutrino energy in the beam

3: Abundance of NuE and AntiNuE relative to NuMu (NuMuBar) as a function of energy

4: Empirical determination of the Pi+, Pi-, K+, and K- yields in p-C interaction using neutrino data: a check of the hadro-production experiment

5: An empirical parametrization of K0L yield in the LBNE beam using the AntiNuE data

6: Measurement of the difference in the energy-scale of Antineutrino versus neutrino induced charged-current (CC) events

7: Measurement of the absolute neutrino/antineutrino flux using neutrino-electron neutral current scattering

8: Determination of the absolute NuMu flux using inverse muon decay (IMD)

Neutral-Pion and Eta Production in Neutrino-Nucleon Interactions
(Dominant background to the NuE/NuEBar Appearance)

9: Exclusive and quasi-exclusive single Pi0 production in NuMu-induced neutral current interactions

10: Exclusive and quasi-exclusive single Pi0 production in antineutrino-induced neutral current interactions

11: Multiplicity and energy distribution Pi0 production in the neutrino-induced neutral and charged current processes as a function of the hadronic energy

12: Multiplicity and energy distribution Pi0 production in the antineutrino-induced neutral and charged current processes as a function of the hadronic energy

13: The cross section of Pi0 production as a function of $\boldsymbol{x_F}$ and $\boldsymbol{P_T}$ in the neutrino charged current interactions

14: The cross section of Pi0 production as a function of $\boldsymbol{x_F}$ and $\boldsymbol{P_T}$ in the antineutrino charged current interactions

15: Multiplicity and energy distribution Eta production in neutral and charged current

processes in neutrino interactions

16: Multiplicity and energy distribution Eta production in neutral and charged current processes in antineutrino interactions

Charged-Pion & Kaon and Proton & Neutron Production in Neutrino & AntiNeutrino Interactions
(Dominant background to the NuMu and AntiNuMu Disappearance)

17: Coherent and quasi-exclusive single Pi+ production in NuMu-induced charged current interactions

18: Coherent and quasi-exclusive single Pi- production in AntiNuMu-induced charged current interactions

19: Charged Pion and Kaon production in the inclusive NuMu-induced neutral current and charged current interactions

20: Charged Pion and Kaon production in the inclusive AntiNuMu-induced neutral current and charged current interactions

21: Proton (Neutron) yield in inclusive NuMu-induced neutral current and charged current interactions

22: Neutron (Proton) yield in inclusive AntiNuMu-induced neutral current and charged current interactions

Neutrino-Electron Scattering

23: Measurement of the space-time structure of the weak current using the IMD

24: Search for the lepton-violating IMD in AntiNuMu interaction

25: Determination of the Weak Mixing Angle (WMA) using the neutrino-electron and antineutrino-electron scattering

26: Measurement of the chiral couplings, gL and gR, using neutrino-electron and antineutrino-electron neutral current interactions

Neutrino- and AntiNeutrino-Nucleon Neutral Current Scattering

27: Measurement of neutrino-induced neutral current to charged current ratio, Rnu, as a function of hadronic energy in the range 0.25–50 GeV

28: Measurement of antineutrino-induced neutral current to charged current ratio, Rnubar, as a function of hadronic energy in the range 0.25–50 GeV

29: Measurement of neutral current to charged current ratio in NuMu and NuMuBar interactions, Rnu and Rnubar, for hadronic energies above 3 GeV and determination of the Weak Mixing Angle

Non-Scaling Charged and Neutral Current Processes

30: Determination of the non-scaling contribution to the neutral current processes using the low hadronic energy interactions

31: Measurement of NuMu quasi-elastic CC interaction

32: Measurement of AntiNuMu quasi-elastic CC interaction

33: Measurement of NuE quasi-elastic CC interaction

34: Measurement of AntiNuE quasi-elastic CC interaction

35: Determination of the axial-mass, MA, from the QE cross section and the shape of the kinematic variables

36: Measurement of the axial form-factor of the nucleon from quasi-elastic interactions

37: Measurement of prompt radiative photon in NuMu and NuE quasi-elastic interactions

38: Measurement of prompt radiative photon in NuMuBar and NuEBar quasi-elastic inter-

actions

39: Measurement of NuMu induced resonance processes

40: Measurement of AntiNuMu induced resonance processes

41: Measurement of NuE induced resonance processes

42: Measurement of AntiNuE induced resonance processes

43: Measurement of resonant form-factors in neutrino interactions

44: Difference in the resonance processes in neutrino versus antineutrino interactions

45: Study of the transition between scaling and non-scaling processes in neutrino and antineutrino interactions

46: Constraints on the Fermi-motion of the nucleons using the 2-track topology of neutrino quasi-elastic interactions

47: Coherent -Rho+ production in neutrino-induced charged current interactions

48: Coherent -Rho- production in antineutrino charged current interactions

49: Measurement of the hadronic content of the weak current in neutrino interactions

50: Measurement of the hadronic content of the weak current in antineutrino interactions

51: Measurement of the absolute flux using the coherent-Rho0 production in antineutrino-nucleus scattering

52: Measurement of the absolute flux using the coherent-Rho0 production in neutrino-nucleus scattering

53: A precise measurement of antineutrino/neutrino flux ratio using the charged coherent-pion events

54: Test of the partially conserved axial current (PCAC) hypothesis using the coherent-pion interactions

55: Test of the conserved vector current (CVC) and vector meson dominance (VMD) hypotheses using coherent-rho interactions

56: Search for coherent-Phi production in neutral current interactions

57: Search for diffractive-J/Psi production in neutral current interactions

58: Neutral Current elastic scattering on proton, nu(bar) + p $\rightarrow$ nu(bar) + p

59: Measurement of the strange quark contribution to the nucleon spin, Delta-S

60: Determination of the weak mixing angle from NC elastic scattering off protons

Inclusive Charged Current Processes

61: Measurement of the inclusive NuMu charged current cross section in the energy range 0.5–50 GeV

62: Measurement of the inclusive AntiNuMu charged current cross section in the energy range 0.5–50 GeV

63: Measurement of the inclusive NuE charged current cross section in the energy range 0.5–40 GeV

64: Measurement of the inclusive NuEBar charged current cross section in the energy range 0.5–40 GeV

65: Measurement of the differential NuMu charged current cross section as a function of xbj, yBJ, and Enu.

66: Measurement of the differential NuMuBar charged current cross section as a function of xbj, yBJ, and Enu.

67: Determination of the xF3 and F2 structure functions in NuMu charged current interactions and the QCD evolution

68: Determination of xF3 and F2 structure functions in AntiNuMu charged current interactions and the QCD evolution

69: Measurement of the longitudinal structure function, FL, in NuMu and NuMuBar charged current interactions and test of QCD

70: Determination of the gluon structure function using NuMu and NuMuBar interactions

71: Quantitating the higher-twist effects in NuMu and NuMuBar interactions

72: Precise tests of the Gross-Llewylyn Smith sum-rules in QPM/QCD

73: Nuclear target and the NuMu and NuMuBar interactions at large-xBJ

74: Measurement of scaled momentum, rapidity, sphericity and thrust in (anti)neutrino charged current interactions

75: Search for rapidity gap in neutrino charged current interactions

76: Checking the quark-hadron duality in (anti)neutrino interactions

77: Determination of R=SigmaL/SigmaT at low momentum transfer

Nuclear Effects in (anti)Neutrino Interactions

78: Measurement of nuclear effects on F2 in (anti)neutrino scattering from ratios of Ar, Pb, Fe and C targets

79: Measurement of nuclear effects on xF3 in (anti)neutrino scattering from ratios of Ar, Pb, Fe and C targets

80: Study of (anti)shadowing in neutrino and antineutrino interactions and impact of axial-vector current

81: Measurement of axial form-factors for the bound nucleons from quasi-elastic interactions on Ar, Pb, Fe and C

82: Measurement of hadron multiplicities and kinematics as a function of the atomic number

Semi-Exclusive and Exclusive Hadron Production in Charged and Neutral Current Interactions

83: Measurement of charm hadron production via dileptons in NuMu, NuE, NuMuBar, and NuEBar CC interactions

84: Determination of the strange sea of the nucleon using the (anti)neutrino charm production and the QCD evolution

85: Search/Measurement of J/Psi production in neutral current interactions

86: Measurement of K0S, Lambda, and AntiLambda production in neutrino CC processes

87: Measurement of K0S, Lambda, and AntiLambda production in antineutrino CC processes

88: Measurement of K0S, Lambda, and AntiLambda production in neutrino NC processes

89: Measurement of K0S, Lambda, and AntiLambda production in antineutrino NC processes

90: Precise measurement of the Lambda and AntiLambda polarization in neutrino charged current interactions

91: Precise measurement of the Lambda and AntiLambda polarization in neutrino neutral current interactions

92: Measurement of the Lambda and AntiLambda polarization in antineutrino charged current interactions

93: Measurement of the Lambda and AntiLambda polarization in antineutrino neutral cur-

rent interactions

94: Inclusive production of rho0(770), f0(980) and f2(1270) mesons in (anti)neutrino charged current interactions

95: Measurement of backward going protons and pions in neutrino CC interactions and constraints on nuclear processes

96: D*+ production in neutrino charged current interactions

97: Determination of the D0, D+, Ds, LambdaC production fractions in (anti)neutrino interactions

98: Production of K*(892)+- vector mesons and their spin alignment in neutrino interactions

Search for New Physics and Exotic Phenomena

99: Search for heavy neutrinos using electronic, muonic and hadronic decays

100: Search for eV (pseudo)scalar penetrating particles

101: Search for NuMu—NuTau transition down to $< \mathbf{10^{-5}}$

102: Search for antiNuMu—antiNuTau transition down to $< \mathbf{10^{-4}}$

103: Search for NuMu—NuE transition down to $< \mathbf{3 \times 10^{-5}}$ and the LSND/MiniBOONE anomaly

104: Search for anitNuMu—anitNuE transition down to $< \mathbf{10^{-4}}$ and the LSND/MiniBOONE anomaly

105: Search for the exotic Theta+ resonance in the neutrino charged current interactions

106: Search for heavy neutrinos mixing with tau neutrinos

107: Search for an anomalous gauge boson in pi0 decays at the 120 GeV proton and primary target interactions

108: Search for anomaly mediated (anti)neutrino induced photons

109: Search for the magnetic moment of neutrinos

110: A test of NuMu–NuE universality down to $\mathbf{10^{-4}}$

111: A test of NuMuBar–NuEbar universality down to $\mathbf{10^{-3}}$ level

112: Search for right-handed current in CC interaction

References

[1] J. Hewett *et al.*, ANL-HEP-TR-12-25 and SLAC-R-991; arXiv:hep-ex/1205.2671.

[2] T. Akiri *et al.*, arXiv:hep-ex/1110.6249.

[3] Approved Physics Research Goals of LBNE before Reconfiguration, LBNE-DocDB-3056.

[4] F. P. An *et al.* (DAYA-BAY Collaboration), Phys. Rev. Lett. **108**, 171803 (2012); arXiv:hep-ex/1203.1669.

[5] F. P. An *et al.* (Daya Bay Collaboration), arXiv:hep-ex/1210.6327.

[6] J. K. Ahn *et al.* (RENO Collaboration), Phys. Rev. Lett. **108**, 191802 (2012); arXiv:hep-ex/1204.0626.

[7] S. R. Mishra, Prog. Part. Nucl. Phys. **64**, 202 (2010); S. Mishra *et al.*, arXiv:hep-ex/0812.4527, to be submitted to NIM; S. R. Mishra *et al.*, Letter of Intent submitted to Fermilab, February 2008, `http://www.fnal.gov/directorate/Longrange/Steering_Public/community_letters.html`.

[8] C. Anderson *et al.*, JINST **7**, P10019 (2012); arXiv:physics.ins-det/1205.6747.

[9] J. Altegoer *et al.*, (NOMAD collaboration), Nucl. Instrum. Meth. A **404**, 96 (1998).

[10] G. Bassompierre *et al.*, Nucl. Instrum. Meth. A **411**, 63 (1998).

[11] P. Astier *et al.*, (NOMAD collaboration), Nucl. Phys. B **611**, 3 (2001); arXiv:hep-ex/0106102.

[12] P. Astier *et al.*, (NOMAD collaboration), Phys. Lett. B **570**, 19 (2003); arXiv:hep-ex/0306037.

[13] C.T. Kullenberg *et al.*, (NOMAD collaboration), Phys. Lett. B **660**, 19 (2008); arXiv:hep-ex/0711.1183.

[14] P. Astier *et al.*, (NOMAD collaboration), Nucl. Phys. B **621**, 3 (2002); arXiv:hep-ex/0111057.

[15] D. Naumov *et al.*, (NOMAD collaboration), Nucl. Phys. B **700**, 51 (2004); arXiv:hep-ex/0409037.

[16] Q. Wu *et al.*, (NOMAD collaboration), Phys. Lett. B **660**, 19 (2008); arXiv:hep-ex/0711.1183.

[17] V. Lyubushkin *et al.*, (NOMAD Collaboration), Eur. Phys. J. C **63**, 355 (2009); arXiv:hep-ex/0812.4543.

[18] C. T. Kullenberg *et al.*, (NOMAD Collaboration), Phys. Lett. B **706**, 268 (2012); arXiv:hep-ex/1111.3713.

[19] T. Akesson *et al.*, Nucl. Instrum. Meth. A **522**, 131 (2004).

[20] T. Akesson *et al.*, Nucl. Instrum. Meth. A **522**, 50 (2004).

[21] T. Akesson *et al.*, IEEE Nucl. Sci. Symp. Conf. Rec. **2**, 1185 (2005).

[22] V. N. Bychkov *et al.*, Particles and Nuclei Letters, 2 (111) June 2002.

[23] K. Platzer *et al.*, IEEE Transactions on Nuclear Science, **52**, 793 (2005).

[24] J. E. Amaro *et al.*, Phys. Rev. C **82**, 044601 (2010).

[25] W. J. Marciano and Z. Parsa, J. Phys. G **29**, 2629 (2003).

[26] S. R. Mishra *et al.*, Phys. Rev. Lett. **63**, 132 (1989).

[27] S. R. Mishra *et al.*, Phys. Lett. B **252**, 170 (1990).

[28] P. Vilain *et al.*, (CHARM-II Collaboration), Phys. Lett. B **364**, 121 (1995).

[29] C. Arroyo *et al.*, (CCFR Collaboration), Phys. Rev. Lett. **72**, 3452 (1994); arXiv:hep-ex/9405008.

[30] G. P. Zeller *et al.*, (NuTeV collaboration), Phys. Rev. Lett. **88**, 091802 (2002); arXiv:hep-ex/0110059.

[31] E. A. Paschos and L. Wolfenstein, Phys. Rev. D **7**, 91 (1973).

[32] A. Kartavtsev, E. A. Paschos and G.J. Gounaris, Phys. Rev. D **74**, 054007 (2006); arXiv:hep-ph/0512139.

[33] A. Czarnecki and W.J. Marciano, Int. J. Mod. Phy. A **15**, 2365 (2000).

[34] S. Alekhin, S. A. Kulagin, and R. Petti, AIP Conf. Proc. **967**, 215 (2007).

[35] S. Alekhin, S. Kulagin, and R. Petti, arXiv:hep-ph/0810.4893.

[36] S. Alekhin, S. Kulagin and R. Petti, Phys. Lett. B **675**, 433 (2009).

[37] A. B. Arbuzov, D. Y. Bardin and L. V. Kalinovskaya, JHEP **78**, 506 (2005); arXiv:hep-ph/0407203.

[38] S. A. Kulagin and R. Petti, Nucl. Phys. A **765**, 126 (2006).

[39] S. A. Kulagin and R. Petti, Phys. Rev. D **76**, 094023 (2007).

[40] S. A. Kulagin and R. Petti, arXiv:hep-ph/1004.3062.

[41] R. Petti and O. Samoylov, Proceedings of DIS10 - Firenze, Italy, April 19-23, 2010.

[42] R. D. Young, J. Roche, R. D. Carlini and A. W. Thomas, Phys. Rev. Lett. **97**, 102002 (2006).

[43] D. B. Leinweber *et al.*, Phys. Rev. Lett. **94**, 212001 (2005).

[44] A. Airapetian *et al.*, Phys. Lett. B **666**, 446 (2008).

[45] L.A. Ahrens *et al.*, Phys. Rev. D **35**, 785 (1987).

[46] G. Garvey *et al.*, Phys. Rev. C **48**, 761 (1993).

[47] W. M. Alberico *et al.*, Nucl. Phys. A **651**, 277 (1999).

[48] L. Bugel *et al.*, arXiv:hep-ex/0402007.

[49] A. Czarnecki and W.J. Marciano, Int. J. Mod. Phy. A **15**, 2365 (2000).

[50] S. C. Bennet and C. E. Wieman, Phys. Rev. Lett. **82**, 2484 (1999).

[51] Particle Data Group, W.-M. Yao *et al.*, Journal of Physics, G **33**, 1 (2006).

[52] P. L. Anthony *et al.*, (E158 collaboration), Phys. Rev. Lett. **95**, 081601 (2005); arXiv:hep-ex/0504049.

[53] S. Alekhin, S. A. Kulagin and R. Petti, AIP Conf. Proc. **967**, 215 (2007); arXiv:hep-ph/0710.0124.

[54] S. Alekhin, S. A. Kulagin and R. Petti, NUINT 07, Fermilab, Batavia, May 30 - June 3, 2007, talks in http://conferences.fnal.gov/nuint07/.

[55] A. B. Arbuzov, D. Y. Bardin and L. V. Kalinovskaya, JHEP **78**, 506 (2005); arXiv:hep-ph/0407203.

[56] K. P. Diener, S. Dittmaier and W. Hollik, Phys. Rev. D **69**, 073005 (2004).

[57] S. A. Kulagin and R. Petti, Nucl. Phys. A **765**, 126 (2006); arXiv:hep-ph/0412425.

[58] S. A. Kulagin and R. Petti, Phys. Rev. D **76**, 094023 (2007); arXiv:hep-ph/0703033.

[59] S. Bultmann (CLAS Collaboration), AIP Conf. Proc. **1369**, 114 (2011).

[60] D. Allasia *et al.*, Z. Phys. C **28**, 321 (1985).

[61] M. Shiozawa, Talk at NNN09: http://nnn09.colostate.edu/Talks/Session02/091007-Shiozawa-Nucleon-decay-searches-dist.pdf

[62] S. Mine *et al.*, (K2K Collaboration), Phys. Rev. D **77**, 032003 (2008); H. Nishino *et al.*, (Super-Kamiokande Collaboration), Phys. Rev. Lett. **102**, 141801 (2009).

[63] T. Adams *et al.*, (NuTeV collaboration), Phys. Rev. Lett. **87**, 041801 (2001); arXiv:hep-ex/0104037.

[64] A. A. Aguilar-Arevalo *et al.*, (MiniBOONE collaboration), Phys. Rev. Lett. **98**, 231801 (2007); arXiv:hep-ex/0704.1500.

[65] T. Asaka and M. Shaposhnikov, Phys. Lett. B **620**, 17 (2005); arXiv:hep-ph/0505013.

[66] D. Gorbunov and M. Shaposhnikov, JHEP **10**, 015 (2007); arXiv:hep-ph/0705.1729. We thank the authors for providing a dedicated calculation for our experiment.

[67] G. Ambrosini *et al.*, (SPY Collaboration), Phys. Lett. B **420**, 225 (1998).

[68] G. Ambrosini *et al.*, (SPY Collaboration), Phys. Lett. B **425**, 208 (1998).

[69] G. Ambrosini *et al.*, Eur. Phys. J., C **10**, 605 (1999).

[70] H.W. Atherton *et al.*, CERN Yellow Report 80-07, 1980.

[71] G. Acquistapace *et al.*, CERN-ECP/95-14.

[72] P. Astier *et al.*, Nucl. Instrum. Meth. A **515**, 800 (2003).

[73] S. R. Mishra, Review talk presented at *Workshop on Hadron Structure Functions and Parton Distributions*, Fermilab, April, 1990; World Scientific, 84-123 (1990), Ed. D. Geesaman *et al.*; Nevis Preprint # 1426, June 1990.

[74] A. Bodek *et al.*, Eur. Phy. J. C **72**, 1973 (2012); arXiv:hep-ex/1201.3025.

[75] I. Stancu *et al.*, arXiv:hep-ex/0910.2698.

[76] The OscSNS Neutrino Experiment: http://physics.calumet.purdue.edu/~oscsns/.

[77] B. Baibussinov *et al.*, arXiv:hep-ex/0909.0355.

[78] S. A. Kulagin and R. Petti, arXiv:hep-ph/1004.3062.

[79] S. A. Kulagin and R. Petti, Nucl. Phys. A **765**, 126 (2006); arXiv:hep-ph/0412425.

[80] S. Alekhin, S. A. Kulagin and R. Petti, AIP Conf. Proc. **967**, 215 (2007); arXiv:hep-ph/0710.0124.

[81] S. A. Kulagin and R. Petti, Phys. Rev. D **76**, 094023 (2007); arXiv:hep-ph/0703033.

[82] A. V. Butkevich and S. A. Kulagin, Phys. Rev. C **76**, 045502 (2007); arXiv:nucl-th/0705.1051.

[83] A. V. Butkevich, Phys. Rev. C **80**, 014610 (2009); arXiv:nucl-th/0904.1472.

[84] A. Boyarsky, O. Ruchayskiy and M. Shaposhnikov, Ann. Rev. Nucl. Part. Sci. **59**, 191 (2009); arXiv:hep-ph/0901.0011.

[85] M. Shaposhnikov, JHEP **08**, 008 (2008); arXiv:hep-ph/0804.4542.

[86] A. M. Cooper-Sarkar *et al.*, (WA66 Collaboration), Phys. Lett. B **160**, 207 (1985).

[87] F. Bergsma *et al.*, (CHARM Collaboration), Phys. Lett. B **166**, 473 (1986).

[88] A. Vaitaitis *et al.*, (NuTeV Collaboration), Phys. Rev. Lett. **83**, 4943 (1999); arXiv:hep-ex/9908011.

[89] G. Bernardi *et al.*, Phys. Lett. B **166**, 479 (1986).

[90] G. Bernardi *et al.*, Phys. Lett. B **203**, 332 (1988).

[91] A. Atre, T. Han, S. Pascoli and B. Zhang, JHEP **05**, 030 (2009); arXiv:hep-ph/0901.3589.

[92] M. Soderberg, arXiv:physics.ins-det/0910.3433.

[93] M. Maltoni and T. Schwetz, arXiv:hep-ph/0705.0107.